Department of Chemical Engineering

Design of metal oxide-based catalysts for the thermo- and photoelectrocatalytic transformation of the greenhouse gas N_2O

PhD Thesis

Doctoral Program in Chemical, Environmental and Process Engineering

A thesis submitted to the Universitat de València to fulfil the requirements for the doctoral degree by

GINEBRA SÁNCHEZ GARCÍA

Thesis supervisors:

Dr. Benjamín E. Solsona Espriu

Dr. Rita Sánchez Tovar

July 2025

INFORME FAVORABLE DE LOS DIRECTORES DE TESIS

Dr. Benjamín Solsona Espriu, catedrático del Departamento de Ingeniería Química de la Universitat de València, y **Dra. Rita Sánchez Tovar**, profesora titular del Departamento de Ingeniería Química de la Universitat de València,

CERTIFICAN que

Dña. Ginebra Cristina Sánchez García, graduada en Ingeniería Química y con título de Máster en Ingeniería Química, ha realizado bajo su dirección el trabajo que bajo el título de "**Design of metal oxide-based catalysts for the thermo- and photoelectrocatalytic transformation of the greenhouse gas N_2O"** presenta en esta Memoria y que constituye su Tesis para optar al Título de Doctor con Mención Internacional por la Universitat de València en el Programa de Doctorado en Ingeniería Química, Ambiental y de Procesos. Y para que conste a los efectos oportunos, firman el presente certificado en Valencia a 8 julio de 2025.

Dr. Benjamín Solsona Espriu Dra. Rita Sánchez Tovar

Agradecimientos

En primer lugar, quiero agradecer a mis directores de tesis, Benjamín Solsona y Rita Sánchez, por haberme dado la oportunidad de realizar esta tesis doctoral bajo su tutela. Nada de esto habría sido posible sin vuestra guía constante, vuestro apoyo, tanto en lo académico como en lo personal, y vuestra plena confianza en mí desde el principio. Gracias por vuestra paciencia y por vuestro compromiso con este trabajo. Ha sido un absoluto privilegio teneros como referentes durante estos años.

Agradezco a la Conselleria de Innovación, Universidades, Ciencia y Sociedad Digital de la Generalitat Valenciana por la subvención obtenida para realizar la presente tesis doctoral (CIACIF/2021/010) y la estancia en un centro de investigación internacional (CIBEFP/2023/161).

También quiero agradecer al grupo de investigación IQCATAL, destacando especialmente a Ramón, María, Rut y Gemma, por ayudarme con todo desde el primer día. Me siento muy orgullosa, además de privilegiada, de haber formado parte de este grupo y de haber podido trabajar rodeada de personas tan comprometidas y generosas. En especial, agradecer a la parte "junior" de este grupo: Adrián, Alberto y Elianny. Sin duda, el doctorado hubiera sido mucho más duro y aburrido sin vosotros. A mis compañeros y compañeras del despacho, gracias por las risas y por los ánimos mutuos cuando más lo necesitábamos. Ha sido una suerte compartir el día a día con vosotros. También me gustaría agradecer al Departamento de Ingeniería Química, por proporcionarme el entorno académico y los recursos necesarios para desarrollar esta tesis. Gracias a todo el personal docente, técnico y administrativo que ha hecho más fácil cada paso.

Por supuesto, quiero agradecer sinceramente a Beatriz Roldán y al Instituto Fritz-Haber de la Sociedad Max Planck por brindarme la oportunidad de formar parte de su equipo. En particular, quiero expresar mi eterna gratitud a Mariana Monteiro

por su cálida acogida, su amabilidad y su apoyo constante durante toda la estancia en el laboratorio. Gracias por hacer que mi experiencia haya sido muy enriquecedora y por ayudarme a crecer como investigadora.

A Max, gracias por estar a mi lado cada día. Gracias por tu apoyo incondicional y tu amor, y por darme un poco de luz en los momentos más estresantes. Esta tesis también es un poco tuya.

Y, por último, pero no menos importante, a mi familia: papá, mamá y Carlota, gracias por estar ahí siempre, sin condiciones. Gracias por haber creído en mí siempre, a pesar de mis múltiples inseguridades, y por ser siempre mi base firme. Este logro no habría sido posible sin vosotros.

Summary:

Nowadays, the global energy supply is predominantly dependent on non-renewable sources, which substantially contribute to the emission of greenhouse gases and, consequently, to the phenomenon of global warming. The primary greenhouse gases contributing to global warming are carbon dioxide, methane, and nitrous oxide (N_2O). However, due to its extended atmospheric lifetime, the global warming potential of nitrous oxide is approximately 300 times greater than that of carbon dioxide, which makes N_2O a notably potent contributor to climate change, even though it is present in much lower atmospheric concentrations. Based on this current situation, this thesis focuses on the design of metal oxide-based catalysts aimed at either valorizing or eliminating N_2O. The thesis is divided into two different sections: the thermocatalytic transformation of N_2O, where multiple catalytic systems are studied in the ethane oxidative dehydrogenation (ODH) assisted by N_2O instead of molecular oxygen; and the photoelectrocatalytic transformation of N_2O, where nanostructured mixed copper oxides and titanium dioxide are tested as photocathode and photoanode, respectively, in the photoelectro-reduction of nitrous oxide.

First of all, NiO/CeO_2-ZrO_2 catalysts were synthesized, characterized and tested in ethane oxidative dehydrogenation, using N_2O as an oxidizing agent. The best ethylene production was achieved with a small amount of zirconium incorporated into the catalyst. The catalytic behavior observed was attributed to differences in oxygen vacancy concentration, crystalline phases, and the type of nickel species present on the surface. The optimized NiO/CeO_2-ZrO_2 catalyst demonstrated excellent catalytic stability. However, overall olefin production remained within modest limits. Further studies led to the preparation of new nickel oxide-based catalyst formulations for ethane ODH assisted by N_2O, with the incorporation of suitable promoters such as niobium improving ethylene yield. The

selectivity towards ethylene was linked to the electrochemical properties of the catalysts, particularly the concentration of defects and charge-transfer resistance at the active sites. Moreover, the niobium-doped NiO catalyst showed outstanding long-term stability, maintaining its activity for at least 24 hours. Overall, the (Nb)NiO catalyst showed the best performance reported in the literature so far. Additionally, catalysts previously reported as highly efficient for ethane ODH assisted by molecular oxygen (such as MoVTeNb mixed oxides with the M1 crystalline phase) were also tested using N_2O. Surprisingly, conducting the reaction with N_2O resulted in a significant decrease in both selectivity to olefins and catalytic activity compared to experiments with O_2. These catalysts were further tested for N_2O decomposition, revealing that M1-phase materials had very limited ability to activate the N_2O molecule.

For the photoelectrocatalytic reduction of N_2O, mixed copper oxides (CuO_X) and titanium dioxide (TiO_2) photoelectrocatalysts were fabricated via electrochemical anodization. Nanostructured CuO_X photocathodes were synthesized in ethylene glycol-based electrolytes using either oxalic acid or sodium fluoride as complexing agents, studying at the same time the influence of adding NaOH. The results showed that anodization for 5 minutes at 250 rpm in the presence of oxalic acid formed a homogeneous CuO_X photocathode composed of nanospheres, with copper (I) oxide as the dominant phase. During photoelectro-reduction of N_2O, nearly complete N_2O elimination was achieved after 1 hour. To the best of our knowledge, this is the first time that catalytic N_2O decomposition has been studied through a combined photo- and electrocatalytic approach. Regarding TiO_2 photoanodes, the thesis investigates the synthesis of titanium dioxide nanotubes using various protic ionic liquids (PILs) to assess their impact on photoanode performance during the photoelectrocatalytic reduction of N_2O. The effects of anodizing under controlled hydrodynamic conditions and during different times have also been studied. A comprehensive morphological, structural, physicochemical and

(photo)electrochemical analysis was conducted to identify the most effective nanostructure for this application. The triethanolamine-based ionic liquid yielded the TiO_2 nanotubes with the best properties. Both long and wide nanotubes were obtained for the photoanode synthesized using an intermediate concentration of this ionic liquid in the anodization electrolyte. The highest photoelectrochemical performance was achieved with the sample anodized at 500 rpm, reaching 97% N_2O removal within 2 hours and complete elimination after 3 hours.

Resumen:

Hoy en día, el suministro global de energía depende predominantemente de fuentes no renovables, las cuales contribuyen sustancialmente a la emisión de gases de efecto invernadero y, en consecuencia, al fenómeno del calentamiento global. Los principales gases de efecto invernadero que contribuyen al calentamiento global son el dióxido de carbono, el metano y el óxido nitroso (N_2O). Sin embargo, debido a su larga vida en la atmósfera, el potencial de calentamiento global del óxido nitroso es aproximadamente 300 veces mayor que el del dióxido de carbono, lo que hace que el N_2O sea un contribuyente notablemente potente al cambio climático, aunque se encuentre en concentraciones atmosféricas mucho más bajas. Basado en esta situación actual, esta tesis se enfoca en el diseño de catalizadores basados en óxidos metálicos para valorizar o eliminar el N_2O. La tesis se divide en dos secciones diferentes: la transformación termocatalítica del N_2O, en la cual se estudian diversos sistemas catalíticos en la deshidrogenación oxidativa de etano (DHO) asistida por N_2O en lugar de oxígeno molecular; y la transformación fotoelectrocatalítica del N_2O, en la que se prueban óxidos de cobre mixtos y dióxido de titanio nanostructurados como fotocátodo y fotoánodo, respectivamente, en la fotoelectro-reducción del óxido nitroso.

En primer lugar, se sintetizaron, caracterizaron y probaron los catalizadores de NiO/CeO_2-ZrO_2 en la deshidrogenación oxidativa de etano, utilizando N_2O como agente oxidante. La mejor producción de etileno se logró con una pequeña cantidad de circonio incorporado en el catalizador. El comportamiento catalítico observado se atribuyó a diferencias en la concentración de vacantes de oxígeno, fases cristalinas y el tipo de especies de níquel presentes en la superficie. El catalizador optimizado de NiO/CeO_2-ZrO_2 demostró una excelente estabilidad catalítica. Sin embargo, la producción total de olefinas permaneció dentro de límites modestos. Estudios adicionales condujeron a la preparación de nuevas formulaciones de catalizadores

basados en óxido de níquel para la DHO de etano asistida por N_2O, con la incorporación de promotores adecuados como el niobio, mejorando el rendimiento de etileno. La selectividad hacia el etileno estuvo relacionada con las propiedades electroquímicas de los catalizadores, particularmente con la concentración de defectos y la resistencia a la transferencia de carga de los sitios activos. Además, el catalizador de NiO dopado con niobio mostró una excelente estabilidad a largo plazo, manteniendo su actividad durante al menos 24 horas. En general, el catalizador de (Nb)NiO mostró el mejor rendimiento registrado hasta la fecha en la literatura. Además, se probaron catalizadores previamente descritos como altamente eficientes para la DHO de etano asistida por oxígeno molecular (tales como los óxidos mixtos de MoVTeNb con la fase cristalina M1) utilizando N_2O. Sorprendentemente, al llevar a cabo la reacción con N_2O, se observó una disminución significativa tanto en la selectividad hacia las olefinas como en la actividad catalítica en comparación con los experimentos realizados con O_2. Estos catalizadores también fueron probados para la descomposición de N_2O, demostrando que los materiales con la fase M1 tenían una capacidad muy limitada para activar la molécula de N_2O.

Para la reducción fotoelectrocatalítica de N_2O, se fabricaron fotoelectrocatalizadores mixtos de óxidos de cobre (CuO_X) y dióxido de titanio (TiO_2) mediante anodizado electroquímico. Los fotocátodos nanostructurados de CuO_X se sintetizaron en electrolitos a base de etilenglicol utilizando ácido oxálico o fluoruro de sodio como agentes complejantes, estudiando al mismo tiempo la influencia de la adición de NaOH. Los resultados mostraron que el anodizado durante 5 minutos a 250 rpm en presencia de ácido oxálico formó un fotocátodo homogéneo de CuO_X compuesto por nanoesferas, con óxido de cobre (I) como fase dominante. Durante la fotoelectro-reducción de N_2O, se logró una eliminación casi completa de N_2O después de 1 hora. Según la información de que se dispone, esta es la primera vez que se ha estudiado la descomposición catalítica de N_2O mediante un enfoque combinado foto- y electrocatálitico. En cuanto a los fotoánodos de TiO_2, la

tesis investiga la síntesis de nanotubos de dióxido de titanio utilizando diversos líquidos iónicos próticos (LIPs) para evaluar su impacto en el rendimiento del fotoánodo durante la reducción fotoelectrocatalítica de N_2O. También se han estudiado los efectos de anodizar bajo condiciones hidrodinámicas controladas y durante diferentes tiempos. Se realizó un análisis morfológico, estructural, físicoquímico y (foto)electroquímico exhaustivo para identificar la nanostructura más efectiva para esta aplicación. El líquido iónico basado en trietanolamina produjo los nanotubos de TiO_2 con las mejores propiedades. Se obtuvieron nanotubos largos y anchos para el fotoánodo sintetizado utilizando una concentración intermedia de este líquido iónico en el electrolito de anodizado. El mejor rendimiento fotoelectroquímico se logró con la muestra anodizada a 500 rpm, alcanzando una eliminación del 97% de N_2O en 2 horas y una eliminación completa después de 3 horas.

Resum:

Hui dia, el subministrament global d'energia depén predominantment de fonts no renovables, les quals contribuïxen substancialment a l'emissió de gasos d'efecte d'hivernacle i, en conseqüència, al fenomen del escalfament global. Els principals gasos d'efecte d'hivernacle que contribuïxen al calfament global són el diòxid de carboni, el metà i l'òxid nitrós (N_2O). No obstant això, a causa de la seua llarga vida en l'atmosfera, el potencial de calfament global de l'òxid nitrós és aproximadament 300 vegades major que el del diòxid de carboni, la qual cosa fa que el N_2O siga un contribuent notablement potent al canvi climàtic, encara que es trobe en concentracions atmosfèriques molt més baixes. Basat en aquesta situació actual, aquesta tesi s'enfoca en el disseny de catalitzadors basats en òxids metàl·lics per a valorar o eliminar el N_2O. La tesi es dividix en dos seccions diferents: la transformació termocatalítica del N_2O, en la qual s'estudien diversos sistemes catalítics en la deshidrogenació oxidativa d'età (DHO) assistida per N_2O en lloc d'oxigen molecular; i la transformació fotoelectrocatalítica del N_2O, en la qual es proven òxids de coure mixtos i diòxid de titani nanostructurats com a fotocàtode i fotoànode, respectivament, en la fotoelectro-reducció de l'òxid nitrós.

En primer lloc, es van sintetitzar, caracteritzar i van provar els catalitzadors de NiO/CeO_2-ZrO_2 en la deshidrogenació oxidativa d'età, utilitzant N_2O com a agent oxidant. La millor producció d'etilé es va aconseguir amb una xicoteta quantitat de zirconi incorporat en el catalitzador. El comportament catalític observat es va atribuir a diferències en la concentració de vacants d'oxigen, fases cristal·lines i el tipus d'espècies de níquel presents en la superfície. El catalitzador optimitzat de NiO/CeO_2-ZrO_2 va demostrar una excel·lent estabilitat catalítica. No obstant això, la producció total d'olefines va romandre dins de límits modestos. Estudis addicionals van conduir a la preparació de noves formulacions de catalitzadors basats en òxid de níquel per a la DHO d'età assistida per N_2O, amb la incorporació de promotors

adequats com el niobi, millorant el rendiment d'etilé. La selectivitat cap a l'etilé va estar relacionada amb les propietats electroquímiques dels catalitzadors, particularment amb la concentració de defectes i la resistència a la transferència de càrrega dels llocs actius. A més, el catalitzador de NiO dopat amb niobi va mostrar una excel·lent estabilitat a llarg termini, mantenint la seua activitat durant almenys 24 hores. En general, el catalitzador de (Nb)NiO va mostrar el millor rendiment registrat fins a la data en la literatura. A més, es van provar catalitzadors prèviament descrits com altament eficients per a la DHO d'età assistida per oxigen molecular (com ara els òxids mixtos de MoVTeNb amb la fase cristal·lina M1) utilitzant N_2O. Sorprenentment, en dur a terme la reacció amb N_2O, es va observar una disminució significativa tant en la selectivitat cap a les olefines com en l'activitat catalítica en comparació amb els experiments realitzats amb O_2. Aquestos catalitzadors també van ser provats per a la descomposició de N_2O, demostrant que els materials amb la fase M1 tenien una capacitat molt limitada per a activar la molècula de N_2O.

Per a la reducció fotoelectrocatalítica de N_2O, es van fabricar fotoelectrocatalitzadors mixtos d'òxids de coure (CuO_X) i diòxid de titani (TiO_2) mitjançant anoditzat electroquímic. Els fotocàtodes nanostructurats de CuO_X es van sintetitzar en electròlits a base d'etilenglicol utilitzant àcid oxàlic o fluorur de sodi com a agents complexants, estudiant al mateix temps la influència de l'addició de NaOH. Els resultats van mostrar que l'anoditzat durant 5 minuts a 250 rpm en presència d'àcid oxàlic va formar un fotocàtode homogeni de CuO_X compost per nanoesferes, amb òxid de coure (I) com a fase dominant. Durant la fotoelectro-reducció de N_2O, es va aconseguir una eliminació quasi completa de N_2O després d'1 hora. Segons la informació de què es disposa, esta és la primera vegada que s'ha estudiat la descomposició catalítica de N_2O mitjançant un enfocament combinat foto- i electrocatàlitic. Pel que fa als fotoànodes de TiO_2, la tesi investiga la síntesi de nanotubs de diòxid de titani utilitzant diversos líquids iònics prótics (LIPs) per a avaluar el seu impacte en el rendiment del fotoànode durant la reducció

fotoelectrocatalítica de N_2O. També s'han estudiat els efectes d'anoditzar sota condicions hidrodinàmiques controlades i durant diferents temps. Es va realitzar una anàlisi morfològica, estructural, fisicoquímic i (foto)electroquímic exhaustiva per a identificar la nanostructura més efectiva per a aquesta aplicació. El líquid iònic basat en trietanolamina va produir els nanotubs de TiO_2 amb les millors propietats. Es van obtindre nanotubs llargs i amples per al fotoànode sintetitzat utilitzant una concentració intermèdia d'aquest líquid iònic en l'electròlit d'anoditzat. El millor rendiment fotoelectroquímic es va aconseguir amb la mostra anoditzada a 500 rpm, aconseguint una eliminació del 97% de N_2O en 2 hores i una eliminació completa després de 3 hores.

Index

Chapter 1:

Introduction

1.1 Environmental crisis

According to the Institute of Energy, the world's population still relies on fossil fuels for energy needs, despite the rapid growth of renewable sources such as solar and wind power. Figure 1.1 displays the global primary energy consumption by source in 2023. Fossil fuels account for 81% of the total energy consumption around the world, which proofs the high dependence nowadays on non-renewable sources to satisfy the growing energy demand.

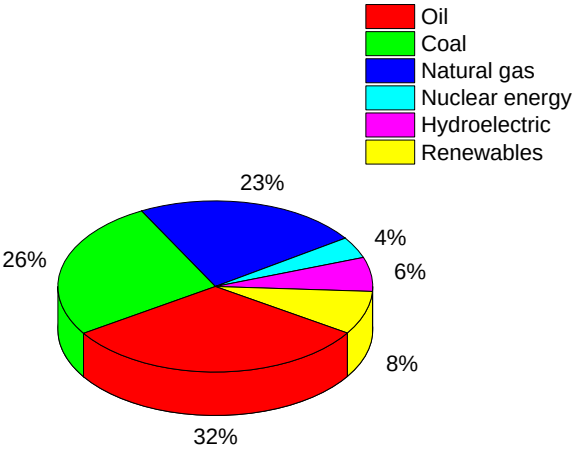

Figure 1. 1. Global primary energy consumption by source 2023 [1].

There are two major problems associated with the high reliance on fossil fuels. First of all, it is well known that fossil fuels are exhaustible and depend on their location and ease of extraction [2]. Unfortunately, an energy system based on non-renewable sources is not sustainable, since the fossil fuels consumed in a year of human activity takes ca. 1 million years to be restored by nature. Furthermore, world population is estimated to grow from 8.2 billion in 2024 to 10.3 billion in 2080 [3], which would increase the energy demand even further. Therefore, there is a need to find renewable and sustainable energy sources that can satisfy a constantly growing population and energy demand [4].

Second of all, massive fossil fuel consumption has led to a huge increase in carbon dioxide emissions, as well as other greenhouse gases. Figure 1.2 depicts the growth in the main greenhouse gas emissions occurred from 1850 to 2023. Particularly, the concentration of nitrous oxide in the atmosphere has increased by 20% in the last two centuries, from ca. 270 ppb in the pre-industrial era to 337 ppb nowadays [5], with a current rate of increase estimated at 2% per decade [6].

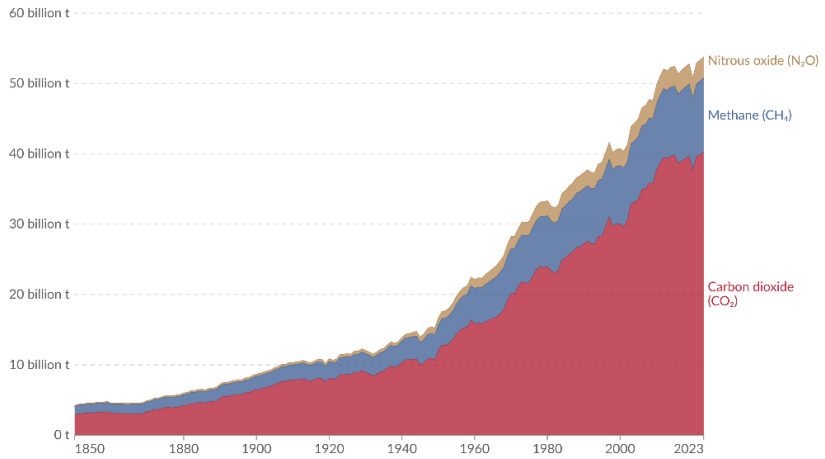

Figure 1. 2. Greenhouse gas emissions by gas, World, 1850 to 2023. Note: Measured in tonnes of carbon dioxide-equivalents over a 100-year timescale [7].

N_2O represents 6% of the total contribution of gases to the greenhouse effect, being the third major contributor to global warming after CO_2 and methane [8]. However, its long lifetime in the atmosphere (over 114 years) causes its global warming potential to be ca. 300 times greater than that of CO_2. In the past 150 years, the increasing atmospheric N_2O concentration has been also partly responsible for the stratospheric ozone depletion [9]. Globally, 40% of N_2O emissions are derived from human activities [8]. The greatest source of anthropogenic nitrous oxide emissions is agriculture, being responsible for 66% of the overall anthropogenic emissions. Agricultural emissions usually involve synthetic fertilizers, manure and crop residues. Almost 20% of the total emissions proceed from wastewater treatment (4%) and the industrial and fossil fuel combustion sector (15%) [10]. Nitrous oxide

is produced as an intermediate product of the denitrification processes during the treatment of wastewater. The main responsible, however, for N_2O emissions during wastewater treatment is the nitrogen removal during the tertiary treatment [11]. Regarding industrial emissions, the processes for nitric and adipic acid production are the main sources, with almost 80% of industrial N_2O emissions being a by-product of the adipic acid process [12].

Nowadays, there are several strategies to reduce nitrous oxide emissions. First, the formation of this gas should be avoided by improving the efficiency of internal combustion engines and equipment, developing electric engines and means of transportation, using biomass in a sustainable way, reducing the use of fossil fuels, etc. Nevertheless, most of these strategies remain under development and have not been implemented yet in the market. Hence, nitrous oxide must be eliminated once it has been formed, employing "after-treatment" technologies in between units of industrial processes. The different after-treatment solutions will be discussed in the next section.

1.2 Nitrous oxide mitigation techniques

Here, the most important after-treatment elimination techniques are discussed. Nitrous oxide decomposition is an exothermic reaction (Eq. 1.1) that can take place both catalytically and thermally. The significantly higher activation energy of the thermal decomposition (E_A~250 kJ/mol) [13] compared to the catalytic route (E_A~50-160 kJ/mol) [14] results in a much higher energy requirement, which means that very high temperatures (ca. 800-1000°C) are needed.

$$2N_2O \rightarrow 2N_2 + O_2 \qquad \Delta H = -163\ kJ/mol \qquad \text{Eq. 1. 1}$$

Generally, extensive thermal decomposition can be achieved in industrial processes where the exhaust gas containing N_2O is already at that high temperatures

by prolonging the residence time before cooling it down. The industrial use of this solution has been outlined in the patent literature [15]. However, this represents a specific strategy designed for a single process and it is only economically viable when the required temperature levels are naturally present in the process, eliminating the need for additional costly measures. Moreover, this technology requires a supplementary fuel supply as well as the control of the temperature in the decomposition zone to prevent the degradation (with process gases) or formation (with waste gases) of nitrogen oxides (NO_X) [16]. Therefore, it can be concluded that this elimination technique has a very poor energetic efficiency and very specific needs in order to work properly.

Selective catalytic reduction (SCR) of nitrous oxide is one of the alternatives to pure thermal decomposition. This treatment consists of catalyzing selectively the reduction of N_2O into nitrogen and oxygen by adding reducing agents such as CO, NH_3, hydrocarbons and H_2. The addition of the reductants improves the catalytic efficiency of the process and reduces the reaction temperature. Nitrous oxide reduction by CO can be useful in some manufacturing process where CO is also present in the exhaust gas, like in the case of oxalic acid production. Rh/ceria catalysts have been reported to be effective at CO-N_2O reduction, but at high temperatures [17]. Using Ru/ceria catalysts instead, N_2O is completely reduced by CO at much lower temperatures (200°C). Palladium and platinum based catalysts have also been reported to promote the effect of CO on the catalytic removal of nitrous oxide [18]. Generally, N_2O-SCR efficiency is affected by inhibiting gases. In fact, oxygen has an inhibiting effect on the catalytic performance of the reduction by CO [19]. In addition, this elimination method presents the disadvantage of producing CO_2 as a by-product. Therefore, the reduction by ammonia seems to be the best option of nitrous oxide SCR. In many N_2O removal scenarios, NO_X and ammonia are also present in the exhaust stream. With the selective catalytic reduction of nitrous oxide with NH_3 as reductant a synergistic removal of both N_2O

and NO_X can be achieved, eliminating as well ammonia. In this case, the most effective catalysts are Fe/MOR catalysts, which are not affected by O_2 inhibition [20].

Nowadays, the most commonly used technique for reducing N_2O emissions is the direct catalytic decomposition, in which nitrous oxide is broken down into nitrogen and oxygen under the influence of a catalyst (Eq. 1.1). This method is the most efficient, cost-effective and environmentally friendly, since temperature reactions are much lower than these of other processes and there are no problems of secondary pollution. Furthermore, very high N_2O conversions can be achieved by this technique (>99%).

Although depending on the catalytic system the reaction mechanism can vary, the N_2O decomposition usually proceeds following a common pattern. Thus, for the decomposition to take place, free N_2O is adsorbed on the catalyst's active center, forming N_2O^* (Eq. 1.2). Active centers of the catalyst are represented as * and adsorbed species are denoted with it. Then, adsorbed electrons form the surface break the N-O bond, which results in the release of nitrogen gas and the creation of absorbed O* (Eq 1.3). The desorption of O* is the key rate-limiting step of the nitrous oxide decomposition, since the occupation of the active center by O* inhibits the adsorption of N_2O. There are two possible mechanisms that can govern the desorption of oxygen. In case active centers are spaced far apart on the surface, a second N_2O molecule combines with the adsorbed oxygen atom to generate nitrogen and oxygen as Eq. 1.4 describes. This is known as the Eley-Rideal mechanism. On the other hand, the Langmuir-Hinshelwood mechanism (Eq. 1.5) takes place in catalytic systems where there are large number of active centers and comparable spacing between them. Here, two adsorbed oxygen species combine to release oxygen.

$$N_2O + * \rightarrow N_2O^* \quad \text{Eq. 1. 2}$$

$$N_2O^* \rightarrow N_2 + O^* \quad \text{Eq. 1. 3}$$

$$N_2O + O^* \rightarrow N_2 + O_2 + * \quad \text{Eq. 1. 4}$$

$$2O^* \rightarrow O_2 + 2* \quad \text{Eq. 1. 5}$$

In spite of the apparent simplicity of both reaction pathways, the location and states of the active centers of the employed catalyst directly influence on the decomposition of N_2O. Two crucial factors must be considered to design active catalysts for nitrous oxide decomposition, i) the oxygen atoms that desorbed and migrate from the surface, and ii) the transfer of electrons from the active center to the N_2O molecule. During the catalytic breakdown of the nitrous oxide molecule, the catalyst must act as both electron donor and acceptor, alternately. Hence, it has been studied that the addition of dopants can improve the activity of the main components of the catalysts, since the electronic energy states on the surface are controlled and the electron transfer properties between the catalyst and nitrous oxide molecules are optimized [21,22].

Catalysts based on noble metals, non-precious metal oxides, and molecular sieve are the materials typically used in the direct catalytic decomposition. Different catalysts are required in the industrial N_2O removal processes, since they take place at different locations with different reaction conditions and gas compositions. For instance, in the manufacture of nitric acid, both high-temperature and low-temperature nitrous oxide decompositions are performed inside the ammonia burner at 800-950°C and at the end of the pipe at 250-450°C [23], respectively. A catalyst stable at very high temperatures is required in the first reaction, whereas the second reaction is in need of a catalyst with high activity at temperatures below 450°C. Several catalytic systems have been studied for this reaction, such as Co_3O_4-based spinels doped with K, Cs, or Zn [24], or zeolites modified with Co, Cu or Fe [25], as

well as loaded Rh or Ag catalysts [26,27]. Unfortunately, noble metal-based catalysts are very expensive, they have low thermal stability and their catalytic efficiency significantly decreases with the presence of impurities, like as water, NO_X and oxygen. Non-noble metal oxides such as those based on nickel, copper and cobalt seem to be the most promising materials, due to their high activity and the lack of inhibiting effect from oxygen. It has been reported that metal oxides with different possible valence states can enhance the mobility of surface oxygen species, increasing the reactivity of the catalyst. A way of modifying the surface properties of the catalysts would be the addition of small amounts of different promoters.

1.3 Thermocatalytic transformation

As has been outlined before, nitrous oxide is produced in great amounts as a by-product during nitric acid and adipic acid manufacture. These outlet streams also contain significant amounts of other gases, such as N_2, O_2, CO_2, as well as traces of NO and NO_2. However, the development of new technologies to isolate high-purity nitrous oxide from this tail gas, has allowed the valorization of N_2O in industrial applications, such as the oxidative dehydrogenation of short alkanes to obtain olefins. The oxidative dehydrogenation of propane or ethane employing molecular oxygen has gained attention as a greener alternative to the typical production processes, such as steam cracking and fluid catalytic cracking (FCC) of naphtha, diesel or other oil by-products.

This work is going to focus on the oxidative dehydrogenation (ODH) of ethane assisted by nitrous oxide to obtain ethylene, since this short chain olefin is one of the most important feedstocks and platform molecules in the chemical industry. Particularly, ethylene is the raw material for the manufacture of polyethylene, which is the most used plastic globally, and it is also involved in the production of ethylene oxide, ethylene glycol and vinyl chloride (Figure 1.3). Therefore, the ethane oxidative dehydrogenation assisted by N_2O (N_2O-ODH)

combats two problems at once: reducing the N_2O emissions, while the most important raw material in petrochemistry is synthesized in a more environmentally friendly process (the main advantages will be shown below).

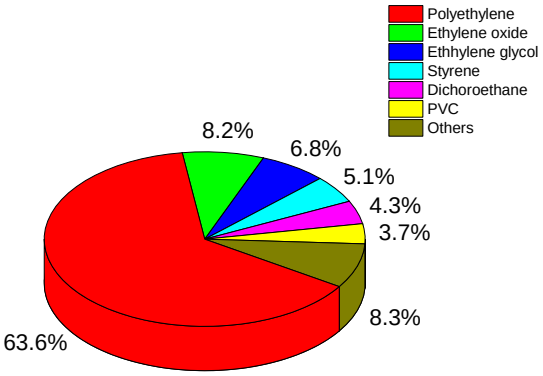

Figure 1. 3. Global Ethylene Market Share by Application (2021). Edited from source [28].

1.3.1 Ethylene: Industry and synthesis methods

Ethylene is the simplest olefin and the largest of the key chemical building blocks. In fact, the global ethylene market reached approximately 196 million tonnes in 2023, expecting to grow at a Compound Annual Growth Rate (CAGR) of 4.25% until 2035 [29]. In 2023, the polyethylene industry accounted for ~60% of the global ethylene [30], since it presents many industrial applications, such as food and beverage packaging, grocery bags, toys, cable insulation, water bottles, etc. Furthermore, ethylene demand continues to grow, as the use of lightweight plastic materials in the automotive and construction industries also increases.

Traditionally, the most widely employed method for ethylene manufacturing is the non-catalytic process known as steam cracking [31–33]. The absence of catalyst in this process presents two main drawbacks. On one hand, it causes the reaction temperature to be high since the reaction rate is not increased by the catalyst. On the other hand, the selectivity towards the desired product is lower than optimal. In this process, high-temperature pyrolysis of ethane (or other mixture of

hydrocarbons) is performed in the presence of diluting steam. First, steam is used to preheat the feed until the initial cracking temperature (500-680°C). Then, complete steam pyrolysis is achieved by feeding the resulting stream to a high-temperature tube reactor (800-950°C). Here, ethane is cracked into small olefins and di-olefins. The effluent is cooled down immediately in order to avoid olefin degradation into non-desired products, such as methane. Finally, ethylene is separated from other products by feeding the outlet stream to a combination of distillation and absorption units. Ethane conversion levels can reach 70% with olefin yields of ca. 50% [34]. However, this process presents many disadvantages. On the one hand, the high temperatures needed to overcome the endothermic reaction causes the process to be significantly energy-intensive. Specifically, ethylene production consumes the amount of 16 GJ/t when ethane is used as feedstock [34]. Additionally, part of the product gas stream has to be combusted to provide heat, leading to the formation of 1-2 tonnes of CO_2 per ton of ethene [35,36]. Consequently, ethylene manufacture is considered as the second-largest contributor to greenhouse gas emissions within the chemical industry. On the other hand, a significant amount of coke deposits is formed during the reaction, causing periodic reactor shut-downs for coke removal [37]. Thus, research has been focusing on new methods and process optimization that are able to improve the efficiency and sustainability of ethylene production.

Among the alternative production methods, (bio)ethanol dehydration, catalytic ethane dehydrogenation and ethane oxidative dehydrogenation stand out as the most promising. Industrial ethanol production from biomass has made it an available good in the biorefinery sector in places like Brazil [38]. Therefore, dehydration of ethanol seems like a feasible route to obtain ethylene in certain locations. The catalyzed endothermic reaction is described in Eq. 1.6, which occurs at ca. 300°C with the help of solid acids [39].

$$C_2H_5OH \rightleftharpoons C_2H_4 + H_2O \qquad \Delta H = 45.6\ kJ/mol \qquad \text{Eq. 1. 6}$$

Ethanol is first heated and fed into a catalytic reactor, where catalysts are acidic and are usually based on silica or alumina. The resulting product stream passes through a gas-liquid separator, obtaining a liquid stream which contains ethanol and water, and a gas stream containing ethylene. Then, the ethylene-containing stream undergoes several purification steps. Compared to steam cracking, this process is less energy-consuming and both CO_2 and N_2O emissions are reduced [34]. Despite the benefits, ethylene production via this method is still low, since previously ethanol has to be generated in a relatively cheap and straightforward way.

Moreover, the lower use of crude oil derivatives and natural gas as fuels to limit carbon dioxide emissions has caused these resources to be available for non-energetic applications, such as their transformation in light olefins. Therefore, it makes sense that processes involving the catalytic transformation of ethane present themselves as the most promising alternatives to steam cracking. The reaction for the catalytic dehydrogenation of ethane to obtain ethene and hydrogen is shown in Eq. 1.7. The endothermic nature of the reaction results in the need for high temperatures and low pressures.

$$C_2H_6 \rightleftharpoons C_2H_4 + H_2 \qquad \Delta H = 136\ kJ/mol \qquad \text{Eq. 1. 7}$$

Despite having reduced the reaction temperature to 550-700°C, it is still a very high temperature to only achieve ethane conversions of 10 and 40%, respectively [31]. In addition, the formation of coke deposits on the catalyst surface results in continued deactivation, which makes periodic regeneration of the catalyst necessary. Overall, this method could not compete with steam cracking due to the relatively low activity of the catalysts.

For all the above-mentioned reasons, oxidative dehydrogenation of ethane has gained attention due to its minimal energy requirements (exothermic reaction) and to the minimized catalyst deactivation owed to the in-situ regeneration of the catalysts through the oxygen-containing feed. The reduced environmental impact of

this process is also in alignment with several of the 2030 sustainable development goals of the United Nations [40]. The goals included are:

- Goal 3, which ensures a healthy living environment by reducing the exposure to hazardous chemicals and air pollution.
- Goal 7, which promotes progress in clean and energy-efficient technologies.
- Goal 13, which addresses climate change and its negative impacts on society.

1.3.2 Oxidative dehydrogenation of ethane

Oxidative dehydrogenation of ethane is an exothermic reaction (Eq. 1.8), in which ethylene can be obtained at relatively low temperatures (300-400°C). It should be noted that this process has not been performed at industrial scale yet, but high feed conversions are already achieved. In fact, companies Clariant and Linde have recently validated the EDHOX technology, combining an appropriate ODH reaction system and a suitable catalyst, in a full-scale demonstration plant [41]. Therefore, a future industrial implementation is expected in the short to medium term. The ODH reaction is shown below.

$$C_2H_6 + \frac{1}{2}O_2 \rightleftharpoons C_2H_4 + H_2O \qquad \Delta H = -105.5\ kJ/mol \qquad \text{Eq. 1. 8}$$

However, some side reactions also take place, as Figure 1.4 illustrates. First, carbon dioxide appears as a consequence of the total oxidation of ethane. Furthermore, carbon monoxide also forms due to the overoxidation of ethylene, as a result of the high reactivity of olefin products [42,43]. As water and carbon oxides are the only by-products of ODHE, fewer separation units are required for this method compared to steam cracking. Also, less energy is required compared to traditional industrial methods, since the reaction is exothermic and activation occurs at much lower temperatures. Additionally, including an oxidant in the feed reduces the coke formation and enhances the catalyst stability [44]. The most common oxidant is oxygen, but CO_2 and N_2O are also available options. Nevertheless, a

suitable catalyst must be employed in order to maximize the selectivity towards ethylene, since yields must be 65-70% to still compete with steam cracking [45,46].

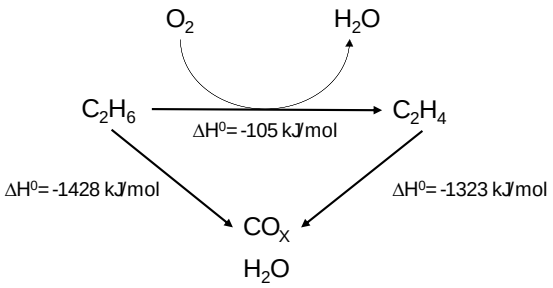

Figure 1. 4. Scheme of reactions taking place during ethane ODH.

Several factors influence on the performance of the catalysts employed in the oxidative dehydrogenation of ethane, such as the metal oxide, the support, surface acidity, available surface, metal distribution, alkane/oxidant ratio, and diluent gas [47]. Metal oxides are typically used as catalysts during ethane ODH due to their oxidation-reduction (redox) properties. Particularly, transition metal-oxides contain cations with multiple oxidation states, a desirable property for selective oxidation together with redox potential [48].

It is well known that ethane oxidative dehydrogenation over easily reducible transition metal oxides takes place through a Mars-van-Krevelen (MVK) redox mechanism. During this mechanism, the surface of the oxide catalyst is reduced as a lattice oxygen atom activates ethane molecules, leading to the formation of olefins. First, ethane is adsorbed to a lattice oxygen atom on the catalyst surface (O*), following Eq. 1.9. Then, the rupture of a C-H bond results in the formation of an ethoxy intermediate and a hydroxyl group (Eq. 1.10). This breakdown of the ethane C-H bond is believed to be the rate-limiting step. In fact, the ethylene formation rate is first order in ethane concentration according to literature [49]. Ethylene and another hydroxyl group are formed from the loss of a hydrogen atom of the adsorbed ethoxy intermediate (Eq. 1.11). According to Eq. 1.12, the hydroxyl groups combine

to form water and a lattice vacancy (V*). Finally, gas-phase oxygen from the oxidant is adsorbed to the vacancy and the active site of the catalyst is re-oxidized (Eq. 1.13).

$$C_2H_6 + O^* \rightleftharpoons C_2H_6O^* \quad \text{Eq. 1. 9}$$

$$C_2H_6O^* + O^* \rightarrow C_2H_5O^* + OH^* \quad \text{Eq. 1. 10}$$

$$C_2H_5O^* + O^* \rightarrow C_2H_4 + OH^* \quad \text{Eq. 1. 11}$$

$$OH^* + OH^* \rightarrow H_2O + O^* + V^* \quad \text{Eq. 1. 12}$$

$$O_2 + V^* \rightarrow 2O^* \quad \text{Eq. 1. 13}$$

The stability of the oxide, as well as the type of reactive oxygen species, can define the selectivity of oxidation reactions. Oxygen ions present in metal oxides can be divided into electrophilic and nucleophilic species. Electrophilic oxygen species include absorbed species like O_2^-, O_2^{2-}, and O^-, while nucleophilic oxygen species have the form of O^{2-}, which result from the saturated species such as final oxygen groups M=O or bridges of MOM. Complete oxidation reactions are performed by O^- species, whereas O^{2-} are responsible for selective partial oxidation reactions. The rate-limiting step in the reaction varies depending on the oxygen species involved. For instance, in the case of nucleophilic species, the activation of hydrocarbons is the limiting step, instead of the adsorption of oxygen on the catalyst surface, as it happens when electrophilic species are involved.

Taking everything into account, it is possible to design catalysts that favor the transformation of ethane into ethylene, minimizing the undesirable total oxidation reactions.

1.3.3 Efficient thermocatalysts for the oxidative dehydrogenation of ethane

The ethane molecule only presents primary carbons, which show a greater C-H bond energy (420 kJ/mol) than that of secondary carbons present in propane and n-butane (401 kJ/mol). Furthermore, ethylene is much more stable than the C_3-C_4 olefins, due to the lower reactivity of the vinyl C-H bonds of ethylene (444

kJ/mol) compared to the alkyl bonds of propylene and C_4 olefins (361 kJ/mol). Therefore, during the ethane ODH high selectivity towards ethylene can be achieved even at high conversions, unlike the ODH of propane and n-butane. It is important to note that, the oxidative dehydrogenation of ethane is favored by acid active sites, whereas the opposite occurs for propane and n-butane ODH reactions, since adsorption and overoxidation of C_3-C_4 olefins is enhanced by acid sites, leading to an excessive formation of carbon oxides.

Some aspects must be considered in order to synthesize effective catalysts for the oxidative dehydrogenation of short alkanes:

- The nature of active sites (coordination and oxidation state).
- Acid-base properties of the catalyst.
- Properties of the support.

The most studied materials for the oxidative dehydrogenation of ethane assisted by molecular oxygen are those based on supported vanadium and molybdenum oxides, promoted nickel oxides and multicomponent Mo-V-Te-Nb-O mixed oxide catalysts presenting the $Te_2M_{20}O_{58}$ (M = Mo, V, Nb) orthorhombic crystalline phase (also called as M1). Regarding supported vanadium (or molybdenum) oxides, selectivity towards olefin formation is usually low at medium/high conversions, since vanadium sites have affinity for olefins, which leads to their overoxidation [50]. Conversely, the ethylene selectivity barely decreases at ethane conversions ca. 40% in the case of promoted NiO based or multicomponent mixed oxide catalysts. The main difference for this result lies in the different active sites involved in the reaction, since reactivity of ethylene is lower than that of ethane in the active sites of NiO and M1 catalysts. Therefore, the most promising catalytic systems for the ethane ODH assisted by molecular oxygen (O_2-ODH) to obtain ethylene are those based on nickel oxide and on mixed MoV oxides with orthorhombic bronze structure.

The multicomponent MoVTeNbO catalysts presenting the $Te_2M_{20}O_{58}$ (M = Mo, V, Nb) orthorhombic crystalline phase have been reported as those with the best catalytic performance in the O_2-ODH of ethane [51–54]. This behavior has been related to the isolated vanadium active sites that contain a suitable V^{4+}/V^{5+} ratio, which results in limited ethylene overoxidation after it is formed [51]. This is opposite to what has been reported for classical supported vanadium catalysts [55–57]. Some studies have proposed the co-existence of a hexagonal phase called M2 together with the M1. The M2 phase is known to favor ethylene formation, once the ethane molecule is activated, but it is unable to transform the ethane molecule. Nevertheless, the presence of both M1 and M2 phases is considered to enhance ethylene selectivity of this type of catalysts. Interestingly, this multicomponent catalysts have very low affinity for the rupture of C-C bonds that would form carbon oxides. Therefore, there are the ideal materials for partial oxidation and dehydrogenation reactions.

At first, it was demonstrated that bulk multicomponent M1 catalysts are highly efficient in the O_2-assisted oxidative dehydrogenation of ethane. Then, M1 phase catalysts were modified by introducing different supports based on metal oxides like SiO_2, γ- and α-Al_2O_3, Nb_2O_5, ZrO_2, SiC foam, etc. [58,59]. Surprisingly, both activity and selectivity to ethylene of supported M1 catalysts decreased compared to the bulk materials. In fact, the interaction between the supports and the active sites resulted in the partial degradation of the M1 phase. The different developed phases were unselective towards olefin formation. It was concluded that the best catalytic performance was provided by the multicomponent mixed oxides with the orthorhombic phase M1 synthesized hydrothermally with activation in an inert atmosphere and in a temperature range of 500-750°C [60]. From this study it was concluded that the activation temperature significantly influenced the catalytic behavior and the development of M1 phase, being the best results of those annealed at the 550-650°C range. Ethylene yields ca. 75% have been achieved with the

multicomponent MoVTeNb-M1 oxide [60], which makes it attractive from a fundamental and industrial perspective, since it can compete with the steam cracking performance.

In addition to the multicomponent Mo-V-Te-Nb-O mixed oxide catalysts, nickel oxide-based catalysts have been reported as the best-performing materials for the oxidative dehydrogenation of ethane with molecular oxygen as an oxidant [61–66]. Nickel oxide (NiO) is a metal oxide with semiconducting properties (p-type semiconductor) that presents high reactivity in reactions that involve a redox Mars-van-Krevelen mechanism. However, this high catalytic activity results in massive carbon dioxide formation [61,67]. At first, different thermal treatments were tested in the synthesis of pure NiO. Despite the catalytic results not being optimized, it was observed that olefin formation was favored by a decrease in the non-stoichiometric oxygen species. This research suggested that selectivity to ethylene could be improved with the incorporation of a heteroatom in the crystalline NiO lattice, since the concentration of non-stoichiometric oxygen species would be reduced.

Therefore, by optimizing the preparation procedure, the selectivity to ethylene of NiO catalysts during ethane ODH can be improved. For instance, the best catalytic performance for NiO-based materials has been observed with the addition of suitable promoters [65,67–69] and supports [70–72]. From these studies, it has been established that when a high valence cation is added to the metal oxide, the unselective high oxidation state nickel oxide is removed [66,67,69,73–75]. Hence, it was concluded that the higher the valence of the dopant, the higher was the selectivity to ethylene during ethane ODH [64,65]. In addition, the positive doping effect has also been related to the decrease in the concentration of electrophilic oxygen species. Nevertheless, electrophilic O^- species are necessary to activate ethane molecules [68], but the concentration must be controlled in order to avoid the formation of carbon oxides [76]. In addition, the presence of promoters generally

improves the catalytic activity of several catalysts. It is believed that the incorporation of a heteroatom leads to an increased surface area. As a consequence, the number of available active sites also increases. Some nickel oxide catalysts increased their surface area from 15 m^2/g to 84 m^2/g and 103 m^2/g with the addition of cerium and tin, respectively [77,78].

In conclusion, the main challenge facing the oxidative dehydrogenation of ethane assisted by molecular oxygen is the undesired formation of CO_X, lowering the selectivity to ethylene. The use of milder oxidants has been reported to enhance the selectivity towards olefin formation. For example, CO_2 can be considered as a viable option when reaction temperatures are higher than 650°C, since carbon dioxide is hard to activate [79,80]. However, the 300 times higher global warming potential of N_2O makes the use of nitrous oxide as oxidizing agent more attractive and arises as a solution for its abatement. Herein, N_2O-assisted ODH of ethane can effectively produce ethylene, at the same time as the environmental impact of N_2O is reduced [42,81].

1.3.4 Nitrous oxide as an oxidant for the oxidative dehydrogenation of ethane

The oxidative dehydrogenation of ethane and other short alkanes assisted by nitrous oxide has been previously studied but not extensively. Most of the work has reported the use of catalysts containing vanadium and iron, particularly supported vanadium [82,83] and iron-modified ZMS-5 catalysts. Surprisingly, the ethane ODH assisted by N_2O over multicomponent MoVTeNb catalysts has not been reported yet. Similarly, NiO-based catalysts have been hardly studied in the ODHE using N_2O as oxidant and no systematic study has been performed.

In the case of the MoVTeNb catalysts, the vanadium sites are responsible for the activation of the ethane molecule. In the case of supported vanadium catalysts selectivity to ethylene remarkably increased when using N_2O instead of O_2 [84]. The use of nitrous oxide during ethane ODH seems to influence on reduction/re-oxidation

rates of the catalyst and the formation of electrophilic oxygen, leading to an improved olefin selectivity during the reaction [84–87]. Therefore, analog behavior can be predicted for the multicomponent MoVTeNb catalysts.

In a similar way, few studies have focused on the N_2O-ODH over the NiO based catalysts. Besides, nickel oxide catalysts are also known to be active in the N_2O decomposition at relatively low temperatures [10,88–90]. In fact, considering pure oxides, one of the highest nitrous oxide decomposition rates is achieved by NiO catalysts [10]. This performance has been attributed to the nickel oxide low heat of formation. Furthermore, reactivity seemed to be improved by doping pure NiO. The addition of bismuth enhanced the activity of the nickel oxide catalyst due to the higher concentration of both Ni^{3+} and surface oxygen vacancies on the NiO lattice [88]. The addition of elements like barium and cerium to nickel oxide ($Ce_{1.0}Ba_{1.5}Ni_9Ox$ catalyst) have also improved the catalytic performance of pure NiO. The addition of Ce favored the N_2O dissociation, while the addition of Ba improved the oxygen desorption [89].

In order to successfully carry out the ethane ODH assisted by N_2O, the employed catalysts must present catalytic sites that activate both N_2O and ethane molecules. As has been outlined before, the promotion of pure nickel oxide with other elements improves the catalytic behavior in both reactions. Some studies have revealed the enhanced performance of Ni-Al mixed oxides obtained from layered double hydroxides [91] and sulfate-modified NiAl mixed oxides [92] when used in the N_2O-ODH of ethane, presenting better results than simple supported NiO/Al_2O_3 catalyst [91]. The presence of isolated O^- species together with a weak adsorption of the olefin, which prevents its further oxidation, resulted in the best performance of the Ni-Al mixed oxides. Mesoporous $Ni–Fe–Al_2O_3$ catalysts have been also tested in the N_2O-ODH of ethane [93]. It was concluded that the best catalytic performance was that of the samples in which Ni^{2+}-species were highly dispersed and iron oxide

species were closely spaced. However, improvement is still need, since yields to ethylene below 20% were obtained in almost every case. A summary of the findings reported in literature is shown in Table 1.1.

Table 1. 1. N_2O-assisted ODH of ethane on representative catalysts reported in the literature.

Catalyst	T (ºC)	Ethane Conversion (%)	Selectivity to ethylene (%)	Reaction conditions	Reference
Supported NiO/Al_2O_3	420	20	60	$C_2H_6/N_2O/He$ = 1/1/48 W/F = 0.6 g·s·cm^{-3}	[91]
Ni_3Al-mixed oxides	420	22	81	$C_2H_6/N_2O/He$ = 1/1/48 W/F = 0.6 g·s·cm^{-3}	[91]
Ni–Fe–Al_2O_3	400	32	58	$C_2H_6/N_2O/He$ = 2.5/2.5/20 W/F = 0.6 g·s·cm^{-3}	[93]
Sulfated NiAl mixed oxides	600	20	95	$C_2H_6/N_2O/He$ = 2/2/26 W/F = 0.6 g·s·cm^{-3}	[92]
	600	52	80	$C_2H_6/N_2O/He$ = 2/2/26 W/F = 2.4 g·s·cm^{-3}	[92]
VO_X/MCM-41	500	8	58	$C_2H_6/N_2O/He$= 40/40/20 W/F = 0.1 g·s·cm^{-3}	[85]
Fe-ZSM5	400	25	65	$C_2H_6/N_2O/He$= 1/1.5/12.5 W/F = 0.8 g·s·cm^{-3}	[84]

Therefore, in the present work an extensive study on nitrous oxide-assisted oxidative dehydrogenation of ethane over NiO-based and multicomponent MoVTeNb catalysts has been undertaken.

1.4 Photoelectrocatalytic transformation

Recently, direct photocatalytic decomposition of nitrous oxide using semiconducting materials exposed to UV or visible light has gained attention due to its efficiency and minimal energy requirements. Titanium dioxide has been the most

studied material up to date in the photocatalytic abatement of N_2O. At first, the highest nitrous oxide conversion obtained was 77% with a 3.4 wt.% Ag-doped TiO_2 photocatalyst [94]. Many synthesis methods and promoting elements have been tested in order to improve further the photocatalytic performance of titania photocatalysts. However, complete mitigation of nitrous oxide with photocatalytic decomposition has not been accomplished yet, reaching only 82% after 18h [95]. Furthermore, electrocatalytic decomposition of N_2O has been also tested as a mitigation technique. In this case, much higher potentials are applied in order to generate the needed electrons for the nitrous oxide reduction. In 1966, Stegen et al. reported the first electrochemical reduction of N_2O in aqueous solution, employing mercury as cathode and obtaining hydrazine as a product [96]. Then, research continued with the electro-decomposition of N_2O intro nitrogen and oxygen using electrodes based on noble metals, such as platinum, in both alkaline [97] and acidic [98] solutions. After, Kudo & Mine studied the electrochemical reduction of nitrous oxide over several electrode materials in an aqueous solution. However, very high reduction potentials (-1.35 $V_{Ag/AgCl}$ for a ZnO electrode) were needed in order to obtain valuable results [99]. Later, a N_2O conversion of 100% was achieved with small copper clusters supported on CeO_2 nanospheres but carrying out the reaction at 550°C [100]. It is believed that the photoelectrocatalytic approach can achieve higher efficiencies, since the application of light together with a small potential facilitates the mechanism for N_2O reduction. Additionally, the mild conditions (room temperature and atmospheric pressure) are additional benefits of this method. In the same way, this technique presents an easy scalability, low energy consumption and the possibility of supplying the required energy with renewable sources. Surprisingly, the photoelectrocatalytic decomposition of nitrous oxide has not been tested yet. However, before diving into the photoelectrocatalytic process, some electrochemistry basics are to be explained.

1.4.1 Principles of electrochemistry

1.4.1.1 Electrochemistry of semiconductors

Photocatalysis and photoelectrocatalysis are based on charge transfer processes through the interface formed between a photocatalyst (material sensitive to radiation) and an electrolyte. Most of the employed catalysts are semiconducting metal oxides, in which the bandgap (E_g) is not as large as in insulators and electrons can be promoted from the valence band (VB) to the conduction band (CB). The bandgap is the energy gap between the highest level of the valence band and lowest level of the conduction band [101,102]. The promotion of electrons leaves a positively charged vacancy or hole (h^+) in the VB. This is known as the formation of electron-hole pairs [101,103]. Therefore, semiconductors have two types of charge carriers: electrons and holes. Migration of electrons is achieved both thermally and photochemically. However, the addition of different elements (doping) also generates charge carriers (electrons or holes). Undoped semiconductors are known as intrinsic semiconductors, and their concentration of electrons and holes are the same. On the other hand, doped semiconductors can be referred to as n-type and p-type semiconductors. **N-type** semiconductors are doped metal oxides in which the dominant charge carriers are electrons, whereas **p-type** semiconductors are those in which holes are the dominant charge carriers [103].

Another important concept is the **Fermi level**. For the electrons at the valence band, the Fermi level is the energy level at 0K in which the probability of finding an electron is ½. For instance, for an intrinsic semiconductor the Fermi level is located at the mid-point of the bandgap [104]. However, doping changes the Fermi level of semiconductors (Figure 1.5). In the case of n-type semiconductors, materials are doped with electron-donor species. Therefore, new occupied energy levels are introduced near the lower end of the conduction band, which shifts the Fermi level towards the conduction band (Figure 1.5A). Conversely, when electron-accepting

species are introduced (p-type semiconductors) the Fermi level is shifted towards the valence band (Figure 1.5B).

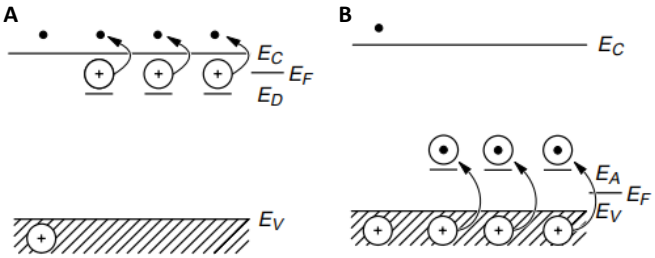

Figure 1. 5. Energy levels in (A) n-type and (B) p-type semiconductors [103].

Furthermore, for the non-stoichiometric semiconducting metal oxides the n- or p-type character of the material can be provided by the presence of point defects, since they can act as both electron-donor or accepting species. Point defects are defined as random errors in a periodic lattice, which can be due to the absence of an atom at its regular place or to the presence of an atom at a site that is not usually occupied (Figure 1.6) [105]. W. Schottky and J. Frenkel identified two types of point defects. First, a **Schottky defect** consists of a vacancy in an otherwise perfectly arranged lattice (Figure 1.6A), meaning there is an atom or ion missing from its usual place in the structure [105,106]. To ensure charge balance in stoichiometric metal oxides, the number of vacancies at cation and anion sites are equal and proportional to the stoichiometry. This way, for a metal oxide MX_2, two anionic vacancies must be created for every lost cation. On the other hand, a **Frenkel defect** is formed when an atom or ion has been displaced onto an interstitial site (Figure 1.6B). This time, the concentration of metal vacancies in stoichiometric metal oxides is the same as that of interstitial ions [105,106].

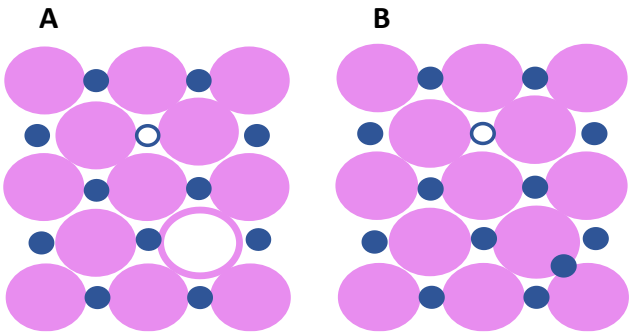

Figure 1. 6. Scheme of (A) a Schottky defect and (B) a Frenkel defect for a stoichiometric 1:1 compound.

Nevertheless, charge balance of point defects in non-stoichiometric compounds is ensured by the formation of electronic defects. In oxygen-deficient metal oxides, an oxygen atom in a regular site of the lattice (O^{2-}) is transferred to gaseous state. The two electrons of the anion can be excited, meaning that oxygen vacancies act as electron donor species [102]. An alternative form of oxygen deficiency in non-stoichiometric metal oxides is a relative excess of metal with respect to the stoichiometric composition. In this case, defects consist of interstitial metal atoms, which means that an atom is transferred to an interstitial site from its usual location. The latter can be successively ionized and act as an electron donor [102]. Conversely, excess of oxygen and metal deficiency in non-stoichiometric metal oxides lead to the formation of metallic vacancies, which act as electron-accepting species. In this way, the semiconductor behavior of a material depends on the point defects that are likely to be introduced into the metal oxide, which is determined by how easily the metal is oxidized or reduced. Therefore, if the metal is easily oxidized an n-type behavior is expected due to the oxygen deficiency generated, whereas if the metal is easily reduced it is expected to exhibit a p-type behavior [105].

1.4.1.2 Photoelectrocatalytic processes

In a photocatalytic process, when the catalyst is radiated with photons of greater energy than the bandgap, electron-hole pairs are formed (Figure 1.7) [107]. These species either recombine or they participate in redox reactions involving the species adsorbed on the catalyst surface.

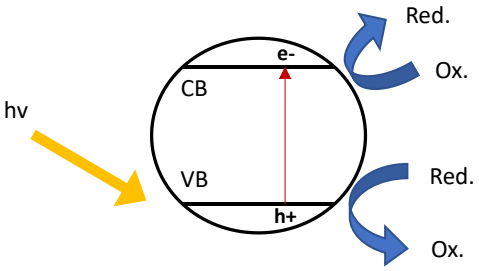

Figure 1. 7. Photocatalytic process induced by the radiation of a semiconductor.

Similarly, photoelectrocatalytic processes take place when a small external potential is applied to the system. Photoelectrochemical processes are carried out in photoelectrochemical cells (PEC). There are several configurations, but the simplest consists of an n-type semiconductor electrode (photocatalyst: photoanode or photocathode), a metallic counterelectrode (cathode) and a reference electrode, all immersed in an electrolyte and exposed to a light source, displayed as in Figure 1.8 with the configuration of a photoanode, for instance. The electric field causes the photogenerated holes to head to the semiconductor surface and participate in oxidation reactions of the electrolyte. Meanwhile, electrons migrate to the back of the semiconductor and, moving through an external circuit, they participate in the reduction of the electrolyte at the cathode [108]. With the application of a small bias, the efficiency of redox reactions is improved respect to photocatalytic reactions, since separation of electron-hole pairs is facilitated and the chances of recombination are reduced [108]. In the same way, the kinetics of the charge transfer process are improved and the overpotential necessary for the redox reactions to take place is provided.

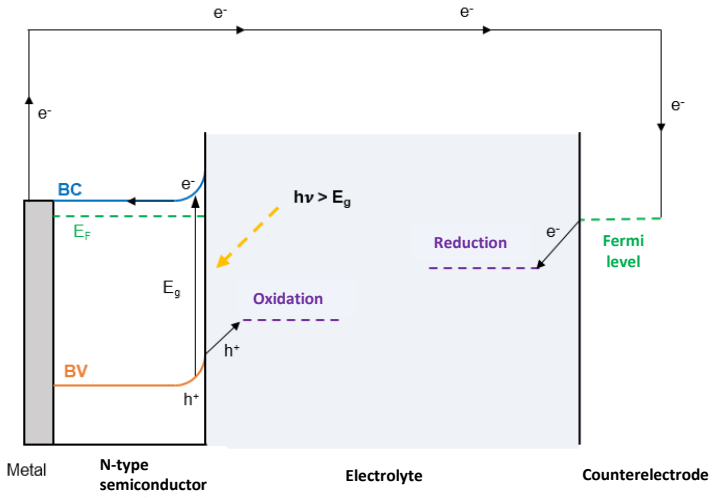

Figure 1. 8. Scheme of a photoelectrocatalytic process using a photoanode.

As has been mentioned before, the efficiency of photoelectrocatalytic reactions depends on the processes of recombination and charge transfer that occur at the interface between the semiconductor and the electrolyte [109]. Therefore, it is important to study the properties of the interface in order to optimize the performance of the semiconductor as a photoanode or photocathode.

In a photoelectrocatalytic system, the Fermi level determines the electrochemical potential of the semiconductor, whereas the electrochemical potential of the electrolyte is determined by its redox potential [110]. When a semiconductor is immersed in an electrolyte both electrochemical potentials must be the same for the two phases to be in equilibrium. Charges reorganize themselves for that purpose and a potential gradient is generated between the electrolyte and the semiconductor [111,112]. First, the excess charge generated to overcompensate the charge of the electrolyte extends into the semiconductor. This region is known as the **space charge region** and has an associated electric field [103]. This electric field is responsible for the effective separation of the photogenerated electron-hole pairs. Moreover, it is believed that a double electric layer is formed from the interface to

the electrolyte, known as **interfacial double layer** (Figure 1.9) [102,111]. The interfacial double layer is the combination of [102,112]:

- The Helmholtz-Perrin layer, a fixed layer of oppositely charged ions in solution.
- Gouy-Chapman or diffuse layer, where ions are spread out in the electrolyte forming a diffuse double layer.

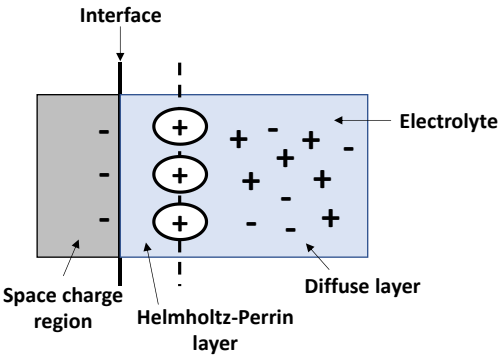

Figure 1. 9. Scheme of the interfacial double layer at the semiconductor/electrolyte interface and of the space charge region.

Furthermore, the potential gradient is responsible for a capacitive behavior at the semiconductor/electrolyte interface. The total capacitance C, can be calculated considering the contributions of the individual capacitance of each one of the three layers, following Eq. 1.14 [102,111,113].

$$\frac{1}{C} = \frac{1}{C_{SC}} + \frac{1}{C_H} + \frac{1}{C_D} \qquad \text{Eq. 1. 14}$$

where C_{SC} is referred to the space charge region capacitance, C_H to the Helmholtz-Perrin layer capacitance and C_D to the diffuse layer capacitance.

The capacitance of the diffuse layer is only considered when solutions are very diluted (10^{-2} – 10^{-3} M). Thus, C_D can be ignored, and Eq. 1.14 turns into Eq. 1.15. This equation will be used for metal oxide semiconductors with a high defect concentration ($N_{D,A}$ ca. 10^{18} – 10^{20} cm^{-3}).

$$\frac{1}{C} = \frac{1}{C_{SC}} + \frac{1}{C_H} \qquad \text{Eq. 1. 15}$$

Additionally, for an n-type semiconductor, the Fermi level is generally higher than the redox potential of the electrolyte, which means that there is an electron transfer from the semiconductor into the solution in order to reach the equilibrium between phases [103,111]. With this electron transfer to the electrolyte, the majority of charge carriers of the semiconductor is removed and a **depletion layer** with a positive charge associated with the space charge region is formed. A decrease in charge carrier concentration leads to a bigger energy difference between the CB and the Fermi level. This is reflected by an upward bending of the band edges, while the difference between the conduction band and the Fermi level at the bulk of the semiconductor in equilibrium remains constant (Figure 1.10A) [102,103]. In p-type semiconductors the opposite happens. To ensure equilibrium, electrons must transfer from the electrolyte to the semiconductor since the Fermi level is lower than the redox potential. A negative charge is generated in the space charge region and band edges in the depletion layer bend downwards (Figure 1.10B) [102,103].

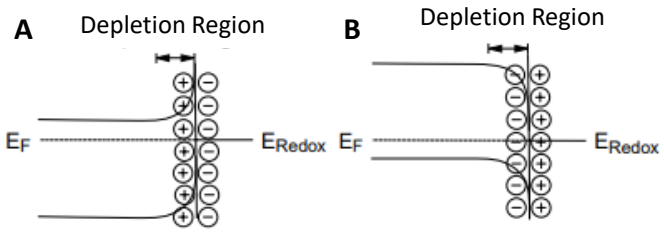

Figure 1. 10. Band bending for (A) n-type and (B) p-type semiconductors in equilibrium with an electrolyte.

Both the Fermi level and the band edges in the interior of the semiconductor vary when the applied potential is changed. The magnitude and direction of the band bending depends on the applied potential:

- At a certain potential, the Fermi level is the same as the solution redox potential, meaning there is no charge transfer, and therefore there is no band

bending. This potential is known as the **Flatband potential (E_{fb})** and its value depends on the employed electrolyte [102,103,111,113].

- For n-type semiconductors, at potentials positive of the flatband potential electrons are transferred from the electrode into the solution leading to the upward bending of the depletion layer. For p-type semiconductors the same happens for negative potentials of E_{fb}.
- At negative potentials of E_{fb} for n-type electrodes an excess of electrons is generated at the space charge region. This is referred to as an **accumulation region** [102,114]. An accumulation region is formed for p-type semiconductors at positive potentials of the flatband potential.

Hence, it can be concluded that the charge transfer process in a semiconductor will depend on the state of the space charge region: depletion or accumulation. If there is an accumulation region, the semiconductor will behave as a metallic electrode due to an excess of charge carriers, and electron transfer will be enhanced. However, if there is a depletion layer, electron transfer occurs more slowly, since there are fewer charge carriers available to transfer [103].

Nevertheless, electrons can be promoted to the conduction band if the electrode is exposed to radiation, as has been outlined before. With this happening in the space charge region, the associated electric field will separate the charges. For instance, in the case of n-type semiconductors, the band edges bend upwards at positive potentials, resulting in the movement of holes towards the interface and of electrons towards the interior of the semiconductor. Holes are high energy species that are able to extract electrons from the electrolyte. Here, the n-type semiconductor is acting as a photoanode. At potentials more negative than E_{fb} an n-type electrode acts as a cathode, both in the dark and upon irradiation, due to the formation of the accumulation layer. At more positive potentials, the depletion layer appears and no oxidative current can be generated under dark conditions. However, under

illumination conditions a photocurrent can be observed at more positive potentials than the flatband potential, since the radiation provides some of the energy required for the oxidation.

1.4.1.3 Photoelectrochemical cell (PEC)

Photoelectrocatalytic processes are carried out in photoelectrochemical cells with the elements described in section 1.4.1.2: anode, cathode and reference electrode. In addition, the cell must have a transparent quartz window that allows the photoelectrode to be illuminated by the light source, and all electrodes must be connected to a potentiostat in order to apply the required potential. A cationic membrane is usually employed to separate the anodic and cathodic compartments and avoid the mixture of the gases formed during the reaction [115].

The reaction at the counterelectrode must be fast and the counterelectrode itself must have high catalytic activity to avoid performance limitations. When the photoelectrode is an n-type semiconductor (photoanode), the counterelectrode acts as a cathode. Platinum (Pt) is the most common material employed as a counterelectrode, due to its good chemical stability and very small overpotential for the hydrogen evolution reaction. Ideally, both electrodes must be facing each other symmetrically to prevent heterogeneous current densities at the anode. A platinum tip or mesh is typically used in most of the PEC configurations [115,116]. However, when the photoelectrode is a p-type semiconductor, the counterelectrode acts as an anode instead. As has been mentioned before, the applied potential is a key element for photoelectrocatalytic reactions. This potential must be measured referred to a fixed reference potential, so that any variation in the applied potential is only reflected in the photoelectrode. The counterelectrode cannot be used for this purpose, since the overpotential at the counterelectrode/electrolyte interface is usually unknown and depends on the current flowing through the system. To prevent this current dependency, a third electrode is introduced to the cell: a reference electrode.

This way, the photoelectrode's potential can be measured in reference to the fixed potential of the reference electrode in which the current flow is negligible. The most commonly used reference electrode is the reversible hydrogen electrode (RHE). A potential equal to zero in the RHE scale stands for the potential redox of H^+/H_2 in a real solution, with no dependence on the pH. Other reference electrodes typically used are the silver/silver chloride electrodes (Ag/AgCl), which have almost totally replaced the traditional saturated calomel electrode (SCE) due to the environmental concerns derived from the use of mercury. An important factor to consider when choosing the reference electrode is its stability in the electrolyte [115]. The electrolyte is just a solution in which the active species that are meant to reduce or oxidize are dissolved.

The key component, however, in the photoelectrocatalytic cell is the photoelectrode, in which the electron-hole pairs are photogenerated. An ideal photoelectrode must have the following properties: i) appropriate bandgap width and band edge positions. Solar light is composed of 5-8% ultraviolet radiation (300-400 nm), 43% visible radiation (400-700 nm) and 52% infrared radiation (700-2500 nm). Therefore, the bandgap must be able to absorb light in the visible region to increase the process efficiency. The theoretical minimum bandgap of an appropriate semiconductor must be ca. 1.23V, since the potential for O_2/H_2O at pH=0 is 1.23V. However, considering the energy loss that takes place during the charge transfer process (0.3-0.4 eV) and the requirement of applying a potential in excess for reasonable surface reaction kinetics (0.4-0.6 eV), a bandgap around 1.9-3.2 eV is needed to obtain significant photocurrents. For an optimized use of visible light, a bandgap of 2.0 eV is preferable. It must be noted that the band edge positions of the semiconductors depend on the pH of the electrolyte [117], usually represented by the Nernst equation. Figure 1.11 illustrates the bandgap and band edge positions for n- and p-type semiconductors typically used in photoelectrocatalytic processes at pH=0.

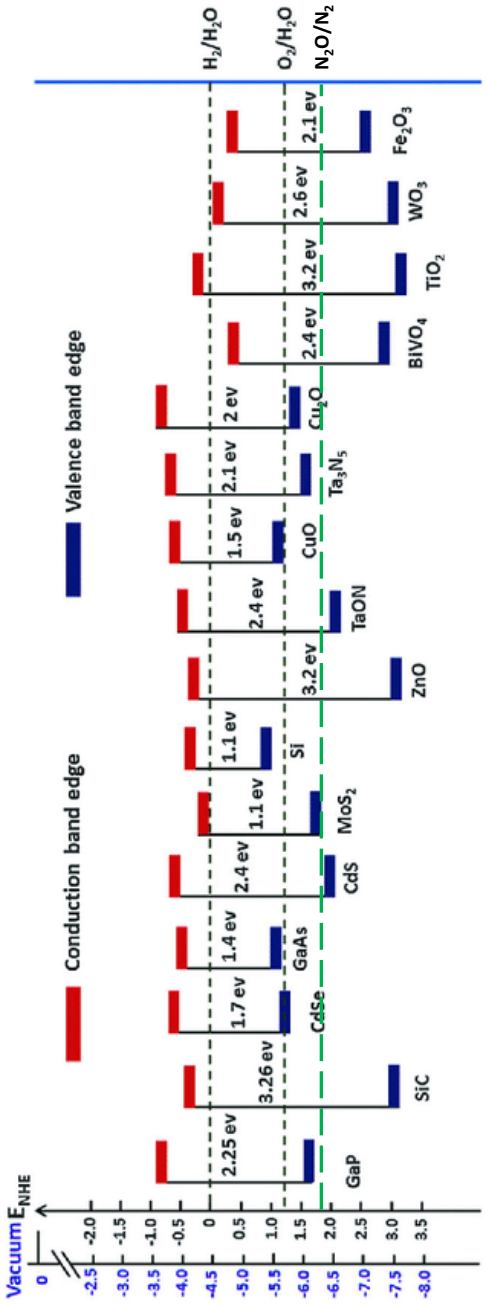

Figure 1. 11. Band edge positions for n- and p-type semiconductors used nowadays in photoelectrocatalytic processes in an aqueous solution at pH = 0 relative to NHE and the vacuum level [118].

ii) Efficient transport and separation of charge carriers in the semiconductor. Charge recombination is known to reduce the efficiency of the photoelectrocatalytic process. The techniques responsible for an effective charge separation and transport depend on both intrinsic (electron-hole pairs mobility) and extrinsic (crystallinity and morphology) properties of the semiconductors. iii) Stability and high catalytic activity: charge accumulation at the surface that would lead to recombination processes can be prevented with appropriate and fast reaction kinetics. Also, is important to consider possible photocorrosion reactions, where the photogenerated electron-hole pairs decompose the photoelectrode instead of participating on redox reactions of interest. Photocorrosion reactions depend on the relative band edge positions of the semiconductors.

The following section describes the interest of the chosen materials as photoanode and photocathode.

1.4.1.4 Photoelectrocatalysts

Photoanodes and photocathodes must be designed to efficiently transform solar energy into hydrogen or even decompose other organic or inorganic compounds, such as N_2O. As has been mentioned before, the photoelectrodes must have low bandgap energy in order to enhance light absorption in the visible region [119–121]. Research has been focusing on materials with bandgaps less than 2eV. Among the studied semiconductors, the III-V systems (GaAs, InP, GaN, etc.) have stood out as the most promising due to their high solar-to-hydrogen (STH) efficiencies. However, these materials present low stability in aqueous electrolytes and are likely to be affected by corrosion. Lately, inexpensive metal oxide semiconductors are being widely studied as photoelectrodes in PEC applications. For instance, typical ceramic oxides like TiO_2, $BiVO_4$ [122,123], WO_3, SnO_2 [124,125], Fe_2O_3 [126,127], Cu_2O and CuO [128,129]. Copper oxides are used as photocathodes

in photoelectrochemical cells, while the rest of materials are employed as photoanodes.

Several preparation methods have been reported in literature for the synthesis of metal oxide nanostructures. Among them, vapor-phase and liquid-phase synthesis methods stand out as the most promising options. Vapor-phase synthesis methods consist of the evaporation of a metallic precursor and its posterior deposition on a metal substrate [130,131]. Depending on the formation mechanism of the nanostructured surface, the vapor deposition can be physical or chemical [132]. Physical vapor deposition (PVD) is based on the evaporation of a precursor in solid or powder state and its condensation over the substrate. Some of the techniques considered as physical vapor deposition are thermal evaporation [133], sputtering [134], pulsed laser deposition [135], electron-beam physical vapor deposition [136] and cathodic arc deposition [137]. On the other hand, chemical vapor deposition (CVD) is based on the reaction or decomposition over the substrate surface of one or more volatile precursors [138]. Volatile by-products are removed by a gaseous stream. Spray pyrolysis [139] and organo-metallic chemical vapor deposition [140] are the most popular methods among CVD techniques. Generally, all vapor-phase deposition methods present very high investment and operational costs, due to the use of noble metal catalysts, high temperatures and low pressures [141].

Liquid-phase deposition has gained attention in recent years due to numerous advantages, including low operational costs, scalability, the use of lower temperatures and a better control over the morphology of the nanostructured materials [138]. The most commonly used liquid phase synthesis methods are the sol-gel method, the hydrothermal synthesis and the electrochemical anodization. During the sol-gel method, a precursor solution suffers a series of hydrolysis and condensation reactions, resulting in the formation of a gel-like network. Finally, the nanostructured material is obtained after the application of a heat treatment to the

formed gel [142,143]. Hydrothermal synthesis consists of a series of reactions in aqueous solutions at high temperature and pressure. A mix of the precursors is introduced into a sealed autoclave and temperature is set above the water boiling point, which results in a drastic pressure increase [144]. Sol-gel and hydrothermal methods present poor control over particle size distribution and morphology. The severe reaction conditions during the hydrothermal method are also an important disadvantage. Therefore, electrochemical anodization has emerged, lately, as one of the most popular synthesis methods. Anodization is carried out in a two-electrode electrochemical cell. The metal of interest acts as an anode, while a noble or inert metal acts as cathode. Both electrodes are immersed in an electrolyte. When an external bias is applied to the system, the metal electrode starts to dissolve and, together with the electrolyte ions, a nanostructured layer is formed on the electrode surface [141]. This way, highly ordered morphologies can be obtained, maintaining relatively low investment and operational costs [115,141,145]. The design and posterior photoelectrochemical performance of the photoelectrocatalysts can be tuned by the controlling anodization parameters like voltage, electrolyte composition, pH and anodization time. Adjusting these parameters, formation speed of the nanostructured layer, size and morphology can be modified [146]. It can also be highlighted the ease of scalability and minimal environmental impact of the procedure [147]. Most importantly, the formed nanostructured layer is very strongly attached to the metal substrate, which leads to high photoconversion efficiencies due to an improved charge transfer and a decrease in the electron-hole pairs recombination. Compared to other synthesis methods, electrochemical anodization also presents higher speed of fabrication and the obtained materials are more reproducible [148,149]. For all the aforementioned reasons, the photocathode and photoanode synthesized in the present thesis have been prepared via electrochemical anodization.

In the present thesis, photocathodes of mixed copper oxides have been prepared and tested in the photoelectrochemical reduction of nitrous oxide. CuO and Cu_2O are p-type semiconductors with narrow bandgaps ranging from 1.3 to 1.6 eV and from 2.0 to 2.5 eV, respectively [150–152]. They present low toxicity, low cost, high abundance in earth crust and high charge carrier mobility, making them very attractive for PEC applications [153,154]. The semiconductor character of these oxides is determined by the presence of cuprous ions vacancies (Cu^+). Both copper oxides have gained attention as promising photocathodes in PEC water splitting due to the suitable CB and VB positions that straddle the water redox potentials (except for the VB of CuO which stands below ~1.5 eV). Nevertheless, based on the smaller bandgap energy, cupric oxide is more thermodynamically suited than cuprous oxide to obtain higher photoconversion efficiencies, due to its wide absorption band in the visible light spectrum. In fact, photoconversion efficiencies of ca. 31% are achieved with CuO as a photocathode versus 18% with Cu_2O [155]. However, Cu_2O presents a much higher charge carrier mobility than CuO (100 vs. 0.1 $cm^2\ V^{-1}\ s^{-1}$, respectively), as well as a greater p-type character associated with a higher concentration of copper vacancies [152].

Copper oxide photoelectrocatalysts can be fabricated by many synthesis routes. Depending on the employed synthesis method, the obtained copper oxide nanoproducts can vary in size and morphology. To date, copper oxide nanostructures include morphologies such as nanowires [156], nanotubes [157], nanorods [158,159], nanosheets [160], etc. Controlling the morphology and dimensions of the nanostructure has a significant impact on important properties like chemical stability, electrochemical activity and mechanical and optical properties [161–163]. In fact, crystal size, surface area, defects and impurities are strongly affected by synthesis procedures and operational parameters. Usually, free-standing copper oxide photoelectrocatalysts are grown on a copper foil by employing electrochemical anodization or chemical oxidation method (COM) followed by annealing in air or in

an inert atmosphere [155]. Despite the benefits of electrochemical anodization, this method has been hardly employed to synthesize copper oxide nanostructures. D. W. Shoesmith et al. (1976) reported the first copper nanocrystal growth by potentiostatic oxidation with LiOH as electrolyte [164]. Later, Ji et al. investigated the effect of the temperature during the anodization process as well as the influence of different additives [165]. Recent studies have focused on the fabrication of these photoelectrocatalysts using aqueous electrolytes containing KOH, NaOH, KCl and NH_4F as complexing agents [166–168].

In the present thesis, copper oxide photoelectrocatalysts have been fabricated by electrochemical anodization employing novel ethylene glycol-based electrolytes containing complexing agents like oxalic acid and sodium fluoride. It is important to select an appropriate complexing agent in order to increase the surface area and improve the electrochemical properties of the oxides. Besides, different electrolyte formulations with various organic solvents have also been tested. The influence of other anodization parameters such as time and hydrodynamic conditions on the obtained photoelectrocatalysts have been studied. In addition, it is believed that the photoelectrocatalytic performance of copper oxide nanostructures is improved by the presence of both copper species. This way, CuO enhances the absorption of light, while Cu_2O favors the mobility of charge carriers and facilitates the photoelectro-reduction of nitrous oxide.

Regarding photoanodes, titanium dioxide is considered as one of the most effective and useful electrodes in spite of the increasing research about materials for photocatalytic and PEC applications. Titania nanostructures stand out due to their chemical and thermal stability, their low fabrication costs and their adequate morphological and optical properties. Several morphologies have been developed such as nanotubes, nanowires and nanorods. Particularly, titanium dioxide nanotubes (NTs) are known to generate higher photocurrents under lower radiation due to an

improved light harvesting [169]. Usually, the TiO_2 nanotube growth by electrochemical anodization is carried out in presence of fluoride ions, as it has been reported that a uniform self-ordered nanotubular structure is obtained [170]. In fact, electrolyte composition is one of the key parameters that determines the morphology and photoelectrochemical performance of the titania nanotubes. The first study about the synthesis of titanium dioxide nanotubes or nanopores with a fluoride-containing electrolyte was reported by Dezfuly et al. (1984) [171]. This study was later continued by Zwilling et al. in 1999, where self-organized nanotubes were obtained by the anodization with hydrofluoric acid in the electrolyte [172].

Electrolytes based on organic solvents like ethylene glycol or glycerol are typically employed, containing as well water and fluoride ions (NH_4F, HF, NaF…) [173–177]. Lately, the synthesis of titania nanotubes with ionic liquids (IL) in the anodization solution has gained popularity. Ionic liquids are organic solvents that present many advantages compared to traditional solvents, including a higher conductivity, higher electrochemical stability and no volatility. Based on their chemical behavior, ionic liquids can be classified in protic and aprotic ionic liquids [178]. Aprotic ionic liquids (AILs) consist of bulky organic cations with long alkyl chain substituents and a wide range of anions. Their application in electrochemical anodization has been extensively explored for the synthesis of efficient photoelectrocatalysts. The obtained nanostructure materials benefit from tailored size and morphology, which increase their specific surface area. For instance, 1-ethyl-3-methylimidazolium tetrafluoroborate [BMIM][BF_4] was the first ionic liquid used in the electrochemical anodization of titanium in 2008 [179]. Research continued with the same IL but adjusting the anodization parameters to obtain improved nanostructured titanium dioxide [174,180–182]. More aprotic ionic liquids have been tested in recent years such as 1-ethyl-3-methylimidazolium tetrafluoroborate [EMIM][BF_4], 3-methyl-1-octyimidazolium tetrafluoroborate [OMIM][BF_4] [183], 1-n-butylpyridinium chloride [BPy] [Cl] [184], 1-n-butyl-3-

methylimidazoly chloride [BMIM][Cl] [180] and ethylammonium nitrate [EAN][NO_3] [185]. Conversely, protic ionic liquids (PILs) are based on substituted amines as cations and organic acids with varying carbon chain lengths as anions. It has been proved that PILs are, generally, an environmentally safer alternative to AILs, due to their lower toxicity and their potential biodegradability in water [186]. Furthermore, PILs are more easily manufactured, and their operational costs are much lower than those of AILs, despite being the protic ionic liquids still in early stages of development. Furthermore, small concentrations of PILs during electrochemical anodization of TiO_2 NTs result in a better photoresponse than increasing the fluoride content in the electrolyte, which leads to a more sustainable and environmentally friendly formulation [187].

Given the many benefits of the titania nanostructures and their easy fabrication employing environmentally friendly ionic liquids, this work aims to synthesize nanotubular titanium dioxide photoelectrodes by electrochemical anodization using various protic ionic liquids. A systematic study was conducted on the influence of anodization parameters including: i) controlled hydrodynamic conditions, ii) type of ionic liquid, and iii) the concentration of the ionic liquid in the anodization electrolyte. After a detailed analysis on the morphology, structure, electrochemical properties and photoelectrocatalytic behavior, the most effective TiO_2 nanostructure was tested as photoanode in the photoelectrochemical reduction of nitrous oxide.

1.5 References

[1] Institute of Energy, Statistical review of world energy 2023, Stat. Rev. World Energy (n.d.). https://www.energyinst.org/statistical-review/home (accessed May 19, 2025).
[2] F. Dawood, M. Anda, G.M. Shafiullah, Hydrogen production for energy: An overview, Int. J. Hydrog. Energy 45 (2020) 3847–3869. https://doi.org/10.1016/j.ijhydene.2019.12.059.
[3] UNITED NATIONS DEPARTMENT FOR ECONOMIC AND SOCIAL AFFAIRS, WORLD POPULATION PROSPECTS 2024: summary of results, UNITED NATIONS, S.l., 2025.
[4] International Energy Agency, World Energy Outlook 2004, OECD, 2004. https://doi.org/10.1787/weo-2004-en.
[5] Overview of Greenhouse Gases | US EPA, (n.d.). https://www.epa.gov/ghgemissions/overview-greenhouse-gases (accessed February 7, 2024).
[6] H. Tian, R. Xu, J.G. Canadell, R.L. Thompson, W. Winiwarter, P. Suntharalingam, E.A. Davidson, P. Ciais, R.B. Jackson, G. Janssens-Maenhout, M.J. Prather, P. Regnier, N. Pan, S. Pan, G.P. Peters, H. Shi, F.N. Tubiello, S. Zaehle, F. Zhou, A. Arneth, G. Battaglia, S. Berthet, L. Bopp, A.F. Bouwman, E.T. Buitenhuis, J. Chang, M.P. Chipperfield, S.R.S. Dangal, E. Dlugokencky, J.W. Elkins, B.D. Eyre, B. Fu, B. Hall, A. Ito, F. Joos, P.B. Krummel, A. Landolfi, G.G. Laruelle, R. Lauerwald, W. Li, S. Lienert, T. Maavara, M. MacLeod, D.B. Millet, S. Olin, P.K. Patra, R.G. Prinn, P.A. Raymond, D.J. Ruiz, G.R. Van Der Werf, N. Vuichard, J. Wang, R.F. Weiss, K.C. Wells, C. Wilson, J. Yang, Y. Yao, A comprehensive quantification of global nitrous oxide sources and sinks, Nature 586 (2020) 248–256. https://doi.org/10.1038/s41586-020-2780-0.
[7] M.W. Jones, G.P. Peters, T. Gasser, R.M. Andrew, C. Schwingshackl, J. Gütschow, R.A. Houghton, P. Friedlingstein, J. Pongratz, C. Le Quéré, National contributions to climate change due to historical emissions of carbon dioxide, methane and nitrous oxide, (2024). https://doi.org/10.5281/zenodo.14054503.
[8] O. US EPA, Nitrous Oxide Emissions, (2025). https://www.epa.gov/ghgemissions/nitrous-oxide-emissions (accessed May 19, 2025).
[9] M.J. Prather, J. Hsu, N.M. DeLuca, C.H. Jackman, L.D. Oman, A.R. Douglass, E.L. Fleming, S.E. Strahan, S.D. Steenrod, O.A. Søvde, I.S.A. Isaksen, L. Froidevaux, B. Funke, Measuring and modeling the lifetime of nitrous oxide including its variability, J. Geophys. Res. Atmospheres 120 (2015) 5693–5705. https://doi.org/10.1002/2015JD023267.
[10] M. Konsolakis, Recent Advances on Nitrous Oxide (N2O) Decomposition over Non-Noble-Metal Oxide Catalysts: Catalytic Performance, Mechanistic

Considerations, and Surface Chemistry Aspects, ACS Catal. 5 (2015) 6397–6421. https://doi.org/10.1021/acscatal.5b01605.
[11] M. Strokal, C. Kroeze, Nitrous oxide (N2O) emissions from human waste in 1970–2050, Curr. Opin. Environ. Sustain. 9–10 (2014) 108–121. https://doi.org/10.1016/j.cosust.2014.09.008.
[12] S. He, Y. Han, X. Qin, Advances in accounting methodology of nitrous oxide emissions from the adipic acid industry, J. Environ. Sci. (2024). https://doi.org/10.1016/j.jes.2024.03.014.
[13] C.H. Bamford, C.F.H. (Charles F.H. Tipper, Reactions of non-metallic inorganic compounds, Elsevier Pub. Co., 1972. https://cir.nii.ac.jp/crid/1130000797722984192 (accessed May 20, 2025).
[14] F. Kapteijn, J. Rodriguez-Mirasol, J.A. Moulijn, Heterogeneous catalytic decomposition of nitrous oxide, Appl. Catal. B Environ. 9 (1996) 25–64. https://doi.org/10.1016/0926-3373(96)90072-7.
[15] E. Fareid, G. Kongshaug, L. Hjornevik, O. Nirisen, Method by reduction of nitrogen oxide, 0 359 286 B1, 1993.
[16] M. Galle, D.W. Agar, O. Watzenberger, Thermal N2O decomposition in regenerative heat exchanger reactors, Chem. Eng. Sci. 56 (2001) 1587–1595. https://doi.org/10.1016/S0009-2509(00)00386-9.
[17] I. Song, Y. Wang, J. Szanyi, K. Khivantsev, Co-existence of atomically dispersed Ru and Ce3+ sites is responsible for excellent low temperature N2O reduction activity of Ru/CeO2, Appl. Catal. B Environ. 343 (2024). https://doi.org/10.1016/j.apcatb.2023.123487.
[18] S. Parres-Esclapez, M.J. Illán-Gómez, C.S.-M. de Lecea, A. Bueno-López, On the importance of the catalyst redox properties in the N2O decomposition over alumina and ceria supported Rh, Pd and Pt, Appl. Catal. B Environ. 96 (2010) 370–378. https://doi.org/10.1016/j.apcatb.2010.02.034.
[19] Y. You, S. Chen, J. Li, J. Zeng, H. Chang, L. Ma, J. Li, Low-temperature selective catalytic reduction of N2O by CO over Fe-ZSM-5 catalysts in the presence of O2, J. Hazard. Mater. 383 (2020). https://doi.org/10.1016/j.jhazmat.2019.121117.
[20] X. Zhang, Q. Shen, C. He, C. Ma, J. Cheng, L. Li, Z. Hao, Investigation of selective catalytic reduction of N 2O by NH 3 over an Fe-mordenite catalyst: Reaction mechanism and O 2 effect, ACS Catal. 2 (2012) 512–520. https://doi.org/10.1021/cs200568w.
[21] H. Yu, X. Wang, Y. Li, Strong impact of cobalt distribution on the activity for Co3O4/CaCO3 catalyzing N2O decomposition, Catal. Today 339 (2020) 274–280. https://doi.org/10.1016/j.cattod.2018.10.036.
[22] H. Liu, J. Chen, Y. Wang, S. Xiong, Z. Su, Y. Wang, W. Yang, X. Chu, W. Yang, Y. Peng, W. Si, J. Li, Boosting nitrous oxide direct decomposition performance based on samarium doping effects, Chem. Eng. J. 414 (2021). https://doi.org/10.1016/j.cej.2021.128643.

[23] J. Pérez-Ramírez, F. Kapteijn, K. Schöffel, J.A. Moulijn, Formation and control of N2O in nitric acid production: Where do we stand today?, Appl. Catal. B Environ. 44 (2003) 117–151. https://doi.org/10.1016/S0926-3373(03)00026-2.
[24] P. Stelmachowski, G. Maniak, A. Kotarba, Z. Sojka, Strong electronic promotion of Co3O4 towards N2O decomposition by surface alkali dopants, Catal. Commun. 10 (2009) 1062–1065. https://doi.org/10.1016/j.catcom.2008.12.057.
[25] M. Rutkowska, L. Chmielarz, M. Jabłońska, C.J. Van Oers, P. Cool, Iron exchanged ZSM-5 and y zeolites calcined at different temperatures: Activity in N2O decomposition, J. Porous Mater. 21 (2014) 91–98. https://doi.org/10.1007/s10934-013-9751-x.
[26] J. Oi, A. Obuchi, G.R. Bamwenda, A. Ogata, H. Yagita, S. Kushiyama, K. Mizuno, Decomposition of nitrous oxide over supported rhodium catalysts and dependency on feed gas composition, Appl. Catal. B Environ. 12 (1997) 277–286. https://doi.org/10.1016/S0926-3373(96)00079-3.
[27] T.N. Angelidis, V. Tzitzios, Promotion of the catalytic activity of a Ag/Al2O3 catalyst for N2O decomposition by the addition of Rh. A comparative activity and kinetic study, Ind. Eng. Chem. Res. 42 (2003) 2996–3000. https://doi.org/10.1021/ie020533b.
[28] Ethylene Global Market and Trend, (n.d.). https://www.hdinresearch.com/news/106 (accessed June 25, 2025).
[29] Ethylene Market Size, Share, Trends, Growth & Forecast, (n.d.). https://www.chemanalyst.com/industry-report/ethylene-market-638 (accessed May 26, 2025).
[30] Ethylene Global Market and Trend, (n.d.). https://www.hdinresearch.com/news/106 (accessed May 28, 2025).
[31] C.A. Gärtner, A.C. vanVeen, J.A. Lercher, Oxidative dehydrogenation of ethane: Common principles and mechanistic aspects, ChemCatChem 5 (2013) 3196–3217. https://doi.org/10.1002/cctc.201200966.
[32] Y. Chen, M. Jen Kuo, R. Lobo, M. Ierapetritou, Ethylene production: process design, techno-economic and life-cycle assessments, Green Chem. 26 (2024) 2903–2911. https://doi.org/10.1039/D3GC03858K.
[33] S. Najari, S. Saeidi, P. Concepcion, D.D. Dionysiou, S.K. Bhargava, A.F. Lee, K. Wilson, Oxidative dehydrogenation of ethane: Catalytic and mechanistic aspects and future trends, Chem. Soc. Rev. 50 (2021) 4564–4605. https://doi.org/10.1039/d0cs01518k.
[34] H. Zimmermann, R. Walzl, Ethylene, in: Ullmanns Encycl. Ind. Chem., John Wiley & Sons, Ltd, 2009. https://doi.org/10.1002/14356007.a10_045.pub3.
[35] Recent Advances in Intensified Ethylene Production—A Review | ACS Catalysis, (n.d.). https://pubs.acs.org/doi/10.1021/acscatal.9b02922 (accessed May 28, 2025).

[36] M. Ghanta, D. Fahey, B. Subramaniam, Environmental impacts of ethylene production from diverse feedstocks and energy sources, Appl. Petrochem. Res. 4 (2014) 167–179. https://doi.org/10.1007/s13203-013-0029-7.
[37] A.S. Bodke, D.A. Olschki, L.D. Schmidt, E. Ranzi, High Selectivities to Ethylene by Partial Oxidation of Ethane, Science 285 (1999) 712–715. https://doi.org/10.1126/science.285.5428.712.
[38] Synthesis of Transportation Fuels from Biomass: Chemistry, Catalysts, and Engineering | Chemical Reviews, (n.d.). https://pubs.acs.org/doi/10.1021/cr068360d (accessed May 28, 2025).
[39] I. Takahara, M. Saito, M. Inaba, K. Murata, Dehydration of Ethanol into Ethylene over Solid Acid Catalysts, Catal. Lett. 105 (2005) 249–252. https://doi.org/10.1007/s10562-005-8698-1.
[40] U.G.A. (70th Sess.: 2015-2016), U.D. of E. and S.A.D. for S.D. Goals, U.G.A. (70th Sess.: 2015-2016), U.D. of E. and S.A.D. for S.D. Goals, Transforming our world : the 2030 Agenda for Sustainable Development, (2015). https://policycommons.net/artifacts/18386159/transforming-our-world/19286553/ (accessed May 28, 2025).
[41] D. Hickman, Clariant and Linde's Catalyst and Technology for Sustainable Ethylene Production, ChemistryViews (2021). https://www.chemistryviews.org/details/news/11296393/Clariant_and_Lindes_Catalyst_and_Technology_for_Sustainable_Ethylene_Production/ (accessed June 25, 2025).
[42] M.P. Woods, B. Mirkelamoglu, U.S. Ozkan, Oxygen and nitrous oxide as oxidants: Implications for ethane oxidative dehydrogenation over silica-titania-supported molybdenum, J. Phys. Chem. C 113 (2009) 10112–10119. https://doi.org/10.1021/jp810664u.
[43] X. Jiang, L. Sharma, V. Fung, S.J. Park, C.W. Jones, B.G. Sumpter, J. Baltrusaitis, Z. Wu, Oxidative dehydrogenation of propane to propylene with soft oxidants via heterogeneous catalysis, ACS Catal. 11 (2021) 2182–2234. https://doi.org/10.1021/acscatal.0c03999.
[44] A. Qiao, V.N. Kalevaru, J. Radnik, A. Martin, Oxidative dehydrogenation of ethane to ethylene over Ni–Nb–M–O catalysts: Effect of promoter metal and CO2-admixture on the performance, Catal. Today 264 (2016) 144–151. https://doi.org/10.1016/j.cattod.2015.08.043.
[45] B. Solsona, J.M. López Nieto, P. Concepción, A. Dejoz, F. Ivars, M.I. Vázquez, Oxidative dehydrogenation of ethane over Ni-W-O mixed metal oxide catalysts, J. Catal. 280 (2011) 28–39. https://doi.org/10.1016/j.jcat.2011.02.010.
[46] J.-P. Lange, R.J. Schoonebeek, P. Mercera, F.W. van Breukelen, Oxycracking of hydrocarbons: Chemistry, technology and economic potential, Appl. Catal. Gen. 283 (2005) 243–253. https://doi.org/10.1016/j.apcata.2005.01.011.
[47] X. Lin, C.A. Hoel, W.M.H. Sachtler, K.R. Poeppelmeier, E. Weitz, Oxidative dehydrogenation (ODH) of ethane with O2 as oxidant on selected transition

metal-loaded zeolites, J. Catal. 265 (2009) 54–62. https://doi.org/10.1016/j.jcat.2009.04.007.
[48] A. Alamdari, R. Karimzadeh, S. Abbasizadeh, Present state of the art of and outlook on oxidative dehydrogenation of ethane: catalysts and mechanisms, Rev. Chem. Eng. 37 (2021) 481–532. https://doi.org/10.1515/revce-2017-0109.
[49] R. Grabowski, Kinetics of Oxidative Dehydrogenation of C2-C3 Alkanes on Oxide Catalysts, Catal. Rev. 48 (2006) 199–268. https://doi.org/10.1080/01614940600631413.
[50] J. Haber, M. Witko, R. Tokarz, Vanadium pentoxide I. Structures and properties, Appl. Catal. Gen. 157 (1997) 3–22. https://doi.org/10.1016/S0926-860X(97)00017-3.
[51] A. de Arriba, G. Sánchez, R. Sánchez-Tovar, P. Concepción, R. Fernández-Domene, B. Solsona, J.M. López Nieto, On the selectivity to ethylene during ethane ODH over M1-based catalysts. A surface and electrochemical study, Catal. Today 418 (2023). https://doi.org/10.1016/j.cattod.2023.114122.
[52] A.M. Gaffney, Q. An, W.A. Goddard, W. Diao, M.V. Glazoff, Toward Concurrent Engineering of the M1-Based Catalytic Systems for Oxidative Dehydrogenation (ODH) of Alkanes, Top. Catal. 63 (2020) 1667–1681. https://doi.org/10.1007/s11244-020-01327-7.
[53] A. de Arriba, B. Solsona, A.M. Dejoz, P. Concepción, N. Homs, P.R. de la Piscina, J.M. López Nieto, Evolution of the optimal catalytic systems for the oxidative dehydrogenation of ethane: The role of adsorption in the catalytic performance, J. Catal. 408 (2022) 388–400. https://doi.org/10.1016/j.jcat.2021.07.015.
[54] J.G. Rivera, M.A. Purino, J.F. Durán, C. Alvarado, A. Hernandez, M.K. Sabbe, C.O. Castillo-Araiza, Multiscale analysis of the M1 MoVNbTeO catalyst for ethylene production via selective ethane oxidation: From atomistic calculations to the industrial reactor, Chem. Eng. J. 506 (2025) 159252. https://doi.org/10.1016/j.cej.2025.159252.
[55] H. Kim, G.A. Ferguson, L. Cheng, S.A. Zygmunt, P.C. Stair, L.A. Curtiss, Structure-Specific Reactivity of Alumina-Supported Monomeric Vanadium Oxide Species, J. Phys. Chem. C 116 (2012) 2927–2932. https://doi.org/10.1021/jp209326h.
[56] M.D. Argyle, K. Chen, A.T. Bell, E. Iglesia, Effect of Catalyst Structure on Oxidative Dehydrogenation of Ethane and Propane on Alumina-Supported Vanadia, J. Catal. 208 (2002) 139–149. https://doi.org/10.1006/JCAT.2002.3570.
[57] K. Chen, A.T. Bell, E. Iglesia, The Relationship between the Electronic and Redox Properties of Dispersed Metal Oxides and Their Turnover Rates in Oxidative Dehydrogenation Reactions, J. Catal. 209 (2002) 35–42. https://doi.org/10.1006/jcat.2002.3620.

[58] T.T. Nguyen, L. Burel, D.L. Nguyen, C. Pham-Huu, J.M.M. Millet, Catalytic performance of MoVTeNbO catalyst supported on SiC foam in oxidative dehydrogenation of ethane and ammoxidation of propane, Appl. Catal. Gen. 433–434 (2012) 41–48. https://doi.org/10.1016/j.apcata.2012.04.038.

[59] B. Solsona, M.I. Vázquez, F. Ivars, A. Dejoz, P. Concepción, J.M. López Nieto, Selective oxidation of propane and ethane on diluted Mo–V–Nb–Te mixed-oxide catalysts, J. Catal. 252 (2007) 271–280. https://doi.org/10.1016/j.jcat.2007.09.019.

[60] J.M.L. Nieto, P. Botella, M.I. Vázquez, A. Dejoz, The selective oxidative dehydrogenation of ethane over hydrothermally synthesised MoVTeNb catalysts, Chem. Commun. (2002) 1906–1907. https://doi.org/10.1039/B204037A.

[61] E. Heracleous, A.A. Lemonidou, Ni–Nb–O mixed oxides as highly active and selective catalysts for ethene production via ethane oxidative dehydrogenation. Part I: Characterization and catalytic performance, J. Catal. 237 (2006) 162–174. https://doi.org/10.1016/J.JCAT.2005.11.002.

[62] D. Delgado, B. Solsona, R. Sanchis, E. Rodríguez-Castellón, J.M. López Nieto, Oxidative dehydrogenation of ethane on diluted or promoted nickel oxide catalysts: Influence of the promoter/diluter, Catal. Today 363 (2021) 27–35. https://doi.org/10.1016/J.CATTOD.2019.06.063.

[63] Y. Abdelbaki, A. de Arriba, B. Solsona, D. Delgado, E. García-González, R. Issaadi, J.M. López Nieto, The nickel-support interaction as determining factor of the selectivity to ethylene in the oxidative dehydrogenation of ethane over nickel oxide/alumina catalysts, Appl. Catal. Gen. 623 (2021) 118242. https://doi.org/10.1016/j.apcata.2021.118242.

[64] E. Heracleous, A.A. Lemonidou, Ni-Me-O mixed metal oxides for the effective oxidative dehydrogenation of ethane to ethylene - Effect of promoting metal Me, J. Catal. 270 (2010) 67–75. https://doi.org/10.1016/j.jcat.2009.12.004.

[65] J.M. López Nieto, B. Solsona, R.K. Grasselli, P. Concepción, Promoted NiO Catalysts for the Oxidative Dehydrogenation of Ethane, Top. Catal. 57 (2014) 1248–1255. https://doi.org/10.1007/s11244-014-0288-2.

[66] B. Savova, S. Loridant, D. Filkova, J.M.M. Millet, Ni–Nb–O catalysts for ethane oxidative dehydrogenation, Appl. Catal. Gen. 390 (2010) 148–157. https://doi.org/10.1016/j.apcata.2010.10.004.

[67] B. Solsona, P. Concepción, B. Demicol, S. Hernández, J.J. Delgado, J.J. Calvino, J.M. López Nieto, Selective oxidative dehydrogenation of ethane over SnO2-promoted NiO catalysts, J. Catal. 295 (2012) 104–114. https://doi.org/10.1016/J.JCAT.2012.07.028.

[68] Z. Skoufa, E. Heracleous, A.A. Lemonidou, On ethane ODH mechanism and nature of active sites over NiO-based catalysts via isotopic labeling and methanol sorption studies, J. Catal. 322 (2015) 118–129. https://doi.org/10.1016/J.JCAT.2014.11.014.

[69] H. Zhu, S. Ould-Chikh, D.H. Anjum, M. Sun, G. Biausque, J.-M. Basset, V. Caps, Nb effect in the nickel oxide-catalyzed low-temperature oxidative dehydrogenation of ethane, J. Catal. 285 (2012) 292–303. https://doi.org/10.1016/j.jcat.2011.10.005.

[70] Ş.B. Ivan, I. Fechete, F. Papa, I.C. Marcu, Ethane oxydehydrogenation over TiP2O7-supported NiO catalysts, Catal. Today 366 (2021) 133–140. https://doi.org/10.1016/j.cattod.2020.02.005.

[71] P. Brussino, E.L. Mehring, M.A. Ulla, J.P. Bortolozzi, Tuning the properties of NiO supported on silicon-aluminum oxides: Influence of the silica amount in the ODH of ethane, Catal. Today (2021). https://doi.org/10.1016/j.cattod.2021.10.017.

[72] J.L. Park, K.A. Canizales, M.D. Argyle, B.F. Woodfield, K.J. Stowers, The effects of doping alumina with silica in alumina-supported NiO catalysts for oxidative dehydrogenation of ethane, Microporous Mesoporous Mater. 293 (2020). https://doi.org/10.1016/j.micromeso.2019.109799.

[73] H. Zhu, D.C. Rosenfeld, M. Harb, D.H. Anjum, M.N. Hedhili, S. Ould-Chikh, J.M. Basset, Ni-M-O (M = Sn, Ti, W) Catalysts Prepared by a Dry Mixing Method for Oxidative Dehydrogenation of Ethane, ACS Catal. 6 (2016) 2852–2866. https://doi.org/10.1021/acscatal.6b00044.

[74] D. Delgado, B. Solsona, A. Ykrelef, A. Rodríguez-Gómez, A. Caballero, E. Rodríguez-Aguado, E. Rodríguez-Castellón, J.M. López Nieto, Redox and Catalytic Properties of Promoted NiO Catalysts for the Oxidative Dehydrogenation of Ethane, J. Phys. Chem. C 121 (2017) 25132–25142. https://doi.org/10.1021/acs.jpcc.7b07066.

[75] Y. Abdelbaki, R. Sánchez-Tovar, A. de Arriba, E. García-González, R. Fernández-Domene, B. Solsona, J.M. López Nieto, Predicting the catalytic performance of Nb-doped nickel oxide catalysts for the oxidative dehydrogenation of ethane by knowing their electrochemical properties, J. Catal. 420 (2023) 9–22. https://doi.org/10.1016/J.JCAT.2023.02.009.

[76] D. Delgado, R. Sanchis, B. Solsona, P. Concepción, J.M. López Nieto, Influence of the Nature of the Promoter in NiO Catalysts on the Selectivity to Olefin During the Oxidative Dehydrogenation of Propane and Ethane, Top. Catal. 63 (2020) 1731–1742. https://doi.org/10.1007/s11244-020-01329-5.

[77] A.H. Mamaghani, F. Haghighat, C.-S. Lee, Photocatalytic oxidation technology for indoor environment air purification: The state-of-the-art, Appl. Catal. B Environ. 203 (2017) 247–269. https://doi.org/10.1016/j.apcatb.2016.10.037.

[78] R. Prasad, Kennedy ,Lawrence A., E. and Ruckenstein, Catalytic Combustion, Catal. Rev. 26 (1984) 1–58. https://doi.org/10.1080/01614948408078059.

[79] M. Myint, B. Yan, J. Wan, S. Zhao, J.G. Chen, Reforming and oxidative dehydrogenation of ethane with CO2 as a soft oxidant over bimetallic catalysts, J. Catal. 343 (2016) 168–177. https://doi.org/10.1016/j.jcat.2016.02.004.

[80] Oxidative Dehydrogenation of Ethane with CO2 over Flame-Made Ga-Loaded TiO2 | ACS Catalysis, (n.d.). https://pubs.acs.org/doi/full/10.1021/cs500685d.
[81] E.V. Kondratenko, O. Ovsitser, Catalytic abatement of nitrous oxide coupled with selective production of hydrogen and ethylene, Angew. Chem. - Int. Ed. 47 (2008) 3227–3229. https://doi.org/10.1002/anie.200705324.
[82] E.V. Kondratenko, M. Cherian, M. Baerns, D. Su, R. Schlögl, X. Wang, I.E. Wachs, Oxidative dehydrogenation of propane over V/MCM-41 catalysts: Comparison of O2 and N2O as oxidants, J. Catal. 234 (2005) 131–142. https://doi.org/10.1016/j.jcat.2005.05.025.
[83] E.V. Kondratenko, M. Baerns, Catalytic oxidative dehydrogenation of propane in the presence of O2 and N2O - The role of vanadia distribution and oxidant activation, Appl. Catal. Gen. 222 (2001) 133–143. https://doi.org/10.1016/S0926-860X(01)00836-5.
[84] A. Held, J. Kowalska, K. Nowińska, Nitrous oxide as an oxidant for ethane oxydehydrogenation, Appl. Catal. B Environ. 64 (2006) 201–208. https://doi.org/10.1016/J.APCATB.2005.11.017.
[85] O. Ovsitser, E.V. Kondratenko, Similarity and differences in the oxidative dehydrogenation of C2–C4 alkanes over nano-sized VOx species using N2O and O2, Catal. Today 142 (2009) 138–142. https://doi.org/10.1016/J.CATTOD.2008.09.012.
[86] X. Rozanska, E.V. Kondratenko, J. Sauer, Oxidative dehydrogenation of propane: Differences between N2O and O2 in the reoxidation of reduced vanadia sites and consequences for selectivity, J. Catal. 256 (2008) 84–94. https://doi.org/10.1016/J.JCAT.2008.03.002.
[87] E.V. Kondratenko, A. Brückner, On the nature and reactivity of active oxygen species formed from O2 and N2O on VO*x*/MCM-41 used for oxidative dehydrogenation of propane, J. Catal. 274 (2010) 111–116. https://doi.org/10.1016/j.jcat.2010.06.010.
[88] M. Xu, H.-X. Wang, H. Ouyang, L. Zhao, Q. Lu, Direct catalytic decomposition of N2O over bismuth modified NiO catalysts, J. Hazard. Mater. 401 (2021) 123334. https://doi.org/10.1016/j.jhazmat.2020.123334.
[89] F. Zhang, X. Wang, X. Zhang, M. Turxun, H. Yu, J. Zhao, The catalytic activity of NiO for N2O decomposition doubly promoted by barium and cerium, Chem. Eng. J. 256 (2014) 365–371. https://doi.org/10.1016/J.CEJ.2014.07.007.
[90] N. Pasha, N. Lingaiah, P. Siva Sankar Reddy, P.S. Sai Prasad, An investigation into the effect of Cs promotion on the catalytic activity of NiO in the direct decomposition of N2O, Catal. Lett. 118 (2007) 64–68. https://doi.org/10.1007/s10562-007-9146-1.
[91] Y. Zhou, J. Lin, L. Li, M. Tian, X. Li, X. Pan, Y. Chen, X. Wang, Improving the selectivity of Ni-Al mixed oxides with isolated oxygen species for oxidative dehydrogenation of ethane with nitrous oxide, J. Catal. 377 (2019) 438–448. https://doi.org/10.1016/j.jcat.2019.07.050.

[92] Y. Zhou, F. Wei, J. Lin, L. Li, X. Li, H. Qi, X. Pan, X. Liu, C. Huang, S. Lin, X. Wang, S. Lin, X. Wang, Sulfate-Modified NiAl Mixed Oxides as Effective C-H Bond-Breaking Agents for the Sole Production of Ethylene from Ethane, ACS Catal. 10 (2020) 7619–7629. https://doi.org/10.1021/acscatal.0c02347.

[93] X. Xu, S.K. Megarajan, X. Xia, A. Toghan, A. Feldhoff, Y. Zhang, H. Jiang, Effect of reduction temperature on the structure and catalytic performance of mesoporous Ni–Fe–Al2O3 in oxidative dehydrogenation of ethane, New J. Chem. 44 (2020) 18994–19001. https://doi.org/10.1039/D0NJ02618B.

[94] K. Kočí, S. Krejčíková, O. Šolcová, L. Obalová, Photocatalytic decomposition of N2O on Ag-TiO2, Catal. Today 191 (2012) 134–137. https://doi.org/10.1016/J.CATTOD.2012.01.021.

[95] K. Kočí, L. Matějová, N. Ambrožová, M. Šihor, I. Troppová, L. Čapek, A. Kotarba, P. Kustrowski, A. Hospodková, L. Obalová, Optimization of cerium doping of TiO2for photocatalytic reduction of CO2and photocatalytic decomposition of N2O, J. Sol-Gel Sci. Technol. 78 (2016) 550–558. https://doi.org/10.1007/S10971-016-3994-3/FIGURES/5.

[96] van der Stegen J.H.G., W. Visscher, J.G. Hoogland, The electrochemical reduction of N2O to hydrazine, Electrochem. Technol. 4 (1966) 564–568.

[97] K.E. Johnson, D.T. Sawyer, The electrochemical reduction of nitrous oxide in alkaline solution, J. Electroanal. Chem. Interfacial Electrochem. 49 (1974) 95–103. https://doi.org/10.1016/S0022-0728(74)80349-9.

[98] H. Ebert, R. Parsons, G. Ritzoulis, T. VanderNoot, The reduction of nitrous oxide on platinum electrodes in acid solution, J. Electroanal. Chem. Interfacial Electrochem. 264 (1989) 181–193. https://doi.org/10.1016/0022-0728(89)80156-1.

[99] A. Kudo, A. Mine, Electrocatalytic reduction of nitrous oxide on metal an oxide electrodes in aqueous solution, 121 (1997) 538–542.

[100] M. Zabilskiy, P. Djinović, B. Erjavec, G. Dražić, A. Pintar, Small CuO clusters on CeO2 nanospheres as active species for catalytic N2O decomposition, Appl. Catal. B Environ. 163 (2015) 113–122. https://doi.org/10.1016/j.apcatb.2014.07.057.

[101] Fundamentos de la Electrónica y los Semiconductores - Universidad de Cádiz, (n.d.). https://tiendaeditorial.uca.es/libro/fundamentos-de-la-electronica-y-los-semiconductores_155449/ (accessed June 5, 2025).

[102] R.M. Fernandez Domene, R. Sanchez Tovar, B. Lucas Granados, J. Garcia Anton, Principios de Fotoelectroquímica, Universitat Politecnica de Valencia, 2018.

[103] A.W. Bott, Electrochemistry of Semiconductors, 17 (1998) 87–91.

[104] A. Rockett, The Materials Science of Semiconductors, Springer US, Boston, MA, 2008. https://doi.org/10.1007/978-0-387-68650-9.

[105] P. Atkins, T. Overton, J. Rourke, M. Weller, F. Armstrong, M. Hagerman, The structures of simple solids, in: Shriver Atkins Inorg. Chem., 5th ed., 2010.

[106] H. Mehrer, ed., Point Defects in Crystals, in: Diffus. Solids Fundam. Methods Mater. Diffus.-Control. Process., Springer, Berlin, Heidelberg, 2007: pp. 69–93. https://doi.org/10.1007/978-3-540-71488-0_5.
[107] P.J. Boddy, The structure of the semiconductor-electrolyte interface, J. Electroanal. Chem. 1959 10 (1965) 199–244. https://doi.org/10.1016/0022-0728(65)85024-0.
[108] R.M. Fernández Domene, R. Sánchez Tovar, G. Roselló Márquez, P. Batista Grau, B. Lucas Granado, J. García Antón, Fotoelectrocatálisis en procesos medioambientales y energéticos, in: Apl. Medioambientales Energéticas Tecnol. Electroquímica 2021 ISBN 9788429170757 Págs 347-366, Reverté, 2021: pp. 347–366. https://dialnet.unirioja.es/servlet/articulo?codigo=8445834 (accessed June 5, 2025).
[109] V. Cristino, S. Marinello, A. Molinari, S. Caramori, S. Carli, R. Boaretto, R. Argazzi, L. Meda, C.A. Bignozzi, Some aspects of the charge transfer dynamics in nanostructured WO3 films, J. Mater. Chem. A 4 (2016) 2995–3006. https://doi.org/10.1039/C5TA06887H.
[110] V.M. Arutyunyan, Physical properties of the semiconductor-electrolyte interface, Sov. Phys. Uspekhi 32 (1989) 521. https://doi.org/10.1070/PU1989v032n06ABEH002726.
[111] J. González-Velasco, Fotoelectroquímica de Semiconductores: Su Aplicación a la Conversión y Almacenamiento de Energía Solar, 2010.
[112] Yu.Ya. Gurevich, Yu.V. Pleskov, Chapter 4 Photoelectrochemistry of Semiconductors, in: R.K. Willardson, A.C. Beer (Eds.), Semicond. Semimet., Elsevier, 1983: pp. 255–328. https://doi.org/10.1016/S0080-8784(08)60277-X.
[113] J.A. Turner, Energetics of the semiconductor-electrolyte interface, J. Chem. Educ. 60 (1983) 327. https://doi.org/10.1021/ed060p327.
[114] R.H. Wilson, Electron transfer processes at the semiconductor-electrolyte interface, Crit. Rev. Solid State Mater. Sci. 10 (1980) 1–41. https://doi.org/10.1080/10408438008243628.
[115] R. Van De Krol, M. Grätzel, eds., Photoelectrochemical Hydrogen Production, Springer US, Boston, MA, 2012. https://doi.org/10.1007/978-1-4614-1380-6.
[116] Z. Wang, L. Wang, Photoelectrode for water splitting: Materials, fabrication and characterization, Sci. China Mater. 61 (2018) 806–821. https://doi.org/10.1007/s40843-018-9240-y.
[117] Visible Light Responsive Metal Oxide Photoanodes for Photoelectrochemical Water Splitting: a Comprehensive Review on Rational Materials Design, (n.d.). https://www.jim.org.cn/EN/10.15541/jim20170352 (accessed June 9, 2025).
[118] A.G. Tamirat, J. Rick, A.A. Dubale, W.-N. Su, B.-J. Hwang, Using hematite for photoelectrochemical water splitting: a review of current progress and

challenges, Nanoscale Horiz. 1 (2016) 243–267. https://doi.org/10.1039/C5NH00098J.
[119] S. Chen, T. Takata, K. Domen, Particulate photocatalysts for overall water splitting, Nat. Rev. Mater. 2 (2017) 1–17. https://doi.org/10.1038/natrevmats.2017.50.
[120] Y. Tachibana, L. Vayssieres, J.R. Durrant, Artificial photosynthesis for solar water-splitting, Nat. Photonics 6 (2012) 511–518. https://doi.org/10.1038/nphoton.2012.175.
[121] C. Jiang, S.J.A. Moniz, A. Wang, T. Zhang, J. Tang, Proton-conducting crystalline porous materials, Chem. Soc. Rev. 46 (2017) 4645.
[122] S. Ju, H.-J. Seok, J. Jun, D. Huh, S. Son, K. Kim, W. Kim, S. Baek, H.-K. Kim, H. Lee, Fully blossomed WO3/BiVO4 structure obtained via active facet engineering of patterned FTO for highly efficient Water splitting, Appl. Catal. B Environ. 263 (2020) 118362. https://doi.org/10.1016/j.apcatb.2019.118362.
[123] S. Wang, P. Chen, Y. Bai, J.-H. Yun, G. Liu, L. Wang, New BiVO4 Dual Photoanodes with Enriched Oxygen Vacancies for Efficient Solar-Driven Water Splitting, Adv. Mater. 30 (2018) 1800486. https://doi.org/10.1002/adma.201800486.
[124] A. Seza, F. Soleimani, N. Naseri, M. Soltaninejad, S.M. Montazeri, S.K. Sadrnezhaad, M.R. Mohammadi, H.A. Moghadam, M. Forouzandeh, M.H. Amin, Novel microwave-assisted synthesis of porous g-C3N4/SnO2 nanocomposite for solar water-splitting, Appl. Surf. Sci. 440 (2018) 153–161. https://doi.org/10.1016/j.apsusc.2018.01.133.
[125] Z. Luo, T. Wang, Gong, Single-crystal silicon-based electrodes for unbiased solar water splitting: current status and prospects, Chem. Soc. Rev. 48 (2019) 2158–2181.
[126] O.S. Hammond, S. Eslava, A.J. Smith, J. Zhang, K.J. Edler, Microwave-assisted deep eutectic-solvothermal preparation of iron oxide nanoparticles for photoelectrochemical solar water splitting, J. Mater. Chem. A 5 (2017) 16189–16199. https://doi.org/10.1039/C7TA02078C.
[127] B. Bazri, E. Kowsari, N. Seifvand, N. Naseri, RGO-α-Fe2O3/β-FeOOH ternary heterostructure with urchin-like morphology for efficient oxygen evolution reaction, J. Electroanal. Chem. 843 (2019) 1–11. https://doi.org/10.1016/j.jelechem.2019.04.069.
[128] T.H. Tran, V.T. Nguyen, Copper Oxide Nanomaterials Prepared by Solution Methods, Some Properties, and Potential Applications: A Brief Review, Int. Sch. Res. Not. 2014 (2014) 856592. https://doi.org/10.1155/2014/856592.
[129] Z. Jin, Z. Hu, J. C. Yu, J. Wang, Room temperature synthesis of a highly active Cu/Cu 2 O photocathode for photoelectrochemical water splitting, J. Mater. Chem. A 4 (2016) 13736–13741. https://doi.org/10.1039/C6TA05274F.
[130] M. i. Maldonado Rubio, W. Gernjak, I. Oller Alberola, J. Blanco Galvez, P. Fernandez-Ibanez, S. Rodriguez, Photo-Fenton degradation of alachlor,

atrazine, chlorfenvinphos, diuron, isoproturon and pentachlorophenol at solar pilot plant, Int. J. Environ. Pollut. 27 (2006) 135–146. https://doi.org/10.1504/IJEP.2006.010459.

[131] J.L. Acero, F.J. Real, F. Javier Benitez, A. González, Oxidation of chlorfenvinphos in ultrapure and natural waters by ozonation and photochemical processes, Water Res. 42 (2008) 3198–3206. https://doi.org/10.1016/j.watres.2008.03.016.

[132] M.I. Maldonado, S. Malato, L.A. Pérez-Estrada, W. Gernjak, I. Oller, X. Doménech, J. Peral, Partial degradation of five pesticides and an industrial pollutant by ozonation in a pilot-plant scale reactor, J. Hazard. Mater. 138 (2006) 363–369. https://doi.org/10.1016/j.jhazmat.2006.05.058.

[133] E. Guinea, J.A. Garrido, R.M. Rodríguez, P.-L. Cabot, C. Arias, F. Centellas, E. Brillas, Degradation of the fluoroquinolone enrofloxacin by electrochemical advanced oxidation processes based on hydrogen peroxide electrogeneration, Electrochimica Acta 55 (2010) 2101–2115. https://doi.org/10.1016/j.electacta.2009.11.040.

[134] H.T. Madsen, E.G. Søgaard, J. Muff, Study of degradation intermediates formed during electrochemical oxidation of pesticide residue 2,6-dichlorobenzamide (BAM) at boron doped diamond (BDD) and platinum–iridium anodes, Chemosphere 109 (2014) 84–91. https://doi.org/10.1016/j.chemosphere.2014.03.020.

[135] A.G. Gutierrez-Mata, S. Velazquez-Martínez, A. Álvarez-Gallegos, M. Ahmadi, J.A. Hernández-Pérez, F. Ghanbari, S. Silva-Martínez, Recent Overview of Solar Photocatalysis and Solar Photo-Fenton Processes for Wastewater Treatment, Int. J. Photoenergy 2017 (2017) 8528063. https://doi.org/10.1155/2017/8528063.

[136] B. Paul, W.N. Martens, R.L. Frost, Immobilised anatase on clay mineral particles as a photocatalyst for herbicides degradation, Appl. Clay Sci. 57 (2012) 49–54. https://doi.org/10.1016/j.clay.2011.12.009.

[137] M.G. Peleyeju, O.A. Arotiba, Recent trend in visible-light photoelectrocatalytic systems for degradation of organic contaminants in water/wastewater, Environ. Sci. Water Res. Technol. 4 (2018) 1389–1411. https://doi.org/10.1039/C8EW00276B.

[138] C. Jiang, S.J.A. Moniz, A. Wang, T. Zhang, J. Tang, Photoelectrochemical devices for solar water splitting – materials and challenges, Chem. Soc. Rev. 46 (2017) 4645–4660. https://doi.org/10.1039/C6CS00306K.

[139] F.-X. Xiao, J. Miao, H.B. Tao, S.-F. Hung, H.-Y. Wang, H.B. Yang, J. Chen, R. Chen, B. Liu, One-Dimensional Hybrid Nanostructures for Heterogeneous Photocatalysis and Photoelectrocatalysis, Small 11 (2015) 2115–2131. https://doi.org/10.1002/smll.201402420.

[140] R. Daghrir, P. Drogui, D. Robert, Photoelectrocatalytic technologies for environmental applications, J. Photochem. Photobiol. Chem. 238 (2012) 41–52. https://doi.org/10.1016/j.jphotochem.2012.04.009.
[141] N. Klamerth, W. Gernjak, S. Malato, A. Agüera, B. Lendl, Photo-Fenton decomposition of chlorfenvinphos: Determination of reaction pathway, Water Res. 43 (2009) 441–449. https://doi.org/10.1016/j.watres.2008.10.013.
[142] A.E. Danks, S.R. Hall, Z. Schnepp, The evolution of 'sol–gel' chemistry as a technique for materials synthesis, Mater. Horiz. 3 (2016) 91–112. https://doi.org/10.1039/C5MH00260E.
[143] D. Bokov, A. Turki Jalil, S. Chupradit, W. Suksatan, M. Javed Ansari, I.H. Shewael, G.H. Valiev, E. Kianfar, Nanomaterial by Sol-Gel Method: Synthesis and Application, Adv. Mater. Sci. Eng. 2021 (2021) 5102014. https://doi.org/10.1155/2021/5102014.
[144] T.V.S.L. Satyavani, A. Srinivas Kumar, P.S.V. Subba Rao, Methods of synthesis and performance improvement of lithium iron phosphate for high rate Li-ion batteries: A review, Eng. Sci. Technol. Int. J. 19 (2016) 178–188. https://doi.org/10.1016/j.jestch.2015.06.002.
[145] E. Zarei, R. Ojani, Fundamentals and some applications of photoelectrocatalysis and effective factors on its efficiency: a review, J. Solid State Electrochem. 21 (2017) 305–336. https://doi.org/10.1007/s10008-016-3385-2.
[146] H. Shemer, K.G. Linden, Degradation and by-product formation of diazinon in water during UV and UV/H2O2 treatment, J. Hazard. Mater. 136 (2006) 553–559. https://doi.org/10.1016/j.jhazmat.2005.12.028.
[147] C. Ponchio, W. Srevarit, Photoelectrocatalytic improvement of copper oxide thin film fabricated using anodization strategy application in nitrite degradation and promoting oxygen evolution, Chem. Pap. 75 (2021) 1123–1132. https://doi.org/10.1007/s11696-020-01369-x.
[148] R. Kara, H. Lahmar, L. Mentar, R. Siab, F. Kadirgan, A. Azizi, Electrochemical growth and characterization of Cu2O:Na/ZnO heterojunctions for solar cells applications, J. Alloys Compd. 817 (2020) 152748. https://doi.org/10.1016/j.jallcom.2019.152748.
[149] C. Ponchio, W. Srevarit, Photoelectrocatalytic improvement of copper oxide thin film fabricated using anodization strategy application in nitrite degradation and promoting oxygen evolution, Chem. Pap. 75 (2021) 1123–1132. https://doi.org/10.1007/s11696-020-01369-x.
[150] K. Nakaoka, J. Ueyama, K. Ogura, Photoelectrochemical behavior of electrodeposited CuO and Cu2O thin films on conducting substrates, J. Electrochem. Soc. 151 (2004) C661–C665. https://doi.org/10.1149/1.1789155.
[151] A.Y. Oral, E. Menşur, M.H. Aslan, E. Başaran, The preparation of copper(II) oxide thin films and the study of their microstructures and optical properties,

Mater. Chem. Phys. 83 (2004) 140–144. https://doi.org/10.1016/j.matchemphys.2003.09.015.

[152] D. Gupta, S.R. Meher, N. Illyaskutty, Z.C. Alex, Facile synthesis of Cu2O and CuO nanoparticles and study of their structural, optical and electronic properties, J. Alloys Compd. 743 (2018) 737–745. https://doi.org/10.1016/j.jallcom.2018.01.181.

[153] T.-H. Yin, B.-J. Liu, Y.-W. Lin, Y.-S. Li, C.-W. Lai, Y.-P. Lan, C. Choi, H.-C. Chang, Y. Choi, Electrodeposition of Copper Oxides as Cost-Effective Heterojunction Photoelectrode Materials for Solar Water Splitting, Coatings 12 (2022) 1839. https://doi.org/10.3390/coatings12121839.

[154] Y. Yang, D. Xu, Q. Wu, P. Diao, Cu2O/CuO Bilayered Composite as a High-Efficiency Photocathode for Photoelectrochemical Hydrogen Evolution Reaction, Sci. Rep. 6 (2016) 35158. https://doi.org/10.1038/srep35158.

[155] M.N.I. Salehmin, L. Jeffery Minggu, K. Arifin, R. Mohamad Yunus, M.A. Mohamed, M.B. Kassim, Recent advances on state-of-the-art copper (I/II) oxide as photoelectrode for solar green fuel generation: Challenges and mitigation strategies, Appl. Catal. Gen. 582 (2019) 117104. https://doi.org/10.1016/j.apcata.2019.06.002.

[156] P. Sheng, W. Li, P. Du, K. Cao, Q. Cai, Multi-functional CuO nanowire/TiO2 nanotube arrays photoelectrode synthesis, characterization, photocatalysis and SERS applications, Talanta 160 (2016) 537–546. https://doi.org/10.1016/j.talanta.2016.07.043.

[157] W. Zhang, X. Wen, S. Yang, Y. Berta, Z.L. Wang, Single-crystalline scroll-type nanotube arrays of copper hydroxide synthesized at room temperature, Adv. Mater. 15 (2003) 822–825. https://doi.org/10.1002/adma.200304840.

[158] U. Shaislamov, K. Krishnamoorthy, S.J. Kim, W. Chun, H.-J. Lee, Facile fabrication and photoelectrochemical properties of a CuO nanorod photocathode with a ZnO nanobranch protective layer, RSC Adv. 6 (2016) 103049–103056. https://doi.org/10.1039/C6RA18832J.

[159] H. Oh, H. Ryu, W.-J. Lee, Effects of copper precursor concentration on the growth of cupric oxide nanorods for photoelectrode using a modified chemical bath deposition method, J. Alloys Compd. 620 (2015) 55–59. https://doi.org/10.1016/j.jallcom.2014.09.108.

[160] X. Tian, Q. Wang, Q. Zhao, L. Qiu, X. Zhang, S. Gao, SILAR deposition of CuO nanosheets on the TiO2 nanotube arrays for the high performance solar cells and photocatalysts, Sep. Purif. Technol. 209 (2019) 368–374. https://doi.org/10.1016/j.seppur.2018.07.057.

[161] Q. Zhang, K. Zhang, D. Xu, G. Yang, H. Huang, F. Nie, C. Liu, S. Yang, CuO nanostructures: Synthesis, characterization, growth mechanisms, fundamental properties, and applications, Prog. Mater. Sci. 60 (2014) 208–337. https://doi.org/10.1016/j.pmatsci.2013.09.003.

[162] S. Moniri Javadhesari, S. Alipour, S. Mohammadnejad, M.R. Akbarpour, Antibacterial activity of ultra-small copper oxide (II) nanoparticles synthesized by mechanochemical processing against *S. aureus* and *E. coli*, Mater. Sci. Eng. C 105 (2019) 110011. https://doi.org/10.1016/j.msec.2019.110011.

[163] S.-K. Li, Y.-Y. Pan, M. Wu, F.-Z. Huang, C.-H. Li, Y.-H. Shen, Large-scale and green synthesis of octahedral flower-like cupric oxide nanocrystals with enhanced photochemical properties, Appl. Surf. Sci. 315 (2014) 169–177. https://doi.org/10.1016/j.apsusc.2014.07.113.

[164] D.W. Shoesmith, T.E. Rummery, D. Owen, W. Lee, Anodic Oxidation of Copper in Alkaline Solutions: I . Nucleation and Growth of Cupric Hydroxide Films, J. Electrochem. Soc. 123 (1976) 790. https://doi.org/10.1149/1.2132934.

[165] J. Ji, W.C. Cooper, Electrochemical preparation of cuprous oxide powder: Part I. Basic electrochemistry, J. Appl. Electrochem. 20 (1990) 818–825. https://doi.org/10.1007/BF01094312.

[166] N.K. Allam, C.A. Grimes, Electrochemical fabrication of complex copper oxide nanoarchitectures via copper anodization in aqueous and non-aqueous electrolytes, Mater. Lett. 65 (2011) 1949–1955. https://doi.org/10.1016/J.MATLET.2011.03.105.

[167] S.K. Kumar, S. Murugesan, S. Suresh, Anodization assisted preparation of diverse nanostructured copper oxide films for solar selective absorber, Opt. Mater. 135 (2023) 113304. https://doi.org/10.1016/j.optmat.2022.113304.

[168] C. Wang, J. Cao, Z. Gao, S. Ji, H. Ma, Y. Wang, Synthesizing robust cuprous oxide film with adjustable morphologies as surface-enhanced Raman scattering substrate by copper anodization, Mater. Chem. Phys. 264 (2021) 124470. https://doi.org/10.1016/j.matchemphys.2021.124470.

[169] C. Boyle, N. Skillen, H.Q.N. Gunaratne, P.K. Sharma, J.A. Byrne, P.K.J. Robertson, The use of titanium dioxide nanotubes as photoanodes for chloride oxidation, Mater. Sci. Semicond. Process. 109 (2020) 104930. https://doi.org/10.1016/j.mssp.2020.104930.

[170] Y. Zhao, N. Hoivik, K. Wang, Recent advance on engineering titanium dioxide nanotubes for photochemical and photoelectrochemical water splitting, Nano Energy 30 (2016) 728–744. https://doi.org/10.1016/j.nanoen.2016.09.027.

[171] M. Asserpouf-Dezfuly, C. Vlachos, E.H. Andrews, Oxide morphology and adhesive bonding on titanium surfaces, J. Mater. Sci. 19 (1984) 3626–3639.

[172] V. Zwilling, E. Darque-Ceretti, A. Boutry-Forveille, D. David, M.Y. Perrin, M. Aucouturier, Structure and Physicochemistry of Anodic Oxide Films on Titanium and TA6V Alloy, Surf. Interface Anal. 27 (1999) 629–637. https://doi.org/10.1002/(SICI)1096-9918(199907)27:7<629::AID-SIA551>3.0.CO;2-0.

[173] P. Roy, S. Berger, P. Schmuki, TiO2 Nanotubes: Synthesis and Applications, Angew. Chem. Int. Ed. 50 (2011) 2904–2939. https://doi.org/10.1002/anie.201001374.

[174] H. Wender, A.F. Feil, L.B. Diaz, C.S. Ribeiro, G.J. Machado, P. Migowski, D.E. Weibel, J. Dupont, S.R. Teixeira, Self-organized TiO 2 nanotube arrays: Synthesis by anodization in an ionic liquid and assessment of photocatalytic properties, ACS Appl. Mater. Interfaces 3 (2011) 1359–1365. https://doi.org/10.1021/AM200156D.

[175] H.E. Prakasam, K. Shankar, M. Paulose, O.K. Varghese, C.A. Grimes, A new benchmark for TiO2 nanotube array growth by anodization, J. Phys. Chem. C 111 (2007) 7235–7746.

[176] J.M. Macak, H. Tsuchiya, L. Taveira, S. Aldabergerova, P. Schmuki, Smooth Anodic TiO2 Nanotubes, Angew. Chem. Int. Ed. 44 (2005) 7463–7465. https://doi.org/10.1002/anie.200502781.

[177] S.P. Albu, A. Ghicov, J.M. Macak, P. Schmuki, 250 μm long anodic TiO2 nanotubes with hexagonal self-ordering, Phys. Status Solidi - Rapid Res. Lett. 1 (2007) R65–R67. https://doi.org/10.1002/pssr.200600069.

[178] W. Kunz, H.J. Gores, Ionic Liquids, in: Encycl. Appl. Electrochem., Springer, New York, NY, 2014: pp. 1106–1111. https://doi.org/10.1007/978-1-4419-6996-5_17.

[179] I. Paramasivam, J.M. Macak, T. Selvam, P. Schmuki, Electrochemical synthesis of self-organized TiO2 nanotubular structures using an ionic liquid (BMIM-BF4), Electrochimica Acta 54 (2008) 643–648. https://doi.org/10.1016/J.ELECTACTA.2008.07.031.

[180] M. Heydari Dokoohaki, F. Mohammadpour, A.R. Zolghadr, New insight into electrosynthesis of ordered TiO 2 nanotubes in EG-based electrolyte solutions: combined experimental and computational assessment, Phys. Chem. Chem. Phys. 22 (2020) 22719–22727. https://doi.org/10.1039/D0CP03684F.

[181] H. Li, J. Qu, Q. Cui, H. Xu, H. Luo, M. Chi, R.A. Meisner, W. Wang, S. Dai, TiO2 nanotube arrays grown in ionic liquids: high-efficiency in photocatalysis and pore-widening, J. Mater. Chem. 21 (2011) 9487–9490. https://doi.org/10.1039/C1JM11540E.

[182] Y. Yu, Y. Jiang, M. Tian, L. Yang, H. Yan, S. Sheng, N-Doped TiO2 Nanotube Arrays: Synthesis by Anodization in an Ionic Liquid ([BMIM]BF4) and Assessment of Photocatalytic Property, Rare Met. Mater. Eng. 45 (2016) 561–566. https://doi.org/10.1016/S1875-5372(16)30072-8.

[183] P. Mazierski, J. Łuczak, W. Lisowski, M.J. Winiarski, T. Klimczuk, A. Zaleska-Medynska, The ILs-assisted electrochemical synthesis of TiO2 nanotubes: The effect of ionic liquids on morphology and photoactivity, Appl. Catal. B Environ. 214 (2017) 100–113. https://doi.org/10.1016/j.apcatb.2017.05.005.

[184] A. Pancielejko, P. Mazierski, W. Lisowski, A. Zaleska-Medynska, J. Łuczak, Ordered TiO2 Nanotubes with Improved Photoactivity through Self-organizing Anodization with the Addition of an Ionic Liquid: Effects of the Preparation Conditions, ACS Sustain. Chem. Eng. 7 (2019) 15585–15596. https://doi.org/10.1021/ACSSUSCHEMENG.9B03589/ASSET/IMAGES/ACSSUSCHEMENG.9B03589.SOCIAL.JPEG_V03.

[185] A. Pancielejko, P. Mazierski, W. Lisowski, A. Zaleska-Medynska, K. Kosek, J. Łuczak, Facile Formation of Self-Organized TiO 2 Nanotubes in Electrolyte Containing Ionic Liquid-Ethylammonium Nitrate and Their Remarkable Photocatalytic Properties, (2018). https://doi.org/10.1021/acssuschemeng.8b03154.

[186] B. Peric, J. Sierra, E. Martí, R. Cruañas, M.A. Garau, J. Arning, U. Bottin-Weber, S. Stolte, (Eco)toxicity and biodegradability of selected protic and aprotic ionic liquids, J. Hazard. Mater. 261 (2013) 99–105. https://doi.org/10.1016/j.jhazmat.2013.06.070.

[187] G. Sánchez-García, E. Da Silva, R.M. Fernández-Domene, A. Cháfer, V. González-Alfaro, B. Solsona, R. Sánchez-Tovar, TiO2 nanostructures synthesized by electrochemical anodization in green protic ionic liquids for photoelectrochemical applications, Ceram. Int. 49 (2023) 26900–26909. https://doi.org/10.1016/j.ceramint.2023.05.227.

[188] F. Yang, X. Zhou, N.T. Plymale, K. Sun, N.S. Lewis, Evaluation of sputtered nickel oxide, cobalt oxide and nickel–cobalt oxide on n-type silicon photoanodes for solar-driven O2(g) evolution from water, J. Mater. Chem. A 8 (2020) 13955–13963. https://doi.org/10.1039/D0TA03725G.

[189] E. Szaniawska, I.A. Rutkowska, M. Frik, A. Wadas, E. Seta, A. Krogul-Sobczak, K. Rajeshwar, P.J. Kulesza, Reduction of carbon dioxide at copper(I) oxide photocathode activated and stabilized by over-coating with oligoaniline, Electrochimica Acta 265 (2018) 400–410. https://doi.org/10.1016/j.electacta.2018.01.116.

[190] A.A.M. Farag, A. Ashery, M.A. Salem, Electrical, dielectric characterizations and optoelectronic applications of epitaxially grown Co/n-CuO/p-Si heterojunctions, Superlattices Microstruct. 135 (2019) 106277. https://doi.org/10.1016/J.SPMI.2019.106277.

[191] C.W. Chu, New ordered phases of slightly reduced rutile and their sharp dielectric absorptions at low temperature, Phys. Rev. B 1 (1970) 4700–4708. https://doi.org/10.1103/PhysRevB.1.4700.

[192] N. Elgrishi, K.J. Rountree, B.D. McCarthy, E.S. Rountree, T.T. Eisenhart, J.L. Dempsey, A Practical Beginner's Guide to Cyclic Voltammetry, J. Chem. Educ. 95 (2018) 197–206. https://doi.org/10.1021/acs.jchemed.7b00361.

Chapter 2: Objectives

The current high dependence on fossil fuels to satisfy the growing energy demand has caused a huge increase in the atmospheric concentration of greenhouse gases. Particularly, N_2O is the third major contributor to global warming after CO_2 and methane and it is estimated to increase 2% per decade. Its long lifetime in the atmosphere causes its global warming potential to be ca. 300 times higher than that of carbon dioxide. Hence, after-treatment technologies must be implemented in between units of industrial processes to eliminate or valorize N_2O after it is formed.

The main **objective of the present thesis** is to study the catalytic transformation either by valorization or decomposition of a gas with a high global warming potential and a mild oxidizing character as the N_2O. These transformations will be conducted by a double approach: i) thermocatalytic and ii) photoelectrocatalytic.

The first part of the thesis is focused on the thermocatalytic valorization of nitrous oxide (**Chapter 4**), at the same time that ethylene is obtained through a more environmentally friendly process. As an alternative to the traditional manufacture process, we propose the oxidative dehydrogenation of ethane which is exothermic and operates at much lower temperatures (300-450°C). Besides, we propose the replacement of O_2 by N_2O as an oxidizing agent to minimize the carbon oxides formation. The N_2O-ODH of ethane combats two problems at once: reduction of atmospheric N_2O concentration and sustainable ethylene production. Two catalytic systems have been studied, including synthesis and characterization: NiO-based and multicomponent MoVTeNb oxide catalysts. Furthermore, an in-depth electrochemical study has been undertaken for all the thermocatalysts due to the redox mechanism (Mars-Van Krevelen) that governs the ODH reaction. It is believed that a thorough analysis of the electrochemical properties can estimate the catalytic behavior of the different materials. To our knowledge, this relationship between electrochemical and catalytic properties has never been stablished before.

The second part of the thesis is focused on the photoelectrocatalytic valorization of nitrous oxide, transforming it into N_2 and O_2 by photoelectro-reduction (**Chapter 5**). For this purpose, mixed copper oxides and titanium dioxide photoelectrocatalysts have been synthesized and characterized to act as photocathode and photoanode in the photoelectrochemical reduction of N_2O, respectively. Novel fabrication conditions have been tested during the electrochemical anodization of both copper and titanium. This way, efficient photoelectrocatalysts have successfully decomposed nitrous oxide at mild reaction conditions with the application of a small bias and light.

Figure 2.1 shows the structure of the present thesis, indicating the sections of the different chapters.

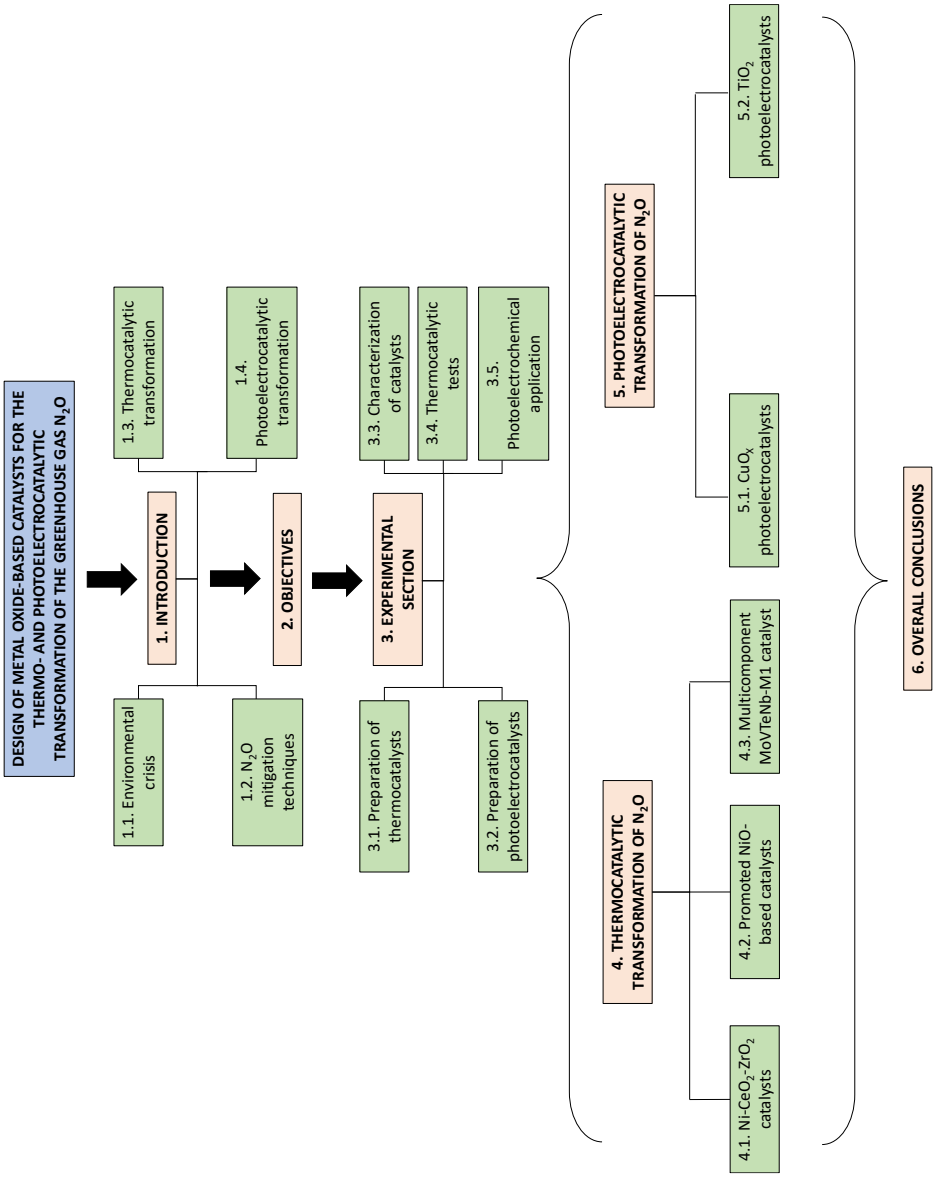

Figure 2. 1. Structure of the present thesis.

Chapter 3:

Experimental Section

3.1 Preparation of thermocatalysts

3.1.1 Materials

For the promoted cerium oxide and nickel oxide catalysts, the chemical precursors employed for the synthesis were: **nickel (II) nitrate hexahydrate** ($Ni(NO_3)_2{\cdot}6H_2O$, Sigma-Aldrich, 99.99%), **cerium (III) nitrate hexahydrate** ($Ce(NO_3)_3{\cdot}6H_2O$, Sigma-Aldrich, 99.99%), z**irconium (IV) oxynitrate hydrate** ($ZrO(NO_3)_3{\cdot}xH_2O$, Sigma-Aldrich, 99. %), **bismuth (III) nitrate pentahydrate** ($Bi(NO_3)_3{\cdot}5H_2O$, Sigma-Aldrich), **iron (III) nitrate nonahydrate** ($Fe(NO_3)_3{\cdot}9H_2O$, Sigma-Aldrich), **indium (III) nitrate hydrate** ($In(NO_3)_3{\cdot}\ xH_2O$, Sigma-Aldrich), **titanium butoxide** ($C_{16}H_{36}O_4Ti$, Sigma-Aldrich), **ammonium niobate (V) oxalate hydrate** ($C_4H_4NNbO_9.xH_2O$, Sigma-Aldrich, 99.99%) and **oxalic acid** (HO_2CCO_2H, Sigma-Aldrich, 98%).

In case of the M1-phase Mo-V-Te-Nb-O oxides, the precursors were: **ammonium heptamolybdate hydrate** ($(NH_4)_6Mo_7O_{24}{\cdot}4H_2O$, Merck, 99%), **vanadyl sulphate hydrate** ($VOSO_4{\cdot}xH_2O$, Sigma-Aldrich, 97%), **tellurium dioxide** (TeO_2, Sigma-Aldrich, 99%), **telluric acid** (H_6TeO_6, Sigma-Aldrich, 99.99%) and **ammonium niobate (V) oxalate hydrate** ($C_4H_4NNbO_9.xH_2O$, Sigma-Aldrich).

3.1.2 Synthesis of Ni-Zr promoted cerium oxide catalysts

First, Ni-CeO_2-ZrO_2 catalysts were prepared by coprecipitation, with a molar ratio of 9 for (Ce+Zr)/Ni and atomic ratios of 0, 0.1, and 0.5 for Zr/Ce. Calculated amounts of $Ni(NO_3)_2{\cdot}6H_2O$, $Ce(NO_3)_3{\cdot}6H_2O$ and $ZrO(NO_3)_3{\cdot}xH_2O$ were diluted in 100 ml of distilled water. Sodium carbonate (Na_2CO_3) 0.1M and sodium hydroxide (NaOH) 0.5M solution was used as a precipitation agent and was added dropwise to the metallic solution under vigorous stirring at room temperature and pH was stabilized at 10 for 30 min. To remove leftover sodium, the resulting mix was washed

and filtered under vacuum. Lastly, samples were calcined at 400ºC for 2h in static air.

Pure NiO and CeO_2 were also synthesized by calcination of $Ni(NO_3)_2 \cdot 6H_2O$ and $Ce(NO_3)_3 \cdot 6H_2O$ at 400ºC for 2h in static air.

3.1.3 Synthesis of promoted NiO catalysts

Metal promoted NiO-X catalysts (X = Nb, Bi, Al, Fe, Ti, Ce) were synthesized by evaporation of aqueous solutions of the metallic precursors. Oxalic acid was added with an oxalic acid/nickel molar ratio of 1, while promoting metals were added with a promoter/nickel molar ratio of 0.1. The presence of oxalic acid allows to obtain smaller crystallite size of NiO phases, which causes the surface area of the catalysts to increase, consequently improving their catalytic behavior [1]. The solutions were left to dry upon stirring at 90ºC and the resulting solids were calcined at 500ºC for 2h in static air [1].

3.1.4 Synthesis of M1 phase MoVTeNb catalyst

The quaternary M1 phase catalyst was synthesized by the hydrothermal method [2–5]. For this purpose, an aqueous solution of the metallic precursors was mixed under stirring conditions in a silica bath at 80°C. The Mo/V/Te/Nb atomic ratio used was 1/0.25/0.17/0.17. Cooled synthesis gel was transferred into a Teflon vessel, that was later put into a stainless-steel autoclave. The preparation was conducted at 175°C for 48h under N_2 atmosphere. After cooling down, the resulting solid was washed, filtered and dried at 100°C for 12h. Finally, this catalyst was thermally activated with a nitrogen stream of 15 $mL \cdot min^{-1} \cdot g_{cat}^{-1}$ at 600°C.

3.2 Preparation of photoelectrocatalysts

In the present thesis, different photoelectrocatalysts have been synthesized by electrochemical anodization of each studied metal. In this way, nanostructured metal oxides have been grown directly into a metal substrate. In order to start from a clean and homogeneous surface, samples were subjected to a conditioning process previous to anodization and, after the synthesis, a thermal treatment was also applied to obtain highly crystalline nanostructures [6–8].

3.2.1 CuOx nanostructures

First, copper foils of high purity (99.9%) and 0.125 mm thickness were cut with an approximate diameter of 1.30 cm. These sheets were ultrasonically washed in 0.1M hydrochloric acid for 15 seconds to remove unwanted oxide layers. Then, they were washed for 30 seconds in acetone, ethanol and deionized water, respectively and finally dried with a N_2 stream.

Electrochemical anodization was performed in a two-electrode electrochemical cell (Figure 3.1.), with the copper foil as the working electrode and a platinum sheet as the counter electrode. Copper foils were fitted into a rotating disk electrode (RDE), which allowed later to vary the revolutions of the electrode and study the influence of controlled hydrodynamic conditions during anodization. To prevent electrolyte filtrations into the RDE, samples were coated with teflon, consequently leaving an exposed area to the anodizing solution of 1.32 cm^2. Current density values reached during anodization were registered by connecting a multimeter in series to the power source which applied the required potential.

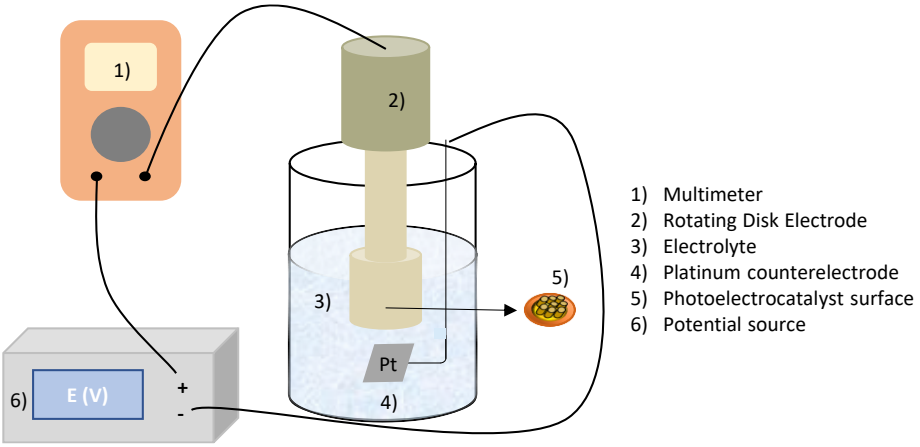

Figure 3. 1. Schematic diagram of the equipment used for metal electrochemical anodization.

Considering previous studies carried out in the research group, the applied potential and the temperature during the anodization were fixed in 20V and 50°C, respectively. Research was first focused on the use of different complexing agents (oxalic acid and sodium fluoride) in ethylene glycol (EG) based electrolytes, studying as well the influence of adding sodium hydroxide to the solution. Samples were anodized for different times, using each of the described electrolytes. Table 3.1 shows the studied anodization parameters for the fabrication of efficient copper oxide nanostructures.

Table 3. 1. Variable parameters during electrochemical anodization of copper.

Time (min)	5, 10, 15			
Electrolyte (70% EG)	0.05M NaF + 0.1M NaOH	0.05M $H_2C_2O_4$ + 0.1M NaOH	0.05M NaF	0.05M $H_2C_2O_4$

Once the process was optimized, different solvents in different concentrations were used as electrolytes. First, different percentages of ethylene glycol (50% and 90% (v/v)) were tested. Then, electrolytes with varying concentrations of ethanol and formamide (50%, 70% and 90% (v/v)) were also

studied. It is noteworthy that both optimal time and electrolyte composition were selected after carrying out the relevant characterization, which is later described in detail.

Finally, after setting the rest of the studied parameters, the influence of hydrodynamic conditions during anodization was evaluated. This study was carried out on the sample synthesized by the optimized process: 5-minute anodization, using a 70% (v/v) ethylene glycol electrolyte with 0.05M oxalic acid. Samples were anodized varying the revolutions of the electrode to 0, 250 y 500 rpm.

After anodization and taking the teflon coating off, samples were rinsed with D. I. water and dried with a N_2 stream in order to remove electrolyte residues from the surface. Subsequently, anodized samples were annealed in a furnace at 250ºC for 1h in order to remove water from their structure and thus obtain nanostructures with high crystallinity with good electrochemical properties [9]. For this purpose, a heating ramp of 10ºC/min was used, and they were left to cool down by natural convection.

3.2.2 TiO_2 nanostructures

For the electrochemical anodization of titanium, foils of 0.125 mm thickness were cut with a diameter of 1.30 cm approximately (99.6+% de purity). Their previous conditioning consisted of three successive washes of 5 minutes each in an ultrasonic bath using acetone, ethanol and deionized water. After, samples were dried with a nitrogen flow, and they were teflon-coated to fit them into the RDE shown in Figure 3.1.

Synthesis of titanium dioxide nanostructures was performed with the same electrochemical cell configuration used for the anodization of copper (Figure 3.1), being this time the working electrode the sheet of titanium. Electrochemical anodization was carried out at room temperature and applying 55V for 30 minutes.

These parameters assured the appropriate nanotubular morphology needed for the posterior photoelectrochemical applications. To be more specific, those values of potential and time were chosen to obtain optimal tube length and diameters, respectively [10–12].

An ethylene glycol based electrolyte (EG), containing 0.05M NH_4F and 1M water was used for electrochemical anodization [12]. The influence of introducing three different ionic liquids in different concentrations to the anodizing electrolyte was investigated in order to reduce fluoride content but without compromising the efficiency of the obtained nanostructures. Particularly, samples were synthesized adding 0.25, 0.5, 1, 2 y 4 % (v/v) of the mono-, di, and triethanolamine based ionic liquids (MEA, DEA and TEA, respectively). Additionally, a control sample was prepared without ionic liquid but with double the content of fluoride to compare the effect of incorporating ionic liquids into the electrolytes (IL-0).

The studied ionic liquids were synthesized in the laboratory by the quaternization reaction of the starting amines. The amines were placed in a three neck round-bottomed flask equipped with a reflux condenser and a dropping funnel. To keep the reaction temperature at 30ºC, the flask was mounted in a thermostatic bath. Under agitation, an excess of acetic acid was added dropwise in about 1h to assure the complete reaction. Stirring continued for 24h after the whole acetic acid was added. The resulting liquid was purified by using a rotary evaporator at room temperature for half an hour.

Afterwards, samples were rinsed with ethanol and deionized water and dried with nitrogen. Lastly, nanostructures were annealed in a furnace at 450ºC for 1h in static air to obtain a crystalline structure. This time, a heating ramp of 10ºC/min was also employed, and samples were cooled down by natural convection.

In order to examine the influence of hydrodynamic conditions on mass transfer in the synthesis of the nanostructures, samples were anodized in the same

electrolyte as before (triethanolamine containing electrolytes) but varying the rotating speed of the RDE: 0, 500, 1000 y 2000 rpm.

3.3 Characterization techniques

3.3.1 Physicochemical characterization

It is very important to know the morphology and structural properties of both thermocatalysts and photoelectrocatalysts in order to obtain the best catalytic results once their synthesis processes are optimized. For this purpose, several techniques have been used to carry out the structural characterization of the catalysts, such as field emission scanning electron microscopy (FE-SEM), X-ray diffraction (XRD), UV-visible spectroscopy, Raman spectroscopy and transmission electron microscopy (TEM). In the following sections, main principles and operation conditions of each technique are described.

3.3.1.1 Field emission scanning electron microscopy (FE-SEM)

Field emission scanning electron microscopy provides a great variety of information about the surface of the analyzed sample, such as morphology, superficial distribution or thickness of a nanostructured layer. This technique is based on the interaction of an electron beam with the surface of the examined sample while potential is being applied. This interaction causes the emission of other electrons (secondary), which are collected by a detector. The angle and speed at which the secondary electrons are emitted allow to know the topography of the samples. Thanks to this information, high resolution digital images (FE-SEM images) are generated.

In this work, a field-emission Hitachi S4800 electron microscope was used to obtain high resolution images of the surfaces of both nanostructures and

thermocatalysts. It must be noted that, for the copper oxide nanostructures a Au/Pd coating was applied through sputtering technique in order to avoid dispersion and excessive reflection of electrons. Images with different magnifications were taken using a 5kV potential.

3.3.1.2 X-ray diffractometry (XRD)

X-ray diffraction allows to identify crystalline phases present in the studied materials, so that both structure and composition of samples are determined. Principles of this technique lie in making an electron beam shine with an θ angle on a plain sample and measure the diffracted radiation (Figure 3.2) [13].

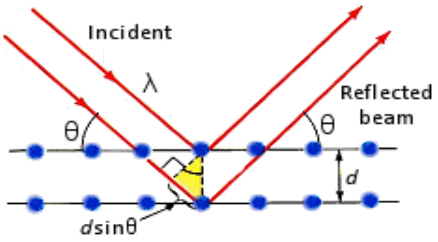

Figure 3. 2. Scheme of X-Ray diffraction phenomena.

The X-ray beam diffraction is caused by the atoms periodically arranged in the different planes that make the crystalline lattice of the samples [14]. For the diffraction to take place, Bragg's Law must be satisfied [15]. This law states that a constructive interference between the incident beam and the reflected one must occur, following Eq. 3.1:

$$n\lambda = 2d_{hkl}sin\theta \qquad \text{Eq. 3. 1}$$

where d_{hkl} is the distance between the planes which cause the diffraction, λ the wavelength of the incident radiation, θ the angle of the reflected X-ray beam and n an integer.

As a result of this analysis, a characteristic diffractogram is generated for each crystallographic structure, where plots of intensity vs. 2θ are represented and are used to identify the composition and crystallinity of samples. In addition, with this technique and Scherrer's equation it is possible to calculate the average particle size of samples:

$$D = \frac{\lambda}{\beta cos\theta} \qquad \text{Eq. 3. 2}$$

where the mean particle size (D) is calculated by the relationship between the wavelength of the radiation (λ) and the line broadening at half maximum intensity (β) of a specific diffraction angle (θ).

The employed equipment for the characterization of all synthesized samples of this thesis was a Philips X'Pert diffractometer, equipped with a graphite monochromator that operated at 40 kV and 30 mA, and using CuKα radiation with a nickel filter (λ=0.1542 nm).

3.3.1.3 Transmission electron microscopy (TEM)

Microstructural characterization of catalysts has been possible due to transmission electron microscopy, in which a very thin sample is hit by an electron beam with a specific wavelength. Some of these electrons are transmitted or dispersed by the atoms of the material, and thanks to the detectors placed behind the sample, it is possible to generate contrast images of the internal structure of the catalysts with atomic resolution [16]. The resolution of the obtained images depends on the power of the employed microscope.

Microscopes that work at potentials up to 100 kV, generate medium-low (1kX-80kX) and medium-high (80kX-200kX) resolution images. In this case, using a microscope that works at higher potentials (200 kV), high resolution images are taken, and the equipment receives the name of high-resolution transmission

microscope. Specifically, HRTEM images in this thesis have been taken using a FEI Tecnai G2 F20 TWIN microscope.

For this characterization technique, both powdered and scratched metal oxide samples were treated with ethanol in an ultrasonic bath for 20 minutes, in order to disperse them. Then, the dispersed samples were deposited onto a copper mesh covered by a thin carbon film and the solvent was evaporated under vacuum conditions. Dried and fixed samples were placed inside the vacuum chamber of the HRTEM microscope.

3.3.1.4 UV-Visible spectroscopy

When electromagnetic radiation is shone onto matter, different spectroscopy techniques allow to examine how matter reacts to it. The wavelength range measured determines the type of spectroscopy being used. For example, in UV-Vis spectroscopy the wavelength range belonging to ultraviolet and visible regions of the electromagnetic spectrum are measured.

The interaction of radiation with matter involves many processes, such as reflection, scattering, absorbance, fluorescence…To determine the UV-vis spectrum of a material, absorbance is measured. Light absorption causes an increase of the energy content of the molecules in the matter. Sometimes, this energy is enough to cause excitation of electrons and their transition to different energy levels. The energy needed to enable this transition from a lower energy level to a higher one is provided by the wavelength of the absorbed light.

For sample analysis, spectrophotometers illuminate the materials with light across the UV to the visible wavelength range (usually 190 to 900 nm). Then, the light absorbed, transmitted or reflected by the sample at each wavelength is measured. Generally, the information provided by this technique is presented as a plot of absorbance vs. wavelength. The absorbance spectrum allows to determine the

chemical or physical properties of the sample, usually using it to identify molecules or to determine the concentration of a specific molecule in solution [17].

UV-Vis spectroscopy was carried out employing a UV-2600 Shimadzu spectrophotometer in the wavelength range of 200-800 nm. To correct the baseline, a sweep of the spectrum was performed on a non-absorbing sample (barium sulfate) using the same wavelength range that would be later used with the samples to be analyzed.

3.3.1.5 Raman spectroscopy

Raman spectroscopy is a non-destructive technique that allows to know the composition and crystalline structure of different materials. For this purpose, a sample is irradiated by a monochromatic light with a determined wavelength and the light scattered by this sample is analyzed. Electrons are excited to higher energy levels when the irradiated photons hit the samples. Then, most of the electrons will experience elastic scattering, which means that they will return to their original energy state emitting a photon with the same wavelength. This is known as Rayleigh scattering and does not give valuable information about composition or crystallinity of samples. However, some light will undergo inelastic scattering or Raman scattering, which means that some electrons will not return to their original energy level and will emit photons with a different wavelength than the incident ones [18]. If electrons return to higher energy levels than initially, Stoke scattering takes place, while anti-Stoke scattering occurs when electrons return to energy states lower than the original [19]. These phenomena have been depicted in Figure 3. 3.

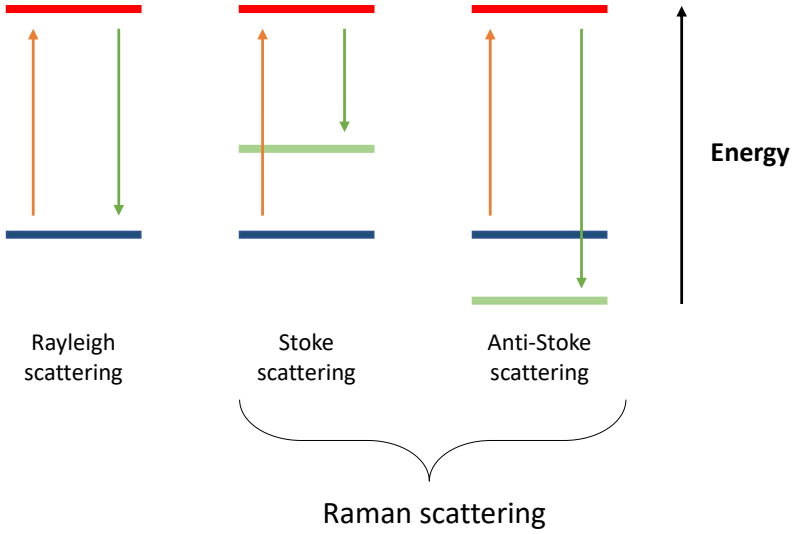

Figure 3. 3. Different forms of light scattering after hitting matter.

In the present thesis, Raman spectra were recorded using a confocal laser Raman microscope (WiTec) with a blue laser (488 nm).

3.3.2 N_2 physisorption

Textural properties, such as specific surface area, of the powdered materials have been determined by the nitrogen physisorption. With this technique it is possible to detect the active sites present in the surface of the catalysts, which is a crucial parameter for the catalytic activity of each material.

First, some assumptions must be made in order to calculate the total surface area of the catalysts from the adsorbed nitrogen on the surface [20,21]:

a) The adsorption surface is flat.
b) There is no interaction between molecules.
c) All sites are energy equivalent.
d) Adsorbed molecules are still.

Nitrogen adsorption was performed in a Micrometrics ASAP 2000 equipment. Degassing of the samples was performed under vacuum conditions before adsorption. Measurements were carried out in the relative pressure range (p/p_0) of 0-1 at -196°C, and surface area calculations were done using the linear form of the Brunauer–Emmett–Teller (BET) equation (Equation 3.3) to determine the monolayer capacity (n_m):

$$\frac{1}{n[\left(\frac{p}{p_0}\right)-1]} = \frac{1}{n_m C} + \frac{p}{p_0} \cdot \frac{C-1}{n_m C} \qquad \text{Eq. 3. 3}$$

where n is the amount of adsorbate, p/p_0 is the relative pressure and C is a constant related with the difference between the adsorption heat of the first and second adsorbed monolayer.

Then, surface area values can be estimated with n_m and Eq. 3.4, where N_A stands for the Avogadro's constant and σ for the cross-sectional area of the Nitrogen molecule (ca. 0.162 nm^2):

$$S_{BET} = n_m N_A \sigma \qquad \text{Eq. 3. 4}$$

3.3.2.1 Temperature-programmed reduction (TPR)

All the thermocatalysts synthesized in the present thesis have been employed in partial oxidation reactions. Therefore, investigating their reducibility (or redox behavior) is essential to understanding their performance in the reactions of interest.

The temperature-programmed reduction technique involves the flow of a reducing gas mixture (H_2 diluted in He or Ar) over a powdered sample while the temperature is increased at a controlled linear rate. As the temperature rises, metal oxides are reduced by the flow of hydrogen, which causes the hydrogen concentration to decrease. This decrease in hydrogen concentration in the gas stream leads to a change in its thermal conductivity, which is detected by a thermal

conductivity detector (TCD). The detector response, recorded as a function of temperature and time, provides a reduction profile characteristic of each sample. The position and shape of the reduction peaks give information on the temperature at which reduction of the metal oxide occurs and the nature of the reducible species. The hydrogen consumption can be determined by integrating the peak areas of the TPR curve, after proper calibration of the detector.

Temperature-programmed reduction with hydrogen measurements (H_2-TPR) were performed with a Micromeritics Autochem 2910 apparatus, equipped with a TCD detector. These experiments consisted of the exposure of 50 mg of each sample to a 50 mL/min Argon stream with 10% of hydrogen, increasing the temperature up to 800°C with a 10°C/min heating ramp.

TPR-N_2O and TPR-N_2O/Ethane experiments were also conducted for the nickel oxide-based catalysts. Experiments took place in a quartz micro reactor attached to a quadrupole mass spectrometer (Omnistar, Balzers). This time, 80 mg of sample was diluted in 320 mg SiC and pre-activated under a 20 vol% O_2 flow (18 mL/min) at 400°C for an hour. Then, the sample was cooled down to 25°C in an oxygen flow of 18 mL/min. For TPR-N_2O, feed was changed to 1 vol % N_2O/He flow 25 mL/min and reaction temperature was increased up to 500°C with a heating ramp of 10 °C/min, while reaction products were monitored online using mass spectrometry. The same set up was used for TPR-N_2O/Ethane measurements, using the same reaction conditions except for the feed, which was a mixture of 5 vol % Ethane and 10 vol % N_2O.

With these analyses it is possible to obtain information about the reducibility of Ni^{2+} species and activation of the N_2O molecule in presence and absence of ethane.

3.3.2.2 X-Ray photoelectron spectroscopy (XPS)

The X-Ray photoelectron spectroscopy is a technique used to identify the near surface composition of catalysts (ca. 50Å), as well as the oxidation state of the elements that form the material. This technique is based on the irradiation of X-Rays on the material surface and detecting the photoelectrons emitted by the sample, whose energy depends on the excitation energy and the core binding energy.

To be more specific, when samples are irradiated by X-Rays, a core-level electron is promoted to an electronic state over the Fermi level (E_F). Each element has a characteristic energy needed to promote one core electron from a given electronic state to the Fermi level, and this is the binding energy (E_b). This binding energy is also characteristic of the orbital where the emitted electron was located. Knowing the kinetic energy of the emitted electron (E_k) and the energy of the incident X-Rays ($h\nu$), the binding energy of each electron can be calculated through Eq. 3.5 [22]:

$$E_b = h\nu - E_k - \emptyset \qquad \text{Eq. 3. 5}$$

in which $\emptyset$ stands for the work function of the XPS device.

In the present thesis, XPS spectra were carried out using a SPECS spectrometer equipped with a Phoibos 150 MCD-9 detector and a monochromatic AlKα (1486.6eV) X-Ray source. Spectra were collected with the analyser operating at a pass energy of 50eV, using an X-ray power of 100W, and under ultra-high vacuum conditions of 10^{-9} mbar. Data processing was performed with the CasaXPS software, referencing the binding energy values to the C1s peak (284.5 eV).

3.3.2.3 Fourier Transform Infrared Spectroscopy (FTIR)

FTIR Spectroscopy is an analysis technique employed to understand the structure of molecules and the composition of molecular mixtures. IR light is usually discussed in terms of wavenumbers rather than wavelengths. Wavenumbers is the

number of wavelengths per unit distance (usually measured in cm^{-1}). A larger wavenumber is referred to light with a shorter wavelength and higher energy. Infrared light can be divided into three regions: near infrared (NIR), mid infrared (MIR) and far infrared (FIR). MIR is the type of infrared radiation typically used when dealing with IR spectroscopy. IR light is absorbed at specific frequencies by the samples, when the energy of the MIR light is equivalent to the atom-to-atom vibrational bond energy in the molecule. Different bonds in a molecule vibrate at different energies and, therefore, absorb different wavenumbers of the IR radiation. The frequency and intensity of these individual absorption bands contribute to the overall spectrum, creating a characteristic fingerprint of the molecule [23].

This technique can be used to study acid sites on solid surfaces by analyzing the infrared absorption spectra of absorbed probe molecules such as pyridine. Pyridine has the ability to interact with Lewis acid sites (LAS), absorbing onto them. A specific IR spectrum is obtained from the pyridine absorbed into Lewis acid sites, which can determine the amount of LAS present in the sample.

A Nexus 8700 FTIR spectrophotometer coupled with a DTGS detector was employed to perform IR-CO measurements at -170 ºC, acquiring data at 4 cm^{-1} resolution. Experiments carried out under controlled atmospheres and temperature were done using a home-made IR cell connected to a vacuum system with gas dosing facility. Samples (~13 mg) were pressed into self-supported wafers and treated in an oxygen flow (20 ml/min) at 200 ºC for 2 h, using a heating ramp of 10 ºC/min. This was followed by evacuation at 150 ºC under 10^{-4} mbar for 1.5h. After, samples were cooled down to -176 ºC under dynamic vacuum conditions, which took approximately 45 minutes. CO was subsequently dosed at increasing pressure (0.05-2 mbar) and IR spectra were recorded after each dosage.

3.3.3 Electrochemical and photoelectrochemical characterization

Electrochemical characterization was applied to the thermocatalysts and to the photoelectrocatalysts, in order to study the influence of the electrochemical properties of the materials on their catalytic or photoelectrocatalytic applications, respectively.

3.3.3.1 Preparation of powdered catalysts

In case of the thermocatalysts, a metallic back contact was necessary to perform the (photo)electrochemical characterization. For this purpose, 30 mg of each catalyst were dissolved in 0.5 ml of ethanol with the help of an ultrasonic bath. Then, with the spin-coating technique, three layers of the catalyst-containing solution were deposited on an FTO and was left to dry overnight at 80ºC in a stove. It should be noted that, for the correct deposition of the catalysts, FTO were previously ultrasonically washed in acetone, ethanol and DI water.

3.3.3.2 Photoelectrochemical cell

Both electrochemical and photoelectrochemical characterization were carried out in the same three-electrode cell (Figure 3.4). A platinum tip and an Ag/AgCl (3M KCl) were used as counterelectrode and reference electrode, respectively, while the studied material was used as working electrode, being 0.5 cm^2 the exposed area to the electrolyte. All electrodes were connected to a potentiostat (PalmSens4) and were immersed in the electrolyte. The employed electrolyte varied with the material being analyzed. For TiO_2 nanostructures KOH 1M was used, while for CuOx nanostructures and catalysts deposited on the FTOs it was Na_2SO_4 0.1M. For photoelectrochemical characterization, a UV-LED lamp (λ=365 nm) of 100 W/cm^2 was used as light source. To simulate chopped-light conditions, the photoelectrochemical cell was situated beneath a metallic structure,

which had an opening at the top where the UV lamp was placed. This opening was covered with a ceramic sheet when dark conditions were needed.

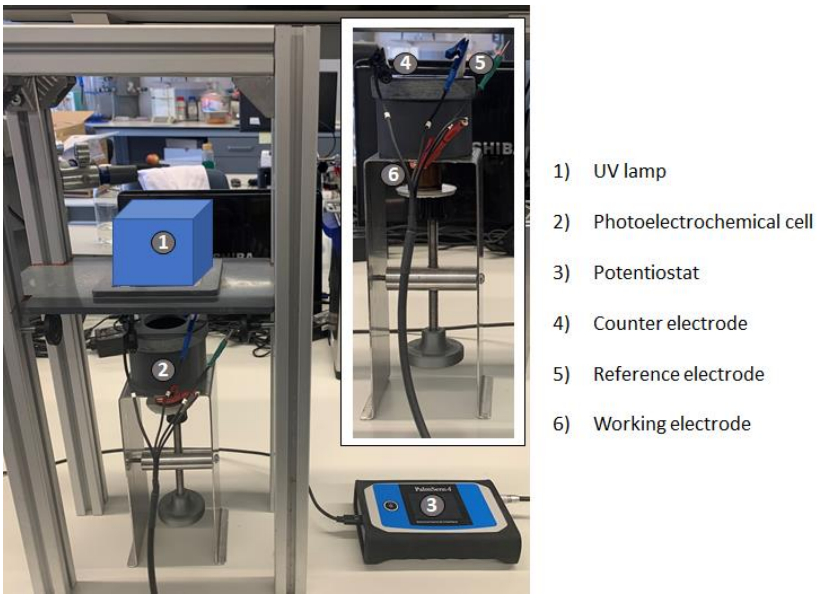

Figure 3. 4. Photoelectrochemical cell with UV lamp.

3.3.3.3 Electrochemical Impedance Spectroscopy (EIS)

Electrochemical impedance spectroscopy (EIS) technique is usually employed to study recombination and charge transfer processes of electrochemical reactions that take place in a semiconductor/electrolyte interface. For this purpose, this interface is considered as a passive element ensemble (impedance, capacitance) of an electrical circuit. Each element will present different time constants (τ=RC), since each electrochemical process will exhibit different time behaviors. This technique is based on the application of a sinusoidal signal (AC voltage) over a wide frequency range to perturb an electrochemical system in equilibrium, and the monitorization of the sinusoidal response (current). It should be noted that the applied potential consists of a small perturbation and does not cause the polarization of the system [24].

According to the Ohm law, impedance is defined as the quotient between the applied potential signal and the response current signal, as described by Equation 3.6, where E_0 and I_0 are the amplitude of the potential and current signals, respectively, ω is the angular frequency (ω = 2πf, being f the frequency), t is time and ϕ the phase shift between the potential and response current signals [25].

$$Z = \frac{E(t)}{I(t)} = \frac{E_0 \cdot \sin(\omega t)}{I_0 \cdot \sin(\omega t + \phi)} = Z_0 \frac{\sin(\omega t)}{\sin(\omega t + \phi)} \qquad \text{Eq. 3. 6}$$

Figure 3.5 represents the sinusoidal signals of the applied potential and the corresponding response current as functions of time. In photoelectrochemical systems, the phase shift will depend on the nature of the photoelectrode being used. For example, if the photoelectrode behaves as a pure resistor, no phase shift will occur (ϕ=0), while for an ideal capacitor, the current will be shifted 90º from the applied potential. In general, the electrochemical processes that take place in a semiconductor/electrolyte interface behave similar to a resistor and a capacitor connected in parallel.

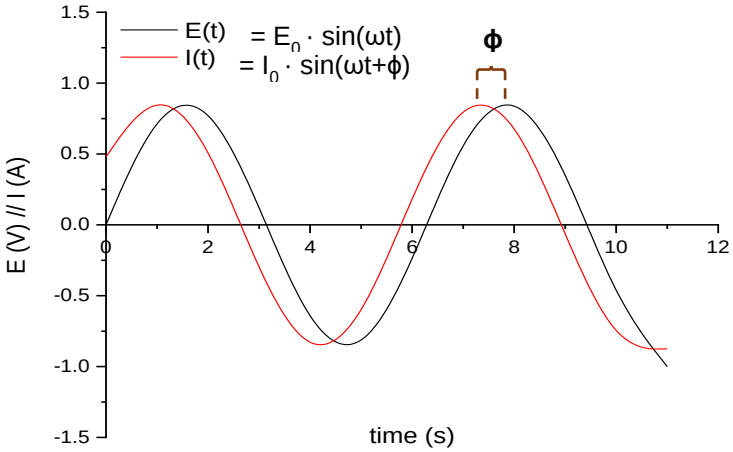

Figure 3. 5. Representation of applied potential and response current signals versus time.

Furthermore, the impedance of a photoelectrochemical system depends on the frequency, which can be written as shown in Eq. 3.7 by applying Euler's formula to Eq. 3.4 [26], being j=√-1.

$$Z(\omega) = Z' - Z''_j \qquad \text{Eq. 3. 7}$$

This means that impedance of photoelectrochemical systems is composed by a real component (Z'), which is associated to resistive behaviors, and an imaginary component (Z''), which is related to capacitative behaviors.

With EIS data, various diagrams can be plotted in order to extract information about the electrochemical properties of the semiconductor/electrolyte interface. The most widely employed diagrams are the Nyquist and Bode plots. For Nyquist diagrams, -Z'' is plotted against Z' [27]. The left side of the x-axis corresponds to high frequency data, while the right side of the axis corresponds to data registered at low frequencies. Depending on the electrochemical processes taking place in the studied interface, Nyquist plots will present one or many semicircles associated to them [28], as it can be clearly seen in Figure 3.6. Some resistance values can be obtained from the analysis of these diagrams, such as the resistance of the electrolyte (R_S) and the total resistance of the electrochemical system (R_T). R_S is determined by the intersection of the semicircle at high frequencies at the x-axis, while the amplitude of the semicircle (or intersection) at low frequencies determines R_T. This type of diagram is usually used to identify the number of electrochemical processes that take place in the interface.

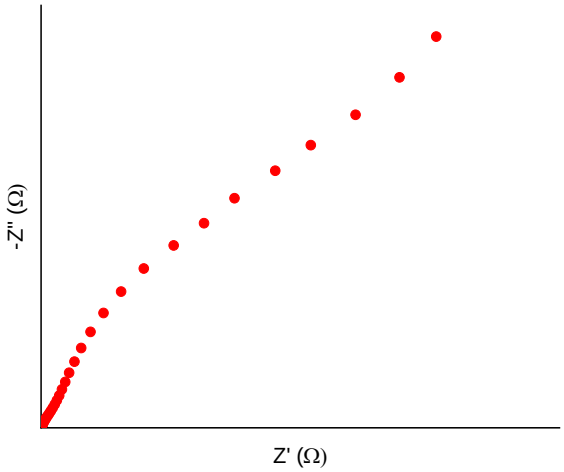

Figure 3. 6. Example of Nyquist Diagram.

In the same way, other plots can be used to obtain similar information. For example, a Bode-module diagram can be used by plotting log(|Z|) versus log(f) (Figure 3.7) [27]. In this representation, R_T can be known at low frequency values, while at high frequency values R_S can also be obtained.

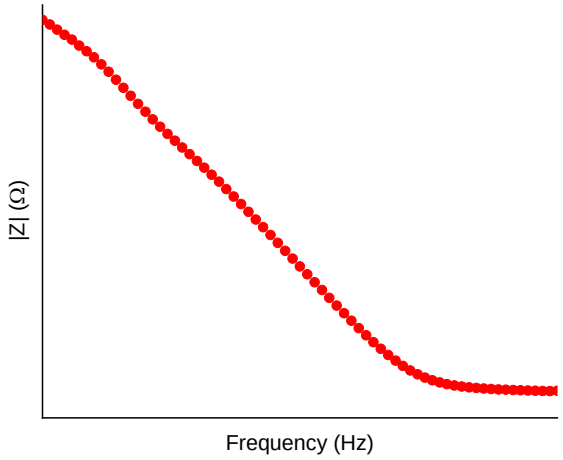

Figure 3. 7. Example of Bode-module plot.

Bode-phase plots are obtained by representing phase angle against log(f) (Figure 3.8) [27]. This diagram typically presents one or more gaussian bells, which depend on the number of electrochemical processes taking place in the studied

interface. The process associated with the time constant will present a more ideal capacitor behavior the closer to -90º is the value of ϕ at the peak of the graph.

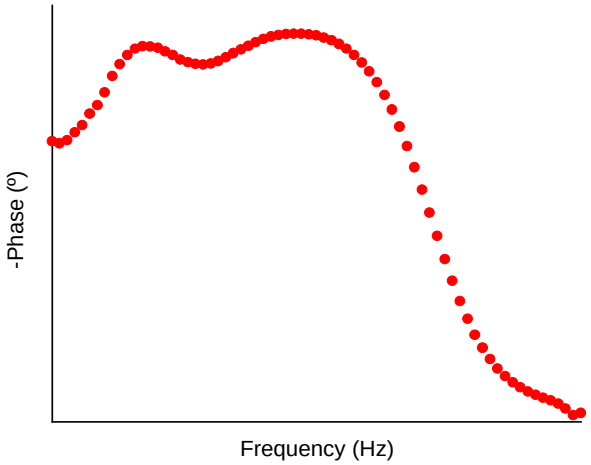

Figure 3. 8. Example of Bode-phase plot.

In order to make a good interpretation of the obtained data, experimental data must be fitted into an equivalent electrical circuit, which is made up of different passive elements (resistors and capacitors). The configuration of the equivalent circuit will depend on the examined electrochemical system. This way, numerical values of each element associated with the different electrochemical processes taking place in the semiconductor/electrolyte interface can be calculated, such as resistance of the electrolyte and resistance and capacitance related to recombination and charge transfer processes.

The EIS tests carried out in the present thesis were performed at open circuit potential (OCP) (vs. Ag/AgCl) for each studied material, using an amplitude of 0.01V and scanning frequencies from 100 kHz to 0.01 Hz. For this purpose, the three-electrode photoelectrochemical cell described in Figure 3.4 was employed. For the fitting of the data to an equivalent circuit, the software Zview4 was used.

3.3.3.4 Mott-Schottky analysis

Apart from the semiconductor character, Mott-Schottky plots can be used to determine the density of donor or acceptor species, as well as the flat band potential of the analyzed samples. This study is based on the calculation of the total capacitance of the semiconductor/electrolyte interface [29], which in a not very diluted solution, Eq. 3.8 and 3.9 can be used for n-type semiconductor and p-type semiconductor, respectively [30,31]:

$$\frac{1}{C^2} = \frac{1}{{C_H}^2} + \frac{1}{{C_{SC}}^2} = \frac{1}{{C_H}^2} + \frac{2}{e \cdot \varepsilon_T \cdot \varepsilon_0 \cdot N_D} \cdot \left(E - E_{FB} - \frac{k \cdot T}{e}\right) \qquad \text{Eq. 3. 8}$$

$$\frac{1}{C^2} = \frac{1}{{C_H}^2} - \frac{1}{{C_{SC}}^2} = \frac{1}{{C_H}^2} - \frac{2}{e \cdot \varepsilon_T \cdot \varepsilon_0 \cdot N_A} \cdot \left(E - E_{FB} - \frac{k \cdot T}{e}\right) \qquad \text{Eq. 3. 9}$$

where C is the total capacitance, C_{SC} is the space charge layer capacitance, C_H is the Helmholtz layer capacitance, e the electron charge ($1.60 \cdot 10^{-19}$ C), ε_0 the vacuum permittivity ($8.85 \cdot 10^{-14}$ F/cm), ε the relative dielectric constant of the studied material, E the applied potential, N_D is the donor density, N_A is the acceptor density, k the Boltzmann constant ($1.38 \cdot 10^{-23}$ J/K) and T the absolute temperature.

This way, the plot of $1/C^2$ vs. E (Figure 3.10) shows a straight line with a positive or a negative slope (in case of a n-type semiconductor or a p-type semiconductor, respectively) [32,33], in which charge carrier density can be determined from the slope, as well as the flat band potential that can be calculated from the interception of the straight line with the x-axis of the MS plot.

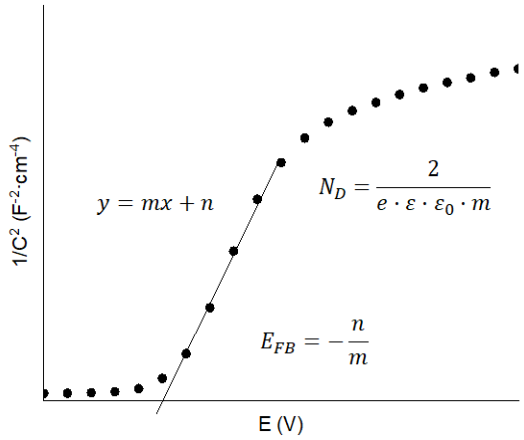

Figure 3. 9. Example of a Mott-Schottky diagram.

Having said that, Mott-Schottky analysis were performed for both thermocatalysts and photoelectrocatalysts, using the same cell configuration and electrolytes as in EIS tests, using a 5000 Hz frequency and scanning the potential in different ranges (Tale 3.2), depending on the sample being analyzed.

Table 3. 2. Potential range scanned during MS analysis for different samples.

Sample	**Potential range ($V_{Ag/AgCl}$)**
Nickel oxide-based catalysts	0.2 to -0.1
MoVTeNb catalysts	0.5 to -1.0
Copper oxide nanostructures	0.1 to -0.5
Titanium dioxide nanostructures	0.5 to -1.0

For the calculations of number of defects with equations 3.8 and 3.9, the relative dielectric constants displayed in Table 3.3 were used for each catalyst being studied.

Table 3. 3. Relative dielectric constants used in the MS equation for the calculation of defects.

Sample	Dielectric constant
Cerium oxide	25 [34–36]
Zirconium oxide	19.5 [37]
Nickel oxide-based catalysts	12 [38]
MoVTeNb catalysts	5.7[a]
Copper oxide nanostructures	12.9 [39,40]
Titanium dioxide nanostructures	100 [41]

[a] dielectric constant for MoO_3 [42].

3.3.3.5 Cyclic voltammetry

Cyclic voltammetry is an electrochemical technique used to study redox properties of chemical species. It provides information about electron transfer processes that take place during oxidation and reduction reactions. For this purpose, a potential waveform is applied to an electrochemical cell and the resulting current is measured. The electrochemical cell consists of a working electrode, a reference electrode and a counter electrode. The redox reactions take place in the working electrode surface. All electrodes are immersed in an electrolyte of choice, that will depend on the system being studied. The potential is scanned linearly with time (usually negatively or cathodically), starting from an initial potential E_0 to a final potential E_f and back to E_0. As the potential is swept, the redox reactions taking place at the working electrode result in a flow of current. Current response is measured by the potentiostat connected to the electrochemical cell and it is plotted as a function of the applied potential, as shown by Figure 3.10.

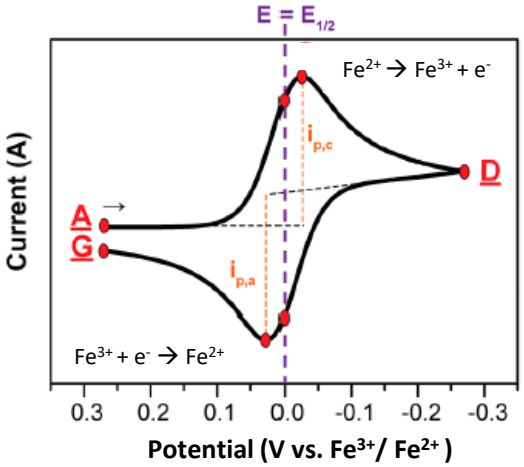

Figure 3. 10. Voltammogram of the reversible reduction of a 1 mM Fe^{3+} solution to Fe^{2+}, at a scan rate of 100 mV s^{-1}[43].

In this study, the same electrochemical cell configuration was used as in EIS and MS analysis, but with a different electrolyte. Instead, a 10 mM solution of $Fe(CN)_6K_4$ was used and the potential sweep was performed in a range of -0.1 to 0.6 $V_{Ag/AgCl}$ at 0.01 V/s.

3.3.3.6 Photoelectrochemical water splitting measurements

To obtain information about the photoelectrochemical performance of the different photoelectrocatalysts, current density vs. applied potential curves under alternating dark and illumination conditions were registered. When photons hit a photoelectrode with higher energy than the bandgap energy of the sample, electron-hole pairs are generated. If the applied potential is big enough, the separation of these photogenerated electron-hole pairs becomes effective and they participate in redox reactions of the electrolyte.

These measurements were performed only for photoelectrocatalysts, since they are the only catalysts involved in photoelectrochemical applications. For each one of them, these tests took place under a UV-LED lamp (λ = 365 nm) at a power of 100 mW/cm^2. Photocurrent density versus applied potential was registered by

chopped light irradiation (16s in the dark and 4s in the light), while scanning different potentials depending on the studied nanostructure (Table 3.4), with a scan rate of 5 mV/s.

Table 3. 4. Scanning potential for the WS measurements for the different nanostructures.

Nanostructures	Scanning potential (V)
CuOx	0.08; −0.80
TiO_2	-0.4; +0.54

3.4 Thermocatalytic tests

All thermocatalytic tests were carried out in a fixed-bed quartz tubular reactor, provided with a ceramic porous plate where the catalysts were placed onto. Both oxidative dehydrogenation of ethane and thermocatalytic decomposition of nitrous oxide reactions were conducted at atmospheric pressure and temperatures ranging from 200 to 500ºC. To reach these temperatures, the reactor was situated inside a metallic chamber, equipped with electrical resistors. A thermocouple attached to the reactor allowed to control the reaction temperature.

In the case of the oxidative dehydrogenation of ethane, tests were performed with different catalyst loadings and flow rates in order to achieve a wider range of conversions (mainly using 0.1-1.0g and 25-100 ml/min). The gas mixture fed to the reactor varied depending on which experiment was being carried out. ODHE-O_2 tests started with molar ratios of C_2H_6/O_2/He de 5/5/90, but in posterior experiments different ratios were tested for some catalysts, including 5/2.5/92.5, 5/10/85 and 5/15/80. In the same way, for the ODHE-N_2O tests, the gas mixture was first fed with a molar ratio of 5/10/85. Later, with catalysts that provided the best results, different ratios were tested such as 5/5/90, 5/20/75 and 5/30/65. For N_2O

thermocatalytic decomposition, 0.2g of catalyst was loaded and 100 ml/min of 1% N_2O and 99% helium was fed.

All catalyst loads were previously pressed, grinded and sieved in order to obtain beds with 0.3-0.5 mm particle size.

Reactants and reaction products were analyzed by an online gas chromatograph, AGILENT 7890A, equipped with a thermal conductivity detector (TCD), using two types of columns:

i) Porapack Q (3 m x 1/8 in.), for the separation of CO_2, water, hydrocarbons and acids.

ii) Molecular sieve 5A (3 m x 1/8 in.), to separate oxygen, nitrogen and CO.

Both columns were arranged in series, passing the sample first through Porapack Q column, and later through molecular sieve 5A, or directly to the exit. Finally, samples reached the thermal conductivity detector. Helium was used as carrier gas with a flow of 20 ml/min. The detector worked at 250ºC, while the injector was kept at 150ºC. For the correct separation of compounds, the analytical conditions were programmed as shown in the following scheme:

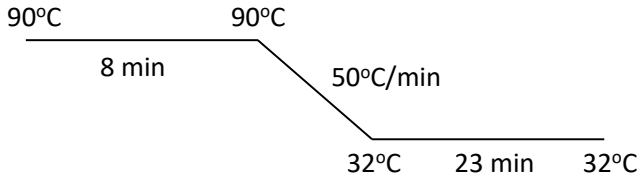

Figure 3. 11. Temperature program for chromatographic cycle in N_2O assisted ODHE.

Gas chromatography separates components based on their different diffusion rates through the chromatographic columns. As a result, each compound exits the column at a specific time, known as retention time. When a component is detected by the TCD, it emits a signal proportional to the quantity present. This signal recorded at a specific retention time appears as a peak in the chromatogram. This

peak is then integrated, and the area under the peak determines the quantity of the detected compound. A correction factor is necessary to relate the area under the peak with the concentration of the detected compound, called response factor. Response factors vary depending on the employed detector, but they do not depend on type and flow of carrier gas, temperature, pressure and concentration of product. Table 3.5 shows both retention time and response factor, which have been experimentally determined, for each compound involved in the reaction. A response factor of 1 for ethane has been taken as a reference in order to determine the rest.

Table 3. 5. Retention times and response factors for the different compounds at the conditions of the chromatograph.

Compound	Retention time	Response factor
CO_2	1.8	0.938
N_2O	2.2	0.777
Ethylene	2.6	0.938
Ethane	3.3	1.0
O_2	16.2	0.781
CO	20.5	0.820

Therefore, knowing both peak area and response factor it is possible to determine the concentration of each compound with the following equation:

$$C_i = \frac{A_i}{F_i} \qquad \text{Eq. 3. 10}$$

being, C_i, the concentration of compound i,

A_i, the area under the peak belonging to compound i,

F_i, the response factor of compound i.

Experimental setup is shown in Figure 3.12. Gases were fed with flowmeters through a pre-heating pipe and entered the reactor, which was at the set temperature due to the chamber around it. Then, the gas outlet was directed through a post-heating pipe to the gas chromatograph for the separation and analysis of the different components.

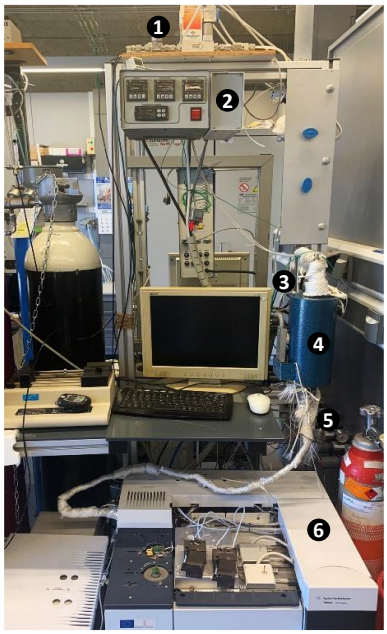

1) Flowmeter
2) Temperature controller
3) Pre-heater
4) Reactor chamber
5) Post-heater
6) Gas chromatograph

Figure 3. 12. Experimental setup for the reactions of ODH and N_2O thermocatalytic decomposition.

In order to know the yield to ethylene of each studied catalyst (Eq. 3.11), it is necessary to calculate conversion and selectivity at each temperature, using Eq. 3.12 and Eq. 3.13.

$$R_{ij} = X_j \times S_{ij} \qquad \text{Eq. 3. 11}$$

$$X_j = \frac{\sum_{products} \frac{A_i}{F_{ij}} \cdot \frac{\omega_i}{\omega_j}}{A_j + \sum_{products} \frac{A_i}{F_{ij}} \cdot \frac{\omega_i}{\omega_j}} \qquad \text{Eq. 3. 12}$$

$$S_{ij} = \frac{\frac{A_i}{F_{ij}} \cdot \frac{\omega_i}{\omega_j}}{\sum_{products} \frac{A_i}{F_{ij}} \cdot \frac{\omega_i}{\omega_j}} \qquad \text{Eq. 3. 13}$$

where:

j is referred to the reactant (ethane),

i is referred to the reaction product (ethylene, CO_2, CO),

Xj is the conversion of reactant j,

F_{ij} is the response factor of product i with respect to reactant j,

ω are the number of carbon atoms in the molecular formula of the products (i) and reactant (j),

S_{ij} is the selectivity to product i with respect to reactant j.

A parameter that must be considered is the contact time (τ), which is defined as the time that the reactant takes to cross the catalytic bed. In this case, the contact time has been determined as the ratio between the mass of catalyst (in grams) and the molar flow rate of ethane in the feeding mixture (in mol C_2/h).

3.5 Photoelectrochemical applications

In accordance with the main objective of the thesis, the different synthesized photoelectrocatalysts (CuO_X and TiO_2 nanostructures) have been used in the photoelectro-decomposition of N_2O. For this purpose, an H-type photoelectrochemical cell is employed. Figure 3.13 depicts a configuration example of the employed photoelectrochemical cell, and the semi-reactions that take place in the anode and cathode. When TiO_2 is used as a photoanode (Figure 3.13), electron-

hole pairs are photogenerated and the external electrical circuit allows the flow of electrons to the cathode, where reduction of nitrous oxide takes place. On the other hand, when a copper oxide photoelectrocatalyst is employed as a photocathode, the photogenerated electrons reduce N_2O directly on this electrode.

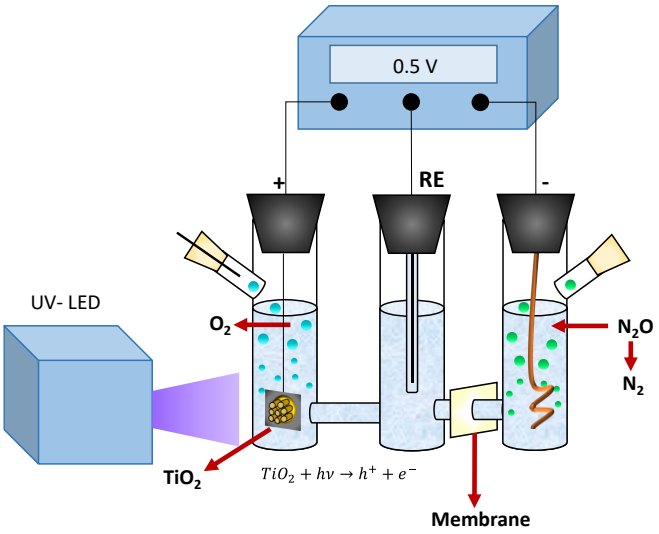

Figure 3. 13. Schematic diagram of the photoelectrochemical cell for N_2O photoelectro-reduction with TiO_2 nanostructure as photoanode.

The cell was composed of the working electrode (studied nanostructure), the counter electrode (copper rod in case of the degradation with TiO_2 and platinum sheet in case of the degradation with CuOx), the reference electrode Ag/AgCl (3M KCl) and three magnetic stirrers, each one in each compartment of the cell. A cationic membrane of 0.180 mm of thickness (Nafion N-117) separated the cell into two chambers and hindered gas crossover. The working electrode was prepared by gluing the nanostructure to a copper wire using copper adhesive tape and silver chloride to improve conductivity. Finally, the entire electrode was teflon-coated except for the nanostructured surface, so that only this part was exposed to the electrolyte. Regarding electrolytes, a 0.1M Na_2SO_4 solution was used for the copper

oxide nanostructures, while a 1M KOH solution was used for the titanium dioxide photoelectrocatalyst.

Before the decomposition reaction, the cell was saturated, at first, with helium with an approximate flow rate of 40 ml/min for 30 minutes, and then with N_2O with a flow rate of 20 ml/min for another 30 minutes. An outlet duct was connected at all times to an extractor in order to avoid overpressures. After the bubbling of N_2O finished, the inlet and extraction were removed and both were closed with a plug and a septum, respectively. The septum was placed so that it was possible to extract liquid samples without opening the sealed system and risking gas loss.

At the same time that potential was being applied to the electrodes of the cell with a connected potentiostat, the photoelectrode was being irradiated with UV light. A UV lamp (λ=365 nm) was situated 3 cm away from the photoelectrocatalyst for this purpose, with 100 W/cm^2 of power. Regarding the applied potential, for the test using the copper oxide nanostructure -0.2 $V_{Ag/AgCl}$ were applied, while for the TiO_2 nanostructure test 0.5 $V_{Ag/AgCl}$.

In order to analyze the evolution of the N_2O concentration inside the system, liquid samples of 1 ml were taken every 30 minutes and were introduced into sealed vials. After leaving the samples inside the vials for 24h, liquid-vapor equilibrium was reached, and the composition of the gas phase was analyzed by an online gas chromatograph (HP 6890). It should be noted that a sample was taken before starting the experiment to know the gas concentration at time.

3.6 References

[1] B. Solsona, J.M. López Nieto, S. Agouram, M.D. Soriano, A. Dejoz, M.I. Vázquez, P. Concepción, Optimizing Both Catalyst Preparation and Catalytic Behaviour for the Oxidative Dehydrogenation of Ethane of Ni-Sn-O Catalysts, Topics in Catalysis 59 (n.d.). https://doi.org/10.1007/s11244-016-0674-z.

[2] T. Katou, D. Vitry, W. Ueda, Hydrothermal Synthesis of A New Mo–V–O Complex Metal Oxide and Its Catalytic Activity for The Oxidation of Propane, Chemistry Letters 32 (2003) 1028–1029. https://doi.org/10.1246/cl.2003.1028.

[3] D. Melzer, G. Mestl, K. Wanninger, Y. Zhu, N.D. Browning, M. Sanchez-Sanchez, J.A. Lercher, Design and synthesis of highly active MoVTeNb-oxides for ethane oxidative dehydrogenation, Nat Commun 10 (2019) 4012. https://doi.org/10.1038/s41467-019-11940-0.

[4] F. Ivars, B. Solsona, E. Rodríguez-Castellón, J.M. López Nieto, Selective propane oxidation over MoVSbO catalysts. On the preparation, characterization and catalytic behavior of M1 phase, Journal of Catalysis 262 (2009) 35–43.

[5] A. Celaya Sanfiz, T.W. Hansen, F. Girgsdies, O. Timpe, E. Rödel, T. Ressler, A. Trunschke, R. Schlögl, Preparation of Phase-Pure M1 MoVTeNb Oxide Catalysts by Hydrothermal Synthesis—Influence of Reaction Parameters on Structure and Morphology, Top Catal 50 (2008) 19–32. https://doi.org/10.1007/s11244-008-9106-z.

[6] M. Afifeh, S.J. Hosseinipour, R. Jamaati, Effect of post-annealing on the microstructure and mechanical properties of nanostructured copper, Materials Science and Engineering: A 802 (2021) 140666. https://doi.org/10.1016/j.msea.2020.140666.

[7] B. Lucas-Granados, R. Sánchez-Tovar, R.M. Fernández-Domene, J. García-Antón, Study of the annealing conditions and photoelectrochemical characterization of a new iron oxide bi-layered nanostructure for water splitting, Solar Energy Materials and Solar Cells 153 (2016) 68–77. https://doi.org/10.1016/j.solmat.2016.04.005.

[8] R. Sánchez-Tovar, K. Lee, J. García-Antón, P. Schmuki, Formation of anodic TiO2 nanotube or nanosponge morphology determined by the electrolyte hydrodynamic conditions, Electrochemistry Communications 26 (2013) 1–4. https://doi.org/10.1016/j.elecom.2012.09.041.

[9] N.A.M. Shanid, M.A. Khadar, Evolution of nanostructure, phase transition and band gap tailoring in oxidized Cu thin films, Thin Solid Films 516 (2008) 6245–6252. https://doi.org/10.1016/j.tsf.2007.11.119.

[10] J. Borràs-Ferrís, R. Sánchez-Tovar, E. Blasco-Tamarit, M.J. Muñoz-Portero, R.M. Fernández-Domene, J. García-Antón, TiO2 Nanostructures for Photoelectrocatalytic Degradation of Acetaminophen, Nanomaterials 9 (2019) 583. https://doi.org/10.3390/nano9040583.

[11] R. Sanchez-Tovar, K. Lee, J. Garcia-Anton, P. Schmuki, Photoelectrochemical poperties of anodic TiO2 nanosponge layers, ECS Electrochemistry Letters 2 (2013) H9–H11. https://doi.org/10.1149/2.005303eel.
[12] R. Sánchez-Tovar, R.M. Fernández-Domene, A. Martínez-Sánchez, E. Blasco-Tamarit, J. García-Antón, Synergistic effect between hydrodynamic conditions during Ti anodization and acidic treatment on the photoelectric properties of TiO2 nanotubes, Journal of Catalysis 330 (2015) 434–441. https://doi.org/10.1016/j.jcat.2015.08.002.
[13] Crystallography | Definition & Facts | Britannica, (n.d.). https://www.britannica.com/science/X-ray-diffraction (accessed June 26, 2025).
[14] Y. Waseda, E. Matsubara, K. Shinoda, X-Ray Diffraction Crystallography: Introduction, Examples and Solved Problems, Springer, Berlin, Heidelberg, 2011. https://doi.org/10.1007/978-3-642-16635-8.
[15] B. Fultz, J. Howe, Transmission Electron Microscopy and Diffractometry of Materials, Springer, Berlin, Heidelberg, 2013. https://doi.org/10.1007/978-3-642-29761-8.
[16] R.F. Egerton, Electron energy-loss spectroscopy in the TEM, Rep. Prog. Phys. 72 (2008) 016502. https://doi.org/10.1088/0034-4885/72/1/016502.
[17] M. L.C. Passos, M.L. M.F.S. Saraiva, Detection in UV-visible spectrophotometry: Detectors, detection systems, and detection strategies, Measurement 135 (2019) 896–904. https://doi.org/10.1016/j.measurement.2018.12.045.
[18] Guide to Raman Spectroscopy, (n.d.). https://www.bruker.com/en/products-and-solutions/infrared-and-raman/raman-spectrometers/what-is-raman-spectroscopy.html (accessed June 26, 2025).
[19] A. Kudelski, Analytical applications of Raman spectroscopy, Talanta 76 (2008) 1–8. https://doi.org/10.1016/j.talanta.2008.02.042.
[20] Surface Area and Porosity Determinations by Physisorption, 2019. https://shop.elsevier.com/books/surface-area-and-porosity-determinations-by-physisorption/condon/978-0-12-818785-2 (accessed June 26, 2025).
[21] K.S.W. Sing, Adsorption methods for the characterization of porous materials, Advances in Colloid and Interface Science 76–77 (1998) 3–11. https://doi.org/10.1016/S0001-8686(98)00038-4.
[22] M.P. Seah, D. Briggs, Practical Surface Analysis by Auger and X-ray Photoelectron Spectroscopy, John Wiley & Sons, Ltd, 1983.
[23] Guide to FT-IR Spectroscopy, (n.d.). https://www.bruker.com/en/products-and-solutions/infrared-and-raman/ft-ir-routine-spectrometer/what-is-ft-ir-spectroscopy.html (accessed June 26, 2025).
[24] A.Ch. Lazanas, M.I. Prodromidis, Electrochemical Impedance Spectroscopy─A Tutorial, ACS Meas. Sci. Au 3 (2023) 162–193. https://doi.org/10.1021/acsmeasuresciau.2c00070.

[25] F.J. Günter, J.B. Habedank, D. Schreiner, T. Neuwirth, R. Gilles, G. Reinhart, Introduction to Electrochemical Impedance Spectroscopy as a Measurement Method for the Wetting Degree of Lithium-Ion Cells, J. Electrochem. Soc. 165 (2018) A3249. https://doi.org/10.1149/2.0081814jes.

[26] J. Flores, R. Romero, J. Genascá, Espectroscopía de Impedancia electroquímica en corrosión, Journal of Chemical Information and Modeling. Retrieved from Http://Books. Google. Com/Books (2014). https://scholar.google.com/scholar?cluster=5072313564641774 05&hl=en&oi=scholarr (accessed June 26, 2025).

[27] N. Bonanos, B.C.H. Steele, E.P. Butler, J.R. Macdonald, W.B. Johnson, W.L. Worrell, G.A. Niklasson, S. Malmgren, M. Strømme, S.K. Sundaram, M.C.H. McKubre, D.D. Macdonald, G.R. Engelhardt, E. Barsoukov, Brian.E. Conway, Wendy.G. Pell, N. Wagner, C.M. Roland, R.S. Eisenberg, Applications of Impedance Spectroscopy, in: Impedance Spectroscopy, John Wiley & Sons, Ltd, 2018: pp. 175–478. https://doi.org/10.1002/9781119381860.ch4.

[28] A. González-Cortés, Electrochemical Impedance Spectroscopy, in: Agricultural and Food Electroanalysis, John Wiley & Sons, Ltd, 2015: pp. 381–419. https://doi.org/10.1002/9781118684030.ch14.

[29] R.M. Fernandez Domene, R. Sanchez Tovar, B. Lucas Granados, J. Garcia Anton, Principios de Fotoelectroquímica, Universitat Politecnica de Valencia, 2018.

[30] Band Bending in Semiconductors: Chemical and Physical Consequences at Surfaces and Interfaces | Chemical Reviews, (n.d.). https://pubs.acs.org/doi/10.1021/cr3000626 (accessed June 26, 2025).

[31] W.J. Albery, G.J. O'Shea, A.L. Smith, Interpretation and use of Mott–Schottky plots at the semiconductor/electrolyte interface, J. Chem. Soc., Faraday Trans. 92 (1996) 4083–4085. https://doi.org/10.1039/FT9969204083.

[32] Hole-Transporting Materials for Perovskite-Sensitized Solar Cells - Dhingra - 2016 - Energy Technology - Wiley Online Library, (n.d.). https://onlinelibrary.wiley.com/doi/full/10.1002/ente.201500534 (accessed June 26, 2025).

[33] K. Gelderman, L. Lee, S.W. Donne, Flat-Band Potential of a Semiconductor: Using the Mott–Schottky Equation, J. Chem. Educ. 84 (2007) 685. https://doi.org/10.1021/ed084p685.

[34] A. García, L. Toca, R.M. Fernández-Domene, F. Ivars-Barceló, E. Montejano-Nares, P. Amorós, R. Sánchez-Tovar, B. Solsona, Defective outermost layers of ceria catalysts determined by electrochemical methods as direct responsible for catalytic activity in total oxidation of a representative VOC, Applied Surface Science 653 (2024) 159354. https://doi.org/10.1016/j.apsusc.2024.159354.

[35] F.-C. Chiu, C.-M. Lai, Optical and electrical characterizations of cerium oxide thin films, J. Phys. D: Appl. Phys. 43 (2010) 075104. https://doi.org/10.1088/0022-3727/43/7/075104.

[36] N. Pradhani, P.K. Mahapatra, R.N.P. Choudhary, Effect of cerium oxide addition on optical, electrical and dielectric characteristics of (Bi0.5Na0.5)TiO3 ceramics, Journal of Physics: Materials 1 (2018) 015007. https://doi.org/10.1088/2515-7639/AACFF0.

[37] Y. Oh, V. Bharambe, B. Mummareddy, J. Martin, J. McKnight, M.A. Abraham, J.M. Walker, K. Rogers, B. Conner, P. Cortes, E. MacDonald, J.J. Adams, Microwave dielectric properties of zirconia fabricated using NanoParticle Jetting™, Additive Manufacturing 27 (2019) 586–594. https://doi.org/10.1016/j.addma.2019.04.005.

[38] F. Yang, X. Zhou, N.T. Plymale, K. Sun, N.S. Lewis, Evaluation of sputtered nickel oxide, cobalt oxide and nickel–cobalt oxide on n-type silicon photoanodes for solar-driven O2(g) evolution from water, J. Mater. Chem. A 8 (2020) 13955–13963. https://doi.org/10.1039/D0TA03725G.

[39] E. Szaniawska, I.A. Rutkowska, M. Frik, A. Wadas, E. Seta, A. Krogul-Sobczak, K. Rajeshwar, P.J. Kulesza, Reduction of carbon dioxide at copper(I) oxide photocathode activated and stabilized by over-coating with oligoaniline, Electrochimica Acta 265 (2018) 400–410. https://doi.org/10.1016/j.electacta.2018.01.116.

[40] A.A.M. Farag, A. Ashery, M.A. Salem, Electrical, dielectric characterizations and optoelectronic applications of epitaxially grown Co/n-CuO/p-Si heterojunctions, Superlattices and Microstructures 135 (2019) 106277. https://doi.org/10.1016/J.SPMI.2019.106277.

[41] C.W. Chu, New ordered phases of slightly reduced rutile and their sharp dielectric absorptions at low temperature, Physical Review B 1 (1970) 4700–4708. https://doi.org/10.1103/PhysRevB.1.4700.

[42] T. Das, S. Tosoni, G. Pacchioni, Structural and electronic properties of bulk and ultrathin layers of V2O5 and MoO3, Computational Materials Science 163 (2019) 230–240. https://doi.org/10.1016/j.commatsci.2019.03.027.

[43] N. Elgrishi, K.J. Rountree, B.D. McCarthy, E.S. Rountree, T.T. Eisenhart, J.L. Dempsey, A Practical Beginner's Guide to Cyclic Voltammetry, J. Chem. Educ. 95 (2018) 197–206. https://doi.org/10.1021/acs.jchemed.7b00361.

Chapter 4: Thermocatalytic transformation of N_2O

The following papers have been published related to the results of the present chapter:

- **Sánchez G.**, Dejoz A.M., Fernández-Domene R., Barroso-Martín I., Ballesteros-Plata D., Infantes-Molina A., Cecilia J.A., Rodríguez-Castellón E., López Nieto J.M., Sánchez-Tovar R., Solsona B., *N_2O Assisted Ethane Transformation into Ethylene Using NiO−CeO2−ZrO_2 Catalysts*, ChemCatChem 16 (2024) art. no. e202400329, https://doi.org/10.1002/cctc.202400329
- **G. Sánchez-García**, A. Pérez-Calvo, B. Moreno-Torralbo, R. Sánchez-Tovar, A.M. Dejoz, P. Concepción, J.M. López Nieto, B. Solsona, *Catalytic activation of N_2O on promoted NiO based materials: Valorization by oxidative dehydrogenation of ethane*, Journal of Catalysis 450 (2025) art. no. 116277, https://doi.org/10.1016/j.jcat.2025.116277

The objective of this chapter is to analyze the catalytic results of different sets of thermocatalysts used in the oxidative dehydrogenation of ethane assisted by nitrous oxide. Several physicochemical and structural characterization techniques were performed in order to explain the catalytic results. Furthermore, an in-depth electrochemical study of these catalysts has been carried out, in order to correlate their performance in the ODH of ethane with their electrochemical properties. Additionally, direct decomposition of N_2O into O_2 and N_2 is tested with some of the studied thermocatalysts. This work successfully covers two aspects: on the one hand, ethylene is obtained in a selective process, using much lower temperatures than traditionally; and, on the other hand, N_2O valorization is achieved by using it as an oxidant during the reaction.

This chapter is divided into three different sections. First, nickel oxide-based catalysts have been reported to be efficient in the oxidative dehydrogenation of ethane assisted by oxygen. Moreover, ceria is one of the standard supports in heterogeneous catalysis, since it presents an elevated oxygen storage capacity (OSC) and a considerable amount of oxygen defects, both factors being highly interesting for catalysis. Furthermore, the introduction of Zr into the CeO_2 lattice has been reported to increase the concentration of oxygen vacancies. Therefore, in the first part of this chapter nickel supported on ceria and ceria/zirconia catalysts have been prepared and tested in the N_2O assisted ODH of ethane. The study about the effect of the partial replacement of Ce^{4+} by Zr^{4+} has been also studied.

Although selectivity to ethylene is enhanced with the use of nitrous oxide in this catalytic system, activity is still an aspect set to improve. For that reason, the next section of the chapter is focused on the effect of different promoters on doped nickel oxide catalysts. Promoted NiO catalysts, with an appropriate dopant, are among the most efficient ones in the O_2-assisted ODH of ethane. However, no systematic study has been undertaken using N_2O as oxidant.

To conclude this chapter, the performance of a multicomponent MoVTeNb catalyst has been tested in the N_2O assisted oxidative dehydrogenation of ethane. This catalyst presents the best catalytic performance reported in the literature for the O_2-ODH. The efficient performance is associated with the presence of the $Te_2M_{20}O_{58}$ (M = Mo, V, Nb) orthorhombic crystalline phase (also called as M1).

The undesired formation of CO_X is perhaps the main disadvantage of the ethane ODH using O_2 as an oxidant. Then, it would be highly interesting to use an oxidizing agent with lower oxidizing potential, such as nitrous oxide, that maybe could lower the oxidation to carbon oxides. Thus, a further study is conducted comparing these results with those obtained for the best nickel oxide-based catalyst synthesized in the previous chapter.

4.1 N_2O assisted ethane oxidative dehydrogenation using Ni-CeO_2-ZrO_2 catalysts

Nickel oxide is considered as one of the most active metal oxides in reactions governed by a redox Mars-Van Krevelen mechanism. However, this activity is mostly directed towards the formation of carbon dioxide. It has been suggested that the addition of suitable dopants or supports can enhance the formation of the desired products. In this way, the use of Ce-Ni-O catalysts has been reported to be more selective towards ethylene in the ODH of ethane when compared to pure NiO or pure CeO_2. Furthermore, Ce is known to facilitate the activation of N_2O. Therefore, the combination of both metal oxides can be an interesting option for the simultaneous decomposition of nitrous oxide and selective transformation of ethane to ethylene during the oxidative dehydrogenation assisted by N_2O. On the other hand, the addition of small amounts of Zr to ceria could improve further the catalytic performance of these materials, since the addition of low amounts of zirconium tend to increase the concentration of oxygen vacancies.

Nickel oxide catalysts supported on ceria and zirconia (Zr/Ce at. ratios of 0, 0.1 and 0.5) were prepared and characterized by different physicochemical techniques, as well as tested in the reaction of interest. Textural properties were determined by N_2 adsorption-desorption. Figure 4.1A displays the isotherms for all samples, as well as for a reference NiO sample. All catalysts present a type IV isotherm with a hysteresis loop, which reveals their mesoporous nature.

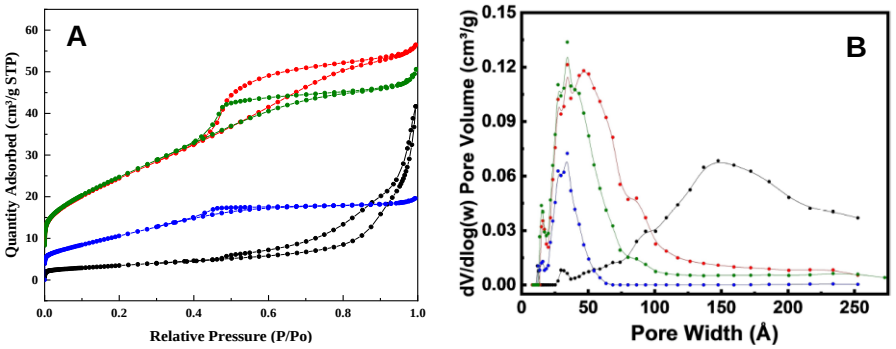

Figure 4. 1. (A) N_2 adsorption-desorption isotherms and (B) DFT pore size distribution (--) NiO, (--) Ni/Ce, (--) Ni/$Ce_{0.9}Zr_{0.1}$, (--) Ni/$Ce_{0.5}Zr_{0.5}$.

Specific surface area and pore size were also calculated using BET and NLDFT (Non-Local Density Functional Theory) method, respectively. Table 4.1 shows a summary of the main results. First, it is noteworthy that the addition of zirconium leads to a significant decrease in both specific surface area (90 vs. 39 m^2/g) and pore volume (0.08 vs. 0.03 cm^3/g).

Table 4. 1. Textural properties of CeZr/Ni samples.

Catalyst	S_{BET} ($m^2 \cdot g^{-1}$)	S_{ext} ($m^2 \cdot g^{-1}$)	S_{micro} ($m^2 \cdot g^{-1}$)	S_{micro}/S_{total} (%)	Pore volume ($cm^3 \cdot g^{-1}$)
NiO	12	-	-	-	0.04
Ni/Ce	90	83	7	8	0.08
Ni/$Ce_{0.9}Zr_{0.1}$	91	71	20	22	0.07
Ni/$Ce_{0.5}Zr_{0.5}$	39	24	15	38	0.03

Furthermore, Figure 4.1B illustrates the pore size distribution for all Ni-CeO_2-ZrO_2 catalysts, including a reference NiO catalyst. According to NLDFT method, all samples present a unimodal pore size distribution of narrow mesopores with an average pore size of 35 Å. In addition, the distribution becomes narrower as the loading of zirconium increases.

The XRD patterns of the prepared catalysts are presented in Figure 4.2A. Diffraction peaks at 2θ = 28.6°, 33.1°, 47.6°, 56.4° and 59.2° evidence the presence of the cubic CeO_2 phase in all samples (JCPDS: 03-065-5923). However, the main peak in the sample with the highest content of Zr is slightly shifted to a higher 2θ value. This shift coincides with the main peak corresponding to $Ce_{0.5}Zr_{0.5}O_2$ oxide, which confirms the development of a Ce-Zr-O solid solution during coprecipitation [1,2]. Furthermore, ***a*** unit cell parameter was calculated using CeO_2 (111) crystalline plane for the samples **Ni/Ce** and **Ni/$Ce_{0.9}Zr_{0.1}$**, being 5.42 Å and 5.40 Å, respectively. The decrease in ***a*** hints the intercalation of Zr^{4+} into the ceria structure, since the ionic radius of Zr^{4+} is smaller than that of Ce^{4+} [3]. In accordance with the previous statement about the formation of the mixed oxide phase, the calculated ***a*** unit cell parameter was 3.76 Å for the **Ni/$Ce_{0.5}Zr_{0.5}$** sample, which is a similar value to that reported in literature for $Ce_{0.5}Zr_{0.5}O_2$ (3.72 Å, JCPDS: 00-038-1436). The wider peaks of this sample imply lower crystallinity of the phase. No peaks of other phases were detected. The absence of NiO peaks is believed to be due to the low loading of nickel but is also a sign of highly dispersed nickel sites on the surface of the catalysts, which will be later proved by EDX mapping.

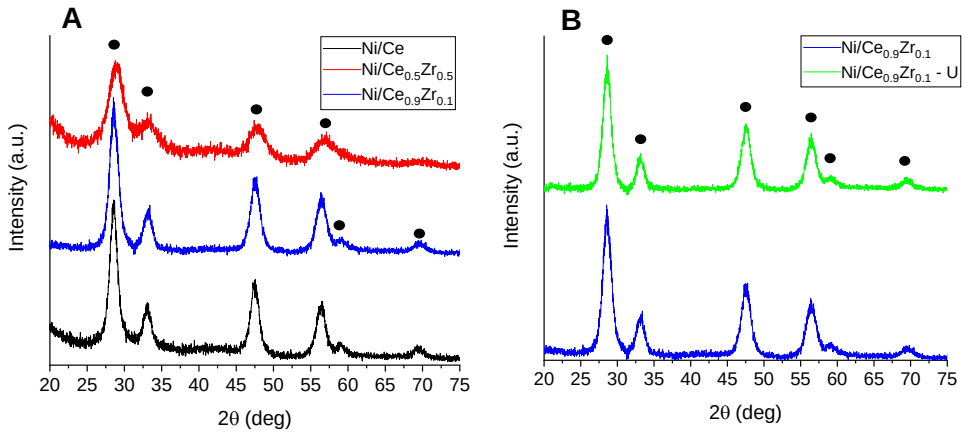

Figure 4. 2. XRD patterns of (A) CeZr/Ni samples, (B) fresh and used $Ce_{0.9}Zr_{0.1}$/Ni samples.

Figure 4.2B displays the XRD pattern of the **Ni/$Ce_{0.9}Zr_{0.1}$** sample before and after use in ODH-N_2O. It is clear that the catalyst does not present substantial changes in its crystalline structure or crystallite size, which suggests the catalyst is stable during the reaction.

An XPS study was conducted to obtain information about the near surface of the prepared catalysts, and the results are plotted in Figure 4.3 and shown in Tables 4.2 and 4.3. Pure NiO has been added to all core level signals for comparative reasons.

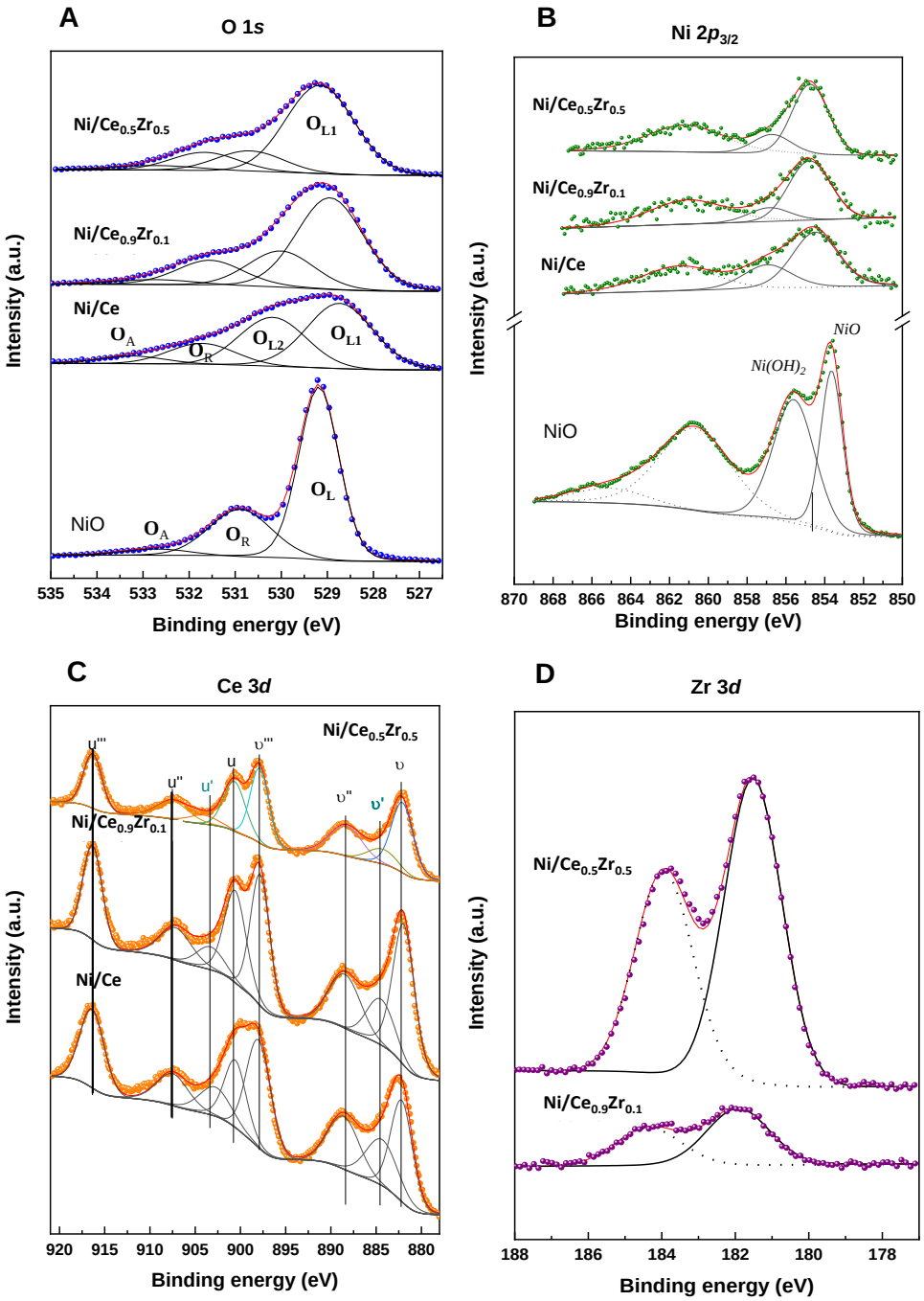

Figure 4. 3. (A) O 1s, (B) Ni 2$p_{3/2}$, (C) Ce 3d and (D) Zr 3d core level spectra for Ni/CeZr catalysts.

First, O 1s core level signals of all samples are shown in Figure 4.3A. The pure NiO pattern could be deconvoluted into three contributions, being the main one at 529.1 eV related to the lattice oxygen. Moreover, agreeing with NiO and $Ni(OH)_2$ species, the second contribution (530.9 eV) could be linked to oxygen deficient regions [4,5]. Finally, the last and smallest contribution at 532.0 eV is related to hydroxyl groups present at the surface of the catalyst and oxygen vacancies with adsorbed surface oxygen species [6]. Regarding samples containing cerium, four contributions can be recognized. Lattice oxygen contribution is at 529.0 eV (O_{L1}) in this case [7]. Lattice oxygen with a more covalent nature (O_{L2}) is also present with a contribution at 530.1 eV, being this the O^{2-} anions bonded to the nickel or cerium sites [2]. The presence of surface reactive oxygen (O_R) species, like O_2^{2-}/O^- adsorbed on oxygen vacancies on the surface (O_V) and surface adsorbed water (O_A), lead to the appearance of 531.7 eV and 533.0 eV contributions, respectively [8]. However, when zirconium is incorporated into the structure, O lattice signals are shifted to higher values. This has been attributed to the Zr incorporation into the ceria lattice, which is in accordance with that observed in the XRD patterns.

Table 4.2 exhibits that each oxygen species contributes to the total spectra of each Ni/CeZr sample.

Table 4. 2. Percentages of surface oxygen species for the prepared samples determined by XPS.

Catalyst	**O_{L1}**	**O_{L2}**	**O_L**	**O_R**
Ni/Ce	49.4	35.4	84.8	15.3
$Ni/Ce_{0.9}Zr_{0.1}$	59.6	23.5	83.0	16.9
$Ni/Ce_{0.5}Zr_{0.5}$	69.8	16.0	85.8	14.3

It can be observed that all three catalysts have very similar O_R contributions (around 15%). Nevertheless, the different types of lattice oxygen species contribute in different ratios depending on the catalyst. For instance, O_{L2} signal decreases as zirconium content increases, while O_{L1} does the opposite. The increase in O_{L1} with

the increasing Zr loading implies the formation of a Ce-Zr-O solid solution, as assumed by the **Ni/Ce$_{0.5}$Zr$_{0.5}$** XRD result.

The study by XPS of nickel species is highly complex, since many environments and several oxidation states can co-exist. Thus, Figure 4.3B displays the registered Ni 2$p_{3/2}$ signal for all catalysts. Three peaks can be detected in the spectrum of the NiO sample. The main peak centered at ca. 854 eV is attributed to stoichiometric Ni^{2+} species, while the one at 856 eV has been linked to Ni^{2+} vacancies, overoxidized Ni^{3+} species or to non-local screening mechanism [9–12]. Moreover, the peak centered at 861 eV has been also related to defective species, which involve a charge transfer ligand-metal [9–12]. The same contributions were detected for the NiO-CeO_2 and NiO-CeO_2-ZrO_2 catalysts, but slightly blue shifted due to the interaction of Ce-Ni or Zr-Ni (electronic Ni transfer to Ce or Zr) [2,13]. Regarding the three catalysts containing Ni-Ce-(Zr), it can be observed how the catalyst with the lowest zirconium loading has the lowest relative intensity of the peaks at 856 and 861 compared to the main one: **Ni/Ce$_{0.9}$Zr$_{0.1}$** < **Ni/Ce$_{0.5}$Zr$_{0.5}$** < **Ni/Ce**. To conclude, Table 4.3 exhibits the amount of nickel near the surface and clarifies that Ni is similarly exposed in all samples and that the Ni-loading is higher in the near surface than in the bulk.

Figure 4.3C exhibits the Ce 3*d* core level spectra of all prepared samples. Both Ce^{3+} and Ce^{4+} species are present in all spectra, the presence of Ce^{4+} being higher due to the calcination of the samples. Ce^{3+} binding energies (BE) were located at 884.4 eV and 902.7 eV, while BE for Ce^{4+} were at 882.2 eV, 900.6 eV, 888.6 eV, 907.5 eV, 898.0 eV and 916.4 eV [2]. Deconvoluting the peaks, it can be observed that the addition of zirconium decreases the amount of Ce^{3+}. In fact, the Ce^{3+}/ Ce^{4+} ratio changes from 0.23 for the **Ni/Ce** sample to 0.11 for the **Ni/Ce$_{0.5}$Zr$_{0.5}$**. Furthermore, the incorporation of Zr did not involve any red or blue shifts of the BEs of the Ce^{3+} and Ce^{4+} contributions [8]. Hence, it can be concluded that the presence

of nickel results in the inverse effect expected in Ni-free materials of Ce-Zr-O. In this case, the presence of Ce^{3+}, which leads to an increase in oxygen vacancies and encourages oxygen mobility, is lower for the samples containing zirconium [14].

To finish the XPS analysis, Zr 3*d* spectra are shown in Figure 4.3D. These spectra have been deconvoluted into two contributions, the first one at 181.5 eV and the second one at 184 eV for the split of the spin orbits Zr $3d_{3/2}$ and Zr $3d_{5/2}$, respectively. The obtained values are lower than those reported for ZrO_2 (182.5 eV) [15] and Ni-Ce-Zr systems [8], but they are similar to those described for the systems with Ce-Zr solid solutions [16,17]. This is in accordance with the XRD findings studied above. Signals belonging to samples with the highest zirconium content suffered a red shift of 0.4 eV, implying an electron transfer from cerium or nickel to zirconium [13].

Table 4.3 collects information about the relative atomic concentrations calculated by the XPS data. From Table 4.3 it can be inferred that nickel is mostly located on the catalysts' surface. In the same way, cerium is more superficially exposed than zirconium, as the Ce/Zr ratio suggests.

Table 4. 3. Relative atomic concentrations calculated by XPS and nominal ones.

	Ni/Ce		**Ni/Zr**		**Ce/Zr**		**Ni/(Ce+Zr)**		**Ni[a]**		**Ce^{3+}/Ce^{4+}**
Catalyst	**XPS**	**Nom**	**XPS**	**Nom**	**XPS**	**Nom**	**XPS**	**Nom**	**SI/MP**	**SII/MP**	
Ni/Ce	0.15	0.11	-	-	-	-	0.15	0.11	0.95	0.45	0.23
$Ni/Ce_{0.9}Zr_{0.1}$	0.15	0.12	2.12	1.11	21.79	9.00	0.14	0.11	0.89	0.23	0.15
$Ni/Ce_{0.5}Zr_{0.5}$	0.25	0.22	0.42	0.22	2.62	1.00	0.16	0.11	1.21	0.29	0.11

HR-TEM images were carried out for all samples in order to analyze their morphology and metallic dispersion, and results are displayed in Figure 4.4.

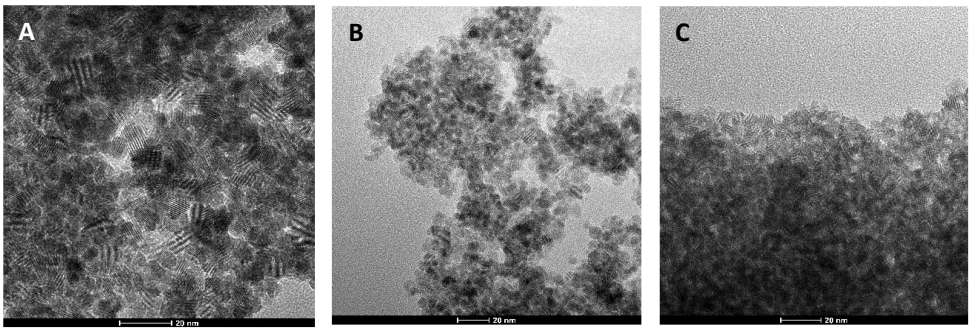

Figure 4. 4. HR-TEM images for (A) Ni/Ce, (B) Ni/$Ce_{0.9}Zr_{0.1}$ and (C) Ni/$Ce_{0.5}Zr_{0.5}$.

It can be inferred that particles presented a uniform and rounded shape in all samples. Furthermore, all catalysts have similar particle size distribution, despite the increase in Zr loading causing a slight decrease in this parameter [18]. In consequence, an increase in zirconium content provokes a decrease in surface area, which can be explained by a change in textural properties as depicted by N_2 isotherms.

EDX-STEM mapping plots with the distribution of nickel, cerium and zirconium are shown in Figure 4.5. A homogeneous distribution of Ni and Ce, with nickel uniformly spread on the Ce-matrix can be noticed in the case of the **Ni/Ce** catalyst (Figure 4.5A). In the same way, Figures 4.5B and C also confirm the good distribution of nickel and cerium in the Ni/CeZr samples. However, some zirconium agglomerates can be detected, which imply the formation of ZrO_2. This effect is more visible in the catalyst with the highest zirconium content (**Ni/$Ce_{0.5}Zr_{0.5}$**). From XRD and TEM results, it can be concluded that zirconium is present in **Ni/$Ce_{0.5}Zr_{0.5}$** as both Ce-Zr-O solid solution and amorphous ZrO_2. Similarly, zirconium is mainly present in the ceria structure in case of **Ni/$Ce_{0.9}Zr_{0.1}$** (Figure 4.5B), but also in the mixed Ce-Zr-O and as amorphous zirconium dioxide.

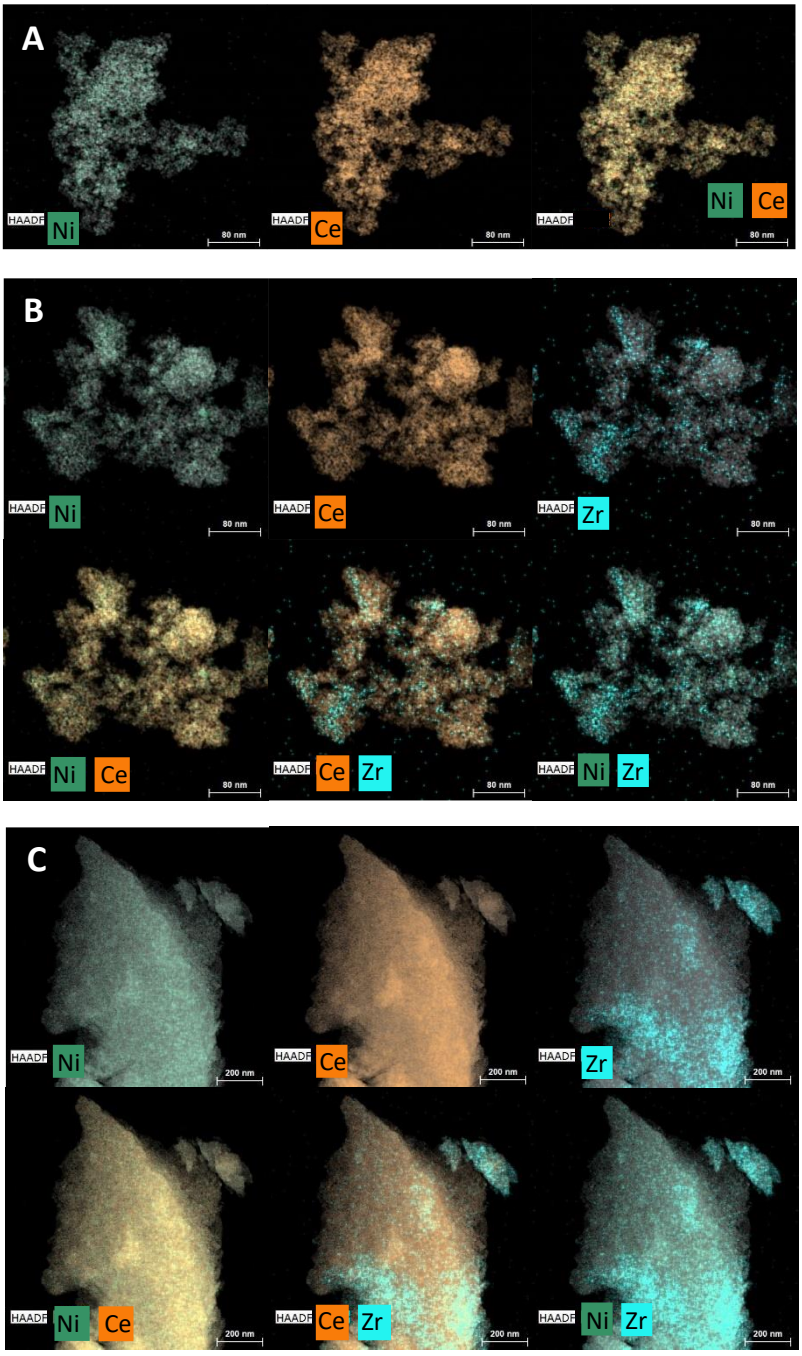

Figure 4. 5. EDX-STEM images with the distribution of different chemical elements for (A) Ni/Ce, (B) $Ni/Ce_{0.9}Zr_{0.1}$ and (C) $Ni/Ce_{0.5}Zr_{0.5}$.

All NiCeZr catalysts were tested in the oxidative dehydrogenation of ethane assisted by nitrous oxide. Ethane and carbon dioxide were the only detected reaction products. Figure 4.6A displays the selectivity to ethylene as a function of ethane conversion for every catalyst. It can be observed that selectivity to ethylene is ca. 60% for the base catalyst (**Ni/Ce**) at low conversions. As conversion increases, the selectivity decreases as a result of the overoxidation of ethylene and its transformation into carbon dioxide [19,20]. The same tendency can be spotted for the catalysts containing zirconium. However, selectivity at low conversions change depending on the catalyst composition, being much higher for the catalyst with the lowest Zr loading. Figure 4.6B shows the variation of both reaction rate and selectivity at isoconversion conditions of all samples. It can be inferred that a partial replacement of cerium by a small amount of zirconium (10%) leads to the highest increase in selectivity. Nevertheless, olefin formation significantly decreases if zirconium content is increased further. In fact, sample **Ni/$Ce_{0.5}Zr_{0.5}$** has the worst catalytic performance of all studied catalysts, including the Zr-free sample. In the same way, catalytic activity follows the same tendency with increasing loading of zirconium. **Ni/$Ce_{0.9}Zr_{0.1}$** was again the catalyst with the highest reaction rate, meaning that this catalyst had the highest yield to ethylene among all tested catalysts. Therefore, a more thorough study of the most efficient catalyst was carried out.

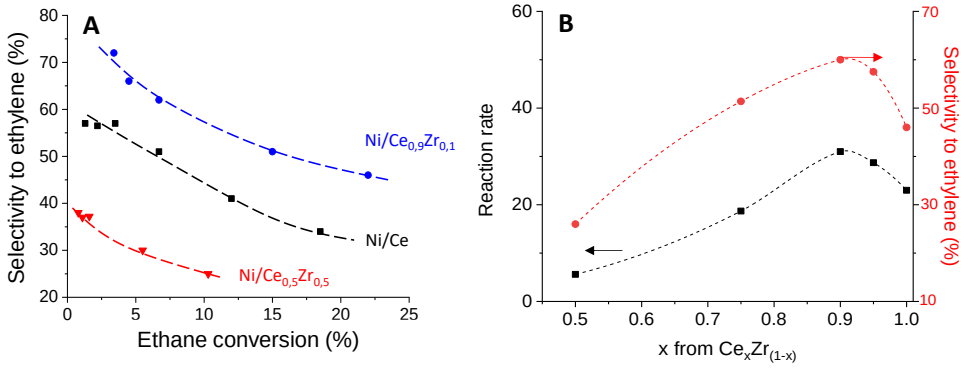

Figure 4. 6. (A) Selectivity to ethylene as a function of ethane conversion at 400°C with a feed of $C_2H_6/N_2O/He$: 5/10/85 molar ratio and using different contact times. (B) Relationship between the Ce/(Ce+Zr) ratio and the reaction rate (in g C_2H_6 kg cat^{-1} h^{-1} determined at 400°C, $C_2H_6/N_2O/He$: 5/10/85 molar ratio, 80 g_{cat} h mol $_{C2H6}^{-1}$); and the selectivity to ethylene (at 400°C, $C_2H_6/N_2O/He$: 5/10/85 molar ratio, isoconversion conditions of 10%).

Figure 4.7A displays the evolution of the selectivity to ethylene with ethane conversion at 400°C using a feed consisting of 5% ethane and different nitrous oxide concentrations for the **$Ni/Ce_{0.9}Zr_{0.1}$** catalyst. Overall, curves of selectivity to ethylene vs. ethane conversion do not suffer significant changes with different N_2O concentrations. However, it can be said that, for a given ethane conversion, olefin selectivity decreases as nitrous oxide concentration gets higher. It could be argued that these slight differences in selectivity could be attributed to the initial olefin formation, and not to the overoxidation of ethylene.

The reaction of oxidative dehydrogenation of ethane has been traditionally studied using molecular oxygen as an oxidant, as reported by literature. Therefore, a study comparing both O_2 and N_2O as oxidizing agents has been conducted, and results are shown in Figure 4.7B.

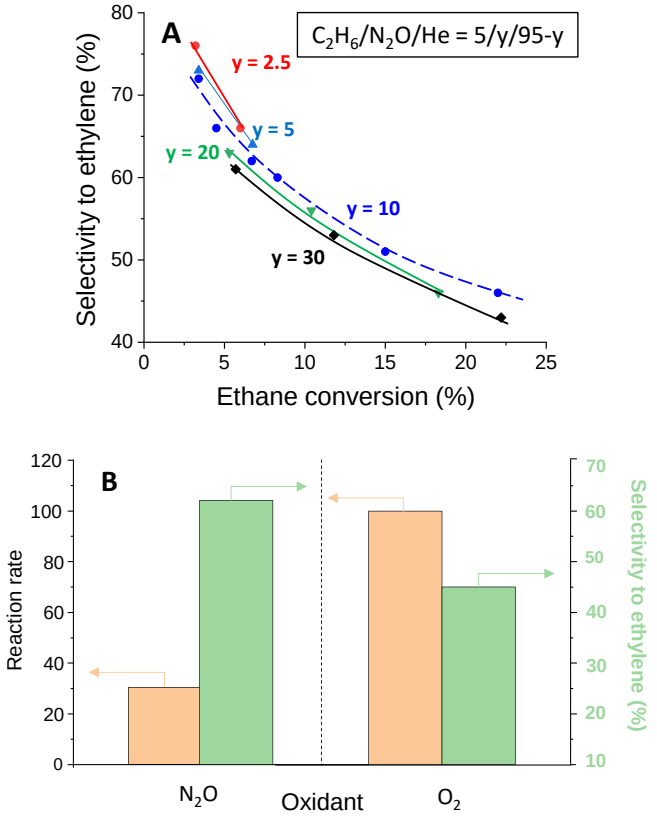

Figure 4. 7. (A) Variation of the selectivity to ethylene with ethane conversion at 400°C with a feed of $C_2H_6/N_2O/He$: 5/y/95-y molar ratio and using different contact times for the $Ni/Ce_{0.9}Zr_{0.1}$ catalyst. (B) (left) Reaction rate using N_2O ($C_2H_6/N_2O/He$: 5/10/85 molar ratio) or O_2 ($C_2H_6/O_2/He$: 5/5/90 molar ratio) as oxidizing agents (in g $C_2H_6 \cdot kg\ cat^{-1} \cdot h^{-1}$ determined at 400°C, $C_2H_6/N_2O/He$: 5/10/85 molar ratio, 80 $g_{cat} \cdot h\ mol_{C2H6}^{-1}$); (right) Selectivity to ethylene using N_2O ($C_2H_6/N_2O/He$: 5/10/85 molar ratio) or O_2 ($C_2H_6/O_2/He$: 5/5/90 molar ratio) as oxidizing agents (400°C, isoconversion of 10%).

The same concentration of oxygen atoms has been used in both reactions in order to carry out the comparative study ($C_2H_6/N_2O/He$: 5/10/85 molar ratio or $C_2H_6/O_2/He$: 5/5/90 molar ratio). From Figure 4.7B it can be inferred that the use of molecular oxygen leads to a greater ethane transformation, the catalytic activity being almost 3 times higher than that reached using N_2O. On the other hand, at isoconversion conditions, selectivity to ethylene is approximately 15 points higher when using N_2O than when using oxygen. It could be argued that the active NiO sites present a lower oxidation state when nitrous oxide is used as an oxidant due to its

milder oxidizing character, although further characterization would be necessary to corroborate this statement. This could explain the higher selectivity to ethylene with N_2O, since overstoichiometric nickel oxide favors the formation of carbon oxides [21]. A similar trend has been previously reported in vanadium-based catalysts [22]. Here, with temperatures higher than 500°C, reduced VO_X surface species were reoxidized more slowly by N_2O than by molecular oxygen. Hence, the amount of active and unselective oxygen species was lower due to the VO_X surface species being in a more reduced state.

A stability test of the **Ni/$Ce_{0.9}Zr_{0.1}$** catalyst was also conducted (Figure 4.8). After 8h at 400°C, both ethane conversion and selectivity to ethylene remained constant. Figure 4.2B shows that the sample did not present appreciable changes in its crystalline phase, confirming the good stability of this sample. Furthermore, additional characterization of the fresh and used catalyst is shown in Table 4.4. Neither the mean ceria crystallite size nor the surface area experienced significant changes after 8h of reaction.

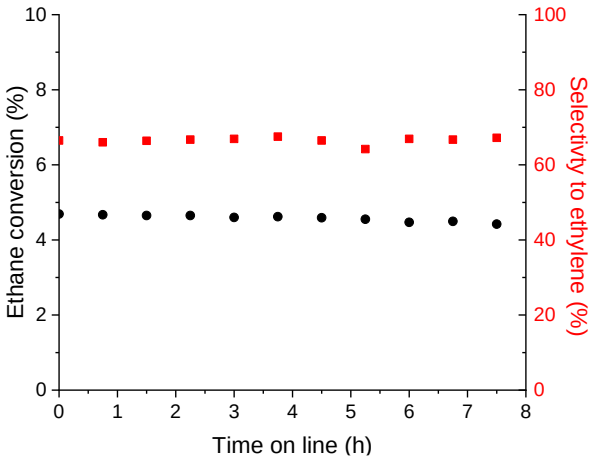

Figure 4. 8. Selectivity to ethylene and ethane conversion as a function of the time on line for the $Ni/Ce_{0.9}Zr_{0.1}$ catalyst. Reaction conditions: 400°C, feed consisting of $C_2H_6/N_2O/He$: 5/10/85 molar ratio and a contact time of 80 g_{cat}·h $(mol_{C2H6})^{-1}$.

Table 4. 4. Crystallite size and surface area of fresh and used Ni/ $Ce_{0.9}Zr_{0.1}$.

State	Crystallite size Ceria (nm)[a]	Surface area (m^2 g^{-1})
FRESH	6.8	91
USED	6.9	89

[a] estimated by XRD

The decomposition of nitrous oxide without ethane was also carried out to assess if the presence of ethane enhanced N_2O conversion. Results are shown in Figure 4.9.

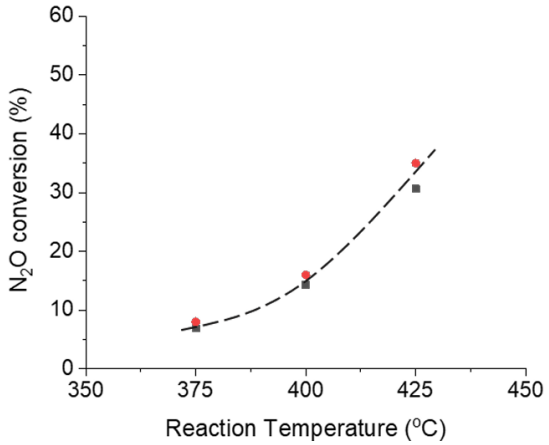

Figure 4. 9. Nitrous oxide conversion as a function of the reaction temperature: influence of the presence of ethane in the feed. Reaction conditions: 0.5 g of catalyst, total flow of 50 ml·min^{-1}, feed consisting of N_2O/C_2H_6/He: 10/0/90 molar ratio (●, experiments without ethane) or 10/5/85 molar ratio (■, experiments with ethane).

From Figure 4.9 it can be concluded that the presence of ethane does not improve the activation of the N_2O molecule, as conversion remains almost the same for every studied temperature regardless of the feed being used. In fact, at 400°C nitrous oxide conversion was ca. 16% in both cases. It has been reported that the alkane usually has a positive effect when the employed alkane/N_2O ratio is high, due to its reducing character [23]. However, the low alkane to nitrous oxide ratio employed in this study might be the reason for not observing any effect.

Considering the redox mechanism involved in the ODH reaction and the corresponding electron transfer, a thorough electrochemical study of all catalysts was carried out. For this purpose, electrochemical impedance spectroscopy measurements were performed. This way, it is possible to know the resistance offered by each sample to charge-transfer processes. Figure 4.10 illustrates the Nyquist and Bode plots extracted from EIS data. Two unfinished semicircles can be spotted in the Nyquist diagram in Figure 4.10A, which correspond to two time constants in the Bode-Phase plot shown in Figure 4.10B. The first semicircle, which is obtained at high/intermediate frequencies, can be related to the charge-transfer processes of the catalyst/electrolyte interface. Therefore, this would provide information about the active surface of the catalyst. On the other hand, at low frequencies the semicircle is attributed to the total resistance of the catalysts, this being the joined response of the bulk oxide (not active part composed by ceria or ceria-zirconium mixed oxide) and the catalytic oxide layer (nickel oxide + cerium/zirconium oxides). Usually, the bigger the semicircle, the higher resistance of the electrochemical process associated with it.

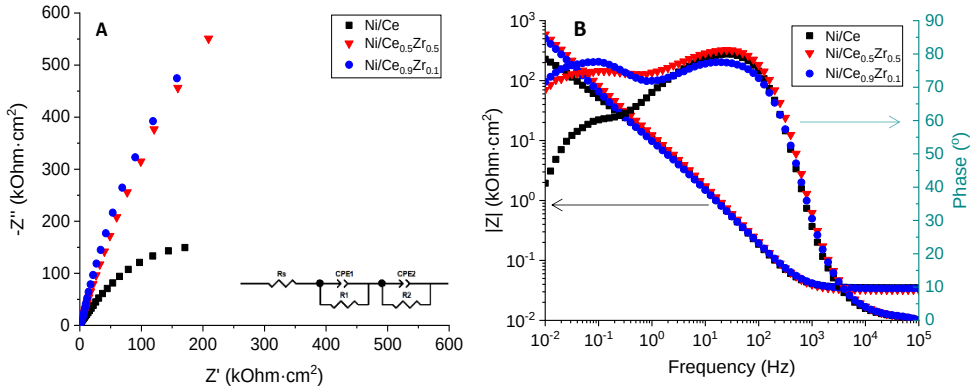

Figure 4. 10. (A) Nyquist and (B) Bode plots for Ni-CeO_2-ZrO_2 catalysts.

According to Figure 4.10A, the **Ni/Ce** sample presents the lowest total resistance value. However, an electrical equivalent circuit with two parallel R-C time

constants in series (inset) was used to fit the EIS data and obtain a better correlation between the electrochemical and catalytic properties. The R_1-CPE_1 is attributed to the outer active oxide layer, thus R_1 refers to the resistance of each sample. Moreover, the second R_2-CPE_2 is related to the bulk of the catalyst. Resistance of the electrolyte (R_S) is obtained at high frequencies in the Bode-module plot and remains constant for every sample. It must be noted that CPEs were used to consider the heterogeneities of the catalysts [24]. For all fittings, the obtained chi-squared (χ^2) values were lower than 10^{-3}, indicating the validation of the chosen circuit. Results of the data fitting for all samples are presented in Table 4.5.

Table 4. 5. R_T (from Bode-module plots) and R_1(from EIS fitting) for each catalyst.

Catalyst	R_T (kOhm·cm^2)	R_1 (kOhm·cm^2)
Ni/Ce	227.0	2.57
Ni/Ce$_{0.9}$Zr$_{0.1}$	500.0	2.46
Ni/Ce$_{0.5}$Zr$_{0.5}$	589.5	2.43

When analyzing R_1, it can be observed that all values are very similar. However, some differences can be spotted in the Bode-phase diagrams in Figure 4.10B. For instance, the **Ni/Ce$_{0.9}$Zr$_{0.1}$** sample has a higher phase angle (ca. 80°) than the **Ni/Ce** sample (ca. 60°). This suggests a more uniform and non-defective inner CeO_2 layer in the catalyst with Ce/Zr = 9. Maybe, this characteristic can be related to the higher olefin formation.

Further electrochemical characterization was carried out performing Mott-Schottky measurements to all samples (Figure 4.11). All Mott-Schottky plots present a positive slope, meaning that all samples possess a n-type semiconductor character. Therefore, the typical n-type character of cerium or cerium/zirconium oxides is not disturbed by the small amount of nickel incorporated into the catalysts. In this type of semiconducting materials, the main defects are oxygen vacancies (V_O^X). Using Eq.

3.8, concentration of these defects can be calculated for each catalyst from the slope of each plot.

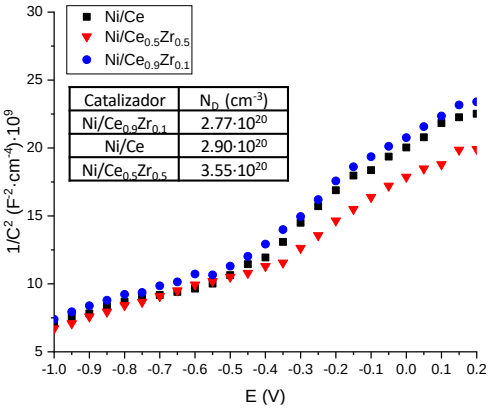

Figure 4. 11. Mott-Schottky plots for the Ni-CeO_2-ZrO_2 catalysts.

Inset of Figure 4.11 shows the concentration of oxygen vacancies of each catalyst, being **$Ni/Ce_{0.9}Zr_{0.1}$** the sample with the lowest concentration. First, it is important to highlight that there are two types of oxygen species that take part in the ODH reaction: electrophilic oxygen species (O^-), which have been related to total oxidation reactions and the formation of carbon oxides; and nucleophilic species (O^{2-}), which favor partial oxidation reactions that lead to the selective formation of ethylene [25–27]. The latter oxygen species are the most abundant in n-type semiconducting materials. However, oxygen vacancies involved in these catalytic systems are created from the transfer of an oxygen atom in a normal site of the lattice (O^{2-}/O_O^X) to the gaseous state, as Eq. 4.1 explains:

$$O_O^X \rightarrow V_O^X + 2e^- + \frac{1}{2}O_2 \qquad \text{Eq. 4. 1}$$

Therefore, a competition exists between the nucleophilic species and oxygen vacancies. For this reaction, catalysts with n-type character should be used in order to obtain a high selectivity towards ethylene. However, an excessive n-type character (high concentration of oxygen vacancies) would mean that nucleophilic oxygen

species are lost, and this would lead to a low ethylene formation rate [28]. Hence, the high oxygen vacancy concentration of **Ni/Ce$_{0.5}$Zr$_{0.5}$** would explain its low selectivity to ethylene during the N_2O-ODH. In the same way, a higher concentration of these oxygen species caused by a lower number of defects would result in enhanced ethylene formation, as **Ni/Ce$_{0.9}$Zr$_{0.1}$** results prove.

Nevertheless, active and selective sites taking part in the ethane oxidative dehydrogenation assisted by nitrous oxide are those belonging to nickel. In fact, pure CeO_2 is both little active and unselective in the formation of ethylene [29]. Interestingly, according to Table 4.3, the catalyst with the lowest loading of zirconium is that with the lowest concentration of defective nickel surface sites on the near surface. It is noteworthy that nickel oxide presents oxygen vacancies as the main defect, since it is a p-type semiconducting material. Hence, it can be concluded that the most selective samples towards ethylene are those with less oxygen vacancies, like the case of **Ni/Ce$_{0.9}$Zr$_{0.1}$**. Moreover, the **Ni/Ce** catalyst presents the highest concentration of non-stoichiometric surface Ce^{3+}, species associated with surface oxygen vacancies, which have a negative effect on ethylene production. On the other hand, the electrochemical study (as shown by the Mott-Schottky plot) reveals that the sample with the highest concentration of surface defects is **Ni/Ce$_{0.5}$Zr$_{0.5}$**. Despite the apparent contradiction, it can be explained by the fact that the surface of these catalysts is not only composed of cerium oxide but also of nickel and zirconium sites. Therefore, the electrochemical study considers all types of oxygen vacancies, not just those surrounding cerium.

In conclusion, when compared to zirconium-free NiO-CeO_2 catalysts, the addition of small amounts of zirconium improves the selectivity towards ethylene in the oxidative dehydrogenation of ethane assisted by nitrous oxide. The presence of fewer electrophilic oxygen species from cationic defective nickel sites and anionic ceria sites is believed to be the main reason for this catalytic result.

4.2 Valorization of N_2O by oxidative dehydrogenation of ethane over promoted NiO based catalysts

Despite having improved the selectivity to ethylene of nickel oxide supported on ceria, the catalytic performance, especially the olefin formation of the optimal Ni/CeZr catalyst, is still unsatisfactory. Therefore, new catalyst formulations have been proposed. Pure NiO catalysts have been reported to be active ethane ODH assisted by oxygen. In spite of having low selectivity towards olefin formation, the results of the ODH assisted by O_2 can be significantly improved by modifying the synthesis method. Therefore, a systematic study has been conducted in the following section to analyze the influence of different promoters on the catalytic results of NiO-based catalysts during the ODH of ethane using N_2O as an oxidant.

Taking into account that alkali and earth alkali have a negative effect in the O_2-assissted ODH of ethane, promoters have been carefully selected to dope the NiO-based catalysts [30]. After calcination in air, the oxidation state of all promoters was established in 3+ or higher. Physicochemical properties of these catalysts are displayed in Table 4.6. **NiO-I** is referred to pure nickel oxide synthesized with oxalic acid, in a similar way that the promoted catalysts, while $\mathbf{NiO_{ref}}$ is just nickel oxide obtained from direct calcination of nickel nitrate. Unpromoted catalysts present both the lowest surface area values, being 18.5 $m^2 \cdot g^{-1}$ for **NiO-I** and 10.7 $m^2 \cdot g^{-1}$ for the reference catalyst. Therefore, the addition of oxalic acid in the synthesis results in an increase of the surface area, since the catalyst synthesized with oxalic acid has a surface area ca. 75% higher than $\mathbf{NiO_{ref}}$. Surface area values increase even further (40-70 $m^2 \cdot g^{-1}$) when promoters become involved. It is believed that the smaller nanoparticle formation is caused by the worse crystallization of the nickel oxide phase due to the incorporation of a heteroatom [31]. Among the promoted catalysts, the lowest surface areas correspond to samples containing bismuth and iron (40-45 $m^2 \cdot g^{-1}$), whereas samples with cerium, titanium and niobium present the highest values (64-68 $m^2 \cdot g^{-1}$).

Table 4. 6. Physicochemical properties of the NiO-based catalysts.

Catalyst	S_{BET} ($m^2\ g^{-1}$)	H_2-TPR T_{max} (°C)[b]	H_2-TPR T_{onset} (°C)[b]	NiO Crystal size (nm)[c]
NiO-I	18.5	305 (329, 358)	241	17.8
(Bi)NiO	41.3	313	242	11.8
(Fe)NiO	44.6	(313) 359	265	12.1
(Ce)NiO	66.7	337	260	9.7
(Nb)NiO	64.6	373	260	10.5
(In)NiO	55.5	397	250	9.8
(Ti)NiO	67.5	424	291	9.8
NiO_{ref}	10.7	(290) 386	261	24.8

[b] Temperature of the maximum reduction (T_{max}) and temperature of onset (T_{onset}) during the TPR-H_2 experiments; reduction temperatures for other shoulders appear in parenthesis; [c] Mean crystallite size determined by XRD using the Scherrer equation considering the peaks at 2θ= 37 and 43° of NiO (JCPDS: 47-1049).

Figure 4.12A shows the XRD patterns for all synthesized catalysts. In all samples, the dominant crystalline phase is the face-centered cubic NiO phase (JCPDS 47–1049). Mean crystallite size of cubic NiO phase was estimated for each sample using the Scherrer equation and results are gathered in Table 4.6. The **NiO_{ref}** catalyst has the largest mean crystallite size (ca. 25 nm). Introducing oxalic acid during the synthesis causes a reduction in the mean crystallite size until approximately 18 nm, agreeing with the observed increase in surface area. Doping with different elements leads to an additional reduction in crystallite size, ranging from 9.7 to 12.1 nm, depending on the promoter. NiO remains the only crystalline phase identified in the undoped catalysts and in those doped with iron and niobium. However, low-intensity peaks belonging to Bi_2O_3 (JCPDS: 78-1793), In_2O_3 (JCPDS: 06-0416), CeO_2 (JCPDS: 34-0394) and anatase TiO_2 (JCPDS: 21-1272) are identified in the catalysts doped with Bi^{3+}, In^{3+}, Ce^{4+} or Ti^{4+}, respectively.

Both ethane oxidative dehydrogenation and nitrous oxide decomposition are redox reactions that take place on the surface of the nickel oxide-based catalysts [27,30,32–41]. Therefore, Temperature Programmed Reaction measurements are

useful in order to study the reducibility of these materials, considering that the limiting step at high reaction temperatures during the O_2-ODH is the reduction part [41,42]. TPR profiles are exhibited in Figure 4.12. Maximum temperature varies from 305 to 425°C depending on the catalyst. For instance, T_{max} for the reference NiO catalyst is located at 386°C, whereas for the **NiO-I** the peak is shifted to 305°C. This shift is attributed to the addition of oxalic acid, which results in an increase in the reducibility of the catalyst, likely due to the easier reduction of smaller nickel oxide crystallites. Moreover, the two shoulders of **NiO-I** at 329 and 359°C have been attributed to the reduction of bulk nickel oxide. It has been reported that distinct shoulders are visible due to the differences in reducibility of different NiO species (including non-stoichiometric NiO or nickel oxide with distinct crystallite size)[43,44]. Thus, the bigger crystallite size of **NiO_{ref}** must be the reason for the lower reducibility of this sample.

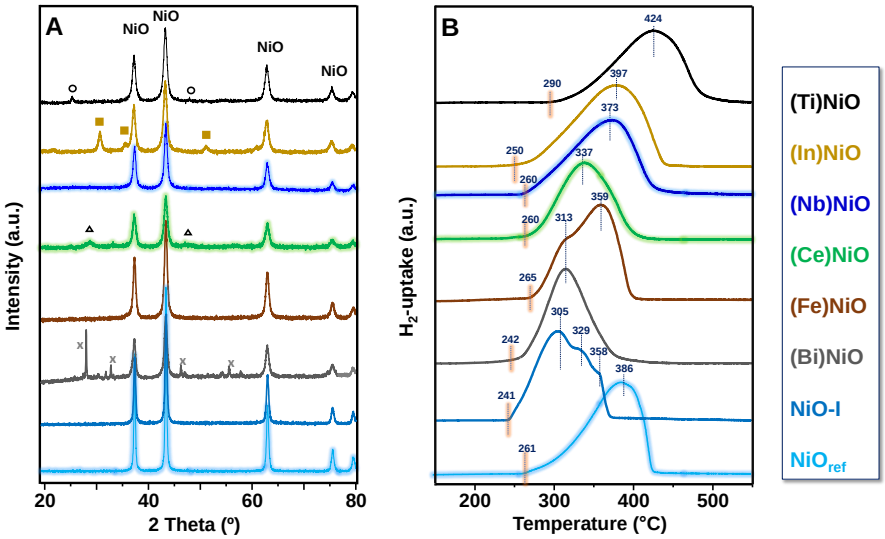

Figure 4. 12. (A) XRD patterns and (B) Temperature Programmed Reduction (H_2-TPR) profiles of unpromoted and promoted NiO catalysts. T_{max} also included in H_2-TPR profiles. Other crystalline phases different from NiO have been detected in Figure 4.12A: Bi_2O_3 (x), CeO_2 (**Δ**), In_2O_3 (■) and anatase TiO_2 (o).

Furthermore, reduction profiles significantly change when promoters are added to the nickel oxide catalyst prepared with oxalic acid. The presence of Fe^{3+}, Nb^{5+} and, especially, Ti^{4+} shifted the reduction bands to higher temperatures. It is believed that this shift is caused by the interaction between nickel oxide particles and the promoters, which are either incorporated to the lattice or present as promoter oxide crystalline phase. However, no correlation has been established between the different shifts with factors such as the valence of the dopants, cation radius, the formation of promoter oxide phases or the surface nickel species.

X-ray photoelectron spectroscopy analysis (XPS) was carried out to study the near surface properties of the prepared catalysts. Regarding the surface nickel, Ni $2p_{3/2}$ core level spectra of representative samples are shown in Figure 4.13. All samples present three deconvoluted peaks at ca. 853.5, 855.7 and 860.5 ± 0.3 eV, which have been reported in literature as the main peak (853.3 ± 0.3 eV) and satellite peaks at 855.4 ± 0.3 eV (Satellite I) and 859.9 ± 0.3 eV (Satellite II) [45]. Specific peak values are gathered in Table 4.7.

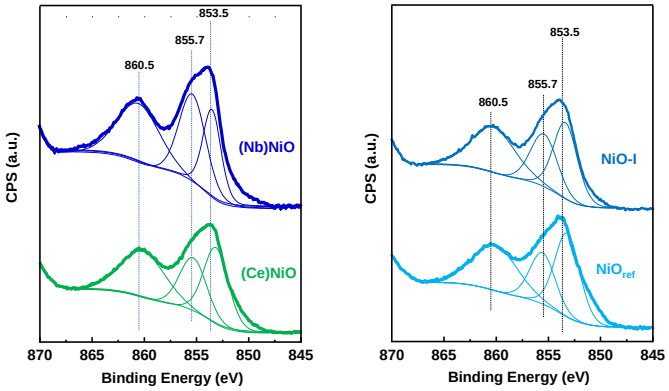

Figure 4. 13. Ni $2p_{3/2}$ XPS spectra of representative promoted and unpromoted NiO catalysts.

Satellite I signal has been related to different species such as Ni^{2+}-OH [10], Ni^{2+} vacancies [12] or a result of non-local screening mechanism [11]. The presence of different nickel species at a given BE makes an accurate interpretation of the XPS results complicated. Differences in the local environment of nickel sites of this

sample can be the reason for this event, as will be proved later with further characterization.

Table 4. 7. XPS spectra deconvolution of the Ni $2p_{3/2}$ core level and quantitative analysis of S1/Main peak of representative promoted and unpromoted NiO catalysts.

Sample	**Ni $2p_{3/2}$**		
	Main	Satellite 1	Satellite 2
NiO_{ref}	853.3	855.3	860.2
NiO-I	853.3	855.4	859.9
(Nb)NiO	853.5	855.7	860.5
(Ce)NiO	853.1	855.3	860.1

Furthermore, O1*s* core level signal for the same representative catalysts is depicted in Figure 4.14. Binding energy values are also displayed in Table 4.8. The signal at 529 eV is assigned to lattice oxygen species, whereas the one at 531.1eV has been assigned to non-stoichiometric or low coordinated oxygen O^- species and the one at 533.1 eV to OH groups [46,47].

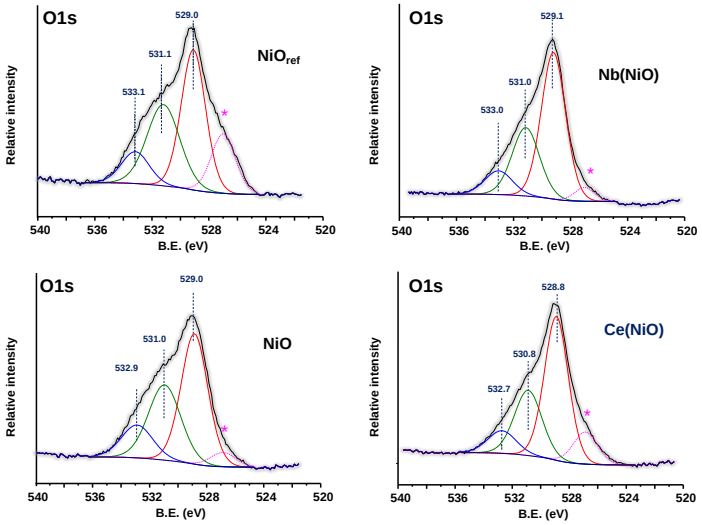

Figure 4. 14. The O1s XPS spectra of representative promoted and unpromoted NiO catalysts. (*) Contribution of the sample holder.

Pure nickel oxide catalysts present a higher contribution of non-stoichiometric surface oxygen species (O^{2-}, O_2^{2-}, or O^-) than **Nb(NiO)** and **Ce(NiO)**, especially the reference sample.

Table 4. 8. XPS results for O1s signal in representative promoted and unpromoted NiO catalysts

Sample	**O1s (BE)** [a]			**Ni/O/Me** [b]	**O/Ni** [b]	**O^-/O_L** [c]
NiO_{ref}	529.0 (48.8%)	531.1 (38.3%)	533.1 (12.7%)	27.4/72.5/0.0	2.6	0.8
NiO-I	529.0 (50.1%)	531.0 (35.0%)	532.9 (14.8%)	38.8/61.2/0.0	1.6	0.7
Ce(NiO)	528.8 (58.6%)	530.8 (30.5%)	532.7 (10.9%)	24.5/66.23/ 9.2	2.7	0.5
Nb(NiO)	529.1 (58.4%)	531.0 (30.7%)	533.0 (10.8%)	28.4/69.36/2.2	2.4	0.5

[a]Values in brackets corresponds to the percent of each specie normalized to the total oxygen species.
[b]Surface composition in molar ratio.
[c]molar ration of low coordinated oxygen species versus lattice oxygen

The determination of the chemical state of metal sites by employing Infrared CO adsorption was used to prove the different environment of the nickel sites outlined above [48]. IR spectra illustrated in Figure 4.15 suggest that promoted catalysts present Lewis sites of higher acid character than those of pure nickel oxide catalysts. This is demonstrated in Figure 4.15 with higher IR bands for **Nb(NiO)** at 2191 and 2179 cm^{-1} and for **Ce(NiO)** at 2161 cm^{-1}, in contrast with the IR bands of unpromoted samples located at 2156-2153 cm^{-1}.

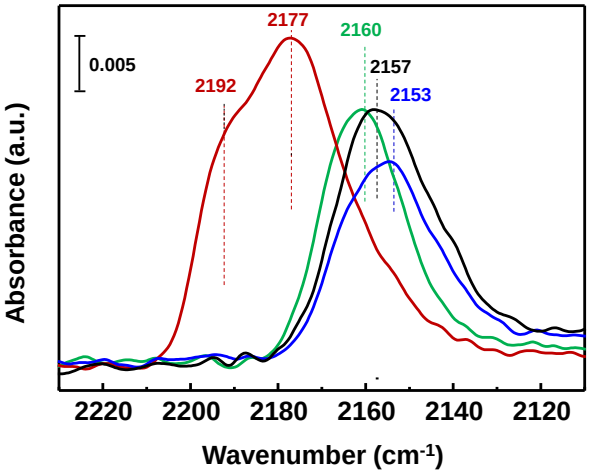

Figure 4. 15. IR spectra of CO adsorption at 0.3 mbar and -176 ºC on Nb(NiO) (red), Ce(NiO) (Green), NiO-I (blue) and NiO_{ref} (black) samples.

A tendency in acid nature of nickel Lewis sites can be established, considering that Lewis acidity is proportional to the CO frequency: **Nb(NiO)** > **Ce(NiO)** > **NiO-I** = **NiO_{ref}**. Therefore, it can be stated that promoters play a very important role on the nature of the nickel species. Previous studies about ethane ODH assisted by oxygen concluded that the valence and acid/base character of metal oxide dopants strongly influenced the nature of the surface sites, affecting the selectivity to ethylene during the reaction [30].

All prepared catalysts were tested in the oxidative dehydrogenation of ethane using N_2O as oxidant. The only carbon containing products detected were ethylene and carbon dioxide. Two representative catalysts (**NiO-I** and **Nb(NiO)**) were also tested in CO oxidation to CO_2, since no CO was detected as a reaction product. Table 4.9 exhibits catalytic results for this reaction. Both samples achieve a CO conversion above 99% at 250°C. Therefore, the ability of these catalysts for CO activation and transformation into CO_2 must have led to the absence of carbon monoxide as a reaction product in the N_2O-ethane ODH[49].

Table 4. 9. Catalytic results of CO oxidation with two representative NiO-based catalysts[a].

Reaction Temperature (ºC)	**CO conversion (%) on NiO-I catalyst**	**CO conversion (%) on (Nb)NiO catalyst**
100	0.99	1.1
150	3.1	3.8
175	15.2	16.3
200	54.8	42.9
225	87.5	78.1
250	>99	>99

[a] Reaction conditions: CO oxidation (0.5%CO/99.5 synthetic air), Catalyst weight =0.2 g, Total flow = 50 ml/min. The only reaction product detected was CO_2.

Catalytic results of all samples in the N_2O-ODH of ehtane are shown in Table 4.10. The **NiO_{ref}** catalyst presents the lowest ethane conversion among all samples, as well as the lowest selectivity to olefin. Ethylene selectivity decreases even further as ethane conversion gets higher, leading to a worse catalytic performance. Nevertheless, both selectivity to ethylene and ethane conversion significantly increase when an appropriate amount of oxalic acid is used during the preparation of the nickel oxide catalyst. In fact, catalytic activity highly increases for **NiO-I** compared to **NiOref**. This improvement is believed to be due to a greater surface area and a smaller crystallize size, as Table 4.6 displays.

Table 4. 10. Catalytic results of NiO based catalysts on oxidative dehydrogenation assisted by N_2O.

Catalyst	Ethane Conversion (%)	Selectivity C_2H_4 (%)	Selectivity CO_2 (%)[b]	Ethylene yield (%)[b]	Catalytic Activity (X<15%)[c,d]	Specific Activity (X<15%)[c,e]	Selectivity to ethylene (X=30%)[f]
NiO-I	51.1	51.8	48.2	26.5	24.4	13.20	60
(Ce)NiO	51.0	57.0	43.0	29.1	27.8	4.16	64
(Bi)NiO	37.7	50.9	49.8	19.2	14.6	3.88	52
(Fe)NiO	27.0	61.7	38.3	16.7	11.0	2.46	59
(In)NiO	34.9	58.3	41.7	20.3	14.3	2.57	60
(Ti)NiO	49.2	67.8	32.2	33.4	24.4	3.62	71
(Nb)NiO	50.2	72.6	27.4	36.5	24.5	3.79	80
NiO_{ref}	18.1	44.0	56.0	8.0	5.49	5.13	37

[a] C_2/N_2O/He: 5/10/85 molar ratio, Reaction temperature = 400 °C. [b] m_{cat} = 0.2 g; Total flow = 50 mL min^{-1}. [c] determined at 400ºC for ethane conversions lower than 15%. [d] in 10^{-3} mol_{C2H6} g_{cat}^{-1} h^{-1}; [e] in 10^{-4} mol_{C2H6} m^{-2} h^{-1}. [f] Selectivity to C_2H_4 (%) at ethane isoconversion of 30% determined at 400 °C (variable contact time).

The incorporation of the different dopants also led to an enhanced performance of nickel oxide-based catalysts. For instance, at isoconversion conditions (30% of ethane conversion) differences in selectivity to ethylene are even more noticeable between the **NiO_{ref}** sample and the doped catalysts. However, the increase in catalytic activity of the promoted catalysts is lower than that experienced when oxalic acid is added, and it varies depending on the nature of the metal oxide promoter. For example, ethane conversion increases by 180% in case of **Nb(NiO)** and **Ce(NiO)**, while it only increases by 50% for **Fe(NiO)**. In addition, considering the specific activity of all catalysts, it can be observed that the improved activity of the oxalic acid-synthesized **NiO-I** is even more obvious. Table 4.10 reveals that **NiO-I** presents a specific activity 3-5 times higher than that of the doped catalysts, having the reference sample an in-between value.

Selectivity to ethylene as a function of ethane conversion for some representative NiO catalysts is depicted in Figure 4.16A. For all samples, a slight decrease in selectivity to olefin can be observed as the ethane conversion increases, which is a consequence of ethylene overoxidation. However, a yield to ethylene of approximately 40% has been reached by using **Nb(NiO)** at non-optimized reaction conditions. Figure 4.16B, on the other hand, displays the results of selectivity to ethylene of all catalysts at 30% conversion and 400°C, which is necessary in order to properly compare all nickel oxide-based catalysts.

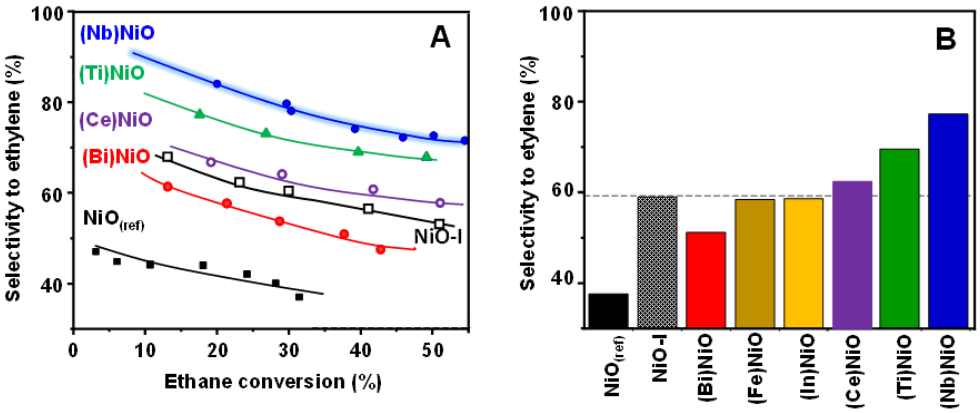

Figure 4. 16. A) Selectivity to ethylene as a function of ethane conversion for representative NiO based catalysts at 400ºC: B**)** Selectivity to ethylene in the N_2O-assisted ODH of ethane at 400ºC, and at isoconversion conditions (30% ethane conversion), for undoped and doped NiO catalysts. Symbols: NiO_{ref} (■); NiO-I (□); (Bi)NiO (●); (Ce)NiO (○); (Ti)NiO (▲); and (Nb)NiO (●).

It is clear that all samples are better than **NiO_{ref}**. Pure nickel oxide treated with oxalic acid presents a 20 point difference in ethylene selectivity. Dopants such as Fe^{3+} and In^{3+} do not have a significant impact on ethylene formation. The addition of bismuth even decreases selectivity to ethylene. However, doping with cerium and, especially, titanium and niobium, results in a remarkable increase in the ethylene selectivity. Therefore, the observed order of selectivity to ethylene is: **NiO_{ref}** < **(Bi)NiO** < **NiO-I**, **(Fe)NiO**, **(In)NiO** < **(Ce)NiO** < **(Ti)NiO** < (**Nb)NiO**.

As has been outlined above, the catalytic behavior of each catalyst could be explained by the reducibility of the nickel sites during the redox mechanism of the ODH reaction (Figure 4.12B). Nevertheless, no correlation has been observed between catalytic activity and the reducibility of the samples, neither with the temperature for maximum hydrogen consumption (TPR_{max}) (Figure 4.17A,B) nor with the onset temperature in the TPR tests (T_{onsets}) (Figure 4.17D,E).

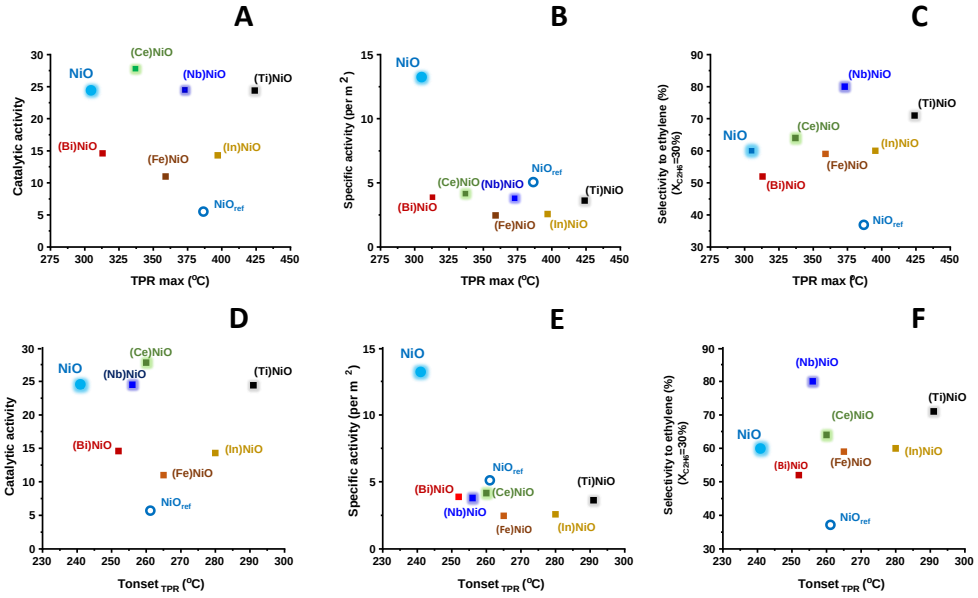

Figure 4. 17. Relationship between (A) the catalytic activity per mass of catalyst, (B) the catalytic activity normalized per surface area and (C) the selectivity to ethylene with the temperature for maximum hydrogen consumption in the TPR experiments. Relationship between (D) the catalytic activity per mass of catalyst, (E) the catalytic activity normalized per surface area and (F) the selectivity to ethylene with the onset temperature in the TPR experiments.
Notes: C_2/N_2O/He: 5/10/85 molar ratio, Reaction temperature = 400 ºC. Catalytic activity per mass or per area has been determined for ethane conversions lower than 15%. Catalytic activity in 10^{-3} mol_{C2H6} g_{cat}^{-1} h^{-1}. Specific activity in 10^{-4} mol_{C2H6} m^{-2} h^{-1}. Selectivity to ethylene determined at 400 ºC, at ethane conversions of 30% (variable contact time).

For some catalysts during O_2-ODH of ethane, easily reducible sites are often associated with unselective electrophilic oxygen species. Hence, the sites with the lowest reducibility are the most selective [40,50]. Again, no relationship has been established between the selectivity to ethylene and the reducibility of the catalysts (Figure 4.17C,F). It could be argued that the different nature of the employed dopants could be one of the reasons for that lack of trend. In the same way, TPR experiments were performed using hydrogen, which is not present in the reaction feed in the ODH reaction. Therefore, further temperature programmed reaction measurements were conducted on representative catalysts for both only nitrous oxide decomposition (Figure 4.18) and the ethane N_2O-ODH (Figure 4.19).

Figure 4.18 reveals that almost no differences exist between samples, since activation of nitrous oxide occurs at low temperatures (below 300°C) for all catalysts. These results suggest that activation of N_2O requires a much lower temperature than that for ethane oxidative dehydrogenation (Figure 4.16).

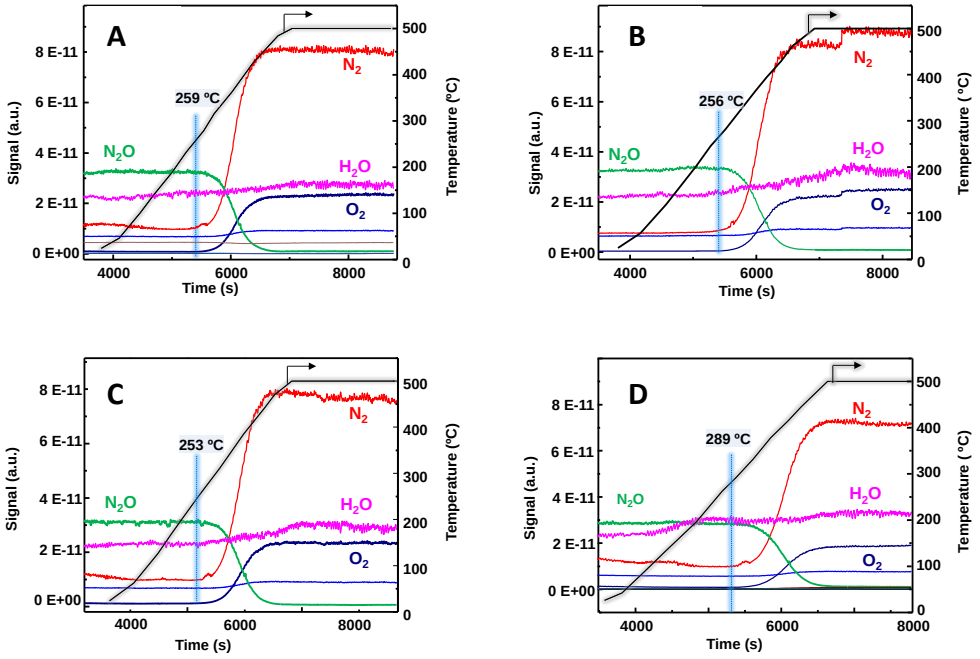

Figure 4. 18. TPR experiments for N_2O decomposition over representative catalysts: (A) NiO-I; (B) (Ti)NiO; (C) (Ce)NiO and (D) (Nb)NiO.

In the same way, Figure 4.19 illustrates that ethane consumption starts at the same temperature as nitrous oxide mitigation and nitrogen formation, being very similar to that for N_2O decomposition in absence of ethane. Additionally, nitrous oxide is totally consumed at temperatures lower than 500°C for all catalysts. In case of both (Ce)NiO and (Ti)NiO hydrogen production is detected once all nitrous oxide has been consumed. On the other hand, no hydrogen is formed in presence of the (Nb)NiO catalyst, even when all the N_2O has been completely consumed.

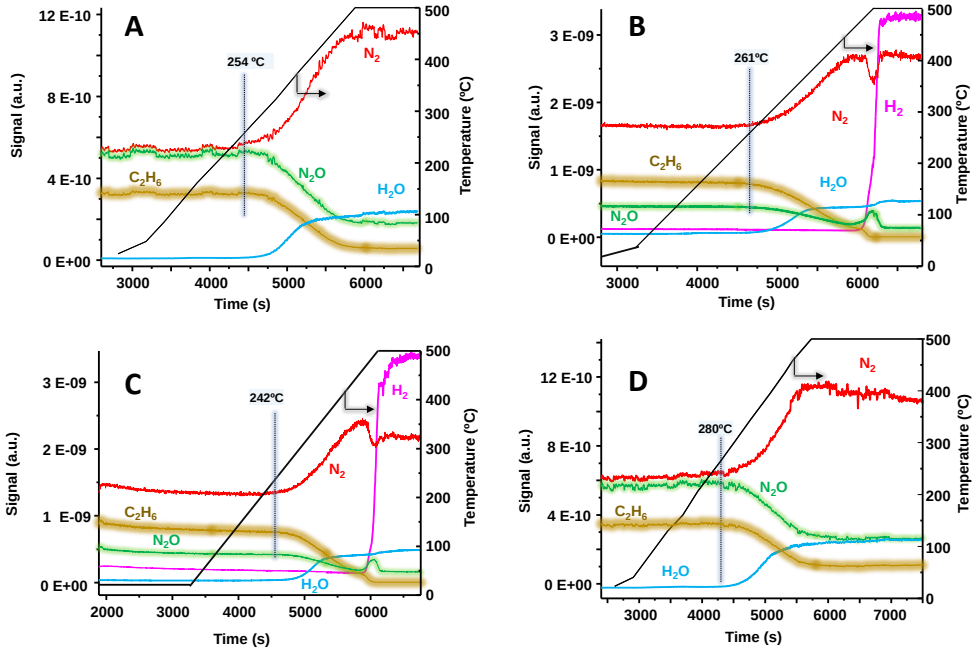

Figure 4. 19. TPR experiments for N_2O/ethane transformation over representative catalysts: (A) NiO-I, (B) (Ti)NiO, (C) (Ce)NiO and (D) (Nb)NiO.

From Figures 4.18 and 4.19, it can be assumed that the activation of nitrous oxide does not appear to be the limiting factor in the oxidative dehydrogenation of ethane assisted by N_2O, since nitrous oxide decomposition occurs at a lower temperature (below 300°C) than ethane ODH (ca. 400°C) (Table 4.10).

Hydrogen formation in presence of some samples raised concerns about stability of the nickel oxide-based catalysts. Stability tests were undertaken for three representative catalysts at 400°C for several hours, monitoring the activity and selectivity. To study the robustness of these catalysts, nitrous oxide conversion needs to be considered, since ethane N_2O-ODH requires catalysts which are able to activate both ethane and nitrous oxide. Thus, the amount of nitrous oxide involved in the transformation of ethane to ethylene during the ODH can be determined by the following equation:

$$C_2H_6 + N_2O \rightarrow C_2H_4 + H_2O + N_2 \quad \text{Eq. 4. 2}$$

Therefore, one molecule of N_2O is needed in order to form one molecule of ethylene. However, carbon dioxide is also formed during the reaction and the nitrous oxide consumption per molecule of reacted ethane in that case is different:

$$C_2H_6 + 7\ N_2O \rightarrow 2\ CO_2 + 3\ H_2O + 7\ N_2 \quad \text{Eq. 4. 3}$$

Here, seven molecules of nitrous oxide are required to obtain two CO_2 molecules from the oxidation of one molecule of ethane. Hence, theoretical nitrous oxide conversion can be calculated from ethane conversion and selectivity to reaction products, considering the resulting stoichiometry. Experimental N_2O conversion was determined by the change in the mols before and after reaction. Theoretical and experimental nitrous oxide conversion match very well for almost all catalysts (Table 4.11).

Table 4. 11. Theoretical and measured N_2O conversion during ethane ODH at 400°C for three representative catalysts.

Catalyst	**Theoretical N_2O conversion (%)**	**Measured N_2O conversion (%)**
NiOref	42	44
(Nb)NiO	66	69
(Ce)NiO	91	84

Figure 4.20 depicts the catalytic results of **NiOref, (Ce)NiO** and **(Nb)NiO**, as well as their XRD patterns before and after use. In case of **NiOref** (Figure 4.20A), both ethane conversion and selectivity to ethylene remained stable after 7h online. Measured nitrous oxide conversion also fits with the estimated one, being the experimental one slightly higher (Table 4.11). Additionally, no changes are detected in the XRD pattern of fresh and used samples: cubic NiO is the only crystalline phase

present. In the same way, no apparent variations are observed in mean crystallite size (24.8 nm for the fresh catalyst and 24.5 nm for the used one).

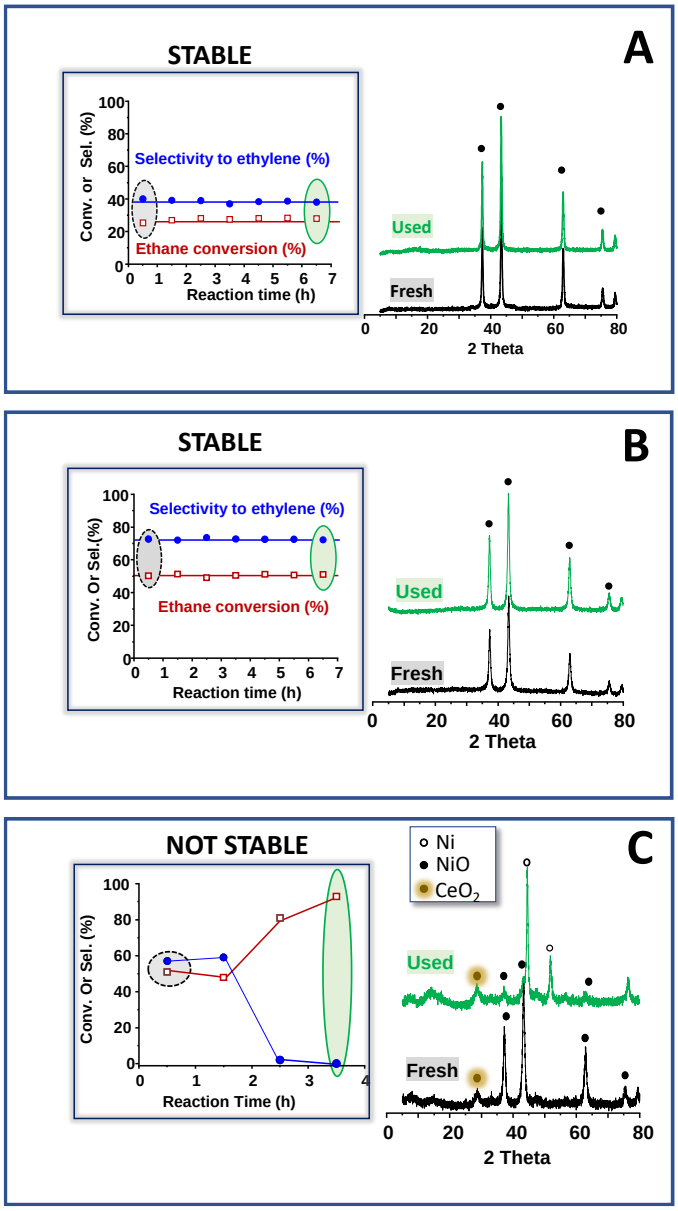

Figure 4. 20. Selectivity to ethylene (•) and ethane conversion (□) at 400 ºC as a function of the reaction time in the N_2O-ODH of ethane (Left graphs). XRD pattern of catalysts both fresh and used after 7 h (Right graphs). Catalysts: **A)** NiO_{ref}; **B)** (Nb)NiO; **C)** (Ce)NiO.

The catalyst promoted with niobium was also tested for 7h and Figure 4.20B also suggests a very stable performance. Both fresh and used catalysts present the same XRD pattern, with a slight increase of the NiO crystallite size after reaction (10.5 nm vs. 11.0 nm). However, (Ce)NiO shows a different behavior (Figure 4.20C). Results of the first analysis exhibit that the achieved ethane conversion was ca. 50%, with 60-65% of selectivity to ethylene and the rest being CO_2. As Table 4.11 illustrates, experimental nitrous oxide conversion was ca. 84%, lower than that required theoretically to obtain the reaction products (ca. 92%). This indicates that the oxygen atoms involved in the product formation come from the lattice of the catalyst, as well as from N_2O. This is in agreement with the drastic change in catalytic performance after 2.5h on line. Ethane conversion increased from 50% to 90%, while selectivity to ethylene significantly dropped from 55% to 0%. Furthermore, the detected reaction products in this situation were carbon dioxide and methane. As a result of the reforming of ethane, hydrogen was also identified as a product. This is in accordance with that observed in Figure 4.19C. The XRD pattern of fresh catalyst shows the presence of mainly cubic NiO with some CeO_2 (JCPDS: 43-1002). On the other hand, diffraction peaks at ca. 44° and ca. 52° in the used sample indicate that the predominant phase after reaction is metallic Ni phase (JCPDS: 4-0850), which is responsible for the reforming reaction. In addition, the reduction of NiO to metallic Ni verifies the exhaustion of the lattice oxygen.

It can be concluded that the nature of the dopant has a direct effect on the relative ethane and nitrous oxide activation. Hence, niobium is considered to be a better dopant than cerium, as it favors the formation of ethylene, which consumes less oxygen than CO_2. At 50% ethane conversion, not all the nitrous oxide is consumed by **(Nb)NiO**, whereas **Ce(NiO)** consumes more oxygen atoms than those provided by the N_2O fed. Therefore, when using the Nb-doped catalyst, stability is achieved due to its ability to activate ethane and N_2O. However, when using **Ce(NiO),** N_2O activation prevails over ethane activation, which leads to CO_2

formation and to the creation of an oxygen poor atmosphere not capable to develop a stable behavior.

In the oxidative dehydrogenation of ethane assisted by oxygen, a correlation exists between the valence of the dopant and the catalytic performance. Generally, when basic promoters (usually low valence elements) are added to an oxide lattice, they force the valence of the nickel site to its highest available valence. On the other hand, acidic promoters, such as high valence elements like niobium, tend to shift the host metal towards its lowest available valence state. Unselective electrophilic oxygen species appear as a consequence of the presence of non-stoichiometric nickel sites, lowering the olefin formation. A relationship has been established between the valence of the dopants and the selectivity to ethylene, this being the higher the valence of the cation dopant, the higher is the selectivity to ethylene [30,36]. This general trend has also been observed in this work, as Figure 4.21 depicts.

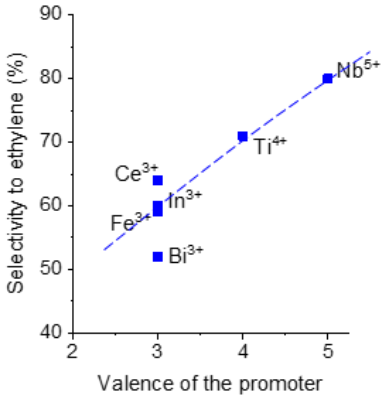

Figure 4. 21. Relationship between the valence of the promoter in NiO-based catalysts and the selectivity to ethylene. Note: Isoconversion (30%), 400ºC, C_2H_6/N_2O/He molar ratio of 5/10/85.

The **Nb(NiO)** catalyst was also tested in the ethane ODH assisted by oxygen for comparative purposes. Figure 4.22 shows the catalytic performance of the Nb-doped catalyst in both N_2O and O_2 atmospheres during the ODH reaction. It is noteworthy that catalytic activity remains almost the same, regardless the oxidant being used (Figure 4.22A), but the selectivity to ethylene remarkably increases at

isoconversion conditions when using nitrous oxide instead of molecular oxygen (Figure 4.22B).

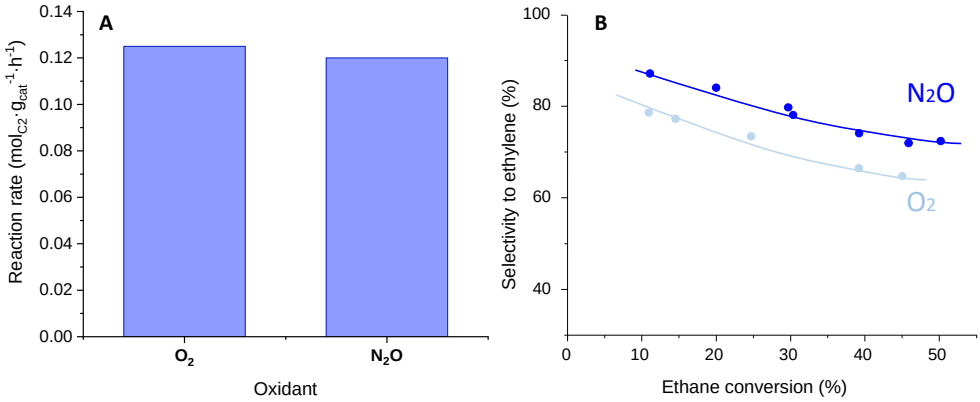

Figure 4. 22. Influence of the type of oxidant on (A) the reaction rate and on the (B) variation of selectivity to ethylene with the ethane conversion for the Nb(NiO) catalyst. Note: T= 425°C, C_2/O_2/He: 5/5/90 or C_2/N_2O/He: 5/10/85 molar ratios and conversions lower than 15% for (B).

A thorough electrochemical study was conducted, due to the mentioned redox mechanism taking place on the catalyst surface during the ethane oxidative dehydrogenation. The intention was to establish a relationship between the electrochemical and catalytic properties of the different catalysts. Some clear correlations have been detected after tests such as electrochemical impedance spectroscopy (Figure 4.23), Mott-Schottky analysis (Figure 4.24) and cyclic voltammetries (Figure 4.25).

Figure 4.23 displays the Nyquist and Bode-module plots extracted from EIS data for each sample.

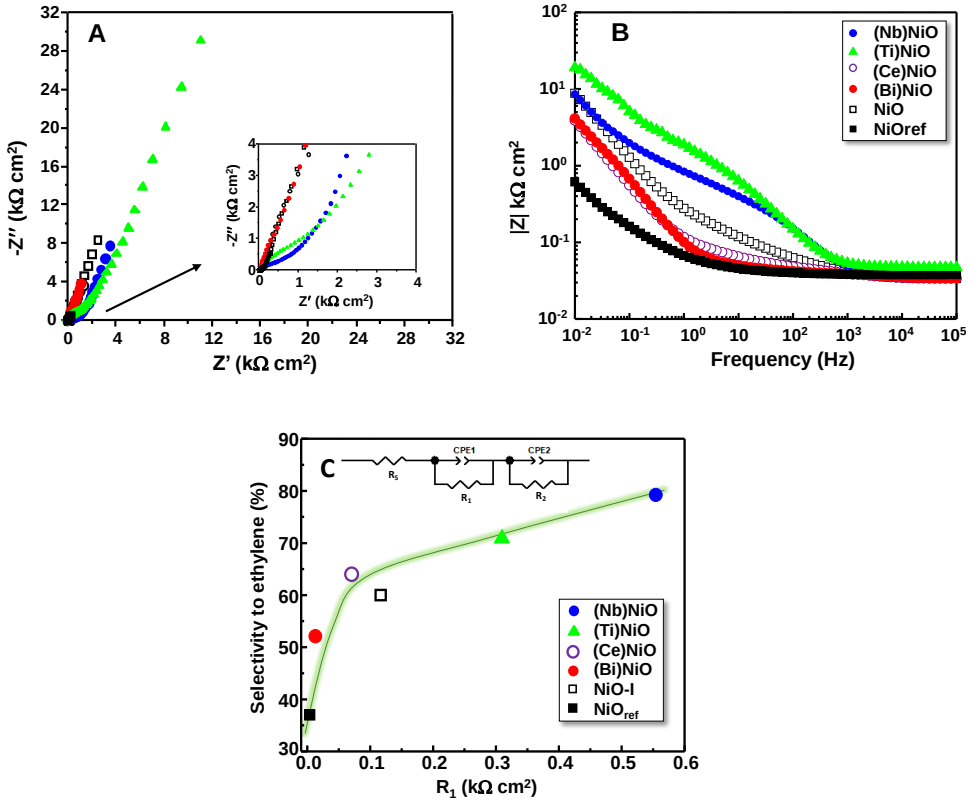

Figure 4. 23. (A) Nyquist and (B) Bode-module plots for all NiO catalysts. (C) Relationship between selectivity to ethylene during ethane oxidative dehydrogenation assisted by N_2O and charge transfer resistance of the active parts of the catalysts (R_1).

Figure 4.23A exhibits two semicircles, at low and high frequencies, indicating the presence of two time constants. Generally, the first semicircle (high frequencies) is associated with the charge transfer response of the oxide/electrolyte interface, while the semicircle at low frequencies is related to the response of the bulk [51,52]. Usually, the active surface of the catalysts can be linked to the response of the charge transfer resistance at the oxide/electrolyte interface [53]. Furthermore, the Bode-module plot depicted in Figure 4.23B presents two different regions. The first, at high frequencies, corresponds to the resistance offered by the electrolyte, whereas the region located at low frequencies is associated with the total resistance

of the catalyst, R_T (active catalytic surface + bulk). According to R_T values, the highest impedance values are those obtained for Nb- and Ti-doped catalysts, while **NiOref** and **Bi(NiO)** present the lowest resistance.

Impedance values were fitted to an equivalent circuit in order to establish a proper relationship between the catalytic results and the resistance offered by the active surface of the catalysts. A circuit of two parallel R-C time constants in series (inset of Figure 4.23C) was used for the EIS data fitting. Resistance of the electrolyte appears as R_S, while charge transfer resistance of the active parts of the catalysts/electrolyte interface and the resistance of the catalyst bulk are represented by R_1 and R_2, respectively. To consider the the non-ideality of the system, constant-phase elements (CPEs) were employed instead of pure capacitors[52,53]. For all fittings, the obtained chi-squared (χ^2) values were lower than 10^{-3}, which confirmed the suitability of the chosen circuit. Figure 4.23C shows the relationship between the selectivity to ethylene of the different catalysts and the resistance of the active surface to charge transfer processes. It is clear that the niobium-containing sample, which is the catalyst with the highest ethylene selectivity, presents the highest resistance of the active surface of the catalyst (R_1). It has been recently reported in literature that a higher resistance leads to limited total oxidation reactions, hindering the formation of CO_2 [28]. Accordingly, the pure nickel oxide catalyst presents the lowest charge transfer resistance.

As Table 4.8 anticipated, the amount of electrophilic oxygen species present in the NiO surface was decreased with the incorporation of high valence cations. These oxygen species are related with non-desired total oxidation reactions and are directly linked to the main charge carrier in p-type catalysts: cationic vacancies [30,36,41,42,54,55]. Therefore, Mott-Schottky analysis were carried out in order to determine the semiconducting properties of all samples. Figure 4.24A illustrates how all samples present a negative slope, except the Nb-doped catalyst, meaning that they

behave as p-type semiconductors. It is well known that nickel oxide is a p-type semiconductor in which positive holes are the main charge carriers. These positive holes are related to both cationic vacancies and lattice O^{2-} anions [25–27,56,57], following equations 4.4 and 4.5, respectively.

$$V_M^X \rightarrow V_M'' + 2h^{\cdot} \quad \text{Eq. 4. 4}$$

$$O_O^X + h^{\cdot} \rightarrow O_O^{\cdot} \quad \text{Eq. 4. 5}$$

Neuter cationic vacancies (V_M^X) take two electrons from neuter lattice oxygen species in regular positions (O_O^X or, in other words, O^{2-}) at the valance band. This results in ionized cationic vacancies and two positively-charged electron holes ($h^{\cdot}$). Similarly, neuter lattice oxygen anions react with electron holes, losing an electron and becoming non-stoichiometric lattice $O_O^{\cdot}$ (O^-) anions [57]. As has been mentioned before, O^- are known as electrophilic oxygen species and it is believed that they are responsible for deep oxidation reactions. Therefore, an excess in cationic vacancies can lead to a loss of O^{2-} species, which are related with selective oxidation reactions [25–27].

However, for the Nb-doped NiO catalyst a positive slope in the linear region can be elucidated in Figure 4.24A, which means that the incorporation of niobium hinders the p-type semiconductivity of the catalyst. Nb_2O_5 presents an n-type semiconductor character with oxygen vacancies and free electrons as main charge carriers [27]. It is accepted that Nb^{5+} presents a compatible ion size, as well as other high valence metals, which makes it possible to fill the Ni^{2+} vacancies in the NiO lattice [25,27,41,56,57]. Consequently, hole concentration decreases in **Nb(NiO)** and it could be argued that the semiconducting character changes from p-type to n-type semiconductivity due to niobium ions acting as electron donors. Hence, the selectivity to ethylene of the nickel oxide doped with niobium is the highest

compared to the rest of promoted NiO catalysts due to the reduced concentration of electrophilic oxygen species.

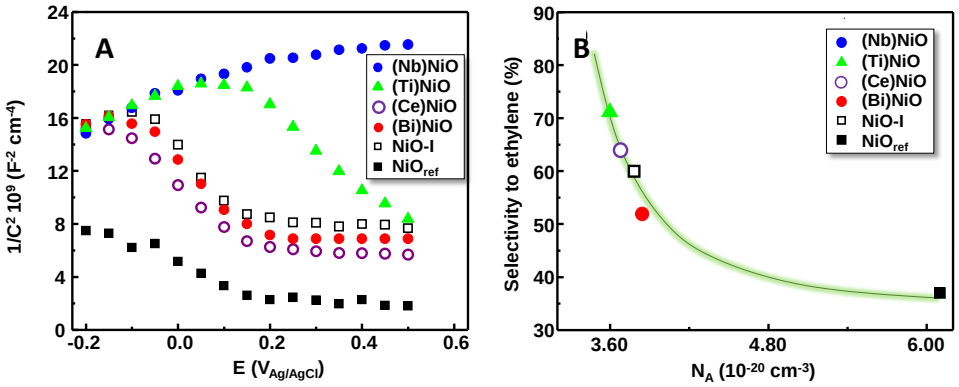

Figure 4. 24. (A) Mott-Schottky plots and (B) the relationship between the selectivity to ethylene during ethane oxidative dehydrogenation assisted by N_2O and density of acceptor defects, N_A.

Concerning the catalysts with p-type semiconductor character, the samples with the highest resistance values are those with the higher slopes. Density of acceptor defects, N_A (or cationic vacancies) can be easily calculated from the slopes of the Mott-Schottky plots [42], using Eq. 3.9 and the corresponding dielectric constant displayed in Table 3.3. Selectivity to ethylene of the different catalysts is plotted as a function of their N_A values in Figure 4.24B. As expected, the samples with the highest number of cationic vacancies (high concentration of electrophilic oxygen species) happen to be the least selective to ethylene formation during the N_2O-ODH of ethane.

To conclude the electrochemical characterization, cyclic voltammetries were performed for 10 cycles, revealing no differences between the first and the last cycle. Cyclic voltammetries during the 10th cycle for all catalysts are exhibited in Figure 4.25A. The two peaks located at ~0.30 $V_{Ag/AgCl}$ (anodic) and ~0.18 $V_{Ag/AgCl}$ (cathodic) correspond to the oxidation/reduction of the Ferro/Ferri couple in the electrolyte. Additionally, Figure 4.25B displays the relationship established between the

selectivity to ethylene during ethane N_2O-ODH and the anodic current density of each sample. An inverse correlation between olefin selectivity and anodic current density can be observed. Anodic current densities are associated with electrochemical activity of the catalysts. A high electrochemical activity means that total oxidation reactions are enhanced, meaning the selectivity to the desired product decreases. Hence, it is logical that **Nb(NiO)** and **Ti(NiO)** have the better catalytic performance, since they present the lowest electrochemical activity (anodic current density), as well as the highest resistance to charge transfer processes and the lowest number of cationic vacancies.

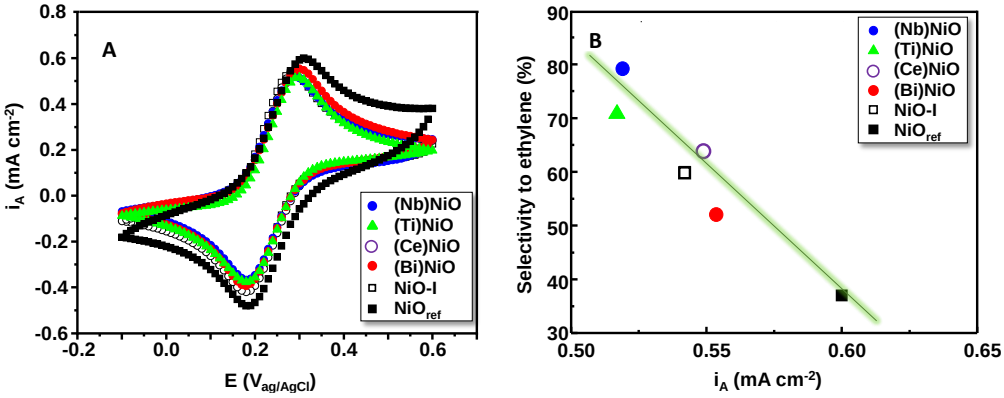

Figure 4. 25. (A) Cyclic voltammetries for the different NiO based catalysts and (B) the relationship between the selectivity to ethylene during ethane oxidative dehydrogenation assisted by N_2O and the anodic current densities.

In conclusion, promoted nickel oxide catalysts can be highly efficient in the ethane ODH assisted by N_2O, if synthesized with the appropriate promoter. Selectivity to ethylene has been improved with the addition of cerium, titanium and, especially, niobium. Despite the reaction conditions not being optimized, yields to ethylene ca. 40% were obtained with the Nb-doped catalyst. Furthermore, with the optimal catalyst ethane conversion and olefin formation remained stable after 8h reactions. This is related to the nickel oxide phase in **Nb(NiO)** not being reduced to metallic nickel after the exhaustion of nitrous oxide during the reaction. What is

more, the catalyst can be re-used further with almost no loss of performance. Conversely, the **Ce(NiO)** catalyst, which is also more selective than unpromoted **NiO-I**, does not provide a stable performance due to the development of metallic nickel once the atmosphere becomes N_2O-free. Therefore, it has been established that the higher the valence of the cation promoter, the higher is the selectivity to ethylene, relationship that had also been reported previously for O_2-assisted ODH.

In addition, it has been proved that electrochemical properties can estimate the selectivity to ethylene of the nickel oxide-based catalysts. High olefin selectivity can be achieved by p-type catalysts with few cationic vacancies and low charge-transfer resistance at their interfacial active sites. Cationic vacancies are the main charge carrier of p-type semiconducting materials and are related to electrophilic oxygen species. It has been proved that the incorporation of high valence cations decreases the concentration of these oxygen species, which are responsible for low ethylene formation, as they favor total deep oxidation reactions.

The N_2O-ODH of ethane improves the selectivity to ethylene compared to the analogous reaction with molecular oxygen. Interestingly, unlike the previous works reported in the literature for other catalytic systems, the catalytic activity with the Nb(NiO) catalyst is similar with N_2O or O_2, in spite of the fact that N_2O is usually significantly less reactive than O_2. A positive feature of NiO-based catalysts is their high capacity for activating the N_2O molecule

4.3 Valorization of N_2O by Oxidative Dehydrogenation of Ethane on a multicomponent MoVTeNb-M1 catalyst

The best catalytic results reported in the literature during the ethane ODH assisted by oxygen have been obtained by multicomponent MoV-based catalysts, especially those composed of MoVTeNb, whenever a specific crystalline phase (called **M1**) is formed. A major drawback of using molecular oxygen as an oxidant during the ethane ODH is the undesired formation of carbon oxides. Thus, the use of a milder oxidizing agent could be a solution to enhance olefin formation. The N_2O-assisted ODH of ethane has been reported in the literature, but, surprisingly, it has not been studied over multicomponent MoVTeNb catalysts. Therefore, in this section, a comprehensive study of the performance of the multicomponent **MoVTeNb-M1** catalyst during the ethane ODH using nitrous oxide as an oxidizing agent has been undertaken.

A multicomponent **M1** catalyst with an optimized composition (Table 4.12) was tested in the N_2O-ODH of ethane. Selectivity to ethylene as a function of ethane conversion at 400-425°C is depicted in Figure 4.26A, using both O_2 and N_2O as oxidants. To obtain these results different contact times were employed but keeping the C_2/N_2O/He: 5/10/85 ratio. It can be observed that ca. 90% of selectivity to ethylene is achieved at 5% of ethane conversion. However, selectivity steadily drops as ethane conversion increases, reaching 80% at 20% conversion. On the other hand, oxygen assisted oxidative dehydrogenation was also studied with the same catalyst, maintaining the reaction temperature and the same concentration of oxygen atoms fed to the system (C_2/O_2/He: 5/5/90 ratio). At these reaction conditions, catalytic behavior is improved, as selectivity to olefin reaches 95% at 20% of ethane conversion.

Table 4. 12. Characteristics of MoVTeNb-M1 catalyst.

Catalyst	Mo/V/Te/Nb at. ratio	S_{BET} (m^2/g)
M1	1/0.25/0.17/0.17	8.8

In order to properly compare catalytic results, further analysis must be conducted. For example, Figure 4.26B illustrates the catalytic activity of the multicomponent catalyst employed in both atmospheres. Considering both reaction rate and turnover frequency, the use of molecular oxygen instead of nitrous oxide leads to a significantly higher catalytic activity. It must be mentioned that the surface area of the catalyst and the vanadium surface content were considered to determine TOF values. It can be concluded that the use of O_2 as an oxidant is preferable to N_2O when using the **M1** catalyst in the ODH reaction, since with nitrous oxide the catalytic activity is ca. 40 times lower than that with oxygen. The bare decomposition of nitrous oxide was also analyzed to understand the reasons behind the different results (Figure 4.26C). At 425°C, less than 1% of nitrous oxide is transformed into N_2 and O_2. Hence, it can be stated that the **MoVTeNb** catalyst does not have the ability to activate the N_2O molecule during the nitrous oxide assisted ODH reaction. Oxidative dehydrogenation of ethane has been reported to take place by a redox Mars-Van Krevelen mechanism, in which lattice vacancies are formed and active sites are left in a reduced state. Therefore, it could be argued that the slower re-oxidation of the active sites due to the low ability of the catalyst to activate nitrous oxide could lead to the poor activity during the N_2O-assisted ODH.

As N_2O is poorly activated by the **MoVTeNb** catalyst, it was suggested that higher nitrous oxide concentrations during the ODH of ethane assisted by N_2O would improve the catalytic activity and enhance the ethylene formation. A higher nitrous oxide concentration would lead to more available oxygen species, since a greater amount of nitrous oxide would be activated. Figure 4.27 shows the evolution of ethane conversion with the time on line for different concentrations of N_2O (A) and

O_2 (B). Different contact times were used during O_2-ODH in order to reach similar conversions and make a proper comparison.

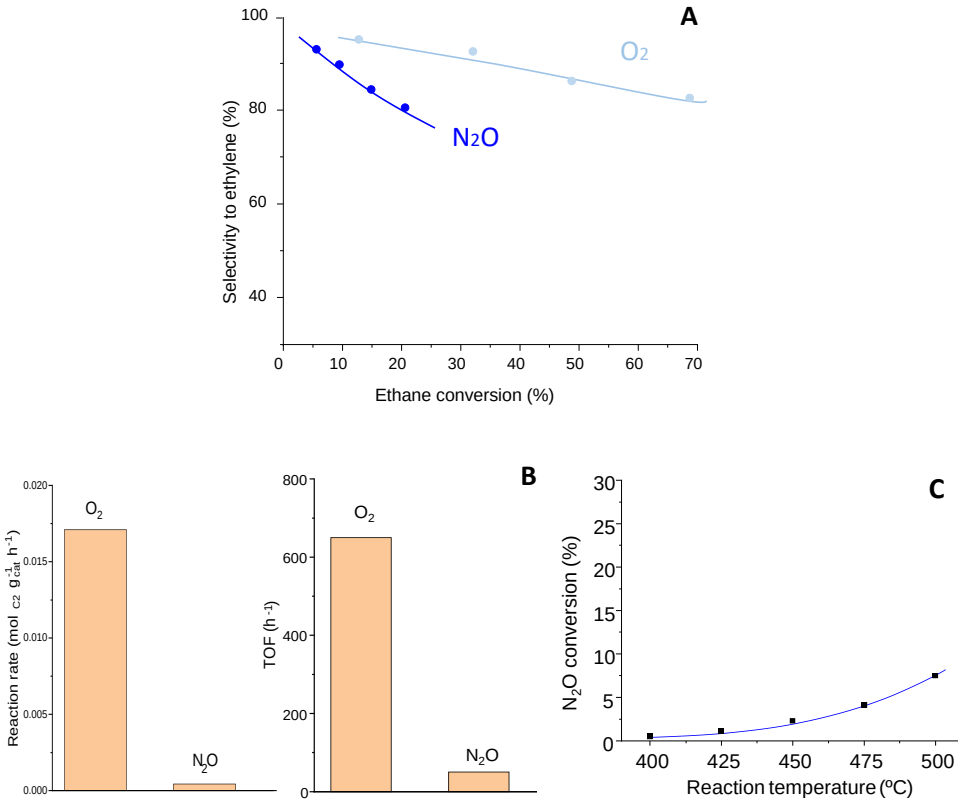

Figure 4. 26. (A) Selectivity to ethylene as a function of ethane conversion in the ODH of ethane over the multicomponent MoVTeNb-M1 catalyst at 400-425°C. (B) Reaction rate (left) or TOF (right) depending on the oxidizing agent during the ODH of ethane. Notes: TOF as ethane molecules reacted by active species atoms (V) on the surface and per unit of time (h^{-1}). Reaction conditions: 425 ºC, C_2/N_2O/He: 5/10/85 or C_2/O_2/He: 5/5/90 molar ratio and conversion lower than 10%. **(C)** Evolution of the N_2O conversion with the reaction temperature in the N_2O decomposition. Reaction conditions: N_2O/He: 10/90, catalyst weight: 1 g, Total flow: 25 ml/min.

Analyzing Figure 4.27, it can be observed that in both cases ethane conversion increases with an increasing concentration of oxidant. However, this increase is more noticeable for the experiments involving N_2O: ethane conversion rises from 12% to 22% by increasing atomic oxygen from 2% to 15%, while it barely rises from 12% to 16% when oxygen is increased in the same amount.

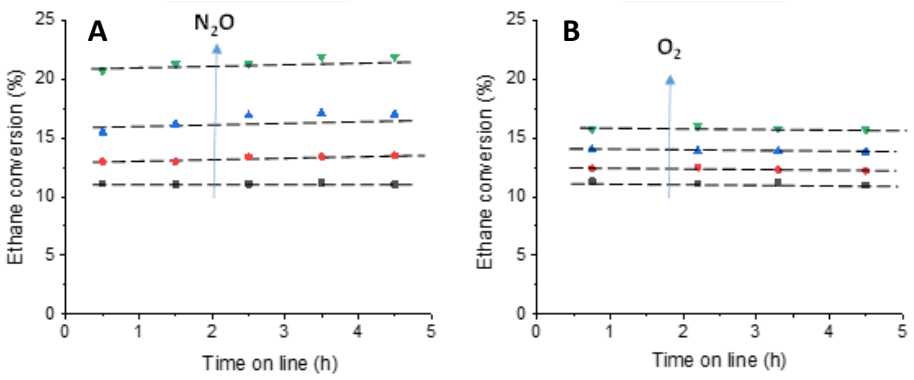

Figure 4. 27 Ethane conversion in the oxidative dehydrogenation of ethane over multicomponent MoVTeNb-M1 catalyst with the time on line for different concentrations of (A) N_2O or (B) O_2. Reaction conditions: 425ºC. C_2 fixed in 5 mol.%. Experiments with N_2O W/F=330 gcat.h/molC_2. Experiments with O_2 W/F=8.2 gcat.h/molC_2. T=425ºC. Symbols: ■ 2.5% O-atoms, ● 5% O-atoms, ▲ 10% O-atoms, ▼ 15% O-atoms.

Additionally, selectivity to ethylene with the increasing concentration of both oxidants was also studied and results are shown in Figure 4.28. The increase in nitrous oxide concentration results in higher selectivity to olefin, while the opposite happens for higher oxygen concentrations. A higher amount of oxygen species in the system would usually enhance the formation of carbon oxides, which could be related to a more oxidized surface.

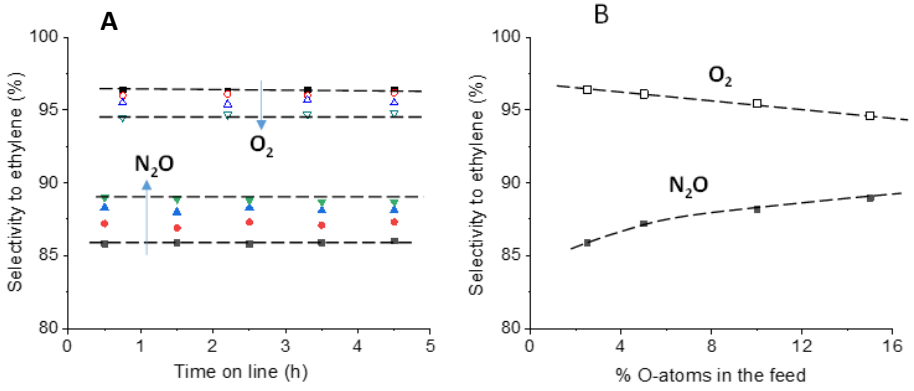

Figure 4. 28. Evolution of the selectivity to ethylene with the time on line for different concentrations of N_2O (filled symbols) or O_2 (open symbols) over multicomponent MoVTeNb-M1 catalyst. Reaction conditions as in Figure 4.26. Symbols: (■, □) 2.5% O-atoms, (●,○) 5% O-atoms, (▲,Δ) 10% O-atoms, (▼, V) 15% O-atoms.

During the MVK mechanism, gas-phase oxygen would adsorb to the lattice vacancy formed and would re-oxidize the active site [19]. However, when N_2O is used as an oxidant, it should fill the same vacancies as oxygen does. Therefore, nitrous oxide inhibits the adsorption of O_2 on the catalyst surface and limits the formation of O^-, which are known to enhance incomplete combustion of alkanes and further oxidation of product olefins [20]. Furthermore, when N_2O is adsorbed on the surface it dissociates to O^{2-}, following Eqs. 4.6-4.7. These oxygen species are known as nucleophilic oxygens and are responsible for partial oxidation of ethane to ethylene.

$$N_2O + e^- \rightarrow N_2 + O^- \quad \text{Eq. 4. 6}$$

$$O^- + e^- \rightarrow O^{2-} \quad \text{Eq. 4. 7}$$

A priori, the formation of ethylene should be favored by using N_2O as an oxidant, since there would be less active oxygen sites that would continue ethylene oxidation [19]. However, with this catalyst the effect is inverse, since the selectivity to the olefin is higher using oxygen. Apparently, the problems of the M1 phase for activating nitrous oxide lead to the surface of the M1 phase to be "too reduced", which apart from hindering the re-oxidation step, is less prone to the dehydrogenation path. It is believed that the formation rate of ethylene increases with increasing concentration of N_2O, since active sites need further oxidation when nitrous oxide is used as oxidant. The higher number of active oxygen species on catalyst surface leads to a higher rate of ethane activation. However, during oxygen assisted ODH, active sites are already fully oxidized, resulting in no change in ethylene formation rate despite increasing O_2 concentration [19]. Not only does selectivity to ethylene not decrease with nitrous oxide concentration, like it does in case of O_2-ODH, but it increases by 3 points with 15% of atomic oxygen. It must be noted that ethylene selectivity merely decreases with oxygen concentration (from 94.8% to 94.1%), since the M1 phase is highly selective towards olefin formation.

However, it could be argued that the differences in the catalytic results can be also explained by the different modifications that the catalyst has depending on the nature of the oxidizing agent. Therefore, several characterization techniques were employed to study the properties of the fresh and used (in both atmospheres) catalysts.

XRD patterns of fresh and used **MoVTeNb-M1** catalyst in O_2- and N_2O-assisted ODH reactions are presented in Figure 4.29. The fresh sample presents the M1 phase typically formed in orthorhombic structured catalysts with diffraction peaks at 2θ = 6.7°, 7.9°, 9.0°, 22.3°, 27.2°, 35.2° and 45.3° [58,59]. Despite being used in oxygen and nitrous oxide assisted ODH reactions, the crystalline structure of the M1 catalyst remains the same. Slight accentuation of the diffractions corresponding to MoO_2 and tetragonal $(Mo_{0.93}V_{0.07})_5O_{14}$ phases cannot be ruled out.

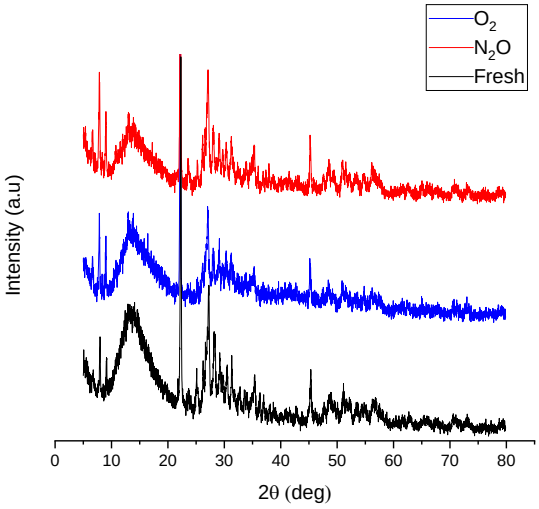

Figure 4. 29. XRD patterns of fresh MoVTeNb-M1 catalyst, as well as those used in N_2O and O_2 assisted ODH of ethane. Note: Catalysts used at 425 ºC for 5 h with $C_2/N_2O/He$: 5/10/85 or $C_2/O_2/He$: 5/5/90 molar ratio.

Given that the ODH mechanism involves a redox reaction, where oxygen species are transferred from the lattice to the surface of the catalyst with the associated electron transfer, electrochemical characterization of the **MoVTeNb-M1**

catalyst was conducted. In the same way, semiconductor properties were also determined. Resistance to the charge-transfer processes at the catalyst surface were determined by Electrochemical impedance spectroscopy. Figure 4.30 display the Nyquist and Bode plots for catalysts before and after use in both oxidative dehydrogenation reactions.

The Nyquist plot of every sample (Figure 4.30A) presents two semicircles, which correspond to two different regions in the Bode plots. The semicircle located at intermediate/high frequencies is usually related to the charge-transfer response of the interface between the metal oxide and the electrolyte. Hence, information of the active surface of the catalysts can be obtained. The semicircle at low frequencies is associated to the bulk of the catalysts. As a general rule, the greater the amplitude of the semicircle, the higher the impedance of the electrochemical process linked to it.

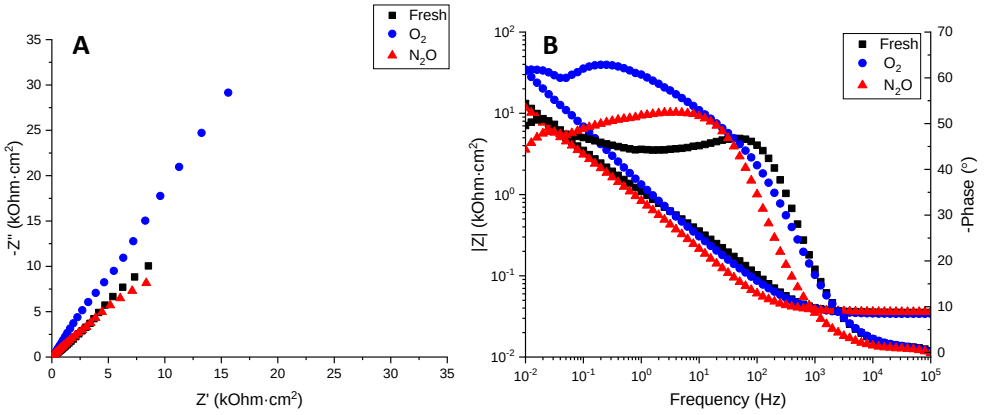

Figure 4. 30. (A) Nyquist plots and (B) Bode plots for MoVTeNb-M1 catalysts before and after use in N_2O and O_2 assisted ODH of ethane.

From Figure 4.30A, it is evident that the **M1** catalyst behaves differently after use in both ODH reactions. First, it is clear that the sample used in O_2-ODH presents a much bigger semicircle than the rest, which means that it holds the highest impedance value among the different samples. Furthermore, this is confirmed by Figure 4.30B, where it is clear that the total resistance offered by the O_2-used sample

is higher than the resistance offered by the N_2O-used and fresh samples. The higher resistance can be a result of a decrease in vacancy concentration, which leads to the formation of fewer carbon oxides. As has been outlined before, the higher resistance values in the active surface of the catalyst are related to higher selectivity in ethylene in O_2-assisted ODH of ethane. Therefore, the EIS and catalytic results are in accordance, since the **M1** catalyst presents a higher selectivity to ethylene when oxygen is used as oxidant during the reaction.

Furthermore, Mott-Schottky measurements were undertaken to understand the effect of the semiconductor properties of the catalyst on its catalytic behavior. Mott-Schottky plots for the catalyst before and after use in oxygen and nitrous oxide ODH reactions are illustrated in Figure 4.31, as well as their defect concentration calculated with the Mott-Schottky equation (Eq. 3.8).

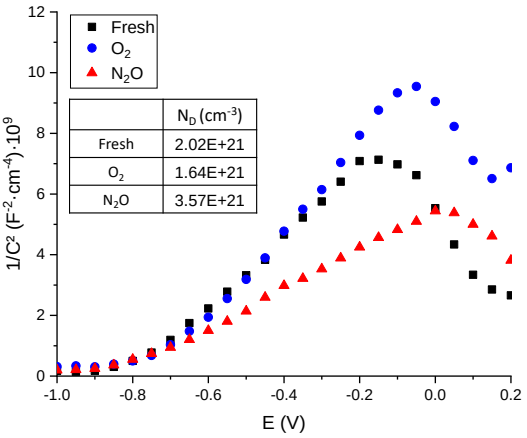

Figure 4. 31. Mott-Schottky plots and defect concentration for MoVTeNb-M1 catalysts before and after use in N_2O and O_2 assisted ODH of ethane.

From Figure 4.31 it can be inferred that the multicomponent **M1** catalyst has mainly a n-type semiconducting behavior, since most of the plot presents a positive slope. It is believed that the n-type semiconductor character is provided by the molybdenum (Mo^{6+}) present in the catalyst, since MoO_3 is a n-type semiconductor [28]. Oxygen vacancies are the main defects of these type of semiconductor

catalysts, which are created from the transformation of lattice oxygen (O^{2-}) to gaseous state, as described by Eq. 4.1. Hence, a high concentration of oxygen vacancies means that there is a loss of nucleophilic oxygen species (O^{2-}), which happen to be responsible for selective ethylene formation. Therefore, among n-type semiconducting catalysts, the most selective one towards ethylene formation will be the sample with a lower oxygen vacancy density. The **M1** sample with the lowest donor density is the one used in the ethane ODH assisted by oxygen, as it can be observed in Figure 4.31. This is in accordance with previous results since it is the sample with the highest impedance value among the **MoVeTeNb-M1** catalysts. Moreover, this catalyst is more selective to ethylene formation when it is used in the ODH reaction with oxygen as an oxidizing agent.

However, negative slopes can be elucidated at higher potentials, indicating p-type semiconducting nature. P-type semiconductivity is attributed to the vanadium content. In fact, V_2O_5 can present a p-type semiconducting nature when the oxidation state of vanadium is lower than 4.6, being V^{4+} the main vanadium species on the surface. In this case, the vanadium present on the surface of the catalyst shows two oxidation states (V^{4+}/V^{5+}), mainly V^{4+} [28]. All catalysts present a similar p-type behavior, except for a slightly smaller slope of the sample used in N_2O-ODH. A smaller slope in p-type semiconducting materials suggests a higher concentration of cationic vacancies. As has been described in equations 4.4 and 4.5, a high cationic vacancy concentration enhances the formation of electrophilic oxygen species (O^-), which results in a lower selectivity to ethylene. This fact would also explain the lower selectivity towards ethylene formation obtained for the **M1** catalysts used in the ODH reaction assisted by nitrous oxide.

4.3.1 Comparative study between the multicomponent M1 and the NiO based catalysts in N_2O- and O_2-assisted ODH of ethane

Currently, besides the multicomponent MoVTeNb catalysts, nickel oxide-based catalysts have been reported as the most efficient materials for the ODH of ethane using molecular oxygen as an oxidizing agent. In the previous chapter section, a detailed study on the effect of different promoters on NiO catalysts was conducted. From this work, it was concluded that nickel oxide promoted with niobium provided the best catalytic performance during ethane ODH assisted by N_2O. Therefore, it has been decided to carry out a comparative study between these two systems: multicomponent **M1** and **Nb(NiO)** catalysts during ODH reactions with both O_2 and N_2O.

First, the **Nb(NiO)** catalyst was tested in the oxidative dehydrogenation of ethane using both oxidizing agents with the same concentration of atomic oxygen. Figure 4.32 shows the variation of the selectivity to ethylene with ethane conversion for both oxidants. It can be elucidated how the **Nb(NiO)** catalyst exhibits high ethylene selectivity values that moderately decrease with increasing ethane conversion during both ODH reactions. Nevertheless, it can be observed that this catalyst is more selective to ethylene when N_2O is being used as an oxidant instead of oxygen, as opposed to the **M1** catalyst. In fact, at isoconversion conditions, selectivity to ethylene is improved by 8-10%.

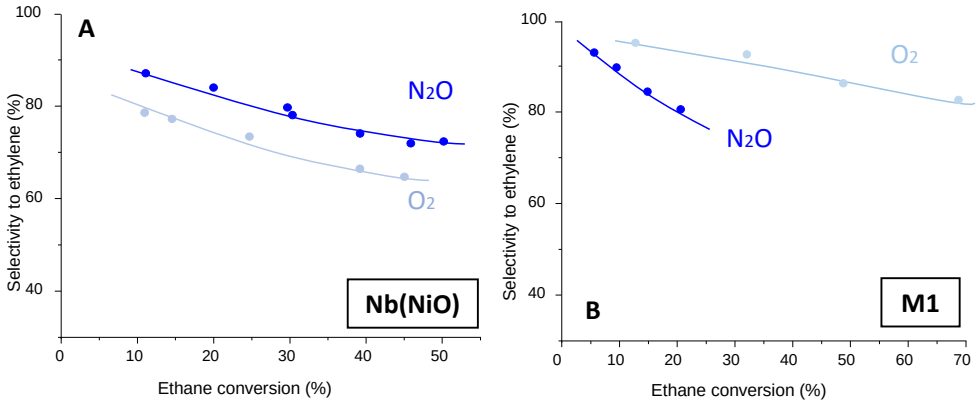

Figure 4. 32. Variation of the selectivity to ethylene with the ethane conversion for (A) (Nb)NiO and for (B) MoVTeNb-M1 catalysts at 400-425°C using N_2O (●) or O_2 (●) as oxidants. Reaction conditions: C_2H_6/N_2O/He molar ratio of 5/10/85 or C_2H_6/O_2/He molar ratio of 5/5/90.

When oxygen is chemisorbed in NiO based catalysts, the main oxygen species formed on the catalyst surface are O^- and O_2^-. As has been outlined before, these species have been reported to be linked to complete oxidation reactions, therefore being less selective to olefin formation [27,60]. However, with nitrous oxide, nucleophilic oxygen species are involved instead, thus the higher selectivity to ethylene being obtained. As has been mentioned in the previous study, the presence of niobium ions reduces the concentration of Ni^{3+} species [27,61], as it pushes the valence state of nickel towards its lowest available valance. This leaves Ni^{2+} vacancies on the catalyst surface which are active in N_2O decomposition [62]. Hence, O^- concentration is limited by maintaining nickel in its reduced valence state [36,63].

Then, different O_2 and N_2O concentrations were tested during both oxidative dehydrogenation of ethane reactions using the **Nb(NiO)** catalyst (Figure 4.33). First, it is noteworthy that, as the concentration of oxidant increases, so does the conversion of ethane, despite the oxidant being used (Figure 4.33A,B). However, selectivity to ethylene experiences different behaviors depending on the oxidant employed during the reaction. For instance, with an increasing oxygen concentration

(Figure 4.33D) the drop in ethylene selectivity is more significant than that experienced with the increasing concentration of nitrous oxide (Figure 4.33C). Consequently, the increase in atomic oxygen from 2% to 15% results in a more pronounced enhancement of the ethylene formation rate when nitrous oxide is used, as compared to oxygen.

Table 4.13 summarizes the key parameters used for the comparative study about the performance of Nb(NiO) and MoVTeNb in the ethane ODH assisted by O_2 and N_2O.

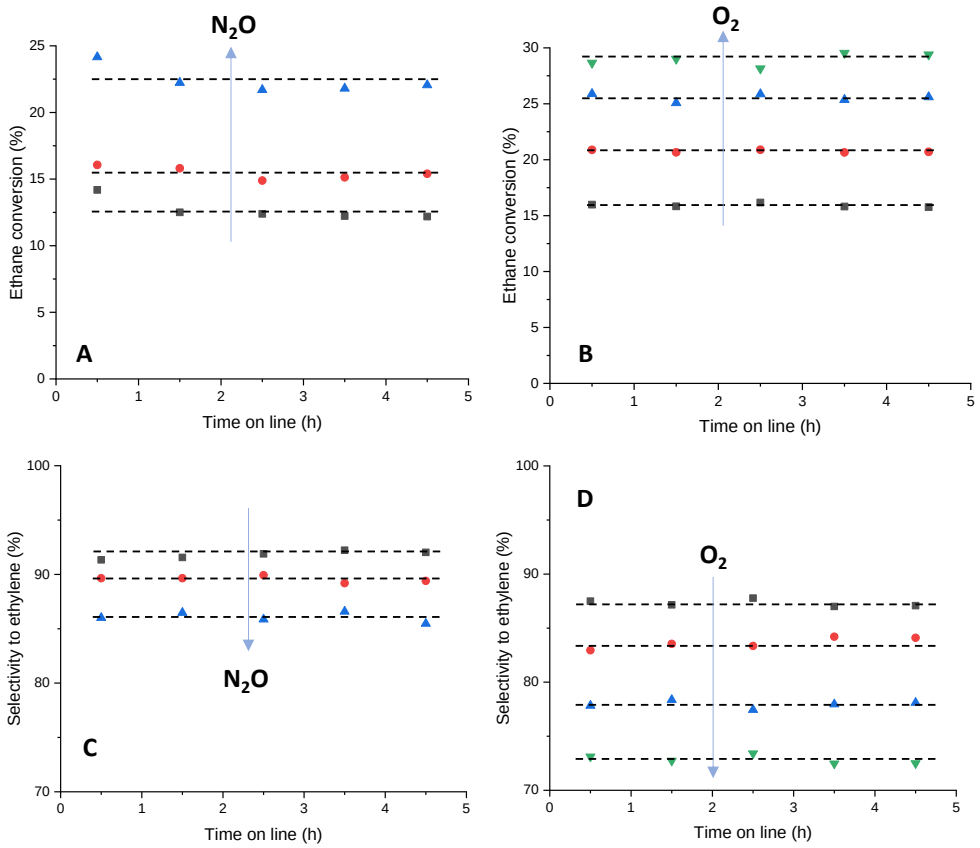

Figure 4. 33. Ethane conversion and selectivity to ethylene in the oxidative dehydrogenation of ethane with the time on line for different concentrations of (A,C) N_2O or (B,D) O_2 for the Nb(NiO catalyst. Reaction conditions: 425ºC. C_2 fixed in 5 mol.%. Experiments with N_2O W/F=330 gcat.h/molC_2. Experiments with O_2 W/F=8.2 gcat.h/molC_2. T=425ºC. Symbols: ■ 2.5% O-atoms, ● 5% O-atoms, ▲ 10% O-atoms, ▼ 15% O-atoms.

Table 4. 13. Comparative study of the performance of Nb(NiO) and MoVTeNb in the O_2 and N_2O ODH of ethane.

Catalyst	Reaction rate ratio O_2/N_2O	Select. O_2 [a] (X = 10%)	Select. N_2O [a] (X = 10%)	Δ Select. 2.5-15% O_2 [b]	Δ Select. 5-30% N_2O [c]
M1	40	96	87	-4	+7
Nb(NiO)	~1.1	79	88	-7	-3

[a] Selectivity to ethylene at 10% conversion and 400°C (C_2/O_2 (N_2O)/He : 5/5(10)/90(85).

[b] Variation of the selectivity to ethylene when increasing the O_2 concentration from 2.5 to 15% (ethane conversion 10%).

[c] Variation of the selectivity to ethylene when increasing the N_2O concentration from 2.5 to 15% (ethane conversion 10%).

The **Nb(NiO)** catalyst was also characterized before and after use in both ODH reactions. Figures 4.34 shows the XRD patterns of the fresh and used samples. It is confirmed that **Nb(NiO)** remains stable after O_2-ODH and N_2O-ODH, since no appreciable differences can be noticed in their XRD patterns before and after use. The detected peaks at ca. 2θ= 37°, 43° and 63° belong to cubic NiO, which suggests that niobium is highly dispersed on the NiO lattice.

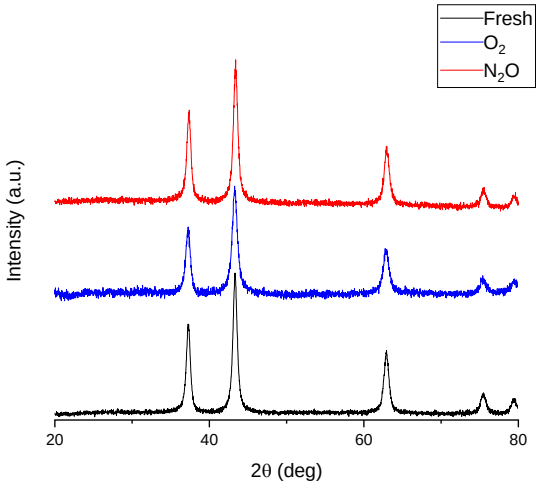

Figure 4. 34. XRD patterns of fresh Nb(NiO), as well as those used in N_2O and O_2 assisted ODH of ethane. Note: Catalysts used at 425 ºC for 5 h with C_2/N_2O/He: 5/10/85 or C_2/O_2/He: 5/5/90 molar ratio.

Electrochemical properties of the **Nb(NiO)** were also determined by electrochemical impedance spectroscopy measurements of fresh and used samples. Figure 4.35 exhibits the Nyquist (A) and Bode plots (B) of the catalyst before and after use in both N_2O and O_2 assisted ODH. Considering the amplitude of the semicircles present in Figure 4.35A, the **Nb(NiO)** sample employed in N_2O-ODH presents the biggest semicircle among all samples. Hence, the catalyst used in the oxidative dehydrogenation of ethane with nitrous oxide as oxidant has the highest resistance value, which agrees with the **Nb(NiO)** catalyst being more selective during N_2O-ODH. The impedances represented in the Bode plots (Figure 4.35B) also confirm that the N_2O sample holds the highest value.

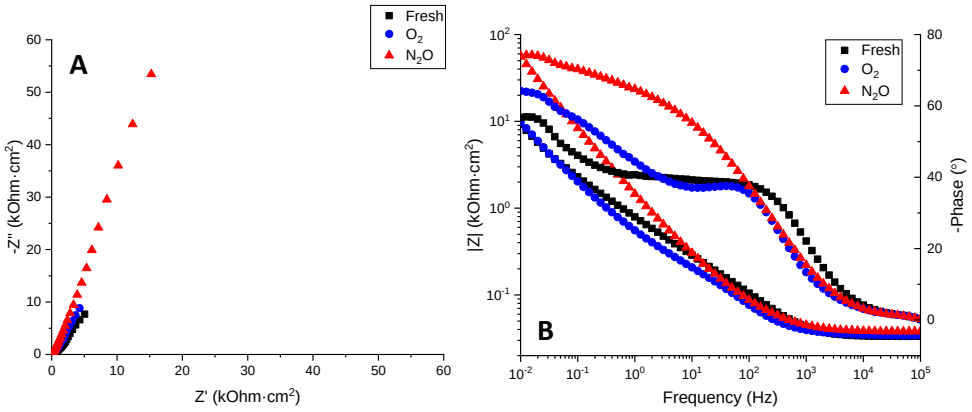

Figure 4. 35. (A) Nyquist plots and (B) Bode plots for Nb(NiO) catalysts before and after use in N_2O and O_2 assisted ODH of ethane

Semiconductor behavior as well as the number of defects were determined by performing Mott-Schottky measurements for the Nb-doped nickel oxide catalyst before and after use in both ODH reactions (Figure 4.36). The positive slopes in Figure 4.36 suggest that the Nb(NiO) catalyst has a n-type semiconductor character, as opposed to the p-type behavior of nickel oxide-based catalysts. As has been observed before, the incorporation of niobium hinders the typical p-type nature of nickel oxide. The number of oxygen vacancies of each sample has been calculated with Eq. 3.8, employing the dielectric constant shown in Table 3.3. Observing the

table included in Figure 4.36, the **Nb(NiO)** catalyst presenting the lowest concentration of oxygen vacancies is the sample used in N_2O-ODH, which is known to have higher ethylene selectivity than when used in oxygen assisted ODH. These findings are supported by EIS results, since it is the **Nb(NiO)** sample used in the nitrous oxide reaction that exhibits the highest resistance value among the rest of the Nb(NiO) catalysts.

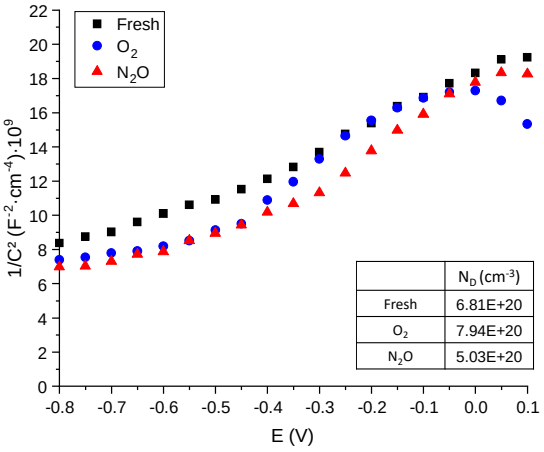

Figure 4. 36. Mott-Schottky plots and defect concentration for Nb(NiO) catalysts before and after use in N_2O and O_2 assisted ODH of ethane.

Overall, a completely different trend has been observed between the **M1** and the **Nb(NiO)** catalysts. In the case of the **M1** catalyst, the catalytic activity drastically decreases when using N_2O compared to the analogous experiments with O_2. This behavior is related to the low capacity of the M1 phase to activate the N_2O molecule. Conversely, the catalytic activity of **Nb(NiO)** is pretty similar when using oxygen or nitrous oxide. The high capacity of NiO catalysts to activate N_2O ($N_2O \rightarrow N_2 + O_2$), makes the overall reaction rate of ODH of ethane be approximately the same.

Regarding the selectivity to ethylene (at isoconversion conditions), the effect between both catalysts is also the opposite. Then, for **M1** the selectivity is higher

when using oxygen than with nitrous oxide. However, for the **Nb(NiO)** catalyst, the values of the selectivity to olefin are higher when using N_2O than with O_2.

We propose that the formation of carbon oxides is related to the presence of defects on the catalyst (either oxygen vacancies or cationic defects, depending on the sample).

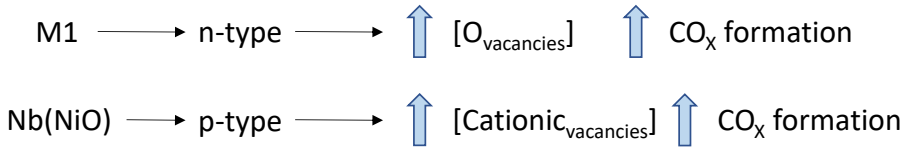

4.4 Conclusions

In this chapter, the catalytic valorization of N_2O through the nitrous oxide-assisted oxidative dehydrogenation of ethane to yield ethylene, the most important raw material in petrochemistry, has been examined. Three different catalytic systems have been studied: i) NiO supported on CeO_2 (or CeO_2/ZrO_2), ii) unpromoted and promoted NiO catalysts and iii) a multicomponent MoVTeNb catalyst presenting the orthorhombic M1 structure.

In the case of the Ni/CeO_2-ZrO_2 catalysts, the production of ethylene through the N_2O assisted ODH of ethane has not been successful, since the carbon dioxide formation has been very important. In any case, the incorporation of low loadings of Zr to the ceria support has meant an increase in the ethylene formation. An excess of Zr, however, makes decrease not only the selectivity to the olefin but also the catalytic activity. On the other hand, it has been observed that the use of nitrous oxide as an oxidant has meant an increase of the selectivity to the olefin of 10-15 points (at isoconversion and isothermal conditions) compared to the analogous reaction using molecular oxygen as an oxidant. Probably, the milder oxidizing character of N_2O has led to a less oxidized catalyst surface, hindering total oxidation reactions. Unfortunately, the reaction rate in the O_2 reaction is ca. 3 times that of the reaction with N_2O.

In the case of nickel oxide-based catalysts, it has been observed that the use of suitable promoters improves the catalytic performance in the N_2O assisted ODH of ethane. In this case, yields to ethylene of ca. 40% have been achieved with the optimal Nb-doped NiO catalyst without carrying out an optimization of the reaction conditions, which suggests that remarkably higher yields could be obtained adjusting different reaction parameters. The oxidation state of the promoter and the consequent formation of suitable surface oxygen species in the NiO matrix explain the behavior obtained. On the other hand, the use of nitrous oxide as an oxidant enhances the

selectivity to ethylene by ca. 8 points compared to the reaction with molecular oxygen. Interestingly, and conversely to the other catalytic systems reported in the literature, the catalytic activity using N_2O is at the same level that using O_2. This interesting behavior can be explained by the high capacity of nickel oxide in the activation of the N_2O molecule at low temperatures.

For the multicomponent MoVTeNbO catalyst presenting the M1 structure (the catalyst that offers in the scientific literature the best catalytic performance during the O_2-ODH) a reasonable catalytic behavior has been observed in the N_2O-ODH. Unfortunately, the use of N_2O as an oxidizing agent presents notorious disadvantages compared to the oxygen assisted ODH of ethane. Thus, at isoconversion and isothermal conditions, the selectivity to the olefin is ca. 10 points lower when using N_2O compared to the reaction with O_2. Probably, this effect is due to the modification of the catalyst observed during the reaction depending on the atmosphere. Moreover, the reaction rate with nitrous oxide is ca. 40 times lower than with molecular oxygen. This negative behavior has been related to the slow re-oxidation of the catalyst when using nitrous oxide, which is needed for the redox cycle to take place. Thus, it has been checked that the M1 catalyst can hardly activate the N_2O molecule at the reaction temperatures studied. Conversely to the O_2 assisted ODH of ethane, promoted NiO catalysts are more promising than the M1-type catalysts for the N_2O assisted ODH of ethane.

Since the multicomponent M1 catalyst is not so efficient in this reaction, a strategy to simultaneously remove N_2O and obtain high concentrations of the olefin can be suggested. Then, the use of a two reactor system has been proposed: i) in the first reactor an efficient catalyst for the N_2O to N_2 and O_2 reaction (for example an alkali doped cobalt oxide) and ii) in the second reactor a MoVTeNbO catalyst to conduct the oxygen assisted oxidative dehydrogenation of ethane.

In general, catalytic results can be related to the electrochemical properties of each set of catalysts. Specifically, the selectivity to ethylene is closely linked with the concentration of defects and resistance to charge-transfer processes at the interfacial active sites of the catalysts. For instance, p-type catalysts (NiO-based, except Nb(NiO)) with the lowest density of cationic vacancies are the most selective towards ethylene formation, since the concentration of electrophilic oxygen species is reduced. Similarly, catalysts with n-type semiconductor behavior, such as Ni/CeZr, MoVTeNb-M1 and Nb(NiO), also present the highest selectivity to ethylene with samples containing a lower amount of defects (oxygen vacancies), since less nucleophilic oxygen species are lost. Overall, the presence of any type of defects favors the reactions of carbon oxides formation.

4.5 References

[1] F.M. Sun, C.F. Yan, Z.D. Wang, C.Q. Guo, S.L. Huang, Ni/Ce–Zr–O catalyst for high CO2 conversion during reverse water gas shift reaction (RWGS), Int. J. Hydrog. Energy 40 (2015) 15985–15993. https://doi.org/10.1016/J.IJHYDENE.2015.10.004.

[2] L. Xu, X. Wen, M. Chen, C. Lv, Y. Cui, X. Wu, C. e. Wu, B. Yang, Z. Miao, X. Hu, Mesoporous Ce-Zr solid solutions supported Ni-based catalysts for low-temperature CO2 methanation by tuning the reaction intermediates, Fuel 282 (2020) 118813. https://doi.org/10.1016/J.FUEL.2020.118813.

[3] C. Larese, M. López Granados, R. Mariscal, J.L.G. Fierro, P.S. Lambrou, A.M. Efstathiou, The effect of calcination temperature on the oxygen storage and release properties of CeO2 and Ce–Zr–O metal oxides modified by phosphorus incorporation, Appl. Catal. B Environ. 59 (2005) 13–25. https://doi.org/10.1016/J.APCATB.2004.12.011.

[4] S. Tong, M. Zheng, Y. Lu, Z. Lin, J. Li, X. Zhang, Y. Shi, P. He, H. Zhou, Mesoporous NiO with a single-crystalline structure utilized as a noble metal-free catalyst for non-aqueous Li–O 2 batteries, J. Mater. Chem. A 3 (2015) 16177–16182. https://doi.org/10.1039/C5TA03685B.

[5] M.A. Peck, M.A. Langell, Comparison of nanoscaled and bulk NiO structural and environmental characteristics by XRD, XAFS, and XPS, Chem. Mater. 24 (2012) 4483–4490. https://doi.org/10.1021/CM300739Y/SUPPL_FILE/CM300739Y_SI_004.PDF.

[6] L.A. do Nascimento, lsabel Barroso-Martín, S.R.S. Peçanha, S. Arias, B.S. Santos, J.G.A. Pacheco, A. Infantes-Molina, E. Rodríguez-Castellón, I. de C.L. Barros, NiAlCe mixed oxides obtained from layered double hydroxides applied to anisole hydrodeoxygenation, Catal. Today 394–396 (2022) 282–294. https://doi.org/10.1016/J.CATTOD.2021.08.026.

[7] T. Bao, H. zhou, Y. Zhang, C. Guo, W. Guo, H. Qin, P. Gao, H. Xiao, W. Liu, Effect of CeO2 on carbon deposition resistance of Ni/CeO2 catalyst supported on SiC porous ceramic for ethanol steam reforming, J. Rare Earths 41 (2023) 1703–1713. https://doi.org/10.1016/J.JRE.2022.09.006.

[8] M. Chen, X. Feng, Y. Wang, D. Liang, C. Li, Z. Yang, J. Wang, Ethanol steam reforming over attapulgite-based MCM-41 supported Ni-Ce-Zr catalyst for hydrogen production, Fuel 346 (2023) 128373. https://doi.org/10.1016/J.FUEL.2023.128373.

[9] M. Tomellini, X-ray photoelectron spectra of defective nickel oxide, J. Chem. Soc. Faraday Trans. 1 Phys. Chem. Condens. Phases 84 (1988) 3501–3510. https://doi.org/10.1039/F19888403501.

[10] J.C. Vedrine, G. Hollinger, T.M. Duc, Investigations of antigorite and nickel supported catalysts by X-ray photoelectron spectroscopy, J. Phys. Chem. 82

(1978) 1515–1520. https://doi.org/10.1021/J100502A011/ASSET/J100502A011.FP.PNG_V03.
[11] V. Biju, M. Abdul Khadar, Electronic structure of nanostructured nickel oxide using Ni 2p XPS analysis, J. Nanoparticle Res. 4 (2002) 247–253. https://doi.org/10.1023/A:1019949805751/METRICS.
[12] M.A. Van Veenendaal, G.A. Sawatzky, Nonlocal screening effects in 2*p* x-ray photoemission spectroscopy core-level line shapes of transition metal compounds, Phys. Rev. Lett. 70 (1993) 2459. https://doi.org/10.1103/PhysRevLett.70.2459.
[13] X. Zhou, Y. Gao, J. Yang, W. Yi, Q. Pang, Z. Liu, B. Liu, M. Zhang, Unraveling the effects of Ce/Zr molar ratio in mesoporous CexZr1−xO2 on the performance of dry reforming of methane over the supported Ni catalysts, Chem. Eng. Res. Des. 193 (2023) 626–640. https://doi.org/10.1016/J.CHERD.2023.04.020.
[14] A.S. Al-Fatesh, Y. Arafat, S.O. Kasim, A.A. Ibrahim, A.E. Abasaeed, A.H. Fakeeha, In situ auto-gasification of coke deposits over a novel Ni-Ce/W-Zr catalyst by sequential generation of oxygen vacancies for remarkably stable syngas production via CO2-reforming of methane, Appl. Catal. B Environ. 280 (2021) 119445. https://doi.org/10.1016/J.APCATB.2020.119445.
[15] B.M. Reddy, B. Chowdhury, P.G. Smirniotis, An XPS study of the dispersion of MoO3 on TiO2–ZrO2, TiO2–SiO2, TiO2–Al2O3, SiO2–ZrO2, and SiO2–TiO2–ZrO2 mixed oxides, Appl. Catal. Gen. 211 (2001) 19–30. https://doi.org/10.1016/S0926-860X(00)00834-6.
[16] A. Galtayries, R. Sporken, J. Riga, G. Blanchard, R. Caudano, XPS comparative study of ceria/zirconia mixed oxides: powders and thin film characterisation, J. Electron Spectrosc. Relat. Phenom. 88–91 (1998) 951–956. https://doi.org/10.1016/S0368-2048(97)00134-5.
[17] A.V. Paladino Lino, C.B. Rodella, E.M. Assaf, J.M. Assaf, Methane tri-reforming for synthesis gas production using Ni/CeZrO2/MgAl2O4 catalysts: Effect of Zr/Ce molar ratio, Int. J. Hydrog. Energy 45 (2020) 8418–8432. https://doi.org/10.1016/J.IJHYDENE.2020.01.002.
[18] M. Zhang, X. Zhou, J. Yang, T. Yang, Z. Liu, Y. Han, Deciphering the ZrO2 phase engineering effects on dry reforming of methane over the Ni/ZrO2 catalysts, Fuel 349 (2023) 128705. https://doi.org/10.1016/J.FUEL.2023.128705.
[19] M.P. Woods, B. Mirkelamoglu, U.S. Ozkan, Oxygen and nitrous oxide as oxidants: Implications for ethane oxidative dehydrogenation over silica-titania-supported molybdenum, J. Phys. Chem. C 113 (2009) 10112–10119. https://doi.org/10.1021/jp810664u.
[20] X. Jiang, L. Sharma, V. Fung, S.J. Park, C.W. Jones, B.G. Sumpter, J. Baltrusaitis, Z. Wu, Oxidative dehydrogenation of propane to propylene with soft oxidants via heterogeneous catalysis, ACS Catal. 11 (2021) 2182–2234. https://doi.org/10.1021/acscatal.0c03999.

[21] B.M. Abu-Zied, S.A. Soliman, S.E. Abdellah, Pure and Ni-substituted Co3O4 spinel catalysts for direct N2O decomposition, Chin. J. Catal. 35 (2014) 1105. https://doi.org/10.1016/S1872-2067(14)60058-9.

[22] X. Rozanska, E.V. Kondratenko, J. Sauer, Oxidative dehydrogenation of propane: Differences between N2O and O2 in the reoxidation of reduced vanadia sites and consequences for selectivity, J. Catal. 256 (2008) 84–94. https://doi.org/10.1016/J.JCAT.2008.03.002.

[23] V.A. Kondratenko, T. Hahn, E.V. Kondratenko, Catalytic Abatement of Nitrous Oxide Coupled with Functionalization of C1–C3 Alkanes, ChemCatChem 4 (2012) 408–414. https://doi.org/10.1002/cctc.201100314.

[24] S.M. Gateman, O. Gharbi, H. Gomes de Melo, K. Ngo, M. Turmine, V. Vivier, On the use of a constant phase element (CPE) in electrochemistry, Curr. Opin. Electrochem. 36 (2022) 101133. https://doi.org/10.1016/J.COELEC.2022.101133.

[25] S. Najari, S. Saeidi, P. Concepcion, D.D. Dionysiou, S.K. Bhargava, A.F. Lee, K. Wilson, Oxidative dehydrogenation of ethane: Catalytic and mechanistic aspects and future trends, Chem. Soc. Rev. 50 (2021) 4564–4605. https://doi.org/10.1039/d0cs01518k.

[26] X. Zhao, M.D. Susman, J.D. Rimer, P. Bollini, Tuning selectivity in nickel oxide-catalyzed oxidative dehydrogenation of ethane through control over non-stoichiometric oxygen density, Catal. Sci. Technol. 11 (2021) 531–541. https://doi.org/10.1039/D0CY01732A.

[27] E. Heracleous, A.A. Lemonidou, Ni-Nb-O mixed oxides as highly active and selective catalysts for ethene production via ethane oxidative dehydrogenation. Part I: Characterization and catalytic performance, J. Catal. 237 (2006) 162–174. https://doi.org/10.1016/j.jcat.2005.11.002.

[28] A. de Arriba, G. Sánchez, R. Sánchez-Tovar, P. Concepción, R. Fernández-Domene, B. Solsona, J.M. López Nieto, On the selectivity to ethylene during ethane ODH over M1-based catalysts. A surface and electrochemical study, Catal. Today 418 (2023). https://doi.org/10.1016/j.cattod.2023.114122.

[29] B. Solsona, P. Concepción, S. Hernández, B. Demicol, J.M.L. Nieto, Oxidative dehydrogenation of ethane over NiO–CeO2 mixed oxides catalysts, Catal. Today 180 (2012) 51–58. https://doi.org/10.1016/J.CATTOD.2011.03.056.

[30] J.M. López Nieto, B. Solsona, R.K. Grasselli, P. Concepción, Promoted NiO catalysts for the oxidative dehydrogenation of ethane, Top. Catal. 57 (2014) 1248–1255. https://doi.org/10.1007/s11244-014-0288-2.

[31] Y. Abdelbaki, A. de Arriba, R. Issaadi, R. Sánchez-Tovar, B. Solsona, J.M. López Nieto, Optimization of the performance of bulk NiO catalyst in the oxidative dehydrogenation of ethane by tuning the synthesis parameters, Fuel Process. Technol. 229 (2022) 107182. https://doi.org/10.1016/j.fuproc.2022.107182.

[32] P. Brussino, E.L. Mehring, M.A. Ulla, J.P. Bortolozzi, Tuning the properties of NiO supported on silicon-aluminum oxides: Influence of the silica amount in the ODH of ethane, Catal. Today (2021). https://doi.org/10.1016/j.cattod.2021.10.017.

[33] D. Delgado, B. Solsona, R. Sanchis, E. Rodríguez-Castellón, J.M. López Nieto, Oxidative dehydrogenation of ethane on diluted or promoted nickel oxide catalysts: Influence of the promoter/diluter, Catal. Today 363 (2021) 27–35. https://doi.org/10.1016/J.CATTOD.2019.06.063.

[34] R. Sanchis, D. Delgado, S. Agouram, M.D. Soriano, M.I. Vázquez, E. Rodríguez-Castellón, B. Solsona, J.M.L. Nieto, NiO diluted in high surface area TiO2 as an efficient catalyst for the oxidative dehydrogenation of ethane, Appl. Catal. Gen. 536 (2017) 18–26. https://doi.org/10.1016/j.apcata.2017.02.012.

[35] Y. Abdelbaki, A. de Arriba, B. Solsona, D. Delgado, E. García-González, R. Issaadi, J.M. López Nieto, The nickel-support interaction as determining factor of the selectivity to ethylene in the oxidative dehydrogenation of ethane over nickel oxide/alumina catalysts, Appl. Catal. Gen. 623 (2021) 118242. https://doi.org/10.1016/j.apcata.2021.118242.

[36] E. Heracleous, A.A. Lemonidou, Ni-Me-O mixed metal oxides for the effective oxidative dehydrogenation of ethane to ethylene - Effect of promoting metal Me, J. Catal. 270 (2010) 67–75. https://doi.org/10.1016/j.jcat.2009.12.004.

[37] B. Savova, S. Loridant, D. Filkova, J.M.M. Millet, Ni–Nb–O catalysts for ethane oxidative dehydrogenation, Appl. Catal. Gen. 390 (2010) 148–157. https://doi.org/10.1016/j.apcata.2010.10.004.

[38] H. Zhu, S. Ould-Chikh, D.H. Anjum, M. Sun, G. Biausque, J.-M. Basset, V. Caps, Nb effect in the nickel oxide-catalyzed low-temperature oxidative dehydrogenation of ethane, J. Catal. 285 (2012) 292–303. https://doi.org/10.1016/j.jcat.2011.10.005.

[39] B. Solsona, P. Concepción, B. Demicol, S. Hernández, J.J. Delgado, J.J. Calvino, J.M. López Nieto, Selective oxidative dehydrogenation of ethane over SnO2-promoted NiO catalysts, J. Catal. 295 (2012) 104–114. https://doi.org/10.1016/J.JCAT.2012.07.028.

[40] H. Zhu, D.C. Rosenfeld, M. Harb, D.H. Anjum, M.N. Hedhili, S. Ould-Chikh, J.M. Basset, Ni-M-O (M = Sn, Ti, W) Catalysts Prepared by a Dry Mixing Method for Oxidative Dehydrogenation of Ethane, ACS Catal. 6 (2016) 2852–2866. https://doi.org/10.1021/acscatal.6b00044.

[41] Z. Skoufa, E. Heracleous, A.A. Lemonidou, On ethane ODH mechanism and nature of active sites over NiO-based catalysts via isotopic labeling and methanol sorption studies, J. Catal. 322 (2015) 118–129. https://doi.org/10.1016/J.JCAT.2014.11.014.

[42] Y. Abdelbaki, R. Sánchez-Tovar, A. de Arriba, E. García-González, R. Fernández-Domene, B. Solsona, J.M. López Nieto, Predicting the catalytic performance of Nb-doped nickel oxide catalysts for the oxidative

dehydrogenation of ethane by knowing their electrochemical properties, J. Catal. 420 (2023) 9–22. https://doi.org/10.1016/J.JCAT.2023.02.009.

[43] Y. Abdelbaki, A. de Arriba, R. Issaadi, R. Sánchez-Tovar, B. Solsona, J.M. López Nieto, Optimization of the performance of bulk NiO catalyst in the oxidative dehydrogenation of ethane by tuning the synthesis parameters, Fuel Process. Technol. 229 (2022) 107182. https://doi.org/10.1016/J.FUPROC.2022.107182.

[44] M. Konsolakis, Recent Advances on Nitrous Oxide (N2O) Decomposition over Non-Noble-Metal Oxide Catalysts: Catalytic Performance, Mechanistic Considerations, and Surface Chemistry Aspects, ACS Catal. 5 (2015) 6397–6421. https://doi.org/10.1021/ACSCATAL.5B01605/ASSET/IMAGES/LARGE/CS-2015-01605M_0019.JPEG.

[45] B. Solsona, J.M. López Nieto, P. Concepción, A. Dejoz, F. Ivars, M.I. Vázquez, Oxidative dehydrogenation of ethane over Ni–W–O mixed metal oxide catalysts, J. Catal. 280 (2011) 28–39. https://doi.org/10.1016/j.jcat.2011.02.010.

[46] Systematic XPS studies of metal oxides, hydroxides and peroxides - Physical Chemistry Chemical Physics (RSC Publishing), (n.d.). https://pubs.rsc.org/en/content/articlelanding/2000/cp/a908800h (accessed May 2, 2025).

[47] X. Wen, K. Xie, Regulating Lattice Oxygen on the Surfaces of Porous Single-Crystalline NiO for Stabilized and Enhanced CO Oxidation, Catalysts 14 (2024) 130. https://doi.org/10.3390/catal14020130.

[48] K.I. Hadjiivanov, G.N. Vayssilov, Characterization of oxide surfaces and zeolites by carbon monoxide as an IR probe molecule, in: Adv. Catal., Academic Press, 2002: pp. 307–511. https://doi.org/10.1016/S0360-0564(02)47008-3.

[49] D. Delgado, R. Sanchis, B. Solsona, P. Concepción, J.M. López Nieto, Influence of the Nature of the Promoter in NiO Catalysts on the Selectivity to Olefin During the Oxidative Dehydrogenation of Propane and Ethane, Top. Catal. 63 (2020) 1731–1742. https://doi.org/10.1007/s11244-020-01329-5.

[50] L. Kong, D. Li, Z. Zhao, J. Li, L. Zhao, X. Fan, X. Xiao, Z. Xie, Preparation, characterization and catalytic performance of rod-like Ni–Nb–O catalysts for the oxidative dehydrogenation of ethane at low temperature, Catal. Sci. Technol. 9 (2019) 3416–3425. https://doi.org/10.1039/C9CY00519F.

[51] K. Bhunia, S. Khilari, M. Chandra, D. Pradhan, S.-J. Kim, Carbon nitride anchored NiO nanoparticles as robust catalyst for electrochemical oxygen evolution reaction, J. Alloys Compd. 935 (2023) 167842. https://doi.org/10.1016/j.jallcom.2022.167842.

[52] L. Bruno, M. Scuderi, F. Priolo, S. Mirabella, Enhanced electrocatalytic activity of low-cost NiO microflowers on graphene paper for the oxygen evolution reaction, Sustain. Energy Fuels 6 (2022) 4498–4505. https://doi.org/10.1039/D2SE00829G.

[53] Electrochemical Impedance Spectroscopy of Metal Oxide Electrodes for Energy Applications | ACS Applied Energy Materials, (n.d.). https://pubs.acs.org/doi/10.1021/acsaem.9b01965 (accessed May 2, 2025).

[54] F. Yang, X. Zhou, N.T. Plymale, K. Sun, N.S. Lewis, Evaluation of sputtered nickel oxide, cobalt oxide and nickel–cobalt oxide on n-type silicon photoanodes for solar-driven O2(g) evolution from water, J. Mater. Chem. A 8 (2020) 13955–13963. https://doi.org/10.1039/D0TA03725G.

[55] A. Ykrelef, L. Nadji, R. Issaadi, S. Agouram, E. Rodríguez-Castellón, B. Solsona, J.M. López Nieto, Mixed oxide TiSiO prepared by non-hydrolytic Xerogel method as a diluter of nickel oxide for the oxidative dehydrogenation of ethane, Catal. Today 299 (2018) 93–101. https://doi.org/10.1016/j.cattod.2017.03.021.

[56] I. Popescu, E. Heracleous, Z. Skoufa, A. Lemonidou, I.C. Marcu, Study by electrical conductivity measurements of semiconductive and redox properties of M-doped NiO (M = Li, Mg, Al, Ga, Ti, Nb) catalysts for the oxidative dehydrogenation of ethane, Phys. Chem. Chem. Phys. 16 (2014) 4962–4970. https://doi.org/10.1039/C3CP54817A.

[57] I. Popescu, Z. Skoufa, E. Heracleous, A. Lemonidou, I.C. Marcu, A study by electrical conductivity measurements of the semiconductive and redox properties of Nb-doped NiO catalysts in correlation with the oxidative dehydrogenation of ethane, Phys. Chem. Chem. Phys. 17 (2015) 8138–8147. https://doi.org/10.1039/C5CP00392J.

[58] K. Amakawa, Y.V. Kolen'ko, A. Villa, M.E. Schuster, L.-I. Csepei, G. Weinberg, S. Wrabetz, R. Naumann d'Alnoncourt, F. Girgsdies, L. Prati, R. Schlögl, A. Trunschke, Multifunctionality of Crystalline MoV(TeNb) M1 Oxide Catalysts in Selective Oxidation of Propane and Benzyl Alcohol, ACS Catal. 3 (2013) 1103–1113. https://doi.org/10.1021/cs400010q.

[59] A.M. Wernbacher, P. Kube, M. Hävecker, R. Schlögl, A. Trunschke, Electronic and Dielectric Propreties of MoV-Oxide (M1 Phase) under Alkane Oxidation Conditios, J. Phys. Chem. C 123 (2019) 13269–13282.

[60] V.D.B.C. Dasireddy, M. Huš, B. Likozar, Effect of O2, CO2 and N2O on Ni-Mo/Al2O3 catalyst oxygen mobility in n-butane activation and conversion to 1,3-butadiene, Catal. Sci. Technol. 7 (2017) 3291–3302. https://doi.org/10.1039/c7cy01033h.

[61] J.M. López Nieto, B. Solsona, R.K. Grasselli, P. Concepción, Promoted NiO Catalysts for the Oxidative Dehydrogenation of Ethane, Top. Catal. 57 (2014) 1248–1255. https://doi.org/10.1007/s11244-014-0288-2.

[62] Y. Zhou, F. Wei, J. Lin, L. Li, X. Li, H. Qi, X. Pan, X. Liu, C. Huang, S. Lin, X. Wang, S. Lin, X. Wang, Sulfate-Modified NiAl Mixed Oxides as Effective C-H Bond-Breaking Agents for the Sole Production of Ethylene from Ethane, ACS Catal. 10 (2020) 7619–7629. https://doi.org/10.1021/acscatal.0c02347.

[63] A. de Arriba, B. Solsona, A.M. Dejoz, P. Concepción, N. Homs, P.R. de la Piscina, J.M. López Nieto, Evolution of the optimal catalytic systems for the oxidative dehydrogenation of ethane: The role of adsorption in the catalytic performance, J. Catal. 408 (2022) 388–400. https://doi.org/10.1016/J.JCAT.2021.07.015.

Chapter 5: Photoelectrocatalytic transformation of N_2O

The following papers have been published related to the results of the present chapter:

- **Sánchez-García G.**, Pérez-Calvo A., Fernández-Domene R.M., Blasco-Tamarit E., Sánchez-Tovar R., Solsona B., *Synthesis of CuO_X nanostructures in novel electrolytes under hydrodynamic conditions for photoelectrochemical applications*, Dalton Transactions 52 (2023) 14453–14464, https://doi.org/10.1039/d3dt02017g
- **Sánchez-García, G.**, Da Silva, E., Fernández-Domene R.M., Cháfer, A., González-Alfaro, V., Solsona, B. and Sánchez-Tovar, R., *TiO_2 nanostructures synthesized by electrochemical anodization in green protic ionic liquids for photoelectrochemical applications*, Ceramics International 49 (2023) 26900-26909, https://doi.org/10.1016/j.ceramint.2023.05.227

The aim of this chapter is to analyze the photoelectrochemical behavior of the synthesized metal oxide nanostructures, in order to assess one of the main goals of this thesis, which is the photoelectrocatalytic reduction of nitrous oxide. This chapter is divided into two sections, each one of them corresponding to different photoelectrocatalysts (metallic oxide semiconductors). In each section, results of characterization and the application in the photoelectro-reduction of N_2O will be discussed.

5.1 CuOx photoelectrocatalysts

In the present thesis, copper oxide photoelectrocatalysts have been synthesized and tested in the N_2O decomposition by photoelectrocatalytic reduction. CuO_X is a p-type semiconductor with interesting photoelectrochemical properties and it has been widely used in CO_2 electro-reduction. Therefore, it has been suggested as a candidate photocathode for the mitigation of nitrous oxide by analogy.

The use of copper oxide photocathodes has drawn attention due to its high absorption coefficient in the UV-Vis region. Both copper oxides have narrow bandgaps: 1.3-1.7 eV (CuO) and 2.0-2.5 eV (Cu_2O) [1]. Copper (II) oxide achieves higher efficiencies than Cu_2O, as it is considered to be better suited thermodynamically, concerning the band gap values. Nanostructures with a higher presence of Cu_2O seem to be more interesting, since this oxide has a greater p-type character (higher number of cationic vacancies) and a higher charge mobility than CuO [1]. Nevertheless, other studies have reported that a mixture of both oxides enhances the photoelectrochemical response of the CuO_X photocathode [2,3].

First of all, different complexing agents in the ethylene glycol-based electrolyte were tested during anodization, in order to determine the best synthesis pathway for efficient copper oxide nanostructures. The use of an appropriate complexing agent has been reported to improve the surface area and the electrochemical properties of bare metal oxides [4,5]. For that purpose, electrochemical anodization of copper was carried out for 5 minutes employing 0.05M solutions of oxalic acid and sodium fluoride, studying the addition of sodium hydroxide 0.1M to both electrolytes as well. In addition, the influence of anodization time, electrolyte base and hydrodynamic conditions was also evaluated, after the optimal complexing agent was chosen. Hence, anodization was carried out for 10 and 15 minutes with the 0.05M oxalic acid and 70% ethylene glycol electrolyte. Apart from ethylene glycol, which was also tested in other proportions (50 and 90%),

formamide and ethanol were also used as electrolytes in the same proportions as the ethylene glycol solutions. Finally, 5 minute-electrochemical anodization under different rotation speeds (0, 250 and 500 rpm) were undertaken for the anodization solution of 0.05M oxalic acid and 70% ethylene glycol. Table 5.1 shows a summary of the different samples synthesized throughout the entire study.

Table 5. 1. All copper oxide photoelectrocatalysts synthesized in this work by electrochemical anodization.

Sample [a]	Electrolyte	CuO_X phase detected
0.05M Ox.	0.05M oxalic acid, 70%EG	Cu_2O >> CuO
0.05M Ox. + NaOH	0.05M oxalic acid + 0.1M sodium hydroxide, 70%EG	Cu_2O > CuO
0.05M NaF	0.05M sodium fluoride, 70%EG	Cu_2O < CuO
0.05M NaF + NaOH	0.05M sodium fluoride + 0.1M sodium hydroxide, 70%EG	Cu_2O, CuO
0.05M Ox-10 min	0.05M oxalic acid, 70%EG	-
0.05M Ox-15 min	0.05M oxalic acid, 70%EG	-
0.05M Ox-50EG	0.05M oxalic acid, 50%EG	-
0.05M Ox-90EG	0.05M oxalic acid, 90%EG	-
0.05M Ox-50FA	0.05M oxalic acid, 50%FA	-
0.05M Ox-70FA	0.05M oxalic acid, 70%FA	-
0.05M Ox-90FA	0.05M oxalic acid, 90%FA	-
0.05M Ox-50EtOH	0.05M oxalic acid, 50%EtOH	-
0.05M Ox-70EtOH	0.05M oxalic acid, 70%EtOH	-
0.05M Ox-90EtOH	0.05M oxalic acid, 90%EtOH	-
0.05M Ox-250 rpm	0.05M oxalic acid, 70%EG	Cu_2O >> CuO
0.05M Ox-500 rpm	0.05M oxalic acid, 70%EG	Cu_2O < CuO

[a] All samples that are not labelled otherwise, are anodized in a 70% (v/v) EG electrolyte, for 5 minutes and under static conditions.

First of all, the results obtained for the CuO_X photocathodes synthesized with different complexing agents are displayed. As has been outlined before in section

3.2.1, copper was anodized at 20V and 50ºC in a 70% (v/v) ethylene glycol electrolyte. Figure 5.1 shows the current density transients registered for all studied samples.

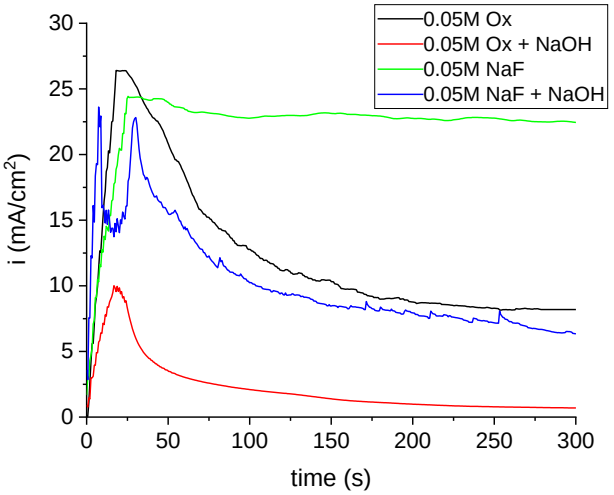

Figure 5. 1. Current density vs. time curves registered during electrochemical anodization at 20V and 50ºC in different 70% (v/v) electrolytes: oxalic acid (Ox) and NaF 0.05M with and without NaOH.

From Figure 5.1, it can be concluded that curves of samples anodized in oxalic acid containing electrolytes show almost no differences in shape, except for the maximum current density reached. First, current density gradually increases as the potential is being slowly applied. Then, two stages of typical anodization curves are clearly appreciated. Once the 20V are fully applied, current density steadily drops (stage I) until it reaches a more or less constant value (stage II). This decrease during stage I is attributed to the formation of a compact layer on the exposed metallic surface. As the copper salt layer grows thicker, less surface area is exposed to the electrolyte, and the flow of current is hindered. In this case, equation 5.1 describes the layer being formed:

$$Cu + {C_2O_4}^{2-} \rightarrow CuC_2O_4 + 2e^- \qquad \text{Eq. 5. 1}$$

This copper oxalate layer is later re-dissolved, leading to the formation of the nanostructure. When this occurs, some surface becomes exposed again and can

result in a slight current density increase. The rates of formation and dissolution of the layer are pretty similar, which is manifested as constant current density values.

On the other hand, anodization curves are different when sodium fluoride is used as a complexing agent. First, the shape of the NaF curve suggests that precipitation does not take place and that the layer does not completely form during the anodization process, which will lead to a different nanostructure morphology. However, the formation of the oxide layer is facilitated by the addition of NaOH to the electrolyte. As can be observed in Figure 5.1, current density in the NaF+NaOH sample exhibits a double peak at the beginning of the process. It is assumed that a soluble and unstable layer is initially formed, and then, the described precipitation-dissolution mechanism takes place. It is believed that when the electrolyte is a basic solution (NaF as a complexing agent or sodium hydroxide being involved) the formation of the precipitate layer follows the next equation:

$$Cu + 2OH^- \rightarrow Cu(OH)_2 + 2e^- \qquad \text{Eq. 5. 2}$$

Therefore, when NaOH is added to the oxalic acid solution it is more likely that Eq. 5.2 takes place instead of Eq. 5.1. In all cases, after anodization a thin blue precipitate covered the nanostructures, but it was mostly washed away when samples were rinsed with D.I water. Copper oxalate and copper hydroxide were decomposed into a mixture of CuO and Cu_2O [6] after annealing.

From the analysis of the anodization curves, it can be concluded that the NaF electrolyte appears to be an inadequate solution for the synthesis of copper oxide nanostructures. However, further characterization of all samples must be carried out in order to determine the nanostructure with the best morphology, composition and electrochemical properties.

Field emission scanning electron microscopy (FE-SEM) was used to study the surface morphology of the anodized nanostructures. Representative images of all samples are shown in Figure 5.2.

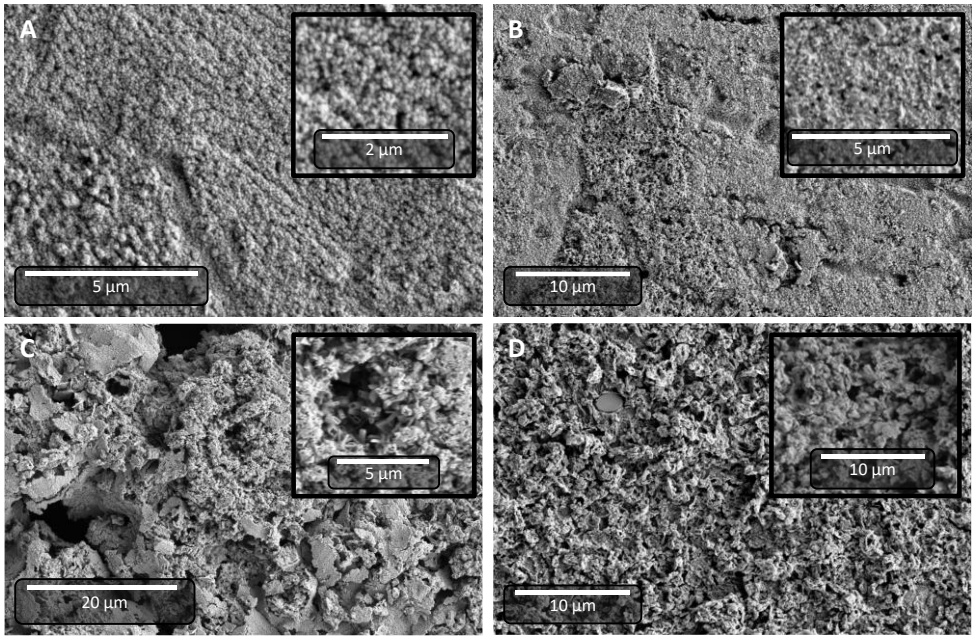

Figure 5. 2. FE-SEM images of copper oxide nanostructures synthesized by copper electrochemical anodization in different 70% (v/v) EG electrolytes: (A) 0.05M oxalic acid, (B) 0.05M oxalic acid + 0.1M NaOH, (C) 0.05M NaF, (D) 0.05M NaF + 0.1M NaOH.

Figure 5.2 confirms the growth of oxide nanostructures during the copper electrochemical anodization using different complexing agents. However, different morphologies are observed, depending on the employed electrolyte. These morphologies are related to the current density transients explained before, since they describe the formation behavior of each sample.

When copper films are anodized in 0.05M oxalic acid electrolyte, a more uniform morphology can be observed, as illustrated by Figure 5.2A. Here, nanostructures are shaped as spheres, with an average diameter of 91 nm. The addition of sodium hydroxide to the mentioned electrolyte has a negative impact on

the synthesized nanostructures. Figure 5.2B shows that nanoparticles lose their shape, leading to a more heterogeneous surface.

Furthermore, Figure 5.2C suggests that nanostructures also become more heterogeneous when NaF is involved during the anodization process. Unshaped regions are predominant, and some brick-like areas are noticed in the surface of the copper oxide film, thanks to the magnification of the FE-SEM image. Figure 5.2D confirms further the heterogeneity of nanostructures with the addition of sodium hydroxide to the anodizing electrolyte.

XRD patterns of all samples are exhibited in Figure 5.3. First, diffraction peaks assigned to the (111), (200) and (220) planes of Cu substrate (■) can be observed at $2\theta = 43.4°$, 50.4° and 74.1°, respectively [7,8] (JCPDS: 04-0836). In Figures 16B and 16C, smaller peaks can be observed at $2\theta = 36.5°$, 38° and 61.5°. The first and last peak can be attributed to the diffraction of (111) and (220) planes of copper (I) oxide, respectively [9,10] (JCPDS: 78-2076), while the peat at $2\theta = 38°$ corresponds to the (200) plane of copper (II) oxide [8,11] (JCPDS: 48-1548).

When copper is anodized in basic solution, Cu^{2+} ions are released and Eq. 5.2 takes place, as has been outlined before [8,11]. Therefore, it is reasonable that samples anodized in NaF electrolytes or with NaOH involved, CuO phases are more present (▲). On the other hand, copper oxalate formed during anodization (Eq. 5.1) transforms into Cu_2O (●), leading to a bigger presence of this phase in samples anodized with oxalic acid.

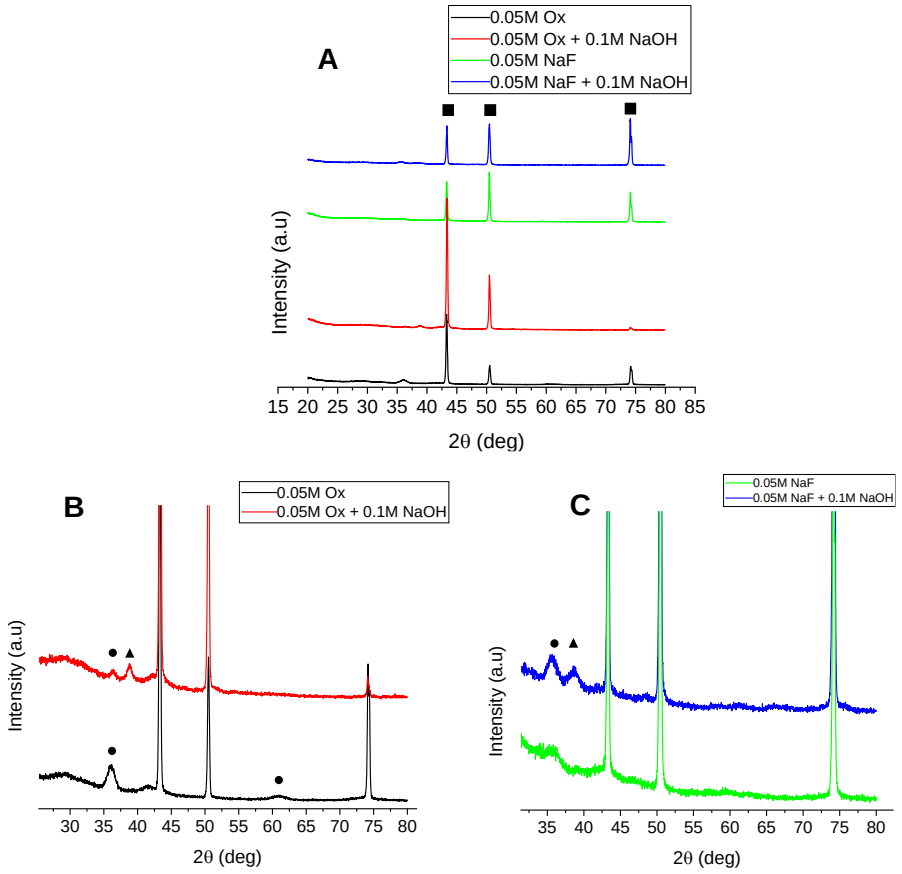

Figure 5. 3. (A) XRD patterns of copper oxide nanostructures after anodization at 20V and 50ºC in different electrolytes with 70% (v/v) EG and at 0 rpm, (B) XRD pattern magnification of oxalic acid anodized samples, (C) XRD pattern magnification of NaF anodized samples. (■) metallic Cu, (▲) CuO, (●) Cu_2O.

Figure 5.4A shows the Raman spectra of the copper oxide nanostructures, which also reveals the presence of both copper oxide phases in all samples. Peaks at 145, 218 and 636 cm^{-1} are attributed to Cu_2O, while peaks at 293, 342 and 620 cm^{-1} correspond to CuO [9,10]. Despite being both phases clearly present in every sample, some differences are noticeable. For instance, peaks at 145, 218 and 636 cm^{-1} are more defined in oxalic acid anodized samples than in NaF anodized samples, meaning that the first nanostructures have a higher presence of Cu_2O. In addition, intensity of CuO peaks grows as intensity of Cu_2O peaks decreases in samples were

NaF is used as complexing agent during anodization, which means that copper (II) oxide prevails over copper (I) oxide in these samples.

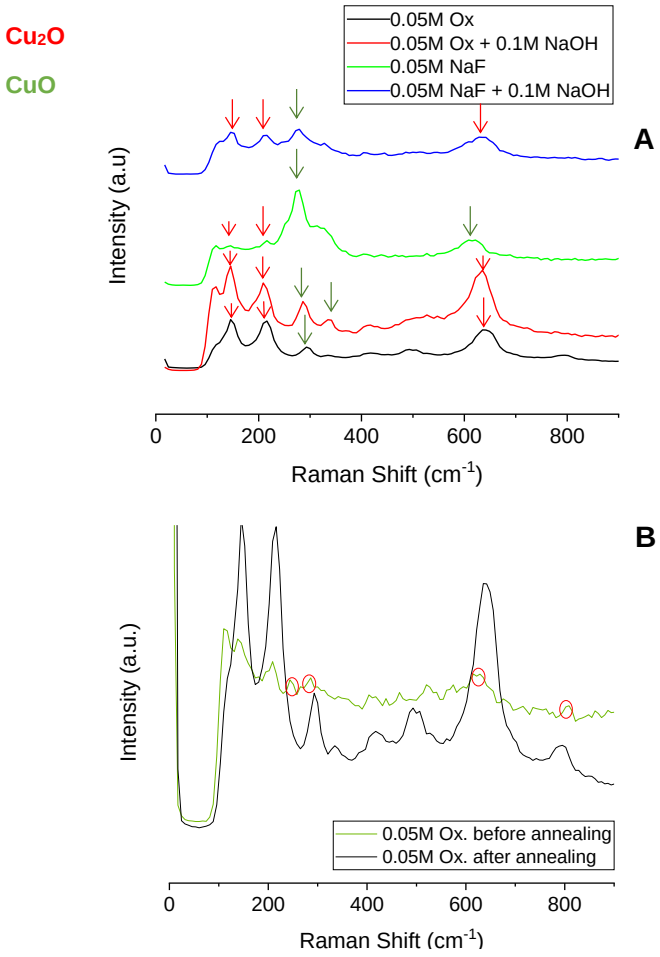

Figure 5. 4. (A) Raman spectra of Cu_2O/CuO nanostructures anodized in different electrolytes with 70% (v/v) EG and at 0 rpm., (B) Raman spectra of the sample anodized in 70% (v/v) EG with 0.05M oxalic acid before and after annealing. Red circles highlight the Raman peaks associated with copper oxalate (CuC_2O_4).

Figure 5.4B confirms what has been stated before about copper oxalate transforming into copper (I) oxide after annealing. It is clear that copper oxalate peaks are absent after the heat treatment and change into a mixture of oxide phases, where cuprous oxide is predominant. Hence, it makes sense that samples anodized

in oxalic acid electrolytes have more Cu_2O than the samples anodized in NaF. Nevertheless, both oxides appear in similar ratios when sodium hydroxide is involved during anodization. This is in accordance with the XRD results, since copper (II) oxide formation is promoted in basic solutions and the addition of NaOH to the oxalic acid electrolyte increases its pH [8,11].

DR-UV-Vis characterization was also carried out to observe the response of the samples to visible and ultraviolet light. Depending on the recorded spectra, different Cu compounds can be identified as well as information about their physical and electronic structures. Absorbance spectra of the copper oxide nanostructures anodized under static conditions and different electrolytes are exhibited in Figure 5.5.

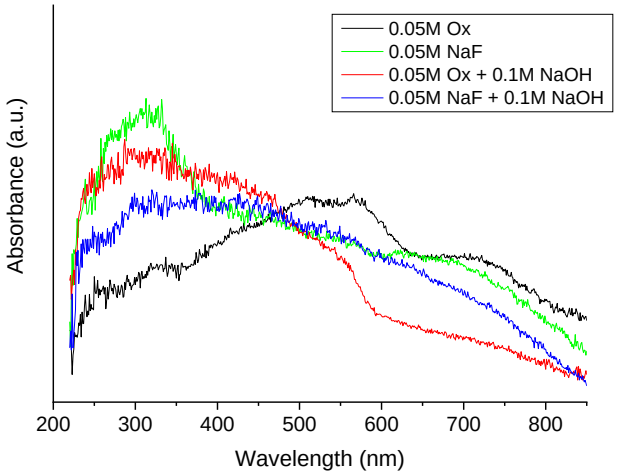

Figure 5. 5. DR-UV-Vis spectra of CuOx nanostructures anodized in different electrolytes with 70% (v/v) EG and under static conditions.

It is clear that, the shape of the spectra is determined by the nature of the complexing agents used during anodization. For example, when samples are synthesized in oxalic acid containing electrolytes the main absorbance band is between 380 and 550 nm, whereas when the complexing agent is NaF the main band becomes between 240 and 380 nm, being the center ca. 300 nm.

Absorbance at intermediate wavelengths (380-550 nm) is known to be associated with the presence of Cu^+ (Cu_2O) [12,13], while lower wavelengths (240-380 nm) are typical of Cu^{2+} species (CuO) [13]. Although it has been stated that CuO enhances absorption at high wavelengths, ca. 700 nm [13,14], this tendency is not clearly observed in these samples. According to the registered spectra, the formation of copper (I) oxide is favored by the presence of oxalic acid during anodization, whereas with NaF, CuO formation prevails. Exact phase identification is not possible from these UV-Vis patterns and it is very likely that both oxides co-exist. However, with the addition of NaOH a very wide band appears, from 200 to 600-800 nm, hinting the formation of both copper oxide phases.

These results are in accordance with XRD and Raman spectra, indicating the presence of both copper oxide phases in all samples, but prevailing one oxide over the other depending on the electrolyte used for anodization.

Figure 5.6 shows the photocurrent densities vs. potential curves for the different nanostructures registered during photoelectrochemical water splitting tests. According to Figure 5.6, all samples behave as p-type semiconductors, due to the negative current densities recorded under illumination (cathodic photocurrent).

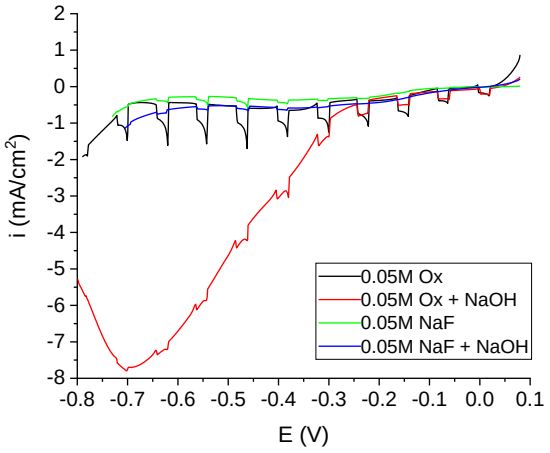

Figure 5. 6. Photocurrent transient vs. potential for the copper oxide nanostructures anodized in different electrolytes with 70% (v/v) EG at stagnant conditions under UV-light (λ = 365 nm).

Copper oxide films anodized in 0.05M oxalic acid electrolyte present the best photoelectrochemical performance, since the generated photocurrent density is the highest (in absolute value). This behavior has been related to several factors.

For instance, from Figure 5.2, it is clear that the 0.05M Ox. sample presents the most homogeneous surface, as well as the existence of spheres, which leads to a better charge carrier mobility. Furthermore, a major presence of highly (111) oriented Cu_2O (Figure 5.3) in the formation of the mixed copper oxide nanostructure (CuO and Cu_2O) can also explain the better photoelectrochemical performance, since this oxide phase improves the hole collection efficiency [15,16]. Moreover, the copper oxide nanostructure synthesized in 0.05M oxalic acid electrolyte presents the lowest Cu metal content (as seen in Figure 5.3), which is known to reduce the photoactivity of nanostructures [9,16].

From Figure 5.4, it can be inferred that electrolytes with oxalic acid as complexing agent produce nanostructures with more copper (I) oxide than the electrolytes containing NaF, where CuO is the predominant oxide phase. Although cupric oxide is known to have a better light absorption due to its narrower band gap (1.3-1.8 eV), Cu_2O has a higher number of copper vacancies and presents a better mobility of these holes, since it has a more p-type character [1]. Thus, it can be concluded that a mixture of both copper oxide phases, but with a bigger presence of copper (I) oxide, improves the photoelectrochemical response of nanostructures.

In addition, longer anodization times were tested in order to see the effect on the photoelectrochemical response. Anodization curves for nanostructures synthesized for 5, 10 and 15 minutes in 0.05M oxalic acid electrolyte are presented in Figure 5.7. As it can be observed, all samples follow the same formation process, where a thin layer of precipitate grows, and it is later re-dissolved so that the structure can develop

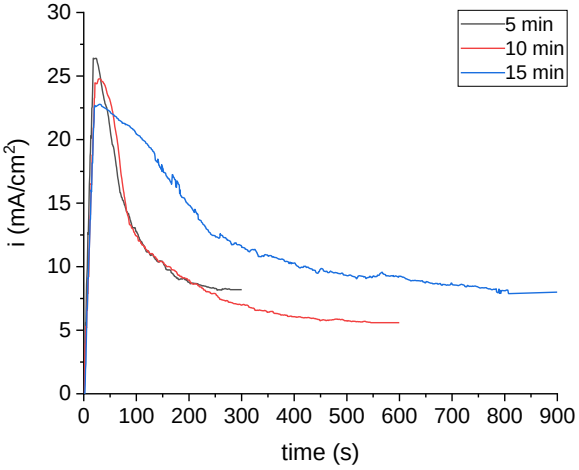

Figure 5. 7. Current density curves registered during electrochemical anodization in 70% (v/v) EG with 0.05M oxalic acid at 0 rpm and at different times: 5, 10 and 15 minutes.

From Figure 5.8, where FESEM images are exhibited, it can be concluded that longer anodization times lead to the growth of bigger but fewer nanospheres, since the nanosphere density decreased from 1556/m^2 at 5 minutes to 201 and 182/m^2 at 10 and 15 minutes, respectively.

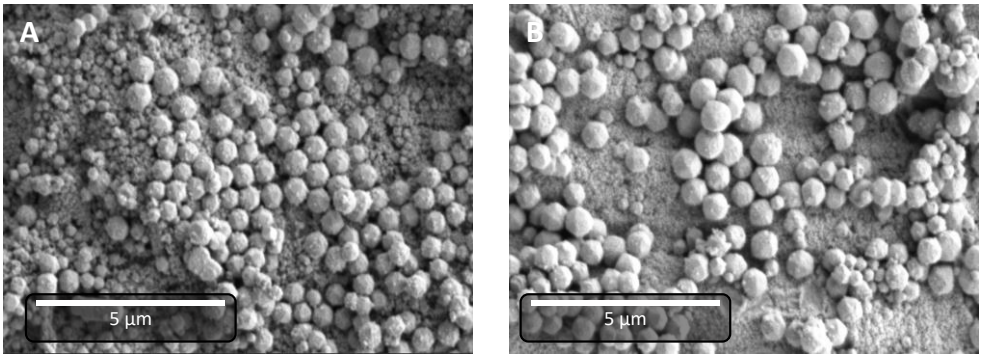

Figure 5. 8. FE-SEM images of the copper oxide nanostructures synthesized by electrochemical anodization in 70% (v/v) EG with 0.05M oxalic acid at 0 rpm and different times: (A) 10 minutes, (B) 15 minutes.

Photocurrent densities vs. potential curves for the samples anodized for different times are shown in Figure 5.9.

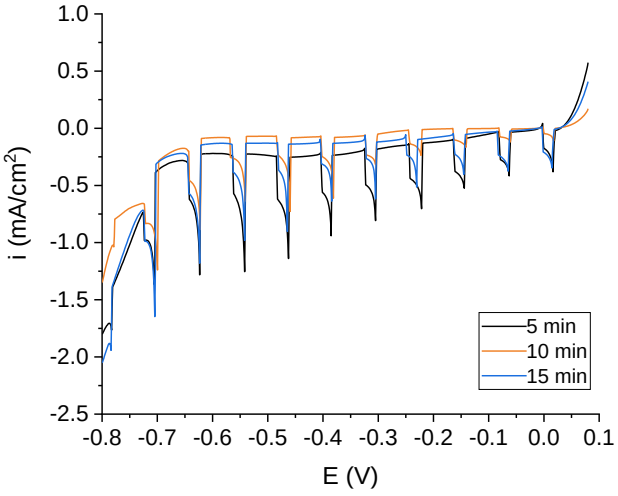

Figure 5. 9. Photocurrent transient vs. potential for the copper oxide nanostructures anodized for different durations in 0.05M oxalic acid, 70% (v/v) EG at stagnant conditions under UV-light (λ = 365 nm).

It should be noted that photocurrent values did not increase despite the longer anodization process and even decreased when anodization was carried out for 15 minutes. This is believed to be due to the fewer nanospheres available to participate in the photoelectrocatalytic process.

Other synthesis formulations (Figure 5.10) were tested in order to try to improve the photoelectrochemical performance of the best nanostructure: 0.05M oxalic acid. For this purpose, samples were anodized in electrolytes containing different ethylene glycol concentrations (50 and 90% (v/v)), and in different solvent electrolytes (ethanol and formamide at 50, 70 and 90% (v/v)). Lower concentrations of these solvents could not be tested due to the vigorous bubble formation during anodization that caused the surface to be too heterogeneous. This led to the collection of irreproducible data.

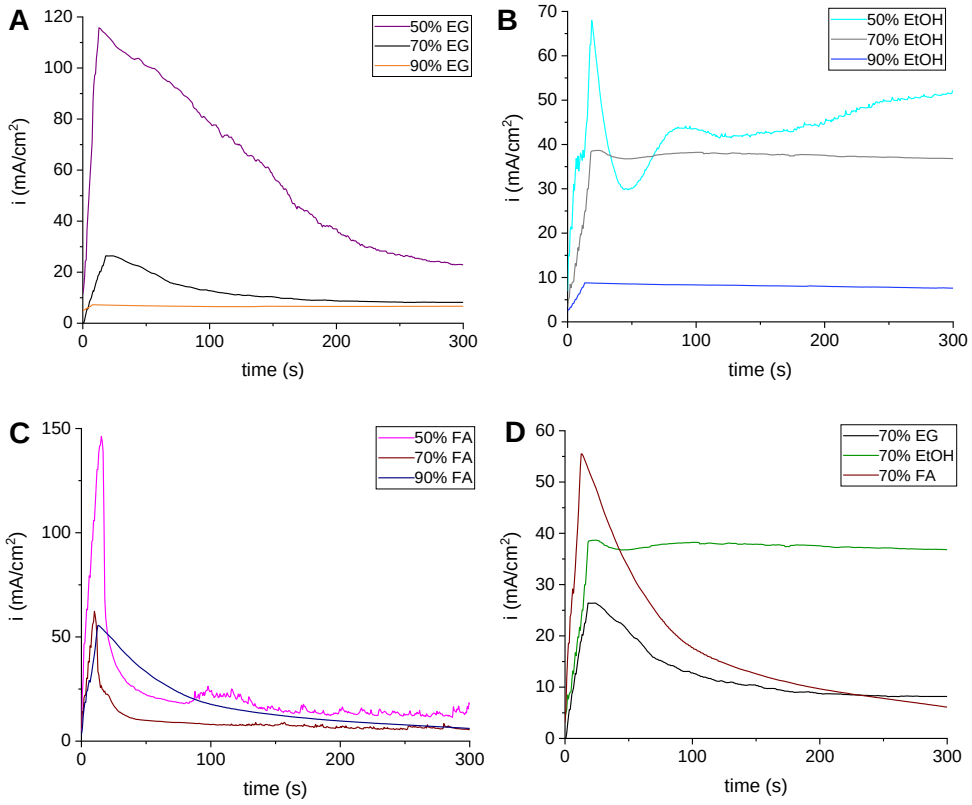

Figure 5. 10.Current density curves registered during electrochemical anodization of copper in different solvents and concentrations: (A) Ethylene glycol 50, 70 and 90% (v/v), (B) ethanol 50, 70 and 90% (v/v), (C) formamide 50, 70 and 90% (v/v), and (D) 70% (v/v) of ethylene glycol, ethanol and formamide.

In all cases, it is clear that 50% of water in the electrolyte gives very high current densities during anodization, which means that the initial dissolution of the metallic layer is taking place. However, the subsequent precipitate layer formation and re-dissolution do not take place in some of the samples. For example, Figure 5.10A suggests that the precipitate layer is not completely developed when anodization with 50% ethylene glycol ends, meaning there is no time left for it to re-dissolve and form the nanostructure. In the same way, with the 90% EG electrolyte the current density curves imply that no precipitate layer is formed at all during the process, since current density stays constant throughout the electrochemical

anodization. This situation can also be appreciated in the curves from 70% and 90% ethanol electrolytes depicted in Figure 5.10B. From Figure 5.10D it could be suggested that well-defined nanostructures are only formed in 70% ethylene glycol and formamide electrolytes, since both anodization curves present the typical shape for nanostructure growth.

Some representative FE-SEM images of these samples are shown in Figure 5.11.

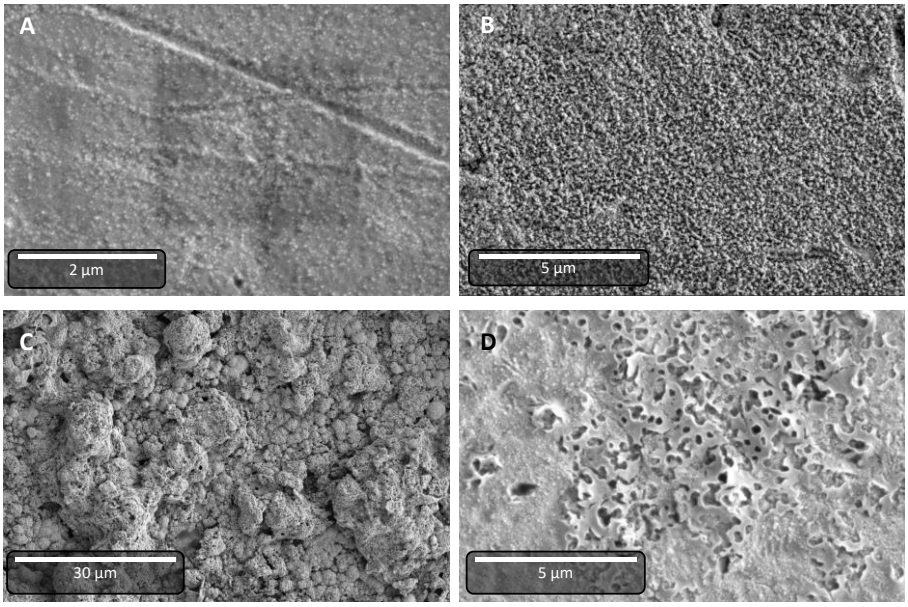

Figure 5. 11. FE-SEM images of copper oxide nanostructures synthesized by electrochemical anodization with 0.05M oxalic acid in different electrolyte organic solvents: (A) 50% ethylene glycol, (B) 90% ethylene glycol, (C) 70% ethanol, and (D) 70% formamide.

From Figure 5.11A, it can be concluded that nanostructures are not completely formed in 50% (v/v) ethylene glycol-containing electrolyte, the surface of it being very heterogeneous. This is in agreement with the shape of the anodization curve of this sample displayed in Figure 5.10A. Furthermore, 90% (v/v) of ethylene glycol in the electrolyte led to the nanoparticles being too packed together, as seen in Figure 5.11B, which could later result in poorer performance. Regarding the other

solvent samples, very amorphous nanostructures are formed with no clear geometry. To be more specific, ethanol forms irregular blocks of oxide due to the precipitate layer not being able to grow consistently (Figure 5.11C). Moreover, Figure 5.11D exhibits the formation of a compact oxide layer when anodization is carried out in a 70% (v/v) FA electrolyte. The higher dielectric constant of the formamide (111 vs. 37 from EG [17]) results in a greater attack from the fluoride ions, which then leads to the growth of a very thick layer. This is in accordance with the higher currents reached during anodization

All samples were tested in photoelectrochemical water splitting and results are shown in Figure 5.12. Ethylene glycol-based electrolytes improve the photoelectrochemical behavior of the catalysts, especially when anodizing with 70% (v/v), according to Figure 5.12.

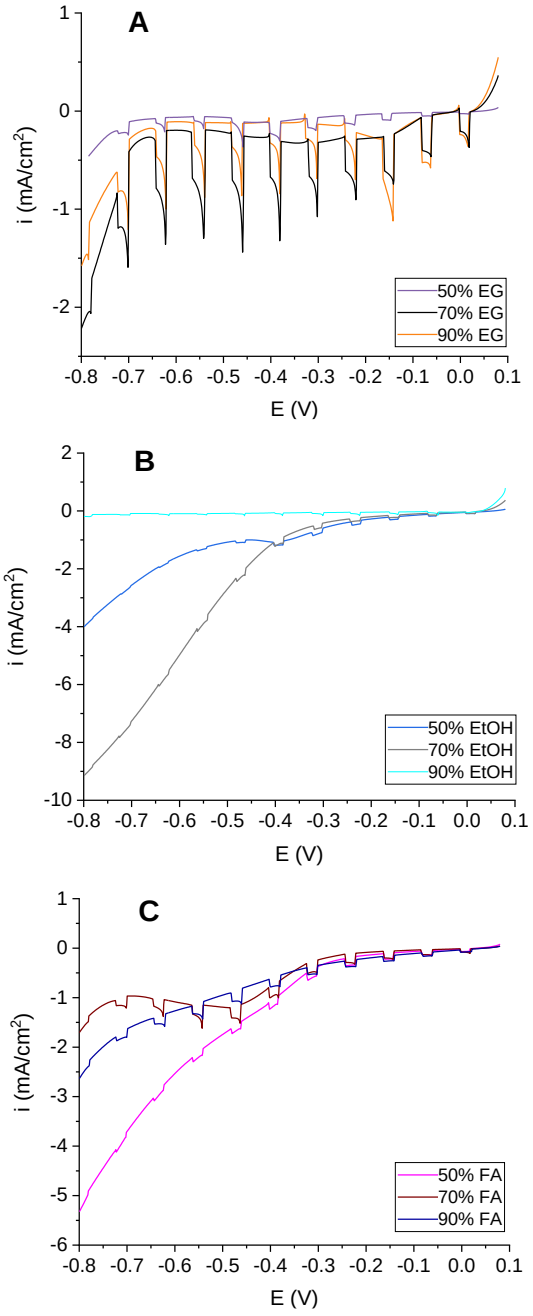

Figure 5. 12. Photocurrent density vs. potential curves for copper oxide nanostructures anodized in the presence of 0.05M oxalic acid using different organic solvent-based electrolytes in different amounts under UV-light (λ=365 nm): (A) ethylene glycol, (B) ethanol, (C) formamide.

The worse photoelectrochemical performance of both 50 and 90% (v/v) ethylene glycol samples (Figure 5.12A) are linked to the morphology issues discussed before, since nanoparticles are not totally formed with 50% and are too packed together when synthesized with 90% EG, which prevents light absorption. The worse charge carrier mobility of ethanol and formamide synthesized samples can be explained by their amorphous morphology, since the formation of irregular blocks eliminates the direct pathways for electron transfer provided by the ordered spheres [18]. As a result, charge recombination processes occur more often, lowering the electron transfer efficiency and leading to a bad photoelectrochemical performance of both solvents. Furthermore, it could be stated that ethanol and formamide anodized samples are more easily unstable under reaction conditions.

The influence of hydrodynamic conditions during the anodization of copper for 5 minutes in 0.05M oxalic acid, 70% (v/v) ethylene glycol-based electrolyte were analyzed. For this purpose, the copper electrode was rotated at 250 and 500 rpm during anodization. Figure 5.13 shows the anodization curves of samples synthesized under different rotation speeds. Each sample follows the same tendency as the 0.05M ox. sample shown in Figure 5.1. Nonetheless, some differences can be emphasized.

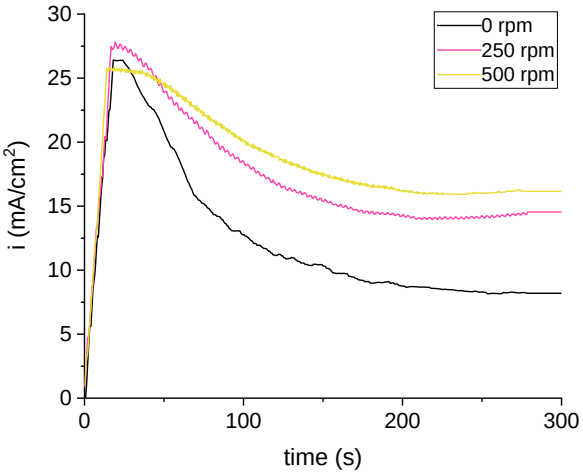

Figure 5. 13. Anodization curves of copper oxide in 70% (v/v) EG with 0.05M oxalic acid at 20V and 50ºC under different hydrodynamic conditions (0 to 500 rpm).

For example, current density decreases more gradually as the rotation speed increases. This means that nanostructure growth takes place at a slower rate. Moreover, when agitation of the electrode during anodization is involved final current density values are much higher, which can be due to the formation of a more porous surface allowing the electrolyte to reach more substrate and generating the higher current density.

FE-SEM images were taken of these samples in order to assess the effect of hydrodynamic conditions on their morphology (Figure 5.14).

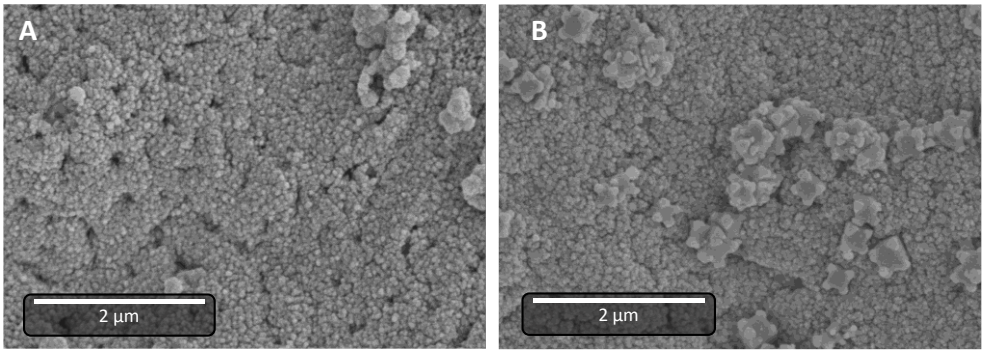

Figure 5. 14. FE-SEM images of copper oxide nanostructures synthesized by electrochemical anodization with 0.05M oxalic acid under different hydrodynamic conditions: (A) 250 rpm and (B) 500 rpm.

It has been reported that, hydrodynamic conditions can affect the nanostructure growth in two different ways. On the one hand, mass transport can be enhanced and more copper species responsible for the formation of the precipitate layer can be generated. On the other hand, excessive rotation speed can remove these species from the electrode surface and delay the precipitation stage [19,20]. When comparing Figure 5.14A and Figure 5.2A (samples anodized at 250 rpm and 0 rpm, respectively), it is clear that the nanoparticle density is higher when the agitation is added to the anodization process, which indicates that the surface area of the active layer is larger. In addition, nanoparticles are significantly smaller when the anodization takes place with a stirring electrode, since diameters drop from 91 nm at

0 rpm to 65 nm and 77 nm at 250 rpm and 500 rpm, respectively. Smaller sphere diameters combined with a greater surface area improve the catalytic surface of the samples. However, higher rotation speeds during anodization present a negative impact on the morphology of the nanostructure, as Figure 5.14B shows. At 500 rpm, the surface becomes more heterogeneous, since clumps of about 25-30 µm start to grow. Both situations indicate that, in this case, hydrodynamic conditions improve mass transport instead of decreasing the rate of nanostructure growth. To conclude, a better photoelectrochemical behavior is expected for nanostructures anodized under hydrodynamic conditions, especially at 250 rpm, due to a major light absorption. Nevertheless, the clumps present in the 500 rpm sample can interfere in the light harvesting of the nanostructures.

Figure 5.15 exhibits the XRD patterns of the copper oxide films synthesized under different hydrodynamic conditions.

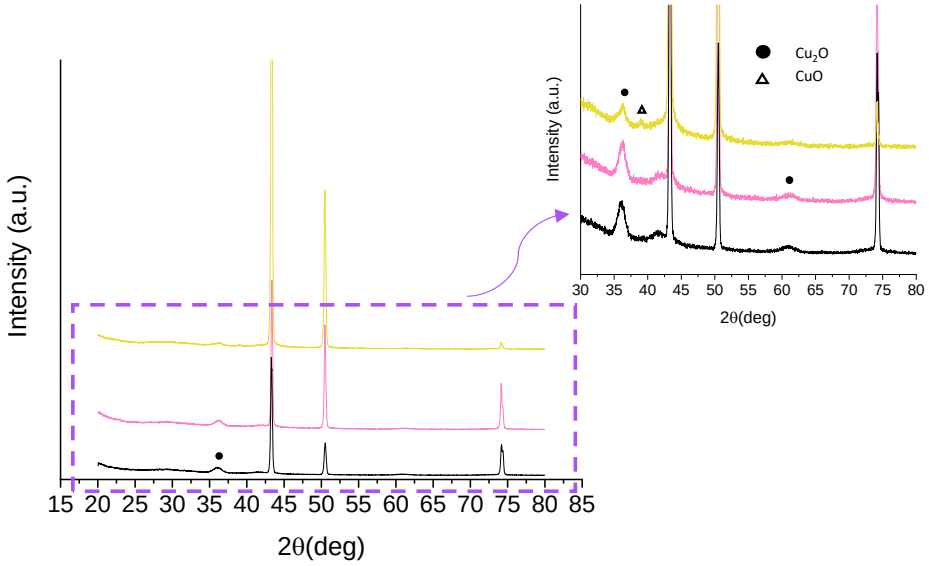

Figure 5. 15. XRD patterns of copper oxide nanostructures synthesized by electrochemical anodization in 70% (v/v) EG and 0.05M oxalic acid electrolyte under different hydrodynamic conditions (0 to 500 rpm).

It can be observed that there are no significant differences between the patterns belonging to 0 and 250 rpm samples. The only copper oxide diffraction peaks detected are at 2θ = 36.5° and 61.5°, which are associated with copper (I) oxide. Nonetheless, the intensity decrease of peaks at 2θ = 36.5° and 61.5° for the 500 rpm sample can be noticed in the magnification of Figure 5.15, meaning that the fraction of Cu_2O is smaller when rotation speed is increased further. Moreover, a new peak can be detected at 2θ = 38°, belonging to CuO. Hence, not only does the amount of cuprous oxide decrease, but the fraction of copper (II) oxide increases when anodization is carried out at 500 rpm.

Raman spectra displayed in Figure 5.16 confirm these results. The Raman spectra presented for each sample show peaks typically assigned to copper (I) oxide (145, 218, 421, 515 and 636 cm^{-1}).

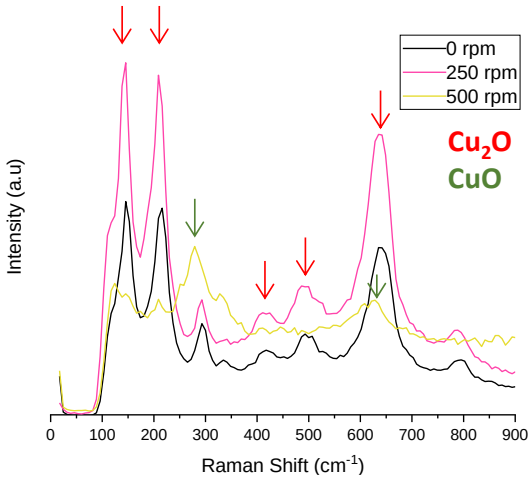

Figure 5. 16. Raman spectra of copper oxide nanostructures synthesized by electrochemical anodization in 70% (v/v) EG and 0.05M oxalic acid electrolyte under different hydrodynamic conditions (0 to 500 rpm).

These peaks decrease in size when the copper electrode rotates at 500 rpm during anodization, while peaks that correspond to copper (II) oxide grow (293 and 620 cm^{-1}). Hence, it could be stated that the presence of CuO prevails over the presence of Cu_2O for rotation speeds above 250 rpm. Having a lower fraction of

cuprous oxide can hinder the mobility of copper vacancies [15], which can lead to a poorer photoelectrochemical performance of the nanostructures.

Transmission electron microscopy analysis was also performed for samples anodized under static (0 rpm) and hydrodynamic conditions (250 and 500 rpm) and results are presented in Figure 5.17.

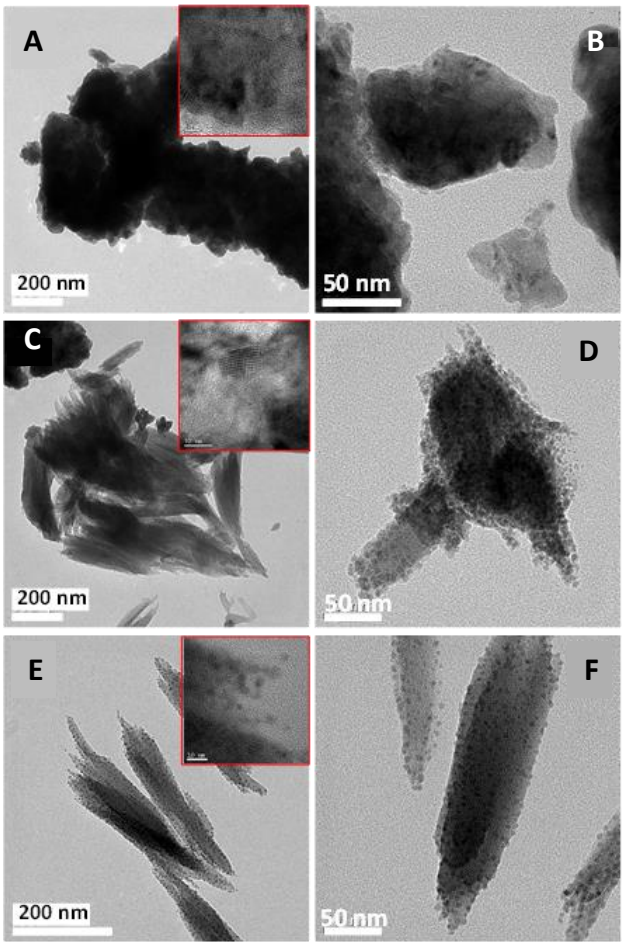

Figure 5. 17. TEM images of copper oxide nanostructures synthesized by electrochemical anodization in 70% (v/v) EG and 0.05M oxalic acid electrolyte under different hydrodynamic conditions (0 to 500 rpm).

From Figures 5.17A,B, it can be seen how samples prepared at 0 rpm present a compact structure. On the other hand, for 250 rpm-anodized samples (Figures

5.17C,D), their structure presents a feather-like shape, despite a few small compact units (minorities). From the magnification in Figure 5.17D, small nanoparticles (3-8 nm) can be noticed scattered over the feather-like units. In the same way, nanostructures synthesized at 500 rpm (Figures 5.17E,F) also present a feather-like shape with units covered by particles of the similar size.

Figure 5.18 shows the DR-UV-Vis spectra of samples anodized in 70% (v/v) EG and 0.05M oxalic acid electrolyte under static and hydrodynamic conditions. From Figure 5.18 it can be inferred as rotation speed increases, so does the absorbance in the UV range. The sample anodized at 0 rpm presents the lowest relative intensity between the band at 200-400 nm and that in the visible range between 400-650 nm. According to this data, as agitation becomes more vigorous during anodization, the Cu^{+}/Cu^{2+} ratio decreases.

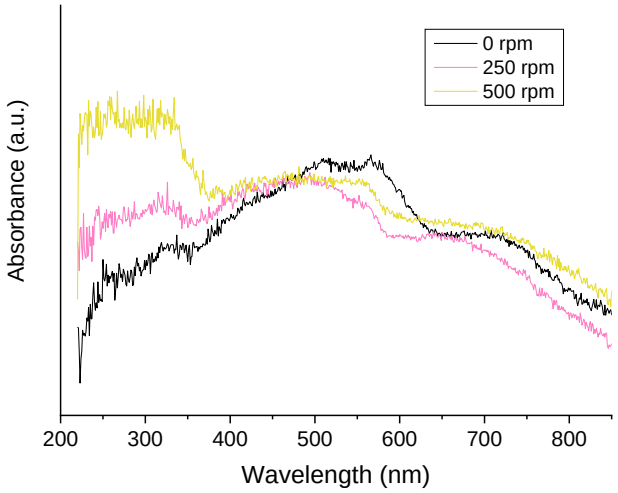

Figure 5. 18. DR-UV-Vis spectra of copper oxide nanostructures synthesized by electrochemical anodization in 70% (v/v) EG and 0.05M oxalic acid electrolyte under different hydrodynamic conditions (0 to 500 rpm).

Due to all samples being a complex mixture of both CuO and Cu_2O, it is difficult to determine the energy band gap.

Photocurrent densities at different applied potentials were recorded at chopped UV-light conditions to study the effect of hydrodynamic conditions on the photoelectrochemical response of the copper oxide nanostructures (see Figure 5.19).

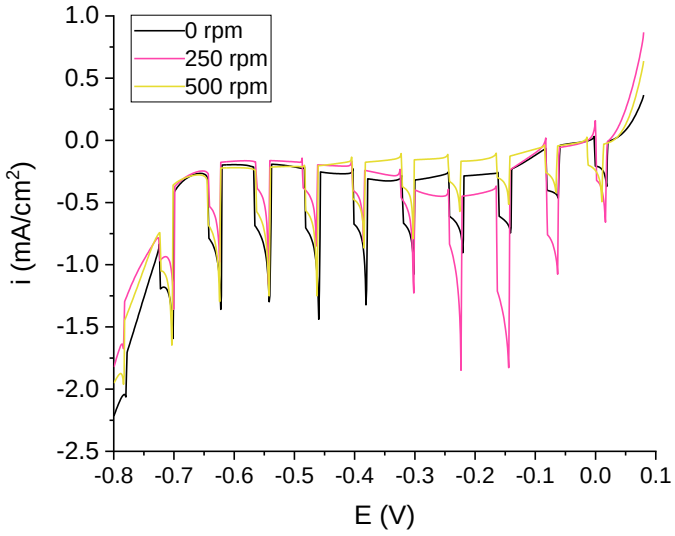

Figure 5. 19. Photocurrent transient vs. potential of copper oxide nanostructures synthesized by electrochemical anodization in 70% (v/v) EG and 0.05M oxalic acid electrolyte under different hydrodynamic conditions (0 to 500 rpm).

As can be seen in Figure 5.19, increasing rotation speed from 0 to 250 rpm has a positive effect on the photoelectrochemical performance of the copper oxide nanostructures. This improved behavior has been associated with the more homogeneous surface observed in Figure 5.14A, where nanoparticles are also smaller and the nanosphere density is higher. Similarly, the lower presence of Cu_2O in the sample anodized at 500 rpm, as seen in Figures 5.15 and 5.16, could be the reason for a worse photoelectrochemical performance, since a smaller fraction of this phase decreases charge carrier mobility. Also, Figure 5.14B displays a more heterogeneous morphology of the 500 rpm anodized nanostructure, which can result in lower light harvesting.

Resistance of the different nanostructures to charge-transfer processes were studied by electrochemical impedance spectroscopy (EIS), and results are shown in

Figure 5.20. Nyquist plots for the different samples in the frequency range from 100 kHz to 1 mHz obtained at a potential of -0.2 V versus Ag/AgCl 3M KCl are presented in Figure 5.20A. Here, two semicircles can be spotted for each plot and they are associated with two different regions of the Bode-module plots in Figure 5.20B. The charge-transfer response of the oxide/electrolyte interface can be used to gather information about the active surface of the nanostructures, and it is usually linked to the semicircle obtained at high and intermediate frequencies [21]. The semicircle at low frequencies, however, is typically related to a compact layer of oxide formed under the nanoparticles [22]. Generally, the impedance of the related electrochemical process is proportional to the amplitude of the semicircle.

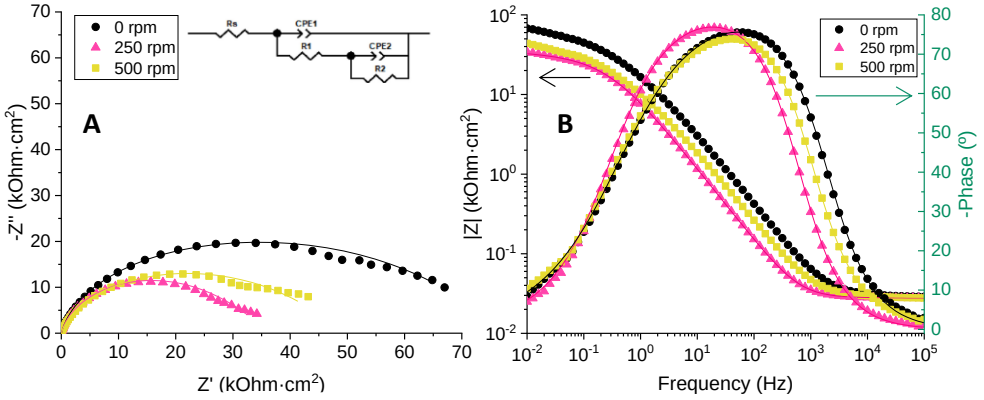

Figure 5. 20. (A) Nyquist plots and (B) Bode plots of copper oxide nanostructures synthesized by electrochemical anodization in 70% (v/v) EG and 0.05M oxalic acid electrolyte under different hydrodynamic conditions (0 to 500 rpm) in 0.1M Na_2SO_4 solution and applied potential of -0.2 $V_{Ag/AgCl}$ (continuous line represents equivalent circuit fitting).

From Figure 5.20A, it can be concluded that the sample anodized at 0 rpm presents the highest impedance, since it is the nanostructure with the largest semicircle. The semicircles of both nanostructures anodized under stirring conditions are smaller, being the smallest the one belonging to the 250 rpm sample. It has been possible to determine the total resistance offered by each nanostructure from the value recorded at the lowest frequency in Figure 5.20B.

According to the two semicircles in the Nyquist plot, an equivalent circuit with two parallel R-C time constants, shown in Figure 5.20A, was used to quantitively study the EIS results. In this case, pure capacitors were substituted by constant phase elements (CPEs) to account for the non-ideality of the system [23,24]. Defective (porous) nanostructures, like these copper oxide photoelectrocatalysts, must be fitted to this type of circuits. It is believed that current can access the compact oxide layer without needing to pass through the nanostructured one first [25]. For this fitting, electrolyte resistance is represented by R_S, while R_1-CPE_1 and R_2-CPE_2 represent charge-transfer resistance at the active parts of the nanostructure/electrolyte interface and resistance offered by the compact copper oxide layer, respectively [26–29]. Table 5.2 shows the results of the total resistance (R_T) and the charge-transfer resistance at the active parts of the nanostructure (R_1) for each nanostructure.

Table 5. 2. Nanostructure resistance: total resistance (R_T) obtained from Bode-module plots and the charge-transfer resistance at the active parts of the nanostructure (R_1) from equivalent circuit fitting.

Sample	**R_T (kOhm·cm^2)**	**R_1 (kOhm·cm^2)**
0rpm	67.70	27.27
250rpm	34.44	9.64
500rpm	43.89	15.00

As expected, the resistance of the active parts of the nanostructures decreases as rotation speed increases, meaning there is an improvement of electrical conductivity of the nanostructures synthesized under hydrodynamic conditions. Therefore, it could be suggested that the better photoelectrochemical behavior of these samples can be due to a better electron transfer and hole diffusion caused by the addition of hydrodynamic conditions. Nevertheless, the sample synthesized at the highest stirring speed (500 rpm) presents a higher resistance than that prepared at 250 rpm, confirming that an excessive stirring can be detrimental for the process (Figure 5.19).

Furthermore, it has been reported that materials with a stronger Cu_2O (111) orientation present lower resistance values [16,30,31]. The copper film anodized at 250 rpm in this study has the highest fraction of copper (I) oxide when compared to the rest of samples (see Figures 5.15 and 5.16). Hence, the greater presence of this copper oxide phase in the 250 rpm nanostructure can result in lower charge transfer resistance. Moreover, lower impedance values can also be justified by an improved electron transfer as a result of a more homogeneous morphology (Figure 5.14A). In the same way, the clumpier surface of the 500 rpm sample (Figure 5.14B) can increase the recombination rate of electron-hole pairs and lead to higher resistance values.

These results are in well agreement with the Mott-Schottky plots shown in Figure 5.21, where carrier density of semiconductors can be calculated by representing $1/C^2$ vs. E $V_{Ag/AgCl}$. The negative slopes confirm that the mixed copper oxide nanostructures are p-type semiconductors, where copper (Cu^+/Cu^{2+}) vacancies are the dominant charge carriers [6,9,32].

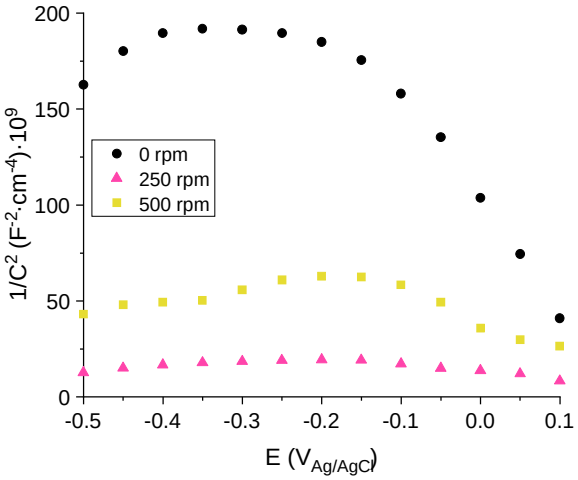

Figure 5. 21. Mott-Schottky plots obtained at a frequency of 5 kHz.

From the slopes of each plot acceptor density (N_A) of each nanostructure can be calculated by using the Mott-Schottky equation (Eq. 3.9), being ε the relative

dielectric constant of CuO_x, displayed in Table 3.3. Table 5.3 summarizes the values of acceptor density (N_A) and flat band potential (E_{FB}) of each sample:

Table 5. 3. Acceptor density (N_A) and flat band potential (E_{FB}) values calculated from MS plots (Figure 5.21) for the nanostructures synthesized by electrochemical anodization in 70% (v/v) EG and 0.05 M oxalic acid electrolyte under different hydrodynamic conditions (0 to 500 rpm).

Sample	**N_A (cm^{-3})**	**E_{FB} ($V_{Ag/AgCl}$)**
0 rpm	$2.01 \cdot 10^{19}$	0.185
250 rpm	$2.68 \cdot 10^{20}$	0.321
500 rpm	$5.55 \cdot 10^{19}$	0.193

Acceptor density is known to be linked to the available copper vacancies on the active surface of the nanostructures. Taking a close look at Table 5.3, it can be said that charge carrier concentration increases when anodization takes place under hydrodynamic conditions, specially at 250 rpm. This can be caused by the larger surface area of the 250 rpm sample being exposed to the electrolyte, leading to an increase in the interfacial capacitance [33]. A relationship can be established between low resistance to charge transfer, high charge carrier density and high photocurrents. A high concentration of copper vacancies enhances electron mobility, which increases the conductivity of the sample (or lowers the resistance) [32] and improves their photoelectrochemical performance when used as photocathodes.

Flat band potentials of the different nanostructures are also displayed in Table 5.3. This is the potential that needs to be applied to the electrode in order to get a photoelectrochemical response. In other words, the onset potential. A higher E_{FB} means that less polarization is needed to achieve response to light, which is the case of the copper oxide nanostructure anodized at 250 rpm. In addition, the more positive the flat band potential, the lower are the chances of electron-hole pairs recombination, which improves the photoelectrochemical efficiency of the nanostructure [3].

5.1.1 Photoelectro-reduction of nitrous oxide with CuO_X as photocathode

Once the preparation of copper oxide nanostructures has been optimized to present suitable electrochemical properties, photoelectro-reduction of nitrous oxide has been studied with the sample that presents the best performance (that prepared at 250 rpm). For a comparative purpose, the sample prepared under static conditions has also been tested. In this case, the synthesized photoelectrocatalyst is used as photocathode, since copper oxide is a p-type semiconductor. Nitrous oxide reduction takes place at the photocathode, while the oxygen evolution reaction takes place at the dark anode. When the photocathode adsorbs light, electrons located in the valence band of the semiconductor are excited and migrate to the conduction band. This leads to the formation of holes, and the overall process is known as the generation of electron-hole pairs (Eq. 5.3). Holes are forced to pass through the external electric circuit to the anode and become responsible for the oxidation of water into oxygen (Eq. 5.4). Meanwhile, electrons travel from the inside of the electrode to the surface and participate in the reduction of nitrous oxide, following equation 5.5 [34,35]. Protons generated as a result of the oxidation of water, pass through the cationic membrane to complete the reduction at the photocathode.

$$CuO_X + h\nu \rightarrow e^- + h^+ \qquad \text{Eq. 5. 3}$$

$$H_2O \rightarrow \frac{1}{2}O_2 + 2H^+ + 2e^- \qquad \text{Eq. 5. 4}$$

$$N_2O + 2H^+ + 2e^- \rightarrow N_2 + H_2O \qquad \text{Eq. 5. 5}$$

Usually, just with the use of light (photocatalytic approach) electron-hole pairs are easily generated. However, the application of an external bias reduces the chances of electron-hole pairs recombination, achieving a higher charge separation and energy conversion efficiency [36,37].

Nanostructured copper oxide anodized at 0 and 250 rpm were tested as photoelectrocatalysts in the reduction of nitrous oxide. Figure 5.22A shows the

evolution of the remaining N_2O during three experiments: a blank test, where no catalyst was employed, and one test for each studied nanostructure.

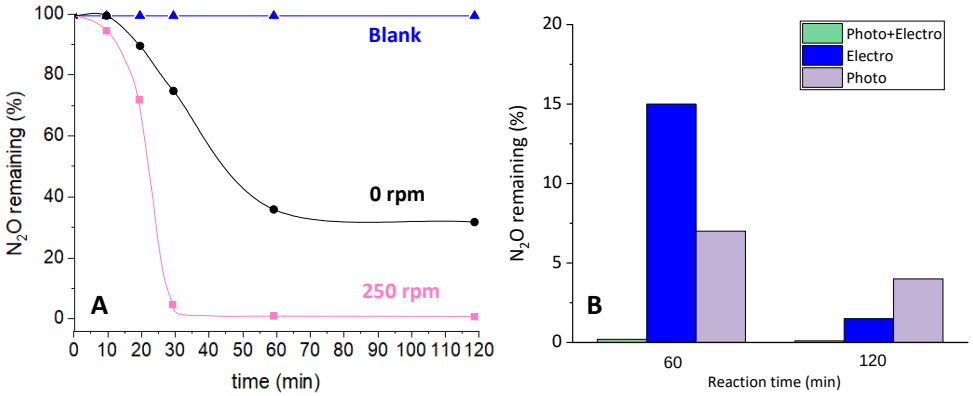

Figure 5. 22. (A) Evolution of the N_2O remaining with the reaction time for the photo+electro combined approach using different photoelectrocatalysts. (B) N_2O remaining after 1 or 2 h of process for the electro ( ), photo ( ) or combined photo+electro ( ) using the sample prepared at 250 rpm.

Both nanostructures follow a similar trend for the first 20 minutes of degradation, where the elimination rate is not very high. However, it can already be appreciated how the 250 rpm sample has a better efficiency than the sample anodized under static conditions. When using the 250 rpm nanostructure, almost no nitrous oxide is left after an hour of experiment, whereas circa 40% still remains with the non-optimized sample. After 2h with the latter sample, nitrous oxide concentration is still significantly high, but complete reduction is achieved with the copper oxide nanostructure anodized at 250 rpm.

Furthermore, the optimized sample was also tested in photo- and electrocatalytic reduction of nitrous oxide to prove that the combined technique (photoelectrocatalysis) is the best approach for this application. Results are displayed in Figure 5.22B. Despite the removal efficiency being quite high for both photo- and electrocatalytic reduction, their results are significantly lower than with the combined approach. Between 5-15% of N_2O is still remaining after an hour with the separate approaches, while only 0.2% remains when photoelectroreduction takes place.

5.2 TiO_2 photoelectrocatalysts

Titanium dioxide has been reported as one of the most effective photoanodes in several photoelectrocatalytic processes, due to its thermal and chemical stability, its appropriate optical and morphological properties and its low manufacture costs [38–40]. Therefore, having previously synthesized the copper oxide photocathode, in this section it has been decided to synthesize an optimized TiO_2 photoanode and test it in the photoelectro-reduction of nitrous oxide.

Titanium dioxide photoelectrocatalysts have been synthesized by many routes. However, electrochemical anodization has proven to provide the best photoelectrocatalytic results with relatively low investment and operational costs [39–41]. Self-organized and well-defined nanotube arrays can be easily developed by controlling the electrolyte and anodization parameters. Moreover, it has been reported that the presence of an ionic liquid in the anodizing electrolyte enhances the photoelectrochemical performance of the formed nanotubes [42]. Therefore, in the present thesis the effect of adding different amounts of a green ionic liquid to the anodizing electrolyte in the synthesis of titanium dioxide photoanodes has been tested. For this purpose, titanium foil was anodized in ethylene glycol based electrolytes (EG), containing 0.05M ammonium fluoride, 1M distilled water, and different concentrations of triethanolamine-based (TEA) ionic liquid (0.25, 0.5, 1.0, 2.0, 4.0% (v/v)). Then, a study about the influence of hydrodynamic conditions on the photoelectrochemical behavior of the best photoelectrocatalysts was also conducted. It must be noted that a sample anodized in an ionic liquid-free electrolyte was also synthesized for comparative reasons, and it is labelled as IL-0. Table 5.4 shows a summary of the different TiO_2 photoelectrocatalysts synthesized throughout the entire study, as well as their anodizing electrolyte.

Table 5. 4. All titanium dioxide photoelectrocatalysts synthesized in this work by electrochemical anodization.

Sample	Electrolyte
IL-0	0.05M NH_4F, 1M H_2O, 70% (v/v) EG
TEA-0.25	0.05M NH_4F, 1M H_2O, 70% (v/v) EG, 0.25% (v/v) TEA IL
TEA-0.50	0.05M NH_4F, 1M H_2O, 70% (v/v) EG, 0.50% (v/v) TEA IL
TEA-1.0	0.05M NH_4F, 1M H_2O, 70% (v/v) EG, 1.0% (v/v) TEA IL
TEA-2.0	0.05M NH_4F, 1M H_2O, 70% (v/v) EG, 2.0% (v/v) TEA IL
TEA-4.0	0.05M NH_4F, 1M H_2O, 70% (v/v) EG, 4.0% (v/v) TEA IL
MEA-1.0	0.05M NH_4F, 1M H_2O, 70% (v/v) EG, 1.0% (v/v) MEA IL
DEA-1.0	0.05M NH_4F, 1M H_2O, 70% (v/v) EG, 1.0% (v/v) DEA IL
TEA-1.0-500 rpm	0.05M NH_4F, 1M H_2O, 70% (v/v) EG, 1.0% (v/v) TEA IL
TEA-1.0-1000 rpm	0.05M NH_4F, 1M H_2O, 70% (v/v) EG, 1.0% (v/v) TEA IL
TEA-1.0-2000 rpm	0.05M NH_4F, 1M H_2O, 70% (v/v) EG, 1.0% (v/v) TEA IL
TEA-0.5-500 rpm	0.05M NH_4F, 1M H_2O, 70% (v/v) EG, 0.50% (v/v) TEA IL
TEA-0.5-1000 rpm	0.05M NH_4F, 1M H_2O, 70% (v/v) EG, 0.50% (v/v) TEA IL
TEA-0.5-2000 rpm	0.05M NH_4F, 1M H_2O, 70% (v/v) EG, 0.50% (v/v) TEA IL
TEA-0.25-500 rpm	0.05M NH_4F, 1M H_2O, 70% (v/v) EG, 0.25% (v/v) TEA IL
TEA-0.25-1000 rpm	0.05M NH_4F, 1M H_2O, 70% (v/v) EG, 0.25% (v/v) TEA IL
TEA-0.25-2000 rpm	0.05M NH_4F, 1M H_2O, 70% (v/v) EG, 0.25% (v/v) TEA IL

First, the results of the titanium dioxide photoanodes anodized with different concentrations of the TEA ionic liquid in the electrolyte are discussed. Electrochemical anodization was performed at 55V for 30 minutes, as has been outlined in section 3.2.2. Figure 5.23 shows the current density curves registered during this process. The inset figure displays how a balance between the rate of titanium oxide formation by applying a potential and the rate of its dissolution due

to the presence of fluoride ions in the electrolyte exists. The three stages of nanotube growth can be recognized in all curves [43].

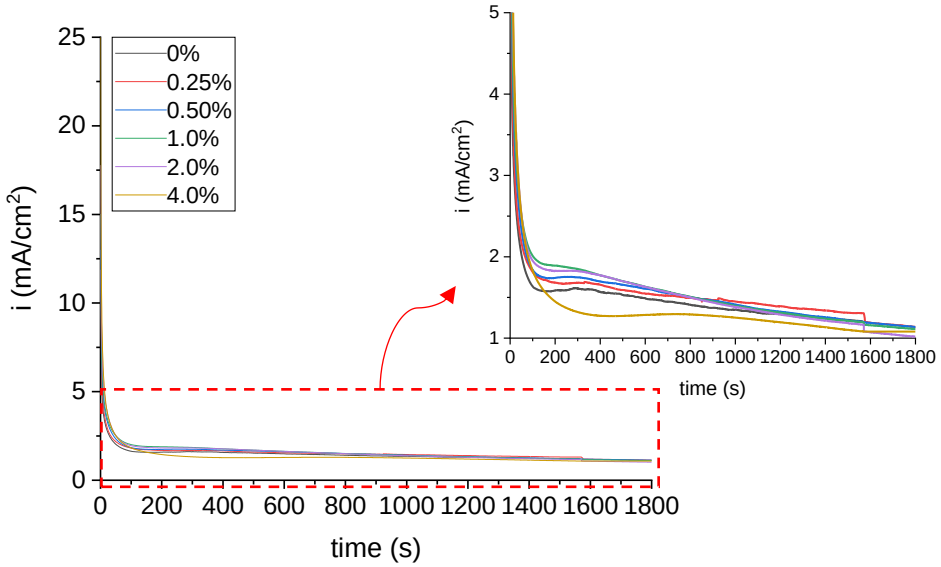

Figure 5. 23. Electrochemical anodization curves for titanium dioxide nanotubes synthesized at 55V using an EG, 1M H_2O, 0.05M NH_4F electrolyte with different TEA concentrations.

The first stage corresponds to a sudden drop in current density provoked by the growth of a compact titanium oxide layer, which blocks the flow of electrons. Here, metallic titanium is oxidized to Ti^{4+} (Eq. 5.6), reacting later with the water of the electrolyte (Eq. 5.7). Then, as the fluoride ions penetrate through the titanium dioxide layer, current density slightly increases and irregular nanopores are formed. This causes the formation of the soluble complex $[TiF_6]^{2-}$ (Eq. 5.8).

$$Ti \rightarrow Ti^{4+} + 4e^- \quad \text{Eq. 5. 6}$$

$$Ti^{4+} + 2H_2O \rightarrow \ TiO_2 + 4H^+ \quad \text{Eq. 5. 7}$$

$$TiO_2 + \ 6F^- + 4H^+ \ \rightarrow \ [TiF_6]^{2-} + \ 2H_2O \quad \text{Eq. 5. 8}$$

Next, regular formation of nanotubes occurs due to the uniform distribution of current density among the pores, which means that the formation of titanium

dioxide prevails over the dissolution by fluoride ions. This stage is shown as a current stabilization, after a slight decrease. From this point on, formation and dissolution rates are almost the same, so nanotubes grow longer until the end of the anodization process [43].

Regarding differences between samples, it can be observed in Figure 5.23 that the current density increases as the electrolyte becomes more concentrated in the ionic liquid. The highest values of current density correspond to the sample anodized with the 1% TEA electrolyte. Conductivity of the electrolyte increases as it gets more concentrated in ionic liquid. This results in a better reagent mobility to the oxide surface, due to the higher ion presence. Consequently, a faster and easier dissolution of the initiation layer is achieved, and this provokes the current density to increase [44]. If ionic liquid concentration is increased further (2% TEA), the maximum current density reached starts to decrease, falling even more when the electrolyte contains 4% TEA. Actually, for this sample nanostructure formation occurs more slowly, since stage II of nanotube growth occurs much later in time, showing a profile typical of the formation of a compact oxide layer. A high ionic liquid concentration means a major presence of large organic molecules that can cause steric hindrance and interfere in the interaction between fluoride ions and the oxide layer [45]. In similar way, the concentration increase in the organic part of the molecule decreases the dielectric constant of the electrolyte. This leads to a lower rate of charge-transfer processes, and the consequent decrease of current density [46]. Furthermore, a greater amount of ionic liquid increases the viscosity of the electrolyte, which can lead to a more difficult diffusion of species through it [44,47].

FE-SEM images of the different samples are shown in Figure 5.24, confirming the nanopore formation during anodization with and without ionic liquid (from IL-0 to IL-2). However, some nanopores become obstructed in the case of the IL-4 sample, as Figure 5.24F reveals. The decrease in the dielectric constant of the

electrolyte can be also the reason for the loss in nanopore morphology, since a lower dielectric constant reduces the dissolution rate of the compact titanium dioxide layer.

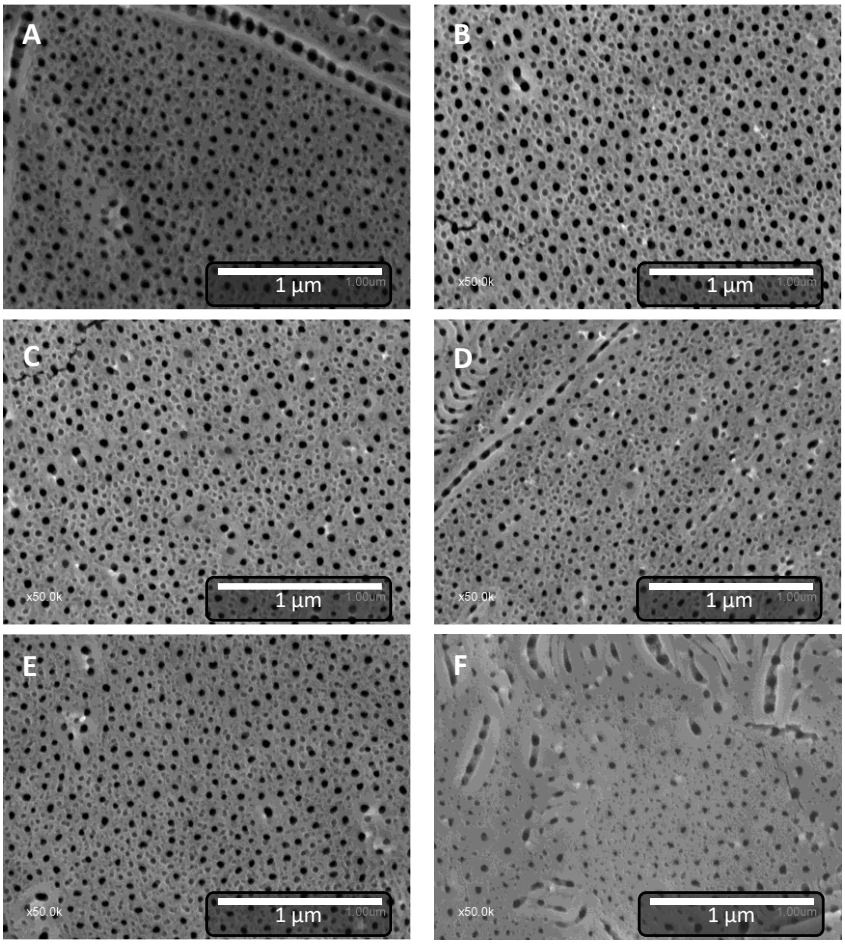

Figure 5. 24. FE-SEM top images of titanium dioxide nanotubes anodized at 55V using an EG, 1M H_2O, 0.05M NH_4F electrolyte with different TEA concentrations: (A) IL-0, (B) TEA-0.25, (C) TEA-0.5, (D) TEA-1, (E) TEA-2, (F) TEA-4.

A careful analysis of FE-SEM images (Figure 5.24) shows significant variations in nanotube dimensions of the different samples. Table 5.5 gathers information about the mean diameters of NTs, as well as the pore density of the nanostructures.

Table 5.5. Mean pore diameter and pore density of titanium dioxide nanostructures anodized in EG, H_2O 1 M, NH_4F 0.05 M and different TEA concentrations.

Nanostructure	D (nm)	Pore density (pores/m^2)[a]
IL-0	38 ± 3	480.4
TEA-0.25	54 ± 3	622.4
TEA-0.5	58 ± 4	708.8
TEA-1	58 ± 3	713.4
TEA-2	44 ± 3	732.5
TEA-4	34 ± 4	400.3

[a] Pore density was calculated using the program ImageJ.

From Table 5.5, it can be inferred that the presence of ionic liquid in the anodizing electrolyte makes the nanopores grow bigger. In fact, diameters increase from 38 nm at IL-0 to 54 nm at TEA-0.25. The highest value is reached at TEA-0.5 and TEA-1 with 58 nm. Again, the increase in electrical conductivity, which causes a faster dissolution of the oxide layer, allows nanotubes to grow wider and thicker. Moreover, inset Figure 5.23 reveals that nanopore formation begins earlier as TEA concentration increases from 0 to 1%. This can be observed by the maximum current density value being reached earlier as ionic liquid concentration gets higher (until 1%). Therefore, nanopores grow larger as they have more time to form [46]. Despite TEA-2 nanopores being bigger than IL-0 (44 nm vs. 38 nm), they start to decrease from this point on, getting even smaller with 4% of ionic liquid in the electrolyte (34 nm). As has been outlined before, an increase in electrolyte viscosity can lead to a more difficult diffusion of fluoride species through the electrolyte, restricting the access to the metal oxide layer [44,47]. Overall, nanotube formation is hindered as ionic liquid concentration increases more than 2%. Regarding pore density, Figure 5.24 and Table 5.5 illustrate that high TEA concentrations lead to an increase in this parameter. However, with 4% of ionic liquid, nanopores spread out more and cause pore density to drastically decrease.

Figure 5.25 displays the cross-section FE-SEM images of all IL nanostructures and proves that nanopores actually develop into nanotubes during anodization.

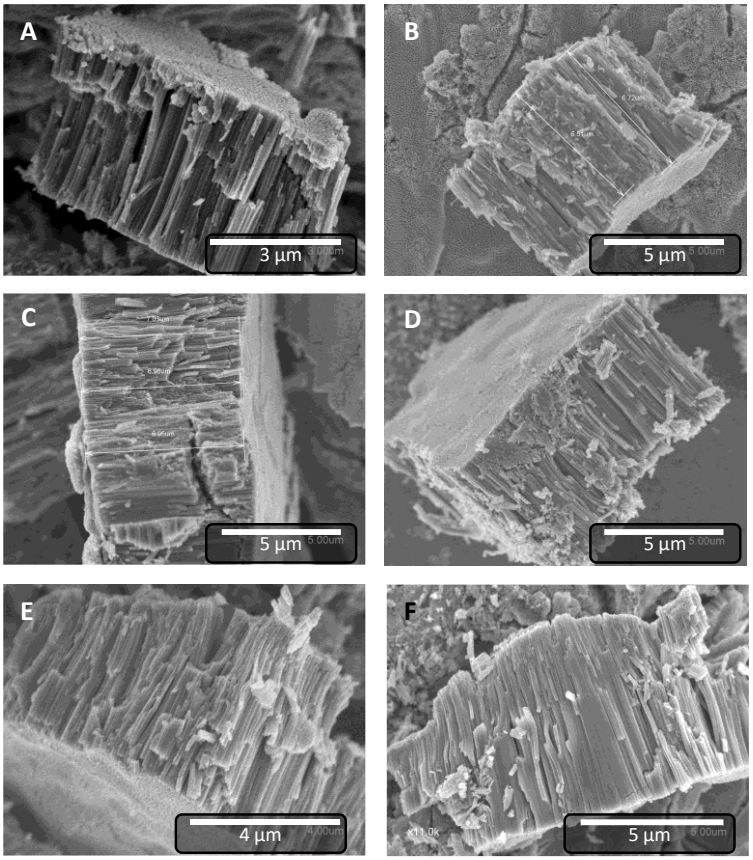

Figure 5. 25. FE-SEM cross-sectional images of titanium dioxide nanotubes anodized at 55V using an EG, 1M H_2O, 0.05M NH_4F electrolyte with different IL concentrations: (A) IL-0, (B) TEA-0.25, (C) TEA-0.5, (D) TEA-1, (E) TEA-2, (F) TEA-4.

Furthermore, the correlation between the thickness of the nanostructured layer (or nanotube length) in each sample and the ionic liquid concentration in the electrolyte is exhibited in Figure 5.26. Just with the presence of ionic liquid in the electrolyte, nanotube length rapidly rises from 4.1 µm (IL-0) to 6.6 µm (TEA-0.25). These nanotubes continue to grow longer as the electrolyte becomes more concentrated in ionic liquid, reaching 8.0 µm for TEA-4. However, it is possible to

appreciate in Figure 5.25F that nanotubes in TEA-4 are merged together, despite the nanostructured layer being thicker. The fusion of nanotubes could affect negatively the photoelectrochemical behavior of TEA-4. Holes (from electron-hole pairs) would be more likely to become trapped (resulting in recombination) and they would be prevented from reaching the electrolyte and oxidize water [48].

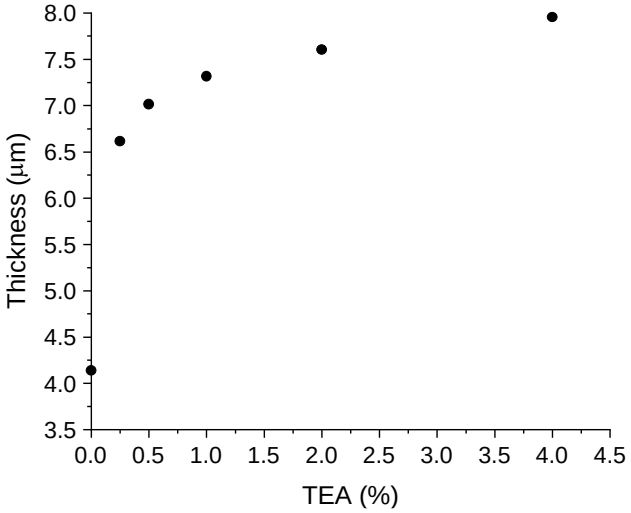

Figure 5. 26. Thickness of the nanostructured layers of TiO_2 anodized with different TEA concentrations in the electrolyte.

All samples were tested in photoelectrochemical water splitting to study their photoelectrochemical performance. Results are displayed in Figure 5.27A. Among all samples, TEA-1 presents the best photoelectrochemical performance. It is believed that the improvement in the catalytic surface is due several factors: i) bigger nanopore diameters, ii) longer nanotubes and iii) higher number of nanopores per unit area. All this, results in more light absorption and, in consequence, better photoelectrochemical behavior. When compared to IL-0, TEA-4 still exhibits better photoelectrocatalytic activity despite having fewer and smaller nanopores. Given that pore density and diameters of both samples are comparable, this might be a result of the nanotubes that are not fused together being significantly longer than in IL-0.

It has been observed that the addition of the TEA ionic liquid has a positive effect on the nanostructure morphological properties and, consequently, on its photoresponse. Therefore, two ionic liquids from the same family (mono- and diethanolamine-based, labelled as MEA and DEA, respectively) were also added to the electrolyte in the optimal concentration (1%) for the synthesis of TiO_2 nanotubes to see if they had the same effect. These photoelectrocatalysts were also tested in photoelectrochemical water splitting (Figure 5.27B). It is important to point out that, after testing all concentrations, the optimal concentration remained at 1% for all ionic liquids [44].

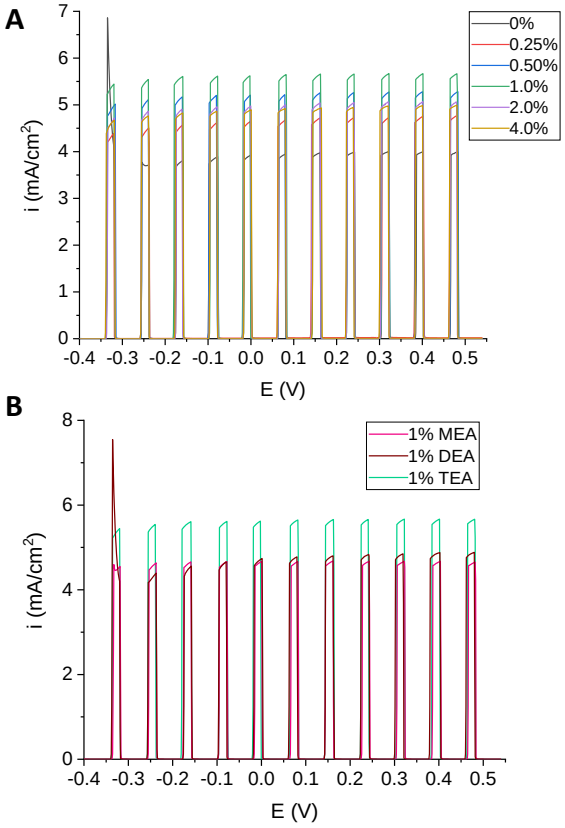

Figure 5. 27. (A) Photocurrent transient vs. potential for titanium dioxide nanotubes synthesized at 55V using an EG, 1M H_2O, 0.05M NH_4F electrolyte with different TEA concentrations under UV- light (λ = 365 nm). (B) Photocurrent transient vs. potential for titanium dioxide nanotubes synthesized at 55V using an EG, 1M H_2O, 0.05M NH_4F electrolyte with 1% (v/v) concentration of different ILs under UV-light (λ = 365 nm).

According to Figure 5.27B it is clear that the best nanostructure for water splitting is that prepared with 1% TEA. The higher presence of hydroxyl groups in the triethanolamine molecules improves the electrolyte conductivity, likely enhancing the diffusion of fluoride ions during anodization.

The triethanolamine-based ionic liquid was chosen as the best performing IL (among the studied PILs) that can be added to the anodizing electrolyte to obtain efficient TiO_2 nanostructures. Therefore, a thorough study about using controlled hydrodynamic conditions (0 to 2000 rpm) during the anodization process was carried out for the different amounts that provided the best photoelectrochemical results: 0.25%, 0.5% and 1%. Electrochemical anodization curves for these samples are shown in Figure 5.28.

From Figure 5.28A it can be observed that the three stages of nanotube formation take place for TEA-0.25 regardless of the rotation speed of the electrode being used. Furthermore, it could be argued that stages are accelerated as stirring becomes more vigorous, making nanotubes grow faster. All nanotube formation stages can be recognized for most of TEA-0.5 samples in Figure 5.28B. Only the curve belonging to the sample anodized at 2000 rpm hints the formation of a compact oxide layer instead. In this case, hydrodynamic conditions do not seem to accelerate nanotube growth. In addition, Figure 5.28C exhibits how all TEA-1 samples synthesized under hydrodynamic conditions have anodization curves which indicate the formation of a compact oxide layer as well. FE-SEM images shown displayed in Figures 5.29, 5.30 and 5.31 confirm the observed in anodization curves for TEA-0.25, TEA-0.5 and TEA-1, respectively.

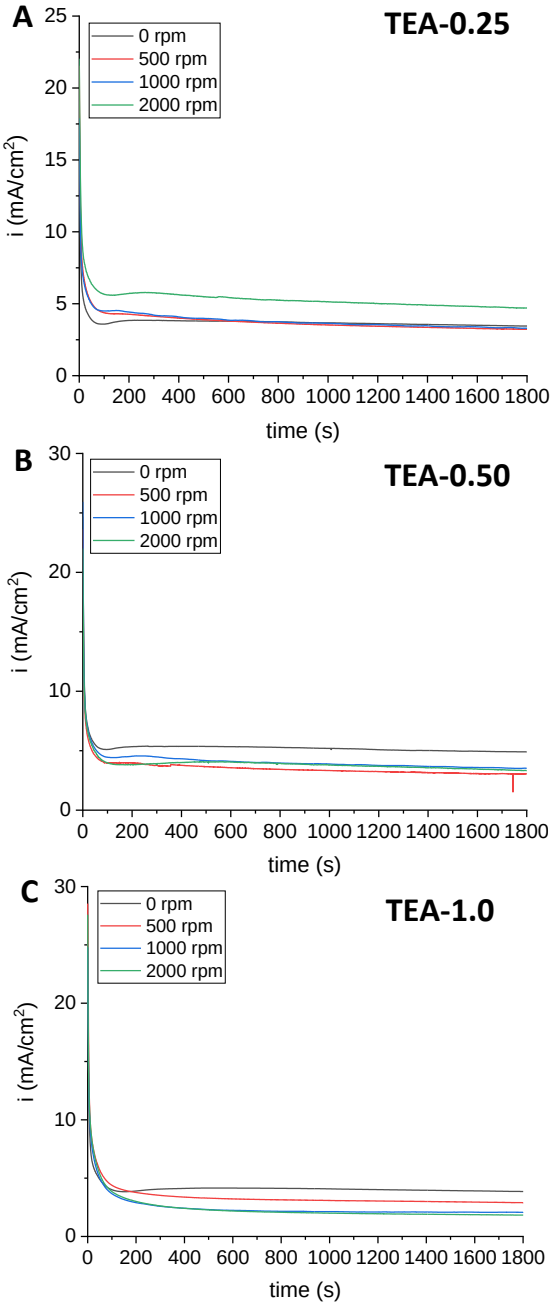

Figure 5. 28. Electrochemical anodization curves for titanium dioxide nanotubes synthesized at 55V using an EG, 1M H_2O, 0.05M NH_4F electrolyte under different hydrodynamic conditions (0 to 2000 rpm) for different IL concentrations (A) TEA-0.25, (B) TEA-0.5, (C) TEA-1.

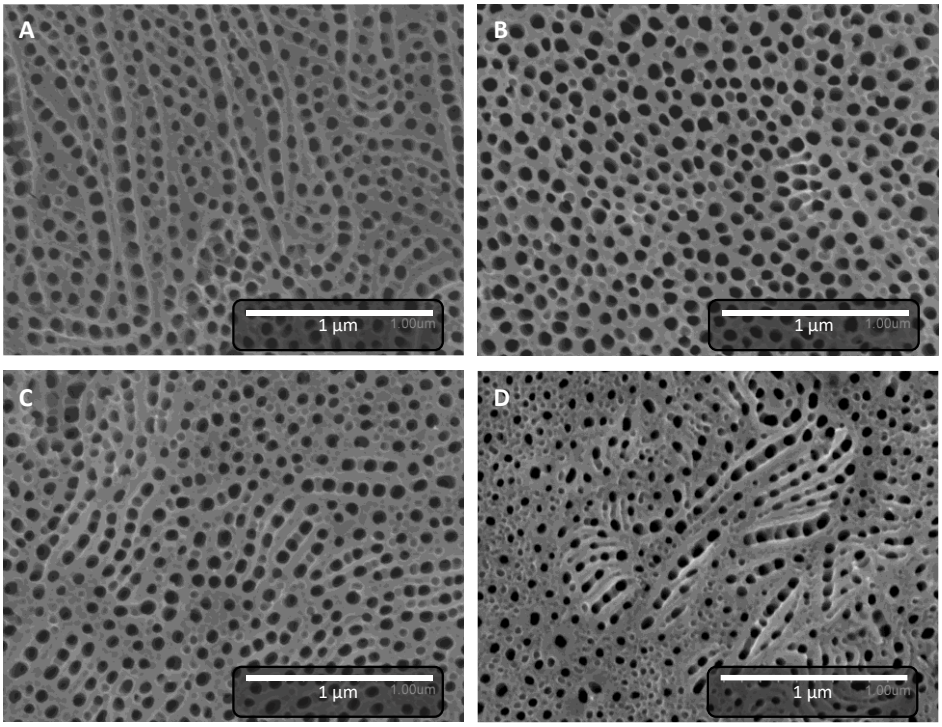

Figure 5. 29. FE-SEM top images of TEA-0.25 titanium dioxide nanotubes anodized at 55V using an EG, 1M H_2O, 0.05M NH_4F electrolyte under different hydrodynamic conditions: (A) 0 rpm, (B) 500 rpm, (C) 1000 rpm, (D) 2000 rpm.

From Figure 5.29 it can be concluded that excessive agitation for TEA-0.25 samples can negatively affect to the nanostructure synthesis, since some regions start to deform at 2000 rpm (Figure 5.29D). Moreover, nanopores begin to decrease in size when TEA-0.5 samples are anodized at 1000 rpm (Figure 5.30C) and even become blocked when rotation speed is set at 2000 rpm (Figure5.30D). Finally, hydrodynamic conditions are detrimental for nanotube synthesis with 1% of ionic liquid in the electrolyte, since it is obvious from Figure 5.31 that nanopores are totally deformed when anodization takes place at 500 rpm, and they even get obstructed at 2000 rpm.

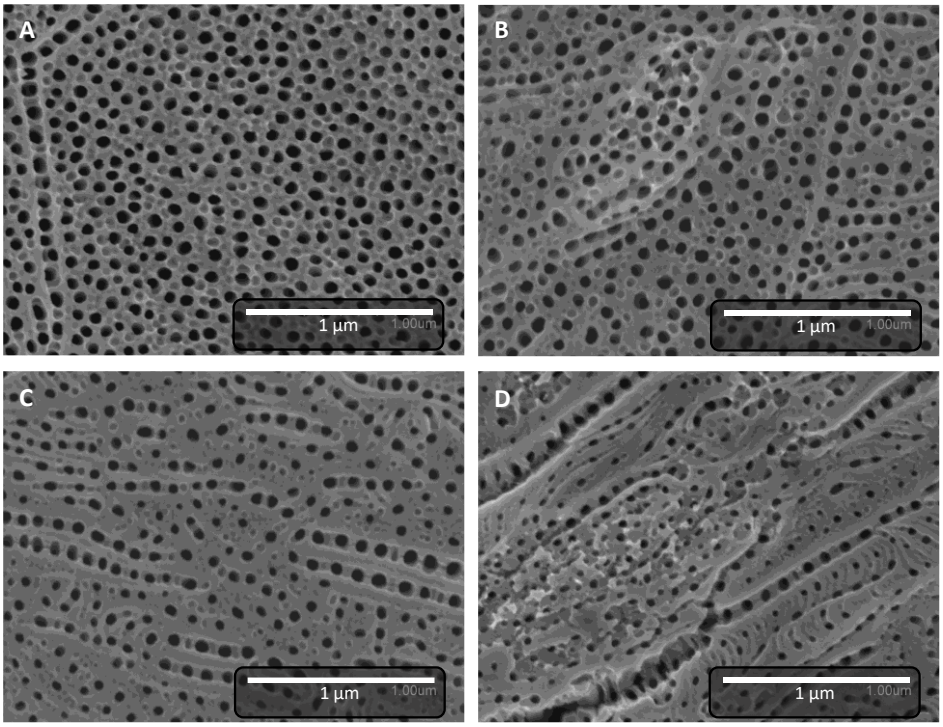

Figure 5. 30. FE-SEM top images of TEA-0.5 titanium dioxide nanotubes anodized at 55V using an EG, 1M H_2O, 0.05M NH_4F electrolyte under different hydrodynamic conditions: (A) 0 rpm, (B) 500 rpm, (C) 1000 rpm, (D) 2000 rpm.

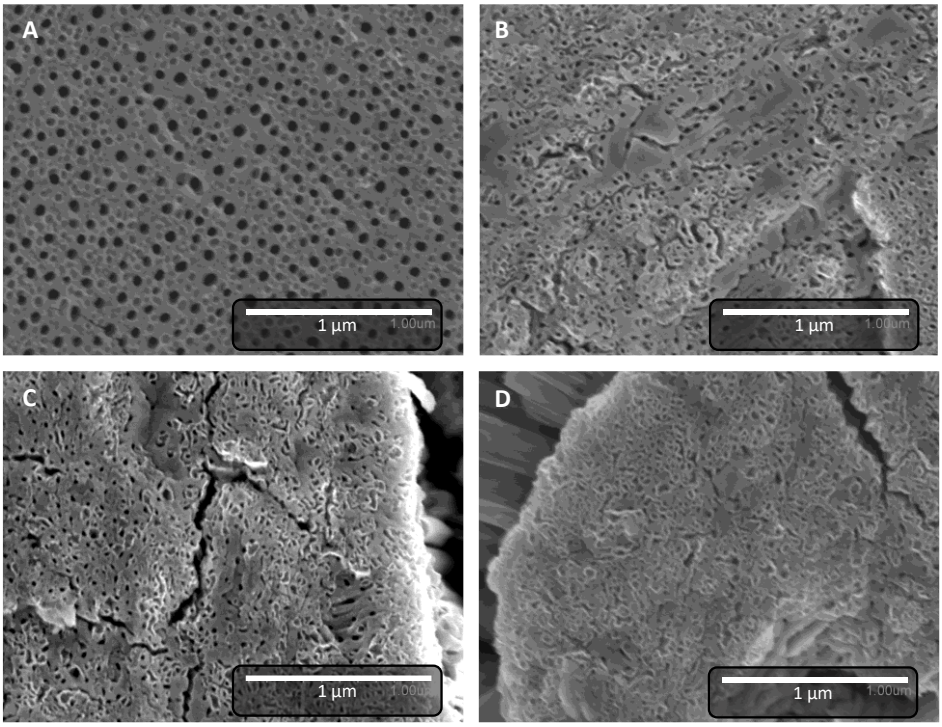

Figure 5. 31. FE-SEM top images of TEA-1 titanium dioxide nanotubes anodized at 55V using an EG, 1M H_2O, 0.05M NH_4F electrolyte under different hydrodynamic conditions: (A) 0 rpm, (B) 500 rpm, (C) 1000 rpm, (D) 2000 rpm.

Figure 5.32 displays the variation of nanotube dimensions with rotation speed and ionic liquid concentration. First, for any ionic liquid concentration, nanotubes grow shorter as rotation speed gets higher, as Figure 5.32A exhibits. When comparing pore diameters in Figure 5.32B, it can be said that TEA-0.25 and TEA-0.5 samples reach their maximum diameter at 500 rpm and later decrease as rotation speed increases. However, for TEA-1 nanotubes, hydrodynamic conditions make them smaller and shorter until they are blocked (as seen in Figure 5.31). It is clear that, depending on the amount of ionic liquid present in the anodizing electrolyte, hydrodynamic conditions affect differently on nanotube dimensions.

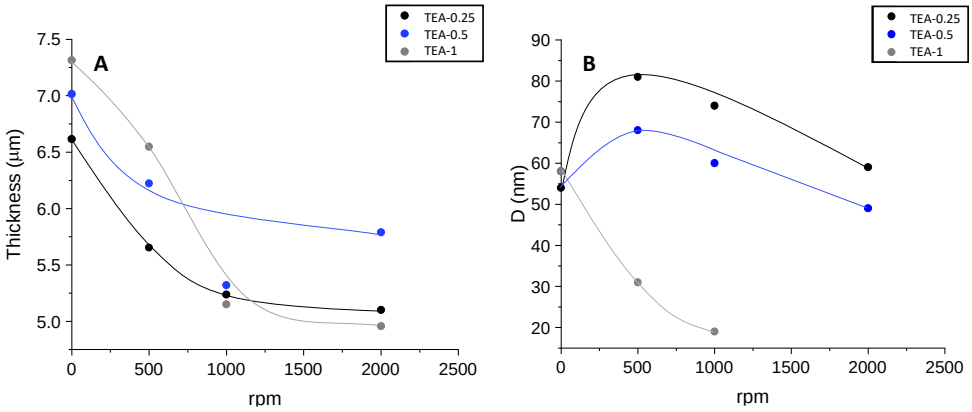

Figure 5. 32. (A) Thickness of the nanostructured layers of TiO_2 anodized under different hydrodynamic conditions and with different TEA concentrations. (B) Diameters of TiO_2 nanotubes anodized under different hydrodynamic conditions and with different TEA concentrations.

It has been reported that mass transport is improved during anodization under stirring conditions, since the diffusion of fluoride species through the electrolyte is facilitated and nanotube growth is favored [49,50]. Nevertheless, excessive agitation can be translated into delayed nanotube development, due to the species responsible for the formation of the nanostructured layer being removed from the interface [20]. Hence, when high rotation speeds are involved, as ionic liquid concentration increases, erosion of the nanostructured layer prevails over the enhanced fluoride diffusion and leads to a worse morphology.

All samples were tested in photoelectrochemical water splitting to assess the effect of hydrodynamic conditions on their performance as photoelectrocatalysts. Results are shown in Figure 5.33. Every set of catalysts is also compared to a sample anodized with no ionic liquid. In all cases, the combination of ionic liquid in the anodizing electrolyte together with stirring conditions improves the photoelectrocatalytic activity of the nanostructures when compared to the base IL-0 sample.

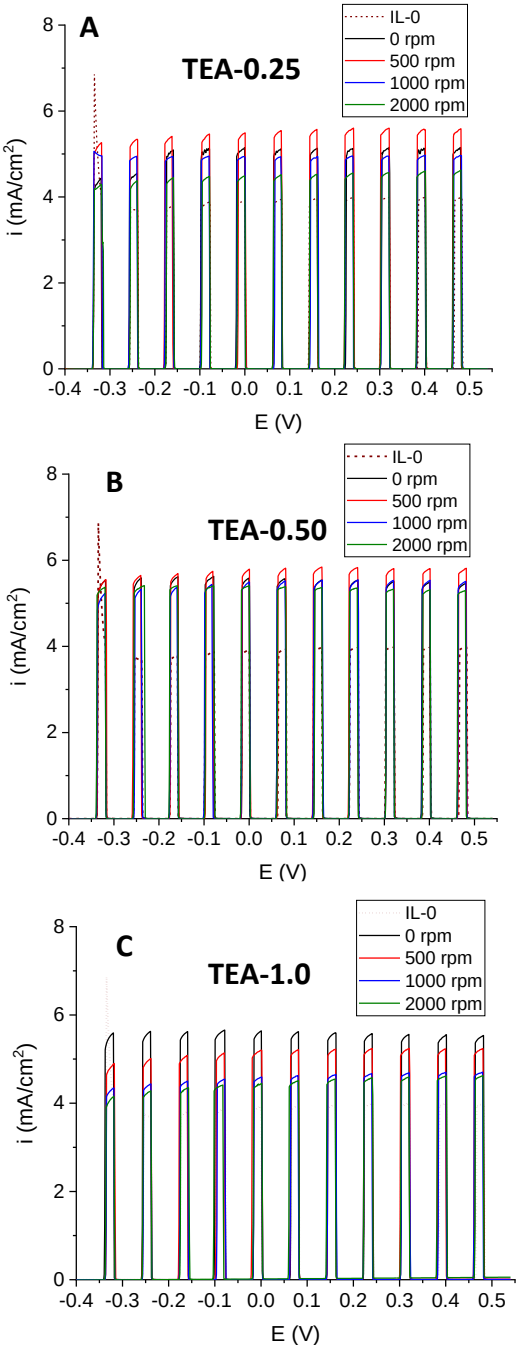

Figure 5. 33. Photocurrent transient vs. potential for titanium dioxide nanotubes synthesized at 55V using an EG, 1M H_2O, 0.05M NH_4F electrolyte at different hydrodynamic conditions under UV- light (λ = 365 nm) with different IL concentrations (A) TEA-0.25, (B) TEA-0.5 and (C) TEA-1.

Regarding the influence of hydrodynamic conditions, it could be stated that anodizing with a rotating electrode does not benefit all samples. For example, a better photoelectrochemical response is only noticed for TEA-0.25 and TEA-0.5 synthesized at 500 rpm. For TEA-1, the best response is achieved by the samples anodized at static conditions. From the previous morphological study, it can be said that the bigger nanopore diameters of both TEA-0.25 and TEA-0.5 anodized at 500 rpm improve the charge carrier mobility. It must be pointed out that these samples still have an appropriate thickness despite being thinner than static samples (5.7 vs. 6.6 μm and 6.2 vs. 7.0 μm, respectively) and that it is greater than the IL-0 thickness (4.2 μm). Both IL-0.25 and IL-0.5 anodized at 500 rpm appear to have a very similar activity. However, TEA-0.25 anodized at 500 rpm was chosen as the optimum sample to carry out a comprehensive study, since less ionic liquid is necessary for a good photoelectrochemical performance. In addition, this study would provide more information on the reasons why this photoelectrocatalyst delivers the best photoelectrochemical performance.

Figure 5.34 shows the additional morphological study to that obtained by FESEM carried out by Transmission Electron Microscopy images. This study allows to get information about the formed tubes, since images are taken from the active oxidized material as a result of scratching the samples.

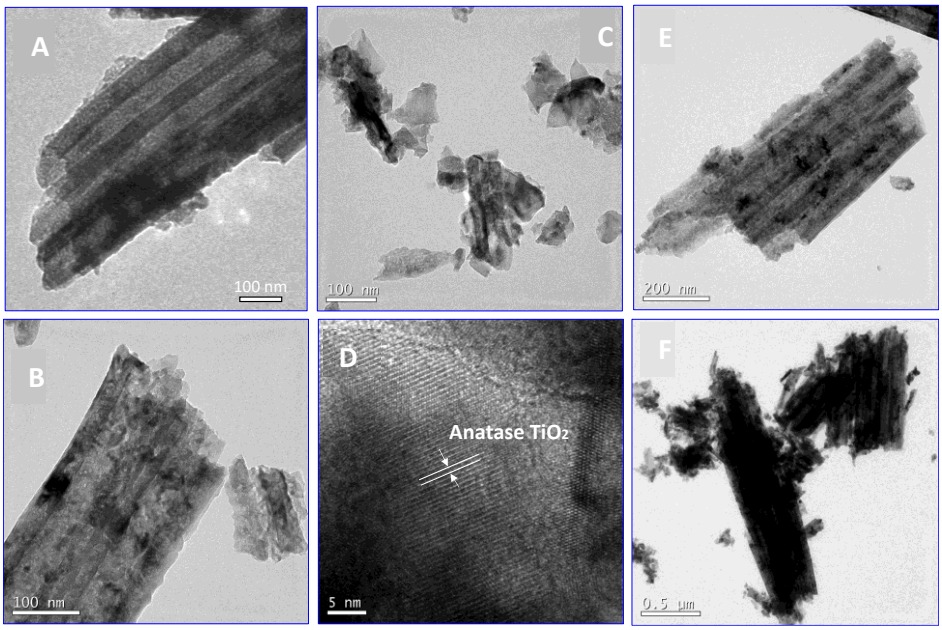

Figure 5. 34. TEM images of the anatase samples: A) IL-0, B) TEA-0.25 at 0 rpm, C) TEA-0.25 at 500 rpm, D) High Resolution TEM TEA-0.25 at 500 rpm, E) TEA-0.25 at 1000 rpm, F) TEA-0.25 at 2000 rpm.

As Figure 5.34A shows, IL-0 presents highly compacted nanotubes with an external diameter of 80-100 nm and walls of 20-30 nm. These nanotubes seem to form aggregated structures with the characteristic of low or non-existent nanoporosity. On the other hand, nanoporosity significantly increases once ionic liquid is added to the synthesis (Figure 5.34B). Compared to IL-0, nanotubes of TEA-0.25 present similar diameters but thinner walls. Furthermore, it has been concluded that the porosity of the samples is due to the use of ionic liquid in the anodizing electrolyte and not to the hydrodynamic conditions, since all samples synthesized under stirring conditions present similar nanoporosity values.

FE-SEM images showed that hydrodynamic conditions affected the samples by enlarging the nanopores (from 58 nm at 0 rpm to 85 nm at 500 rpm). This effect is not observed in TEM images, since nanotubes broke due to the scratching process needed for the study. HR-TEM image of TEA-0.25 at 500 rpm displayed in Figure

5.34D confirms that the interplanar distances correspond to the anatase TiO_2 phase (JCPDS: 21-1272), as well as all of the other samples.

Increasing further the rotation speed to 1000 rpm does not lead to significant changes compared to the static sample, since diameters are 100-120 nm and walls are 30-40 nm (Figure 5.34E). To conclude, the sample anodized at 2000 rpm presents similar morphology but much smaller pores that the rest of the samples. Figure 5.34F shows how the sample is mainly composed by highly compact tubes and the low presence of pores agrees with the small pores observed by FE-SEM.

XRD patterns of all TEA-0.25 samples are exhibited in Figure 5.35. The formation of anatase phase after annealing at 450ºC is confirmed by diffraction peaks at 2θ = 25.2, 37.87 and 48.1º [51]. No remarkable differences can be noticed in the formation of this phase among the different samples. Peaks at 2θ = 38.2, 40.9, 53.9 and 70.9º belong to the metallic titanium underlayer.

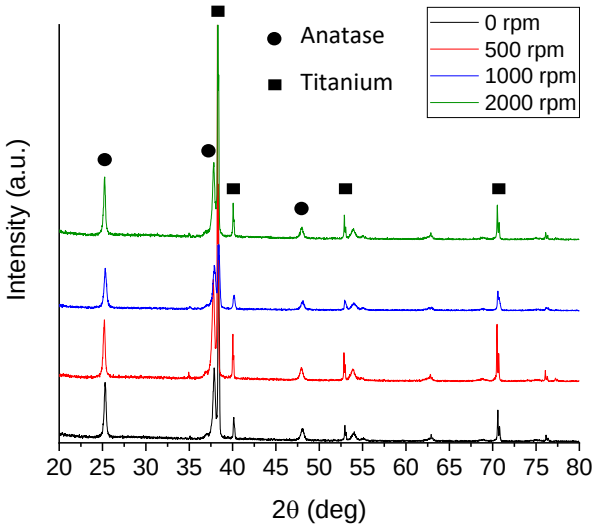

Figure 5.35. XRD patterns for titanium dioxide TEA-0.25 samples anodized at different hydrodynamic conditions.

Electrochemical properties were determined by EIS measurements, as well as by Mott-Schottky analysis. Figure 5.36 shows the experimental Nyquist and Bode plots for the titanium dioxide TEA-0.25 samples anodized at different hydrodynamic conditions. Taking a closer look at inset Figure 5.36A, each Nyquist plot presents two semicircles, which are related to two different regions from the Bode-module plots. Information about the charge-transfer response of the nanotubular structure can be obtained from the semicircle recorded at high and intermediate frequencies, while information about the compact titanium dioxide underlayer is usually obtained from the semicircle registered at low frequencies.

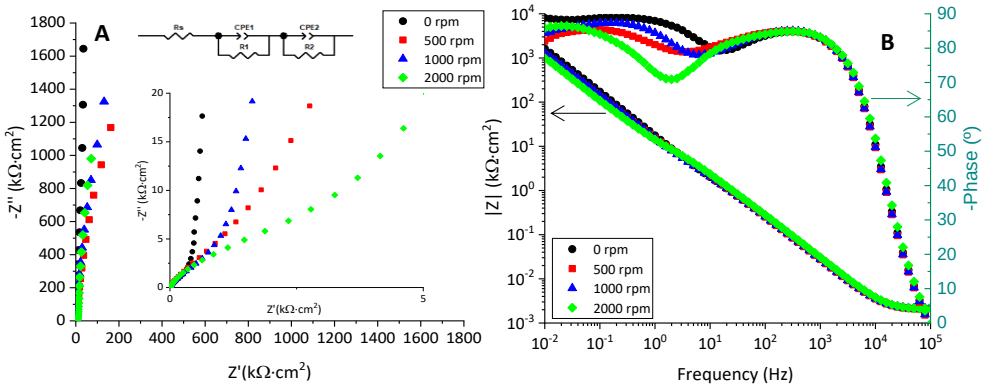

Figure 5.36. (A) Experimental Nyquist of the EIS data and magnification for titanium dioxide TEA-0.25 samples anodized at different hydrodynamic conditions, (B) Bode-module and Bode-phase plots for the titanium dioxide TEA-0.25 samples anodized at different hydrodynamic conditions and total resistance (R_T) offered by the catalysts.

The impedance associated with the electrochemical process taking place is, generally, related to the semicircle amplitude. From Figure 5.36A, it can be observed how the sample anodized under static conditions presents the largest semicircle, which means that this nanostructure offers the highest resistance to charge mobility. Moreover, when hydrodynamic conditions are involved in the anodization process, samples present lower impedance values. Therefore, it can be argued that when electrochemical anodization is carried out under stirring conditions, electrical conductivity of titanium dioxide nanotubes is improved. These results have been analyzed quantitively by fitting the EIS data to the equivalent circuit displayed in

Figure 5.36A. R_S represents electrolyte resistance, while R_1-CPE_1 and R_2-CPE_2 represent charge-transfer resistance at the active parts of the nanostructure/electrolyte interface and resistance offered by the compact titanium oxide layer, respectively [26–29]. This time, a series equivalent circuit has been chosen for the fitting. These circuits are typically employed to describe the behavior of titanium dioxide nanotubes, since their closed end at the bottom of the tubes clearly divide the active layer from the compact oxide one [54]. Results are gathered in Table 5.6.

Table 5. 6. Resistance values from EIS data fitting and from Bode-module plot.

Sample	**R_1 (kOhm·cm^2)**	**R_2 (kOhm·cm^2)**	**$R_1 + R_2$ (kOhm·cm^2)**	**R_{TBode} (kOhm·cm^2)**
TEA-0.25 0 rpm	0.6	24500	~24500	1645
TEA-0.25 500 rpm	0.5	5500	~5500	1179
TEA-0.25 1000 rpm	1.0	22000	~22000	1339
TEA-0.25 2000 rpm	4.8	5050	~5050	983

Resistance values obtained from the Bode-module plots at low frequencies (R_T) and total resistance values calculated from the fitting R_1+R_2, follow the same trend. Excluding the 2000 rpm sample, which has clearly a worse photoelectrochemical performance due to its poorer morphology and larger crystallite size, the sample anodized at 500 rpm exhibits the lowest charge resistance value (R_1). It is well known that low charge-transfer resistance improves electron transfer and hole diffusion. Hence, the reduced charge-transfer resistance offered by the 500 rpm sample would explain the better photoelectrochemical activity.

According to Figure 5.37, which displays the Mott-Schottky plots for all samples, titanium dioxide nanostructures are n-type semiconductors, electrons being the dominant charge carriers, due to the positive slopes of the plots.

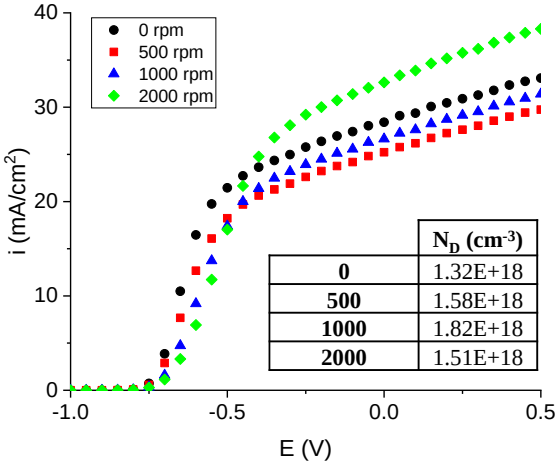

Figure 5. 37. Mott-Schottky plots obtained at a frequency of 5 kHz and charge donor density for titanium dioxide TEA-0.25 samples anodized at different hydrodynamic conditions.

Donor density (N_D) of each nanostructure has been calculated with the Mott-Schottky equation (Eq. 3.8), being ε the relative dielectric constant of TiO_2. For this type of nanostructures, donor density is related to the oxygen vacancies present in their active surface [55]. From the table inset of Figure 5.37 it can be inferred that defect concentration increases with the presence of hydrodynamic conditions. This is translated into a better photoelectrochemical behavior of the nanostructures, since a higher number of oxygen vacancies improves the electrical conductivity of the samples [56]. Nevertheless, an excessive number of defects can act as traps and enhance the recombination of electron-hole pairs [57].

At the same time, photoelectrochemical water splitting results of the TEA-0.25 samples anodized under different hydrodynamic conditions (Figure 5.33) can be explained. For instance, electrochemical anodization at 500 rpm is enough to generate the ideal amount of oxygen vacancies and provide the best photoelectrochemical performance. However, if rotation speed is increased further donor density becomes too high and photoelectrochemical behavior of the sample anodized at 1000 rpm worsens compared to the 0 rpm sample. These results are in agreement with that obtained from EIS measurements.

DR-UV-visible spectra of the titanium dioxide TEA-0.25 samples anodized under different rotation speeds are displayed in Figure 5.38. From Figure 5.38A it can be observed that all samples present spectra with similar shape with a relatively intense band from 200 to 400 nm and a second wide band between 400 and 800 nm. Nevertheless, different intensity of the absorbance bands can be noticed in Figure 5.38B. For instance, samples anodized at 0 and 500 rpm present the highest absorbance in the ultraviolet range (until 400 nm), whereas the sample synthesized at 2000 rpm shows the lowest. It must be noted that spectra of all samples fit in both the ultraviolet and visible regions with those of anatase titanium dioxide[58–60]. Moreover, the tendency in the visible range goes: 500 rpm > 1000 rpm > 0 rpm > 2000 rpm. Hence, it can be concluded that the highest absorption in UV-vis range belongs to the 500 rpm sample, as expected due to the better photoresponse of this sample. This nanostructure presents enhanced photoelectrochemical properties, as shown in Figure 5.29B, where the homogeneous and improved morphology leads to an easier electron mobility.

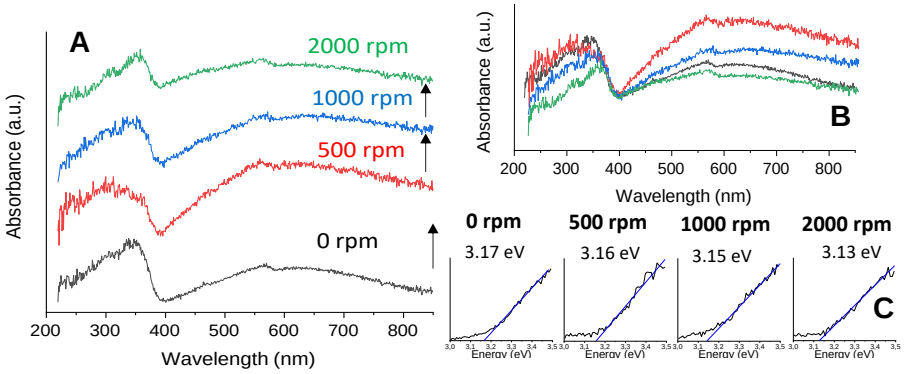

Figure 5. 38. DR-UV-Vis. spectra of TiO_2 TEA-0.25 samples anodized at different hydrodynamic conditions and their corresponding determination of the energy band gaps.

Energy band gaps of these samples were calculated using the Tauc equation [61] and are exhibited in Figure 5.38C. With a band gap of 3.17 eV, the sample anodized under static conditions is very similar to the value reported for standard

anatase titanium dioxide (ca. 3.2 eV) [62]. Slightly lower values were obtained for samples anodized under hydrodynamic conditions: from 3.16 eV for the 500 rpm sample to 3.13 eV for the 2000 rpm sample. Differences are so small that they can be located within the error bars. Therefore, it can be concluded that there is no correlation between the energy band gap values and the photoelectrochemical performance of the nanostructures.

5.2.1 Photoelectro-reduction of nitrous oxide with TiO_2 as photoanode

As has been outlined before, titanium dioxide photoelectrocatalysts are used as photoanodes in photoelectrochemical reactions due to their n-type semiconductor behavior. Electron-hole pairs are generated as a result of the photoexcitation of electrons from the valence band to the conduction band of the material (Eq. 5.9). Electrons migrate to the cathode via the external electric circuit and participate in the reduction of the adsorbed nitrous oxide, as described in equation 5.10. O^- species are later oxidized into oxygen, that desorbs into the electrolyte (Eq. 5.11). Equation 5.12 describes the overall reaction that takes place in the photoelectron-reduction of nitrous oxide with TiO_2 in alkaline media [63,64].

$$TiO_2 + h\nu \rightarrow e^- + h^+ \qquad \text{Eq. 5. 9}$$

$$(N_2O_{ads} + e^- \rightarrow N_2 + \cdot O^-)x2 \qquad \text{Eq. 5. 10}$$

$$2 \cdot O^- \rightarrow O_2 + 2e^- \qquad \text{Eq. 5. 11}$$

$$2N_2O \rightarrow 2N_2 + O_2 \qquad \text{Eq. 5. 12}$$

The TEA-0.25 500 rpm catalysts and a non-optimized sample (as reference) were tested in the photoelectrochemical elimination of nitrous oxide. Figure 5.39 shows the evolution of N_2O elimination during the 3h experiment. Elimination reached 97% after 2 hours of experiment with the TEA-0.25 500 rpm sample, achieving 100% in the last hour.

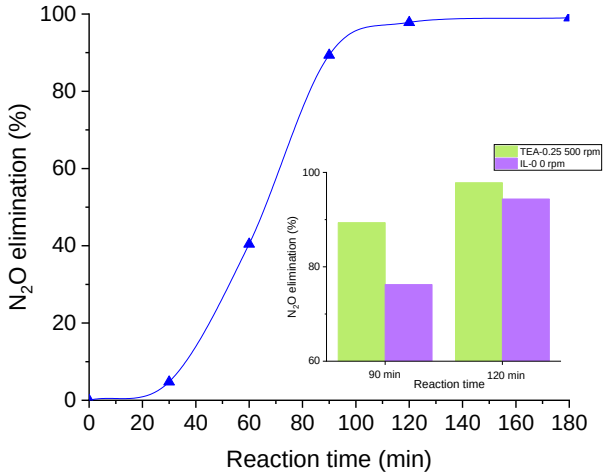

Figure 5. 39. Evolution with time of the elimination of nitrous oxide during the photoelectro-reduction.

Inset of Figure 5.39. confirms that the addition of ionic liquid and the presence of hydrodynamic conditions improve the performance of the titanium dioxide nanotubes in the photoelectroreduction of nitrous oxide. After 90 minutes, the optimized sample has removed 90% of the gas, while with the sample anodized without ionic liquid and under static conditions only 75% is achieved. Degradation is almost complete after 2h in both cases. Therefore, the main advantage of this synthesis method is the ability to obtain efficient nanostructures that accelerate the elimination reaction, leading to a much lower energy consumption.

5.3 Conclusions

In the present chapter, different photoelectrocatalysts have been synthesized in order to achieve the main goal of this thesis: the valorization of nitrous oxide. For this purpose, by employing electrochemical anodization, the influence of different electrolytes in the synthesis of both copper oxide and titanium dioxide nanostructures has been investigated. In addition, the use of hydrodynamic conditions during anodization was also considered after the electrolyte was set.

For the copper oxide photoelectrocatalysts, different complexing agents, as well as different organic solvents in different amounts, were tested. In this case, oxalic acid 0.05M in a 70% (v/v) ethylene glycol-based electrolyte anodized for 5 minutes at 250 rpm gave the best results. The better photoelectrochemical response was attributed to a homogeneous nanospherical morphology, to the formation of both CuO and Cu_2O phases, with a higher presence of copper (I) oxide, and a higher electrical conductivity due to a greater number of copper vacancies. These properties led to an efficient photoelectro-reduction of N_2O, achieving almost 100% of elimination after 1h of experiment. Furthermore, by using this nanostructure, the photoelectrocatalytic approach was proved to be more efficient than both photo- and electrocatalytic approaches for the reduction of nitrous oxide.

Regarding the titanium dioxide photoelectrocatalysts, different concentrations of a green protic ionic liquid (based in triethanolamine) were used in the synthesis. First, the sample anodized under static conditions with 1% of ionic liquid in the electrolyte presented the best photoelectrocatalytic performance. A higher nanopore density, as well as bigger pore diameters and a thicker nanostructured layer, resulted in more surface area available for light absorption. Therefore, it can be concluded that PILs play a key role in tuning the morphology and electrochemical properties of TiO_2 nanostructures. Interestingly, results changed when hydrodynamic conditions were involved in the synthesis. Increasing rotation

speed during anodization became detrimental for nanotube formation, as ionic liquid concentration got higher. The sample anodized in a 0.25% ionic liquid containing electrolyte at 500 rpm turned out to be the most suitable for the application of interest. Apart from a uniform morphology, which involved again a high surface area, the enhanced photoelectrochemical behavior was attributed to a greater number (but not excessive) of oxygen vacancies that led to a better flow of electrons. Total photoelectro-reduction of nitrous oxide was achieved after 3h, meaning that the main goal of the thesis has been carried out successfully.

5.4 References

[1] D. Gupta, S.R. Meher, N. Illyaskutty, Z.C. Alex, Facile synthesis of Cu2O and CuO nanoparticles and study of their structural, optical and electronic properties, J. Alloys Compd. 743 (2018) 737–745. https://doi.org/10.1016/j.jallcom.2018.01.181.

[2] Y. Yang, D. Xu, Q. Wu, P. Diao, Cu2O/CuO Bilayered Composite as a High-Efficiency Photocathode for Photoelectrochemical Hydrogen Evolution Reaction, Sci. Rep. 6 (2016) 35158. https://doi.org/10.1038/srep35158.

[3] T.H. Yin, B.J. Liu, Y.W. Lin, Y.S. Li, C.W. Lai, Y.P. Lan, C. Choi, H.C. Chang, Y.M. Choi, Electrodeposition of Copper Oxides as Cost-Effective Heterojunction Photoelectrode Materials for Solar Water Splitting, Coatings 12 (2022) 1839. https://doi.org/10.3390/coatings12121839.

[4] W. Zhang, H. Chen, Q. Peng, X. Liu, L. Dian, W. Ye, Y. Chang, X. Ma, H. Wang, Controlled fabrication of WO3 nanoplate films and its photoelectrochemical properties, Mater. Res. Express 6 (2019) 095901. https://doi.org/10.1088/2053-1591/ab2cc3.

[5] A.K. Nayak, S. Lee, Y.I. Choi, H.J. Yoon, Y. Sohn, D. Pradhan, Crystal Phase and Size-Controlled Synthesis of Tungsten Trioxide Hydrate Nanoplates at Room Temperature: Enhanced Cr(VI) Photoreduction and Methylene Blue Adsorption Properties, ACS Sustain. Chem. Eng. 5 (2017) 2741–2750. https://doi.org/10.1021/acssuschemeng.6b03084.

[6] J. Luo, L. Steier, M.-K. Son, M. Schreier, M.T. Mayer, M. Grätzel, Cu2O Nanowire Photocathodes for Efficient and Durable Solar Water Splitting, Nano Lett. 16 (2016) 1848–1857. https://doi.org/10.1021/acs.nanolett.5b04929.

[7] C. Wang, J. Cao, Z. Gao, S. Ji, H. Ma, Y. Wang, Synthesizing robust cuprous oxide film with adjustable morphologies as surface-enhanced Raman scattering substrate by copper anodization, Mater. Chem. Phys. 264 (2021) 124470. https://doi.org/10.1016/j.matchemphys.2021.124470.

[8] S. Karthick Kumar, S. Murugesan, S. Suresh, Preparation and characterization of CuO nanostructures on copper substrate as selective solar absorbers, Mater. Chem. Phys. 143 (2014) 1209–1214. https://doi.org/10.1016/j.matchemphys.2013.11.023.

[9] M.-C. Huang, T. Wang, W.-S. Chang, J.-C. Lin, C.-C. Wu, I.-C. Chen, K.-C. Peng, S.-W. Lee, Temperature dependence on p-Cu2O thin film electrochemically deposited onto copper substrate, Appl. Surf. Sci. 301 (2014) 369–377. https://doi.org/10.1016/j.apsusc.2014.02.085.

[10] M. Balık, V. Bulut, I.Y. Erdogan, Optical, structural and phase transition properties of Cu2O, CuO and Cu2O/CuO: Their photoelectrochemical sensor applications, Int. J. Hydrog. Energy 44 (2019) 18744–18755. https://doi.org/10.1016/j.ijhydene.2018.08.159.

[11] S. Jana, S. Das, N.S. Das, K.K. Chattopadhyay, CuO nanostructures on copper foil by a simple wet chemical route at room temperature, Mater. Res. Bull. 45 (2010) 693–698. https://doi.org/10.1016/j.materresbull.2010.02.014.
[12] N. Dasineh Khiavi, R. Katal, S. Kholghi Eshkalak, S. Masudy-Panah, S. Ramakrishna, H. Jiangyong, Visible Light Driven Heterojunction Photocatalyst of CuO–Cu2O Thin Films for Photocatalytic Degradation of Organic Pollutants, Nanomaterials 9 (2019) 1011. https://doi.org/10.3390/nano9071011.
[13] A. El-Trass, H. ElShamy, I. El-Mehasseb, M. El-Kemary, CuO nanoparticles: Synthesis, characterization, optical properties and interaction with amino acids, Appl. Surf. Sci. 258 (2012) 2997–3001. https://doi.org/10.1016/j.apsusc.2011.11.025.
[14] T. Baran, A. Visibile, M. Busch, X. He, S. Wojtyla, S. Rondinini, A. Minguzzi, A. Vertova, Copper oxide-based photocatalysts and photocathodes: Fundamentals and recent advances, Molecules 26 (2021). https://doi.org/10.3390/molecules26237271.
[15] K. Mizuno, M. Izaki, K. Murase, T. Shinagawa, M. Chigane, M. Inaba, A. Tasaka, Y. Awakura, Structural and Electrical Characterizations of Electrodeposited p-Type Semiconductor Cu2O Films, J. Electrochem. Soc. 152 (2005) C179. https://doi.org/10.1149/1.1862478.
[16] A. Paracchino, J.C. Brauer, J.E. Moser, E. Thimsen, M. Graetzel, Synthesis and characterization of high-photoactivity electrodeposited Cu 2O solar absorber by photoelectrochemistry and ultrafast spectroscopy, J. Phys. Chem. C 116 (2012) 7341–7350. https://doi.org/10.1021/jp301176y.
[17] Dielectric constants of common solvents.pdf, (n.d.). https://depts.washington.edu/eooptic/linkfiles/dielectric_chart%5B1%5D.pdf (accessed February 19, 2025).
[18] J. Yang, W. Li, J. Li, D. Sun, Q. Chen, Hydrothermal synthesis and photoelectrochemical properties of vertically aligned tungsten trioxide (hydrate) plate-like arrays fabricated directly on FTO substrates, J. Mater. Chem. 22 (2012) 17744–17752. https://doi.org/10.1039/C2JM33199C.
[19] R.M. Fernández-Domene, R. Sánchez-Tovar, E. Segura-Sanchís, J. García-Antón, Novel tree-like WO3 nanoplatelets with very high surface area synthesized by anodization under controlled hydrodynamic conditions, Chem. Eng. J. 286 (2016) 59–67. https://doi.org/10.1016/J.CEJ.2015.10.069.
[20] P. Batista-Grau, R. Sánchez-Tovar, R.M. Fernández-Domene, J. García-Antón, Formation of ZnO nanowires by anodization under hydrodynamic conditions for photoelectrochemical water splitting, Surf. Coat. Technol. 381 (2020) 125197. https://doi.org/10.1016/J.SURFCOAT.2019.125197.
[21] R.M. Fernández-Domene, R. Sánchez-Tovar, B. Lucas-granados, M.J. Muñoz-Portero, J. García-Antón, Elimination of pesticide atrazine by photoelectrocatalysis using a photoanode based on WO3 nanosheets, Chem. Eng. J. 350 (2018) 1114–1124. https://doi.org/10.1016/j.cej.2018.06.015.

[22] R.M. Fernández-Domene, G. Roselló-Márquez, R. Sánchez-Tovar, B. Lucas-Granados, J. García-Antón, Photoelectrochemical removal of chlorfenvinphos by using WO3 nanorods: Influence of annealing temperature and operation pH, Sep. Purif. Technol. 212 (2019) 458–464. https://doi.org/10.1016/j.seppur.2018.11.049.
[23] S.M. Gateman, O. Gharbi, H. Gomes De Melo, K. Ngo, M. Turmine, V. Vivier, On the use of a constant phase element (CPE) in electrochemistry, Curr. Opin. Electrochem. 36 (2022) 101133. https://doi.org/10.1016/j.coelec.2022.101133.
[24] L. Li, S. Xiao, R. Li, Y. Cao, Y. Chen, Z. Li, G. Li, H. Li, Nanotube Array-Like WO3 Photoanode with Dual-Layer Oxygen-Evolution Cocatalysts for Photoelectrocatalytic Overall Water Splitting, ACS Appl. Energy Mater. 1 (2018) 6871–6880. https://doi.org/10.1021/acsaem.8b01215.
[25] Basics of EIS: Electrochemical Research-Impedance Gamry Instruments, (n.d.). https://www.gamry.com/application-notes/EIS/basics-of-electrochemical-impedance-spectroscopy/ (accessed February 18, 2025).
[26] W.H. Leng, Z. Zhang, J.Q. Zhang, C.N. Cao, Investigation of the kinetics of a TiO2 photoelectrocatalytic reaction involving charge transfer and recombination through surface states by electrochemical impedance spectroscopy, J. Phys. Chem. B 109 (2005) 15008–15023. https://doi.org/10.1021/jp051821z.
[27] S. Palmas, A.M. Polcaro, J.R. Ruiz, A. Da Pozzo, M. Mascia, A. Vacca, TiO2 photoanodes for electrically enhanced water splitting, Int. J. Hydrog. Energy 35 (2010) 6561–6570. https://doi.org/10.1016/j.ijhydene.2010.04.039.
[28] A.G. Muñoz, Semiconducting properties of self-organized TiO2 nanotubes, Electrochimica Acta 52 (2007) 4167–4176. https://doi.org/10.1016/j.electacta.2006.11.035.
[29] A.G. Muñoz, Q. Chen, P. Schmuki, Interfacial properties of self-organized TiO2 nanotubes studied by impedance spectroscopy, J. Solid State Electrochem. 11 (2007) 1077–1084. https://doi.org/10.1007/s10008-006-0241-9.
[30] C. Ponchio, W. Srevarit, Photoelectrocatalytic improvement of copper oxide thin film fabricated using anodization strategy application in nitrite degradation and promoting oxygen evolution, Chem. Pap. 75 (2021) 1123–1132. https://doi.org/10.1007/s11696-020-01369-x.
[31] G. Solomon, M. Lecca, M. Bisetto, M. Gilzad Kohan, I. Concina, M.M. Natile, A. Vomiero, Engineering Cu2O Nanowire Surfaces for Photoelectrochemical Hydrogen Evolution Reaction, ACS Appl. Energy Mater. 6 (2023) 832–840. https://doi.org/10.1021/acsaem.2c03122.
[32] D.O. Scanlon, B.J. Morgan, G.W. Watson, A. Walsh, Acceptor levels in p-type Cu2O: Rationalizing theory and Experiment, Phys. Rev. Lett. 103 (2009) 096405. https://doi.org/10.1103/PhysRevLett.103.096405.
[33] R.M. Fernández-Domene, R. Sánchez-Tovar, B. Lucas-Granados, J. García-Antón, Improvement in photocatalytic activity of stable WO3 nanoplatelet

globular clusters arranged in a tree-like fashion: Influence of rotation velocity during anodization, Appl. Catal. B Environ. 189 (2016) 266–282. https://doi.org/10.1016/j.apcatb.2016.02.065.

[34] Q. Wang, J. Liu, Q. Li, J. Yang, Stability of Photocathodes: A Review on Principles, Design, and Strategies, ChemSusChem 16 (2023) e202202186. https://doi.org/10.1002/cssc.202202186.

[35] M. Gopannagari, D.A. Reddy, D.H. Hong, K.A.J. Reddy, D.P. Kumar, H.S. Ahn, T.K. Kim, Augmented photoelectrochemical water reduction: influence of copper vacancies and hole-transport layer on CuBi2O4 photocathode, J. Mater. Chem. A 10 (2022) 6623–6635. https://doi.org/10.1039/D1TA09956F.

[36] P. Ding, T. Jiang, N. Han, Y. Li, Photocathode engineering for efficient photoelectrochemical CO2 reduction, Mater. Today Nano 10 (2020) 100077. https://doi.org/10.1016/j.mtnano.2020.100077.

[37] P. Wang, S. Wang, H. Wang, Z. Wu, L. Wang, Recent Progress on Photo-Electrocatalytic Reduction of Carbon Dioxide, Part. Part. Syst. Charact. 35 (2018) 1700371. https://doi.org/10.1002/ppsc.201700371.

[38] P. Roy, S. Berger, P. Schmuki, TiO2 Nanotubes: Synthesis and Applications, Angew. Chem. Int. Ed. 50 (2011) 2904–2939. https://doi.org/10.1002/anie.201001374.

[39] N.T. Sahrin, R. Nawaz, C. Fai Kait, S.L. Lee, M.D.H. Wirzal, Visible Light Photodegradation of Formaldehyde over TiO2 Nanotubes Synthesized via Electrochemical Anodization of Titanium Foil, Nanomaterials 10 (2020) 128. https://doi.org/10.3390/nano10010128.

[40] N.T. Sahrin, R. Nawaz, F.K. Chong, S.L. Lee, M.D.H. Wirzal, Current perspectives of anodized TiO2 nanotubes towards photodegradation of formaldehyde: A short review, Environ. Technol. Innov. 22 (2021) 101418. https://doi.org/10.1016/J.ETI.2021.101418.

[41] Y. Fu, A. Mo, A Review on the Electrochemically Self-organized Titania Nanotube Arrays: Synthesis, Modifications, and Biomedical Applications, Nanoscale Res. Lett. 13 (2018) 187. https://doi.org/10.1186/s11671-018-2597-z.

[42] O. Lebedeva, D. Kultin, L. Kustov, Electrochemical Synthesis of Unique Nanomaterials in Ionic Liquids, Nanomaterials 11 (2021) 3270. https://doi.org/10.3390/nano11123270.

[43] R. Beranek, H. Hildebrand, P. Schmuki, Self-Organized Porous Titanium Oxide Prepared in H[sub 2]SO[sub 4]/HF Electrolytes, Electrochem. Solid-State Lett. 6 (2003) B12. https://doi.org/10.1149/1.1545192.

[44] G. Sánchez-García, E. Da Silva, R.M. Fernández-Domene, A. Cháfer, V. González-Alfaro, B. Solsona, R. Sánchez-Tovar, TiO2 nanostructures synthesized by electrochemical anodization in green protic ionic liquids for photoelectrochemical applications, Ceram. Int. 49 (2023) 26900–26909. https://doi.org/10.1016/j.ceramint.2023.05.227.

[45] Z. He, P. Alexandridis, Nanoparticles in ionic liquids: interactions and organization, Phys. Chem. Chem. Phys. 17 (2015) 18238–18261. https://doi.org/10.1039/C5CP01620G.
[46] R.M. Fernández-Domene, A. Cháfer-Ortega, J.A. Lombana-Fernández, R. Sánchez-Tovar, B. Solsona, Ionic liquids and nanotechnology: Synthesis of WO3 nanostructures by anodization as photoelectrocatalysts, Ceram. Int. 49 (2023) 15434–15441. https://doi.org/10.1016/j.ceramint.2023.01.128.
[47] M. Nischk, P. Mazierski, M. Gazda, A. Zaleska, Ordered TiO2 nanotubes: The effect of preparation parameters on the photocatalytic activity in air purification process, Appl. Catal. B Environ. 144 (2014) 674–685. https://doi.org/10.1016/J.APCATB.2013.07.041.
[48] Efficient Photoelectrolysis of Water using TiO2 Nanotube Arrays by Minimizing Recombination Losses with Organic Additives | The Journal of Physical Chemistry C, (n.d.). https://pubs.acs.org/doi/full/10.1021/jp7100539 (accessed February 19, 2025).
[49] E. Blasco-Tamarit, B. Solsona, R. Sánchez-Tovar, D. García-García, R.M. Fernández-Domene, J. García-Antón, Influence of annealing atmosphere on photoelectrochemical response of TiO2 nanotubes anodized under controlled hydrodynamic conditions, J. Electroanal. Chem. 897 (2021) 115579. https://doi.org/10.1016/J.JELECHEM.2021.115579.
[50] J. Borràs-Ferrís, R. Sánchez-Tovar, E. Blasco-Tamarit, R.M. Fernández-Domene, J. García-Antón, Effect of Reynolds number and lithium cation insertion on titanium anodization, Electrochimica Acta 196 (2016) 24–32. https://doi.org/10.1016/J.ELECTACTA.2016.02.160.
[51] G. Zu, H. Li, S. Liu, D. Li, J. Wang, J. Zhao, Highly efficient mass determination of TiO2 nanotube arrays and its application in lithium-ion batteries, Sustain. Mater. Technol. 18 (2018) e00079. https://doi.org/10.1016/J.SUSMAT.2018.E00079.
[52] Y. Guo, X. Quan, N. Lu, H. Zhao, S. Chen, High photocatalytic capability of self-assembled nanoporous WO3 with preferential orientation of (002) planes, Environ. Sci. Technol. 41 (2007) 4422–4427. https://doi.org/10.1021/ES062546C/ASSET/IMAGES/LARGE/ES062546CF00008.JPEG.
[53] Z.F. Huang, J. Song, L. Pan, X. Zhang, L. Wang, J.J. Zou, Tungsten Oxides for Photocatalysis, Electrochemistry, and Phototherapy, Adv. Mater. 27 (2015) 5309–5327. https://doi.org/10.1002/ADMA.201501217.
[54] R. Sánchez-Tovar, R.M. Fernández-Domene, D.M. García-García, J. García-Antón, Enhancement of photoelectrochemical activity for water splitting by controlling hydrodynamic conditions on titanium anodization, J. Power Sources 286 (2015) 224–231. https://doi.org/10.1016/j.jpowsour.2015.03.174.
[55] N. Serpone, Is the band gap of pristine TiO2 narrowed by anion- and cation-doping of titanium dioxide in second-generation photocatalysts?, J. Phys. Chem.

B 110 (2006) 24287–24293. https://doi.org/10.1021/JP065659R/ASSET/IMAGES/MEDIUM/JP065659RE00001.GIF.

[56] R. Verma, S.K. Samdarshi, Correlating oxygen vacancies and phase ratio/interface with efficient photocatalytic activity in mixed phase TiO2, J. Alloys Compd. 629 (2015) 105–112. https://doi.org/10.1016/J.JALLCOM.2014.12.218.

[57] T.K. Das, P. Ilaiyaraja, P.S.V. Mocherla, G.M. Bhalerao, C. Sudakar, Influence of surface disorder, oxygen defects and bandgap in TiO2 nanostructures on the photovoltaic properties of dye sensitized solar cells, Sol. Energy Mater. Sol. Cells 144 (2016) 194–209. https://doi.org/10.1016/J.SOLMAT.2015.08.036.

[58] J. Ananpattarachai, P. Kajitvichyanukul, S. Seraphin, Visible light absorption ability and photocatalytic oxidation activity of various interstitial N-doped TiO2 prepared from different nitrogen dopants, J. Hazard. Mater. 168 (2009) 253–261. https://doi.org/10.1016/J.JHAZMAT.2009.02.036.

[59] A.K. Wahab, S. Ould-Chikh, K. Meyer, H. Idriss, On the "possible" synergism of the different phases of TiO2 in photo-catalysis for hydrogen production, J. Catal. 352 (2017) 657–671. https://doi.org/10.1016/J.JCAT.2017.04.033.

[60] W. Zhao, Y. Wang, A. Wang, L. Wu, Q. Wang, Facile synthesis and photocatalytic activity of a novel titanium dioxide nanocomposite coupled with zinc porphyrin, Nanomater. Nanotechnol. 6 (2016) 1–6. https://doi.org/10.1177/1847980416669487.

[61] J. Tauc, R. Grigorovici, A. Vancu, Optical Properties and Electronic Structure of Amorphous Germanium, Phys. Status Solidi B 15 (1966) 627–637. https://doi.org/10.1002/PSSB.19660150224.

[62] K.M. Reddy, S.V. Manorama, A.R. Reddy, Bandgap studies on anatase titanium dioxide nanoparticles, Mater. Chem. Phys. 78 (2003) 239–245. https://doi.org/10.1016/S0254-0584(02)00343-7.

[63] X. Wu, J. Du, Y. Gao, H. Wang, C. Zhang, R. Zhang, H. He, G. (Max) Lu, Z. Wu, Progress and challenges in nitrous oxide decomposition and valorization, Chem. Soc. Rev. 53 (2024) 8379–8423. https://doi.org/10.1039/D3CS00919J.

[64] K. Kočí, M. Reli, I. Troppová, M. Šihor, J. Kupková, P. Kustrowski, P. Praus, Photocatalytic decomposition of N2O over TiO2/g-C3N4 photocatalysts heterojunction, Appl. Surf. Sci. 396 (2017) 1685–1695. https://doi.org/10.1016/j.apsusc.2016.11.242.

Chapter 6: Overall Conclusions

The present thesis provides some guidelines on how the design of metal oxide catalysts, together with the study of their properties, can lead to the valorization or elimination of a highly contributing greenhouse gas to global warming: nitrous oxide.

Thermocatalytic valorization of N_2O has been achieved by employing it as an oxidizing agent in the oxidative dehydrogenation of ethane to obtain ethylene. For the nickel oxide catalysts supported on ceria, it has been concluded that Ni/Ce is not a suitable catalyst for the proposed reaction due to the low selectivity to ethylene, despite both metal oxides being active in ethane ODH and N_2O decomposition. Thus, the catalyst was modified with the incorporation of different Zr loadings. A small loading of zirconia led to an increased selectivity to ethylene, while an excess provoked a drop in both selectivity and activity. Interestingly, the replacement of molecular oxygen by nitrous oxide in the ethane ODH over these Ni/CeO_2-ZrO_2 catalysts resulted in a significant improvement in selectivity towards olefin formation, but also in a much lower catalytic activity. In any case, the results obtained are not competitive and it seems that this catalytic system is not worthy to be explored in the future.

The study on oxidative dehydrogenation of ethane assisted by nitrous oxide was continued over bulk (non-supported) nickel oxide-based catalysts. It has been concluded that the incorporation of a high valence promoter remarkably enhances the catalytic performance of the NiO catalysts. Particularly, ethylene yields of ca. 40% have been achieved under unoptimized reaction conditions using the Nb-doped catalyst. In this case, when compared to the experiments carried out with molecular oxygen, selectivity to ethylene significantly increased with the use of nitrous oxide as an oxidant, while the catalytic activity remained the same. Moreover, this catalyst resulted to be highly stable in reaction. These results are, to our knowledge, among the best reported to date for ethane ODH assisted by N_2O.

MoVTeNb-M1 catalysts were also tested in the N_2O-ODH of ethane, as they offer the best catalytic results reported in the literature for the ODH reaction with O_2. Unfortunately, the use of nitrous oxide was shown to be detrimental for both selectivity to ethylene and catalytic activity compared to analogous experiments with molecular oxygen. Selectivity to olefin decreases by 10 points when compared to the O_2-ODH results, and the activity is 40 times lower with N_2O than with O_2. Consequently, N_2O decomposition experiments were carried out for these catalysts, concluding that M1 catalysts hardly activate the N_2O molecule. Therefore, the poor ability to break down nitrous oxide into nitrogen and oxygen limits the re-oxidation of the catalyst active sites during the redox cycle. It can be concluded that one of the main factors to consider when choosing the catalyst for N_2O-ODH should be the ability to activate both ethane and N_2O. Hence, the NiO-based catalysts appear to be the most promising materials for further research on N_2O-ODH.

Furthermore, the catalytic results of the three studied catalytic systems have been related to the electrochemical properties. In particular, selectivity to olefins has been associated with the concentration of defects and the charge-transfer resistance at the surface active sites of the catalysts. Overall, regardless of the type of catalyst, an excess of defects favors the formation of carbon oxides.

Regarding the synthesized photoelectrocatalysts, N_2O photoelectrocatalytic reduction has been successfully achieved. Mixed copper oxides photocathodes were easily fabricated by electrochemical anodization, employing novel electrolytes and under novel synthesis conditions (hydrodynamic conditions). This way, photocathodes with homogeneous morphologies and high electrical conductivity, due to an important presence of copper vacancies, were obtained. The optimized CuO_X photocathode has set an example in the photoelectro-reduction of N_2O, proving the better efficiency of the photoelectrocatalytic approach against the photo-

or electrocatalytic approaches at the same time that N_2O was totally removed in only 1h.

Similarly, the morphological and electrochemical properties of titania nanotubes were improved with the addition of a protic ionic liquid to the anodization electrolyte. It was demonstrated that the photoelectrochemical performance can be enhanced by the tailored morphology provided by the ionic liquids. Anodization conditions were optimized further with the incorporation of controlled hydrodynamic conditions. The titanium electrochemical anodization combining mild rotation speeds with low concentrations of both fluoride species and PILs significantly improves the photoelectrochemical response of the obtained photoanodes, achieving total nitrous oxide elimination after 3h.

Resumen Extendido

En la actualidad, el suministro mundial de energía depende de fuentes no renovables, lo que contribuye a las emisiones de gases de efecto invernadero y, en consecuencia, al calentamiento global. Los tres principales gases de efecto invernadero son el dióxido de carbono, el metano y el óxido nitroso. Sin embargo, la larga vida del N_2O en la atmósfera ha provocado que su potencial de calentamiento global sea unas 300 veces superior al del dióxido de carbono. En los dos últimos siglos, la concentración atmosférica de N_2O ha aumentado un 20%, desde 270 ppb aproximadamente en la era preindustrial a unos 337 ppb actualmente, con un aumento estimado del 2% por década. El 40% de las emisiones del óxido nitroso son derivadas de la actividad humana. En concreto, la producción de ácido nítrico y de ácido adípico contribuyen en gran medida a la emisión de este gas, siendo el 80% de las emisiones industriales de N_2O un subproducto en la producción de ácido adípico. Para poder reducir las emisiones de óxido nitroso, se debería evitar su formación, mejorando la eficacia de procesos y equipos, y reduciendo el consumo de combustibles fósiles. La mayoría de la tecnología que se podría emplear para evitar la formación de N_2O se encuentra aún bajo desarrollo y todavía no se ha podido implementar. Por ello, se deben incluir técnicas de eliminación entre las unidades de los distintos procesos que producen óxido nitroso como subproducto.

Existen diferentes técnicas de eliminación de N_2O y, entre ellas, destaca la descomposición directa del óxido nitroso, que puede ser por vía térmica o por vía catalítica. La descomposición térmica es un proceso que requiere elevadas temperaturas, por lo que solo es económicamente viable incluirla en procesos donde se alcanzan dichas temperaturas en las etapas en las que se forma el N_2O. Se considera que esta técnica de eliminación tiene requisitos muy específicos para poder funcionar correctamente como, por ejemplo, la necesidad de controlar la temperatura en la zona de descomposición para prevenir la formación de óxidos de nitrógeno. Por lo tanto, se deben considerar otras técnicas más eficientes. En la actualidad, la técnica más empleada en la industria es la descomposición catalítica del N_2O, en la

que la descomposición directa se lleva a cabo en presencia de un catalizador. De esta forma, la descomposición es más eficiente, más barata y más respetuosa con el medio ambiente, ya que la incorporación de un catalizador disminuye la energía de activación y, con ella, la temperatura de reacción. Además, con esta técnica, se han alcanzado conversiones de N_2O superiores al 99%.

Por otro lado, el avance en las etapas de separación incluidas en los procesos industriales ha hecho posible aislar el N_2O de los demás gases de escape para así poder valorizarlo en otras aplicaciones industriales. Por ejemplo, se ha prestado atención al uso de óxido nitroso como agente oxidante en la deshidrogenación oxidativa (DHO) de etano para obtener etileno, reacción que hasta la fecha se ha realizado mayoritariamente con oxígeno molecular. Este proceso se presenta como una alternativa al proceso de obtención de etileno tradicional, la pirólisis con vapor, que requiere de temperaturas de reacción muy elevadas, al no contar con un catalizador. Esto provoca un consumo energético muy elevado (16 GJ/tonelada de etileno producido al emplear etano como materia prima). Además, se generan entre 1 y 2 toneladas de CO_2 por cada tonelada de etileno producido. Al mismo tiempo, la gran cantidad de coque que se forma en el reactor resulta en la necesidad de paradas periódicas del reactor para llevar a cabo su limpieza. Entre los métodos de producción de etileno alternativos, destacan la deshidratación de (bio)etanol, la deshidrogenación catalítica de etano y la deshidrogenación oxidativa de etano. El consumo energético y las emisiones de CO_2 y N_2O en la deshidratación de (bio)etanol es mucho menor que en la pirólisis con vapor. Sin embargo, la producción de etileno mediante este método es muy reducida debido a que el etanol debe ser generado previamente de manera barata y directa. En cuanto a la deshidrogenación catalítica de etano, a pesar de haber reducido la temperatura de reacción respecto a la pirólisis con vapor, el rendimiento a etileno sigue siendo bajo y la desactivación del catalizador por la formación de depósitos de coque requiere regeneraciones periódicas del mismo.

La deshidrogenación oxidativa de etano es una reacción exotérmica, en la que, al alimentar un oxidante, se produce la regeneración in-situ del catalizador y se minimiza su desactivación. Sin embargo, existen reacciones secundarias que disminuyen la eficacia del proceso. En primer lugar, se puede producir la oxidación de etano, dando lugar a dióxido de carbono. Por otro lado, la sobre-oxidación del etileno ya formado da lugar a monóxido de carbono. No obstante, el consumo energético de la DHO de etano es mucho menor que el de la pirólisis con vapor, ya que la activación se produce a temperaturas mucho menores. Además, requiere menos etapas de separación, debido a un reducido número de productos secundarios (óxidos de carbono y agua). El oxidante más empleado es el oxígeno, pero el CO_2 y el N_2O se presentan como alternativas viables, puesto que su carácter oxidante más suave se estima que puede evitar la formación excesiva de óxidos de carbono y aumentar la selectividad a etileno. Hasta la fecha, los catalizadores más eficientes en la DHO de etano asistida por oxígeno son los basados en óxidos mixtos multicomponentes (Mo-V-Te-Nb) y en óxidos de níquel. En la presente tesis se lleva a cabo un estudio pormenorizado del uso de estos catalizadores en la deshidrogenación oxidativa de etano asistida por N_2O, ya que no se ha realizado ninguna investigación exhaustiva hasta la fecha.

Recientemente, la descomposición fotocatalítica del N_2O, empleando un material semiconductor expuesto a luz visible o ultravioleta, se ha popularizado debido a su eficiencia y su bajo requerimiento energético. Sin embargo, todavía se necesitan elevados tiempos de reacción para obtener resultados competitivos. Por otro lado, también se han realizado ensayos de reducción electrocatalítica del óxido nitroso. Se han logrado conversiones elevadas de N_2O, pero realizando los ensayos en condiciones severas de reacción (elevado potencial y temperatura). Con la descomposición fotoelectrocatalítica se mejora la eficacia del proceso, puesto que el mecanismo de reducción del N_2O se favorece al aplicar conjuntamente una fuente de luz y un pequeño potencial externo. Además, es posible llevar a cabo dicho proceso

en condiciones suaves de operación (temperatura y presión ambiente). Esta técnica presenta además las ventajas de fácil escalado, bajo consumo energético y la posibilidad de suministrar la energía necesaria mediante fuentes renovables. Sorprendentemente la descomposición fotoelectrocatalítica del N_2O no se ha llevado a cabo en ningún estudio. En la presente tesis se ha llevado a cabo la fotoelectro-reducción del óxido nitroso, empleando un fotocátodo de óxidos mixtos de cobre y un fotoánodo de dióxido de titanio.

En base a todo lo comentado, la presente tesis se centra en el diseño de catalizadores basados en óxidos metálicos capaces de valorizar o eliminar el óxido nitroso, como solución al incremento de la concentración atmosférica de N_2O (de más del doble) previsto para 2050. La tesis se divide claramente en dos secciones: la transformación termocatalítica del N_2O, donde se estudian múltiples sistemas catalíticos en la deshidrogenación oxidativa del etano asistida por N_2O (NiO/CeO_2-ZrO_2, óxidos de níquel promovidos y óxidos mixtos de MoVTeNb); y la eliminación fotoelectrocatalítica del N_2O, donde se han sintetizado por anodizado electroquímico óxidos mixtos de cobre y dióxido de titanio nanoestructurados para ser empleados como fotocátodo y fotoánodo, respectivamente, en la fotoelectro-reducción del óxido nitroso.

En primer lugar, se han sintetizado catalizadores de NiO/CeO_2 y NiO/CeO_2-ZrO_2 mediante la coprecipitación de sales metálicas de Ni, Ce y Zr, calcinados para obtener la fase activa NiO soportada en CeO_2 o CeO_2–ZrO_2. Todos los catalizadores muestran áreas superficiales específicas entre 40 y 90 m^2/g, aproximadamente. La incorporación de una carga baja de Zr aumentó ligeramente el área específica. Sin embargo, el aumento excesivo del contenido de circonio redujo el área específica de 90 hasta 39 m^2/g.

A continuación, se evaluaron en la deshidrogenación oxidativa de etano en un reactor de lecho fijo, con una corriente de alimentación de composición 5/10/85

de etano/N_2O/helio. La producción óptima de etileno se ha alcanzado con la incorporación de una baja carga de circonio (relación Zr/Ce=0.1 at.), superando la obtenida por el catalizador NiO/CeO_2 sin circonio. Por el contrario, mayores contenidos de circonio condujeron a una menor formación de olefinas. El comportamiento catalítico observado se ha atribuido a diferencias en la concentración de vacantes de oxígeno, las fases cristalinas presentes y el tipo de especies de níquel en la superficie. Concretamente, mediante la difracción de rayos X se ha confirmado la formación de la fase cúbica de CeO_2 y la dispersión del níquel en la superficie del catalizador al no identificarse los picos atribuibles al NiO cristalino. El mismo difractograma se ha observado en los catalizadores dopados con Zr^{4+}, con una leve **c**ontracción de la celda unitaria**,** que indica la incorporación efectiva del Zr en la red de CeO_2**.** También se ha realizado la difracción de rayos X del catalizador más activo/selectivo, $Ni\text{-}Ce_{0.9}Zr_{0.1}$, tras emplearse en la reacción. El catalizador no presenta ninguna modificación en su estructura cristalina ni en su tamaño de cristal, lo que confirma la estabilidad del catalizador. La microscopía electrónica de transmisión revela la geometría esférica y uniforme de las partículas. Además, la técnica EDX indica la distribución homogénea del níquel sobre la matriz del óxido de cerio en el catalizador Ni-Ce. En los catalizadores con circonio, tanto el níquel como el cerio se encuentran bien distribuidos en la superficie del catalizador. Sin embargo, en el catalizador con elevada carga de Zr, se puede apreciar la presencia de aglomerados de zirconio. Mediante la técnica de espectroscopía de fotoelectrones de rayos X ha sido posible confirmar la presencia de Ni^{2+}**,** Ce^{4+}/Ce^{3+} y Zr^{4+} en la superficie de los diferentes catalizadores. A pesar de la mayor proporción de Ce^{4+}, se ha detectado una proporción significativa de Ce^{3+}, lo que indica la existencia de vacantes de oxígeno, esenciales para la activación del N_2O, pero perjudiciales para la formación de etileno. De hecho, una concentración de circonio demasiado elevada aumenta la presencia de especies de níquel no estequiométricas, lo que conduce a una disminución en la selectividad a etileno. Sin embargo, el dopaje

con una pequeña cantidad de Zr provoca la disminución de esta especie y la consiguiente mejora en el rendimiento.

En la presente tesis, ha sido posible establecer una relación entre las propiedades catalíticas y las electroquímicas. Los ensayos de Mott-Schottky revelan el carácter semiconductor tipo n de los catalizadores estudiados. Para este tipo de materiales, los catalizadores con menor número de defectos (vacantes de oxígeno) se consideran los más selectivos a etileno. Esto se debe a que una elevada concentración de vacantes de oxígeno implica la pérdida de oxígenos nucleofílicos al transformarse en oxígeno gaseoso, ya que estas especies de oxígeno son las responsables de la oxidación parcial del etano para obtener etileno. De este estudio, se ha podido comprobar que el catalizador dopado con una pequeña cantidad de circonio, presenta el menor número de vacantes de oxígeno, lo que explica su mejor selectividad a etileno. Como resultado a destacar, se ha logrado aumentar significativamente la selectividad a etileno con el uso de óxido nitroso como oxidante, en comparación con los resultados obtenidos utilizando oxígeno molecular. De hecho, en condiciones de isoconversión, la selectividad a la olefina es aproximadamente 15 puntos mayor con óxido nitroso que con oxígeno molecular. Además, el catalizador NiO/CeO_2-ZrO_2 optimizado presenta una excelente estabilidad catalítica. Desgraciadamente, la formación global de olefinas con el catalizador óptimo sigue siendo bastante modesta.

Debido a esta formación limitada de etileno, en la siguiente sección de la presente tesis se han preparado nuevas formulaciones catalíticas basadas en óxido de níquel para obtener mejores resultados catalíticos durante la DHO de etano asistida por óxido nitroso. Estos catalizadores se han sintetizado mediante el método de coprecipitación, a partir de la mezcla acuosa de los precursores metálicos y de una cantidad óptima de ácido oxálico. Teniendo en cuenta los resultados de área específica obtenidos a partir del estudio BET, se puede concluir que añadir ácido

oxálico en la síntesis del óxido de níquel sin dopar aumenta el área específica un 75%. Del mismo modo, la incorporación de diferentes dopantes ha provocado un aumento considerable en el área específica de estos materiales. Dopando el óxido de níquel con Ce^{4+}, Ti^{4+} y Nb^{5+} se ha logrado el mayor incremento en el área específica (65-68 m^2/g). También se puede destacar que en la mayoría de los casos la fase cristalina principal es la correspondiente al NiO cúbico, detectándose algunos picos de baja intensidad correspondientes a Bi_2O_3, In_2O_3, CeO_2 y TiO_2 en las muestras dopadas con bismuto, indio, cerio y titanio, respectivamente.

Tras emplear los catalizadores en la DHO de etano, con una corriente de alimentación de composición 5/10/85 de etano/N_2O/helio, se ha comprobado que la incorporación de ácido oxálico durante la síntesis del catalizador NiO provoca una mejora significativa tanto en la actividad catalítica (aumento del 185%) como en la selectividad a etileno, que se ha atribuido, en parte, al incremento en el área específica. Por otro lado, la introducción de algunos promotores metálicos (Ce^{4+}, Ti^{4+} o Nb^{5+}) también mejora la selectividad. Al comparar selectividades a 400 °C y a la misma conversión (30 % de etano), todos los catalizadores dopados superan al óxido de níquel puro sin ácido oxálico, siendo el NiO dopado con Nb^{5+} el más selectivo (hasta 40 puntos porcentuales por encima del NiO de referencia), seguido por los dopados con Ti^{4+} y Ce^{4+}. Por ello, se ha demostrado que la incorporación de promotores adecuados, como el niobio, favorece la formación de etileno (rendimiento de hasta un 40%) con una selectividad a etileno del 72%, manteniendo una conversión a etano del 55%. Cabe destacar que, además de la mayor selectividad a etileno, el NiO dopado con niobio muestra una excelente estabilidad a largo plazo, manteniendo la actividad durante, por lo menos, 24 horas. En general, el catalizador óptimo (Nb)NiO muestra el mejor rendimiento descrito hasta la fecha en la bibliografía. En general, los resultados catalíticos para la deshidrogenación oxidativa de etano asistida por N_2O sobre catalizadores basados en NiO muestran una mayor selectividad hacia el etileno en comparación con la reacción asistida por oxígeno.

Todos los catalizadores muestran una alta eficacia en la descomposición del N_2O, lo que garantiza una rápida velocidad de reoxidación del catalizador durante las pruebas catalíticas.

Las diferencias en los resultados catalíticos para la DHO asistida por N_2O están relacionadas con los cambios producidos en el catalizador como consecuencia de la presencia de diferentes promotores. Por lo tanto, el rendimiento catalítico global depende en gran medida tanto de la presencia como de la naturaleza del dopante. De este modo, se ha observado que al incorporar dopantes básicos (típicamente elementos de baja valencia) en un óxido, se eleva la valencia del níquel hasta su estado más alto accesible. Sin embargo, los dopantes ácidos (elementos con un estado de valencia alto, como el Nb^{5+}) reducen el estado de valencia del metal huésped hacia su valencia más baja disponible. Los sitios de níquel no estequiométricos estabilizan especies de oxígeno electrofílicas no selectivas, y en consecuencia se observa una menor formación de etileno. Por tanto, se ha establecido una correlación entre la valencia del promotor y la selectividad hacia el etileno, de manera que cuanto mayor es la valencia del catión promotor, mayor es la selectividad hacia la olefina.

Por otro lado, no se ha encontrado ninguna correlación entre la formación de etileno y los resultados obtenidos mediante TPR-H_2 (reducibilidad) o por XPS (características de las especies de níquel en la superficie cercana). Sin embargo, la selectividad hacia etileno se ha relacionado con las propiedades electroquímicas de los catalizadores, en particular, con la concentración de defectos y la resistencia a la transferencia de carga en sus sitios activos interfaciales. Realizando medidas de espectroscopía de impedancia electroquímica, se ha podido establecer que los catalizadores más selectivos a etileno son aquellos que presentan la mayor resistencia al transporte de carga en la superficie activa del material. Esto está correlacionado con los portadores de carga presentes en los distintos catalizadores basados en óxido

de níquel. Todos los catalizadores, a excepción del dopado con niobio, presentan un carácter semiconductor p, según los resultados de los ensayos de Mott-Schottky. En este tipo de materiales, los portadores de carga principales son los huecos, que están relacionados con las vacantes catiónicas y con los aniones O^{2-} de red. Para este tipo de catalizadores, un elevado número de vacantes catiónicas implica la pérdida de las especies O^{2-} y la aparición de especies O^{-}, que son responsables de las reacciones de oxidación total de etano a óxidos de carbono. Por tanto, se ha establecido que cuanto mayor es el número de vacantes catiónicas en los catalizadores basados en NiO, menor es su selectividad a etileno. Como tendencia general, aquellos catalizadores con una superficie menos oxidada tienden a ser más selectivos hacia la formación de etileno, como también se ha propuesto para la DHO de etano asistida por O_2. Además, se ha podido apreciar que el niobio elimina el carácter p típico de los óxidos de níquel, al mostrar su gráfico de Mott-Schottky una ligera tendencia lineal positiva. El Nb^{5+} presenta un tamaño iónico suficiente para ocupar las vacantes Ni^{2+} en la red del óxido de níquel. De esta forma, el niobio actúa como especie donante de electrones y reduce la concentración de oxígenos electrofílicos, lo que explica su selectividad a etileno bastante superior al resto de catalizadores de NiO dopados. Para concluir con la caracterización electroquímica, se ha podido determinar con las voltamperometrías cíclicas la actividad electroquímica de los distintos materiales. Se ha observado que la actividad electroquímica es inversamente proporcional a la selectividad a etileno de los catalizadores de NiO, puesto que una elevada actividad electroquímica favorece las reacciones de oxidación total y la formación de óxidos de carbono. Por tanto, es lógico que los catalizadores más selectivos (dopados con niobio y titanio) sean los que presentan menor actividad electroquímica.

Como último paso en la transformación termocatalítica del N_2O, se han evaluado los catalizadores que han sido considerados en la literatura como los más eficientes en la deshidrogenación oxidativa de etano asistida por oxígeno molecular (óxidos mixtos MoVTeNb que presentan la fase cristalina M1). Sorprendentemente,

la reacción de DHO de etano con N_2O ha conducido a una caída significativa tanto de la selectividad a olefina como de la actividad catalítica en comparación con los experimentos análogos con O_2. En ambos casos, se empleó un alimento con la misma concentración de átomos de oxígeno. La selectividad a etileno con óxido nitroso es 10 puntos menor que la obtenida en O_2-DHO, y la actividad catalítica muestra una caída drástica de la actividad con una disminución total de 40 puntos.

Estos catalizadores se emplearon en la descomposición del óxido nitroso y se comprobó que los materiales que presentan la fase M1 muestran una capacidad muy limitada para activar la molécula de N_2O, puesto que menos del 1% de N_2O se transformó a oxígeno y nitrógeno a 425°C. Se cree que esto ralentiza la reoxidación de los sitios activos en la superficie del catalizador durante el ciclo redox, limitando en última instancia el rendimiento catalítico durante la DHO con N_2O. Por ello, se decidió aumentar la concentración de N_2O en la corriente alimento para intentar aumentar su conversión y la cantidad de especies de oxígeno disponibles para la DHO. Se hizo un estudio comparativo aumentando también la concentración de oxígeno en la DHO asistida por O_2. De este estudio se ha podido apreciar que el aumento en la concentración de N_2O supone un mayor incremento en la actividad que el aumento en la concentración de oxígeno. Además, una mayor proporción de óxido nitroso en el alimento ha conducido a un aumento de la selectividad a etileno, mientras que un aumento en la concentración de oxígeno ha derivado en lo contrario. Es posible que esta diferencia en los resultados se deba al distinto carácter oxidante del óxido nitroso y del oxígeno, dando lugar a diferentes velocidades de reoxidación de la superficie.

Sin embargo, se llevó a cabo la caracterización del catalizador tanto fresco como usado en ambas atmósferas para verificar si las propiedades del catalizador se modificaban tras su uso. Del análisis de XRD, se pudo observar que la estructura cristalina no se modificó tras usarse en ambas reacciones. Por otro lado, de la

caracterización electroquímica se ha podido apreciar un comportamiento diferente para cada muestra según el agente oxidante empleado. En primer lugar, la muestra utilizada en la reacción asistida por oxígeno presenta la mayor resistencia a la transferencia de carga en la superficie activa del catalizador. Como se ha comentado anteriormente, una mayor resistencia a la trasferencia de carga está relacionada con una mayor selectividad a etileno por la limitación de las reacciones de oxidación total. Por tanto, los resultados de la espectroscopía de impedancia electroquímica concuerdan con los resultados catalíticos, pues el catalizador presenta la mayor selectividad a etileno el emplearse en la DHO de etano asistida por O_2. Adicionalmente, se llevaron a cabo ensayos de Mott-Schottky para determinar el carácter semiconductor del catalizador y el número de defectos en cada muestra. De este estudio, se ha podido concluir que este tipo de catalizadores presentan principalmente una semiconductividad tipo n, donde las vacantes de oxígeno son el defecto mayoritario. Un elevado número de vacantes de oxígeno supone una pérdida de oxígenos nucleofílicos, que son los responsables de la transformación de etano a etileno. Por ello, la muestra con mayor número de vacantes de oxígeno, el catalizador empleado en la DHO con N_2O, es la de menor selectividad a etileno. Además, se puede apreciar un carácter semiconductor tipo p a mayores potenciales. En este tipo de semiconductores, el defecto principal son las vacantes catiónicas, que favorecen la formación de oxígenos electrofílicos. Una mayor concentración de vacantes catiónicas, que se puede estimar por una menor pendiente de la zona lineal negativa, resulta en una menor selectividad a etileno. Este fenómeno también podría explicar por qué el catalizador M1 presenta una menor selectividad a etileno al usarse en la reacción con N_2O.

Para concluir el capítulo de la transformación termocatalítca de N_2O, se ha llevado a cabo un estudio comparativo del catalizador más eficiente en la deshidrogenación oxidativa de etano asistida por N_2O, el de óxido de níquel dopado con niobio, y el más eficiente en la DHO asistida por oxígeno, el MoVTeNb. Se ha

estudiado el comportamiento de ambos catalizadores en la DHO de etano asistida por ambos agentes oxidantes, oxígeno y óxido nitroso. En general, se ha observado una tendencia totalmente opuesta entre el Nb(NiO) y el MoVTeNb. La actividad del catalizador M1 cae drásticamente al emplear óxido nitroso como oxidante debido a la incapacidad de activar la molécula del N_2O, mientras que para el Nb(NiO) la actividad es prácticamente la misma independientemente del oxidante empleado. En cuanto a la selectividad, la tendencia sigue siendo la opuesta. El catalizador MoVTeNb presenta mejor selectividad a etileno cuando se usa en la reacción con oxígeno, mientras que en el caso del Nb(NiO) la mejor selectividad a etileno se consigue empleando N_2O como oxidante. Es más, se pueden apreciar aún más diferencias cuando se incrementa la proporción de oxidante en la corriente de alimento. Por ejemplo, la caída en la selectividad a etileno del Nb(NiO) es más pronunciada al emplear O_2 como oxidante en la DHO de etano. Además, aunque la actividad catalítica aumenta al alimentar en mayor proporción ambos oxidantes, el incremento en la actividad es más acentuado cuando se aumenta la concentración de N_2O que cuando se aumenta la del oxígeno.

Este comportamiento diferente se ha asociado con las propiedades electroquímicas de cada catalizador. Se ha podido establecer que, a pesar de ser catalizadores con distinto carácter semiconductor, en ambos casos la formación de óxidos de carbono está relacionada con la concentración de defectos en la superficie del catalizador. Para un semiconductor tipo n (M1), la formación de óxidos de carbono se verá favorecida por un elevado número de vacantes de oxígeno, mientras que para un semiconductor tipo p, la aparición de estos productos de carbono se verá favorecida por un número elevado vacantes catiónicas.

Del estudio de la transformación termocatalítica de N_2O, se ha podido concluir que los catalizadores más eficientes en la deshidrogenación oxidativa de etano asistida por óxido nitroso son aquellos basados en óxidos de níquel. Sin

optimizar las condiciones de reacción ha sido posible obtener los mejores resultados en la DHO con N_2O hasta la fecha. También se puede concluir que, a pesar de ser los más eficientes en la DHO asistida por oxígeno, los óxidos mixtos multicomponentes (MoVTeNb) no son los idóneos para llevar a cabo esta reacción con óxido nitroso.

En lo que respecta a la reducción fotoelectrocatalítica del óxido nitroso, se han fabricado fotoelectrocatalizadores de óxidos de cobre mixtos y de dióxido de titanio mediante anodizado electroquímico para obtener un fotocátodo y un fotoánodo, respectivamente. Se han sintetizado fotocátodos de CuO_X (x = 1 y 2) nanoestructurados mediante anodizado electroquímico en electrolitos basados en etilenglicol utilizando ácido oxálico o fluoruro sódico como agentes complejantes, estudiando al mismo tiempo la influencia de la adición de NaOH. De este estudio se concluyó, que la síntesis basada solo en ácido oxálico produce los fotoelectrocatalizadores con mejores propiedades (foto)electroquímicas. Entre los diferentes motivos destacan la morfología más homogénea y la mayor presencia de Cu_2O, confirmada por las técnicas de XRD, Raman y DR-UV-visible. Adicionalmente, se han investigado los efectos del anodizado durante diferentes tiempos y empleando diferentes proporciones (50, 70 y 90%) de distintos disolventes orgánicos (etanol, etilenglicol y formamida).

El anodizado durante tiempos más largos condujo a una pérdida en el área específica por el crecimiento de un menor número de nanoesferas y de mayor tamaño. Esto se tradujo en una menor foto-respuesta de los fotoelectrocatalizadores. Analizando las curvas de anodizado con diferentes disolventes y proporciones, se ha podido concluir que la correspondiente al anodizado con un electrolito del 70% de etilenglicol es la única que sugiere la formación de una nanoestructura bien definida, lo que se ha podido confirmar con el estudio morfológico mediante el FE-SEM. Tras probar todas las muestras en la ruptura fotoelectroquímica del agua, se ha podido

concluir que, efectivamente, el fotoelectrocatalizador con mayor foto-respuesta es el sintetizado en un electrolito con 70% de etilenglicol.

Por último, se ha estudiado el efecto de llevar a cabo el anodizado electroquímico de óxido de cobre en condiciones hidrodinámicas de flujo controladas. Se sintetizaron fotoelectrocatalizadores a 0, 250 y 500 rpm. El anodizado electroquímico a 250 rpm condujo a la formación de un fotocátodo homogéneo compuesto por pequeñas nanoesferas, con óxido de cobre (I) como fase predominante. Al realizar el anodizado en condiciones de agitación excesivas, se formaron aglomerados de las nanoesferas, reduciendo así también el área específica, y se disminutó la fracción de Cu_2O presente, aumentando a la vez la fracción de CuO. Tras evaluar las 3 muestras en la ruptura fotoelectrocatalítica del agua, se comprobó que el fotoelectrodo sintetizado a 250 rpm presenta el mejor comportamiento fotoelectrocatalítico. De hecho, al emplearse como fotocátodo durante la fotoelectro-reducción de óxido nitroso, se consiguió eliminar casi por completo el N_2O tras 1 hora. Además, este fotocátodo mostró un rendimiento fotoelectrocatalítico muy superior en comparación con los enfoques puramente foto o electrocatalíticos. De acuerdo con los datos disponibles hasta la fecha, esta es la primera vez que se ha investigado la descomposición catalítica utilizando un enfoque combinado foto y electrocatalítico.

En cuanto a los fotoánodos de TiO_2, la presente tesis se ha centrado en la síntesis de nanotubos de dióxido de titanio empleando diferentes líquidos iónicos próticos (LIPs) para evaluar su influencia en el rendimiento del fotoánodo durante la reducción fotoelectrocatalítica de N_2O. En estudios previos, se concluyó que la incorporación de una pequeña cantidad (1%) de un líquido iónico basado en monoetanolamina (MEA) mejoraba el comportamiento fotoelectrocatalítico, en mayor medida, que el obtenido al doblar la concentración de fluoruros en el electrolito de anodizado. Por ello, se ha llevado a cabo un estudio similar empleando

un líquido iónico basado en trietanolamina (TEA). Las diferentes muestras se sometieron a una exhaustiva caracterización morfológica, estructural, fisicoquímica y (foto)electroquímica para determinar la nanoestructura más eficaz en la aplicación de interés. El líquido iónico TEA proporcionó mejores resultados que los obtenidos para los líquidos iónicos próticos basados en etanolaminas (MEA y dietanolamina, DEA) en los ensayos de ruptura fotoelectrocatalítica del agua.

Por ello, se decidió escoger dicho LIP y optimizar aún más el proceso de anodizado electroquímico variando las condiciones hidrodinámicas (0, 500, 1000 y 2000 rpm). Al introducir la rotación del electrodo durante el anodizado, se obtuvo que para las muestras sintetizadas con 1% de TEA en el electrolito las condiciones hidrodinámicas eran perjudiciales para las mismas, ya que los tubos empezaban a deformarse hasta obturarse por completo. Se decidió realizar el estudio de la influencia de las condiciones hidrodinámicas para electrolitos menos concentrados en TEA. Tras realizar la caracterización morfológica y electroquímica se ha podido concluir que los nanotubos con mejores dimensiones y mejor respuesta a la luz son los sintetizados con una concentración intermedia de TEA (0.25%) a una velocidad de rotación del electrodo de 500 rpm. Estos resultados han sido respaldados por la caracterización electroquímica. De los ensayos de espectroscopía de impedancia electroquímica, se ha podido observar que la muestra con menor resistencia a la transferencia de carga en la superficie activa del fotocatalizador es la sintetizada a 500 rpm, lo que implica una mejor movilidad de electrones y, por tanto, una mayor actividad fotoelectroquímica. En concordancia con estos resultados, los ensayos de Mott-Schottky revelan que el anodizado en condiciones hidrodinámicas aumenta la concentración de defectos en dichas nanoestructuras, lo que se traduce en un mejor comportamiento fotoelectroquímico por un aumento en la conductividad eléctrica de las muestras. La reducción fotoelectrocatalítica de N_2O se llevó a cabo empleando, por un lado, la nanoestructura determinada como óptima (0.25% TEA y 500 rpm), y por otro la nanoestructura base (sin TEA y sin revoluciones). El mejor rendimiento

fotoelectroquímico se obtuvo con la muestra anodizada con TEA a 500 rpm, consiguiéndose una eliminación del 97% de N_2O en 2 horas y una eliminación completa al cabo de 3 horas.

En conclusión, se ha logrado satisfactoriamente el principal objetivo de la tesis doctoral: diseñar y optimizar catalizadores capaces de valorizar o eliminar el gas de efecto invernadero N_2O. Con el fin de alcanzar este propósito, se han llevado a cabo diferentes métodos de síntesis de catalizadores nanoestructurados, empleando en algunas ocasiones condiciones experimentales novedosas. Además, se ha logrado establecer por primera vez para estos sistemas catalíticos, una relación entre las propiedades electroquímicas y los resultados catalíticos de todos los termocatalizadores estudiados.

Appendix I

Index of Figures

Chapter 1: Introduction

Chapter 3: Experimental Section

Chapter 4: Thermocatalytic transformation of N_2O

Chapter 5: Photoelectrocatalytic transformation of N_2O

Appendix II

Index of Tables

Chapter 1: Introduction

Chapter 3: Experimental Section

Chapter 4: Thermocatalytic transformation of N_2O

Chapter 5: Photoelectrocatalytic transformation of N_2O